Synthesis of New Composites of Inorganic Polymers (Geopolymers) with Metal Oxide Nanoparticles and their Photodegradation of Organic Pollutants

By

Mahroo Falah

A thesis
Submitted to Victoria University of Wellington
in fulfilment of the requirements for the degree of
Doctor of Philosophy in Chemistry

TE WHARE WĀNANGA O TE ŪPOKO O TE IKA A MĀUI

VICTORIA
UNIVERSITY OF WELLINGTON

Victoria University of Wellington

2015

Synthesis of New Composites of Inorganic Polymers (Geopolymers) with Metal Oxide Nanoparticles and their Photodegradation of Organic Pollutants

Abstract

This thesis describes the development and performance of novel photocatalytic inorganic polymer (geopolymer) composites for photodegradation of environmentally harmful organic materials. Nanometer-sized cubic cuprous oxide nanoparticles and spherical Cu_2O/TiO_2 nano-heterostructures were synthesized *via* a precipitation method and then added to a metakaolinite-based geopolymer matrix prior to curing at ambient temperature.

The morphology of the homogeneous oxide nanoparticle dispersion within the geopolymer matrix was demonstrated by SEM/EDS and HRTEM. FTIR spectroscopy confirmed the formation of a well-reacted geopolymer matrix that was unaffected by the insertion of the Cu_2O and Cu_2O/TiO_2 nanoparticles. The structures of these new composites were determined by ^{27}Al and ^{29}Si MAS NMR spectroscopy. ^{63}Cu NQR spectroscopy and XRD confirmed that the metal oxide nanoparticles are unchanged by their incorporation in the geopolymer composite and after the photodegradation reactions. The nitrogen adsorption-desorption isotherms were determined, providing information about the specific surface areas and total pore volumes of the composites. The action of the composites in the adsorption and photocatalytic destruction of the model organic compound MB was determined under dark and UV illumination conditions. Experiments in dark conditions and under UV irradiation showed that these materials efficiently remove a model organic pollutant (MB dye) from solution by a dual process of adsorption on the geopolymer matrix, and photodecomposition of the dye without destroying the geopolymer structure. The adsorption kinetics of the dye are best described by a pseudo first-order model and the adsorption process by Langmuir-Freundlich isotherms.

In a novel extension of this research, the metakaolinite-based geopolymer matrix was modified with a surfactant (cetyltrimethylammonium bromide, CTAB), exploiting the cation exchange capacity of the geopolymers structure. The nano oxide composites were synthesised by adding different amounts of as-prepared metal oxide nanoparticles to the modified geoplymer to produce a hydrophobic photocatalyst composite with improved photocatalytic activity arising from the dispersion of the metal oxide nanoparticles in the external surfaces

and interlayers of the geopolymer matrix. This method has the advantage of producing geopolymer composites with a stable pH which are more suitable for dye degradation studies. At concentrations >20 wt%, the photo-oxide component decreases the adsorption rate by blocking the active adsorption sites of the geopolymer. Under UV radiation, the composites remove the MB by a combination of adsorption and photodegradation, without deterioration of the geopolymer structure or the photoactive metal oxide component.

In addition these studies show that the metal oxide-geopolymer nano composites have significantly improved photocatalytic activity compared with the oxide nanoparticles alone, because of the unique properties of these inorganic polymers. These results demonstrate that composites of nanosized Cu_2O particles and photoreactive TiO_2 in an aluminosilicate inorganic polymer matrix constitute new and novel materials with potential environmental protection applications to efficiently remove organic pollutants from water or the atmosphere.

Acknowledgements

Mahroo

Table of Contents   **<u>Page</u>**

Chapter 4 ....**60**

Synthesis and characterization of new photoactive geopolymer composites with Cu_2O nanoparticles

Chapter 5 ....**85**

Synthesis, characterization and photoactive properties of geopolymer composites with Cu_2O /TiO_2 nano-heterostructures and P25 titania

List of Tables

List of Figures

Publications and conference presentations arising from this work

M. Fallah, K.J.D. MacKenzie, J.V. Hanna, S.J. Page, Novel photoactive inorganic polymer composites of inorganic polymers with copper (I) oxide nanoparticles. *Journal of Materials Science* (Published).

M. Falah, K. J.D. MacKenzie. Synthesis and properties of novel photoactive composites of P25 titanium dioxide and copper (I) oxide with inorganic polymers. *Ceramics International* (Published).

M. Falah, K. J.D. MacKenzie, J. V. Hanna, S. J. Page. Synthesis, structure and photoactivity of new composites of nanoparticle Cu (I) oxide supported on a novel aluminosilicate inorganic polymer with an expanded structure. (In preparation)

M. Falah, Photoactive inorganic polymer composites with oxide nanoparticles. 13th International Ceramics Congress (CIMTEC 2014), June 8th-13th 2014, Montecatini Terme, Italy. **Invited oral presentation**.

M. Falah. Novel Photoactive Inorganic Polymer Composites with Metal Oxide Nanoparticles. Asia Nanotechnology camp, (ANC 2014), October 8th -15th 2014, Tehran, Iran. (Poster presentation).

M. Falah, Novel Photoactive Inorganic Polymer Composites with Oxide Nanoparticles. AMN7 Conference, Nelson, New Zealand, February 2015. (Poster presentation).

M. Falah, Incorporation of photoactive Cu_2O in a metakaolinite inorganic polymer. AMN-6, Auckland, February 11th-13th 2013. (Poster presentation).

M. Falah, K. J. D. MacKenzie, New composites of inorganic polymers (GPs) with Cu_2O nanoparticles for photodegradation of organic pollutants. International Conference on Traditional and Advanced Ceramics (ICTA2013), Bangkok, Thailand, September 11th -13th, 2013. **Invited Presentation**.

List of Abbreviations

BET	Brunauer–Emmett–Teller
BG	Energy Band Gap
BJH	Barrett, Joyner, Halenda
CEC	Cation Exchange Capacity
CB	Conduction Band
CTAB	Cetyltrimethylammonium bromide
Cu_2O	Cuprous Oxide
EDS	Energy Dispersive X-ray Spectroscopy
FTIR	Fourier Transform Infrared Spectroscopy
FFT	Fast Fourier Transformation
GP	Geopolymer
HRTEM	High Resolution Transmission Electron Microscopy
MB	Methylene Blue
M-GP	Modified geopolymer CTAB
MMT	Montmorillinite
MO	Methyl Orange
Na-GP	Sodium Geopolymer
NMR	Nuclear Magnetic Resonance Spectroscopy
NQR	Nuclear Quadrupole Resonance
PVP	polyvinylpyrrolidone
SAED	Selected Area Diffraction
SEM	Scanning Electron Microscopy
STEM	Scanning transmission electron microscopy

TEM	Transition Electron Microscopy
TiO_2	Titanium Dioxide
UV	Ultraviolet
UV-Vis	Ultraviolet-visible Spectroscopy
VB	Valence Band
XRD	X-Ray Diffraction
XRF	X-Ray Fluorescence Spectroscopy

Chapter 1

Introduction

1.1 Background to the research problem

Air pollution poses a serious warning to human health and the environment. Pollutants from exhaust systems can cause unsightly blackening and costly degradation of walls and building facades. In most developed areas, the main sources of pollutants are automobile emissions, industrial activities, and heating systems.[1] These produce a mix of nitrogen oxides (NO_X), volatile organic compounds (VOCs), carbon monoxide (CO), sulphur oxides (SO_X), and particulate matter (PM).[1] The poisonous effects of these pollutants may spread out over the source of emission.[2] NO_2 and VOCs react in the atmosphere and produce secondary pollutants, such as acid rain, smog, and ozone. In order to create a more ecological world, engineers and scientists must develop greener building materials[2] by selecting suitable construction materials to reduce the negative impact of air pollution. Concrete is one of the most popular structural construction materials with a verified history over many years; it has an ability to produce strong creative and cost effective systems. The main ingredient in concrete is Portland cement, consisting of limestone (calcium carbonate, $CaCO_3$) and kaolinite clay which must be heated up to 1450 ºC.[3] Currently the contribution of Portland cement production worldwide to the greenhouse gas problem is about 1.35 billion tons of CO_2 annually or about 7% of the total greenhouse gas emissions into the earth's atmosphere.[4] Photocatalytic reactions can remove the air pollutants that are typically results in discoloration of exposed surfaces from the atmosphere. The basic photocatalyst reactions oxidize both organic and inorganic compounds by using the energy from ultraviolet (UV) rays through the photocatalytic materials.[2] New photocatalytic cements containing a photoactive oxide like TiO_2 have been produced, saving on maintenance costs and providing a cleaner environment.[2] The organic and inorganic pollutants produce staining on the surface of concrete. Novel self-cleaning concrete created to remove significant amounts of environmental pollutants considered harmful to human health,[2] should provide significant improvements in urban air quality, as it also can reduce micro-organisms such as bacteria and fungi and is capable of eliminating odours associated with pollutants. Other applications of these photocatalytic cements include architectural concrete panels, pavements, road surfaces, concrete masonry units, roof tiles and cement-based tiles.[2] The best application has developed an artificial lighting system that generates enough UV light to activate the photocatalytic

process. This product is a concrete with transparent property and the ability to transmit light; this light can pass through it and also show objects behind it. The lighting system and photocatalytic concrete cement have been used in the renovation of a heavily trafficked tunnel in Rome.[2]

According to the air quality standards in some parts of the world (Milan Italy), where occasionally automobile traffic has to be shut down for a full day, this transparent concrete can be helpful and also help with maintenance costs and a cleaner environment.[2] It is estimated that if just 15% of the buildings and roads were resurfaced with photocatalytic cement products Milan could become 50% cleaner. Nanoparticle photocatalytic cement containing titanium oxide as the photocatalytic agent is already being used for applications such as sound barriers, facade elements, pavement and road surfacing.[2]

Many research centres have been involved in examining the pollution-reducing capability of photocatalytic compounds, particularly those containing TiO_2. TiO_2 photocatalyts in the presence of sun or artificial light react with air pollutants and oxidize the organic and inorganic air pollutants, converting them into small amounts of relatively benign molecules. Both laboratory and field experiments disclose that adding TiO_2 to the surface of a pavement or building material can expressly reduce air pollution by up to 60% in some applications.[5] It is obvious that reduction of the negative impact of air pollution with nano TiO_2 is effective. Air pollution can be controlled by using photocatalytic TiO_2 in concrete or as a surface covering.[6] Figure 1.1. shows the photocatalysis reaction of precast and architectural Portland concrete panels in the presence of sunlight and how a photocatalytic city would work. The efficiency of the novel photocatalytic cement materials provides a real eco-sustainable value and according to the researchers this material can reduce pollution up to 75% under just 3 min. UV irradiation.[7] This phenomenon is similar to photosynthesis in nature; therefore, the light irradiation causes the oxidation process and decomposition of the pollutants, converting them to benign compounds. Subsequently these contaminants can be removed and washed away by rain.

Figure 1.1. Inorganic pollutant: CO, VOC (benzene, toluene, etc), methyl mercaptan (gas), organic chlorinated compounds, polycondensed aromatic compounds, acetaldehyde, formaldehyde. Organic pollutant: NO_X, SO_X, NH_3 (gas).[7]

Water is the one of the sources of all life on Earth; nevertheless, 1.3 billion people do not have access to safe drinking water. Furthermore, polluted water is implicated in 80% of all cases of sickness and disease according to the World Health Organization.[8] Water must be purified to remove harmful materials and make it suitable for human use.[8] UV light is an effective cleanser but is energy intensive, and its application in large-scale systems is sometimes considered to be of unreasonable cost.[8] Nanotechnology is opening new doors to water decontamination, purification and providing improved detection of water-borne harmful substances.[8] Photocatalytic nanomaterials enable UV light to destroy pesticides, industrial solvents and germs. TiO_2 can be used to decontaminate bacteria-ridden water. When exposed to light, it breaks down bacterial cell membranes, killing the bacteria by the photochemical reactions which create hydroxyl radicals and superoxide anions under UV irradiation.[8]

Researchers at the Queensland University of Technology have developed a novel form of titanium dioxide and a process for producing an environmentally-friendly product that purifies water (Figure 1.2).
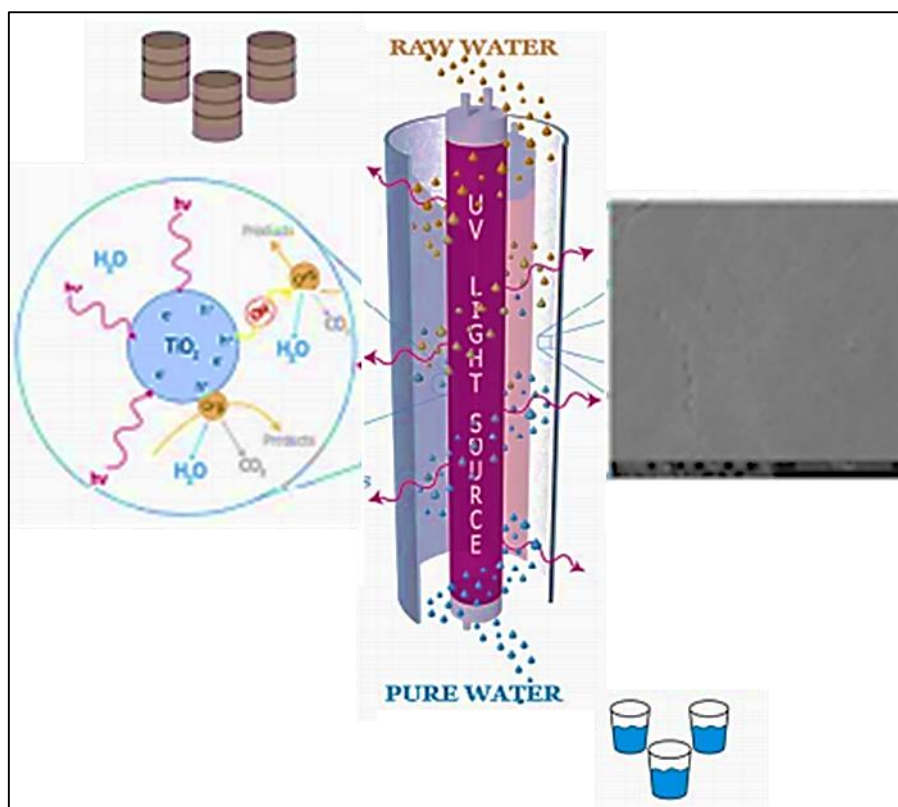
Figure 1.2. Titanium Dioxide nanoparticles used in an environmentally-friendly water purification system.[8]

1.2 The goals of this research

Although Copper (I) oxide (Cu_2O) has not been as extensively considered as Titanium Dioxide (TiO_2) as a photocatalytic oxide, its bandgap suggests that it might be as efficient, if not more so, especially in conjunction with an environmentally-friendly matrix such as an inorganic polymer (geopolymer). In this study, several approaches for the preparation and characterization of different oxide nanoparticles (*i.e.*, Cu_2O, Cu_2O/TiO_2 and TiO_2) were investigated, and the most promising of these products were inserted at various concentrations into unmodified and modified metakaolinite-based geopolymer prior to curing. A modified geopolymer matrix was also prepared by using a small amount of surfactant to expand the pore structure and control their size and shape.[9] The aim of this project is therefore to develop and test new photocatalyst materials that combine an geopolymer matrix with photoactive oxide nanoparticles to promote adsorption of environmental pollutants and their photodegradation. By suspending oxide nanoparticles in these geopolymers, the filtering action should be improved, allowing the destruction of organic molecules, pesticides, dyes and other materials in wastewater. In other cases,

photocatalysts have been used to increase the photodecomposition rate of pesticides or pollutants.[10] To verify the catalytic effect of these newly developed materials, reliable methods to determine the photocatalytic activity were necessary.

Based on studies of other nano photocatalytic materials it was presumed that the Cu_2O nanoparticles used in this study should have similar photocatalytic properties to TiO_2. By comparison with TiO_2, nanostructured Cu_2O is even more attractive, being an inexpensive readily available p-type semiconductor with a direct band gap of 2.2 eV and a high optical absorption coefficient.[11, 12] Cu_2O is also a powerful absorber of molecular O_2, and can scavenge photoelectrons, thereby interfering with the combination of electrons and holes.[13] This suggests that Cu_2O should act as a stable photocatalyst for the photochemical decomposition of H_2O with the generation of O_2 and H_2 under visible light irradiation, and should also be a good candidate for the photocatalytic degradation of organic pollutants under visible light irradiation. A further major attraction of Cu_2O is its low toxicity, with a band gap that can be tuned by adjusting its particle size.[14] Cu_2O nanoparticles can be prepared in a range of colours from yellow to dark brown, raising the possibility of its use in coloured geopolymer composites. Furthermore, geopolymers are porous, suggesting a possible use as water purifying filters when used as a matrix in conjunction with Cu_2O nanoparticles.

Based on these previously reported observations, a series of new composites of Cu_2O/TiO_2 nano-heterostructures incorporated into geopolymer matrix have also been prepared. The Cu_2O was synthesized as cubic nanocrystals, and the TiO_2 was commercial P25. The combination of nanosized Cu_2O particles and photoreactive P25 titania in an aluminosilicate geopolymer matrix was found to be a more efficient photocatalyst under UV irradiation than geopolymer composites containing either of the individual oxides alone. These new geopolymer composites show promise as ecologically-friendly materials that can efficiently remove organic pollutants from water or the atmosphere.

The use of geopolymer matrices modified by the inclusion of a large quaternary ammonium ion, cetyltrimethylammonium bromide (CTAB) was also investigated in this work. These modified Cu_2O-geopolymer and Cu_2O/TiO_2-geopolymer composites have much better photocatalyst properties than Cu_2O and Cu_2O/TiO_2 alone due to the improved dispersion of metal oxide nanoparticles at the external and interlayers of the geopolymer matrix.

The combination of ecologically-friendly geopolymers and nanocrystalline Cu_2O and Cu_2O/TiO_2 for absorption and photodegradation of harmful organic substances has not previously been investigated in detail, neither has the use of CTAB to expand the

geopolymers matrix previously been considered. The present work showed that both these factor can be combined to produce extremely efficient materials for photodestruction of harmful organic compounds.

1.3 Dissertation Objectives and Motivation

Extensive work on geopolymer research has been conducted so far. Therefore, this Thesis focuses on a developing field that utilizes environmentally-friendly, cheap and plentiful aluminosilicate materials to make a geopolymer matrix containing efficient nanoparticle oxide photoactive components. The main objectives are:

- To identify a suitable synthesis for nanoparticle Cu_2O.
- To develop a process for inserting the nanoparticles into a geopolymer matrix.
- To characterise the product (XRD, FTIR, SEM/EDX, TEM, MAS NMR, Cu NQR, BET)
- To test the performance of these catalysts for photodegradation of methylene blue (MB).
- To improve the photocatalyst action by combining Cu_2O with TiO_2.
- To improve the performance of the geopolymer matrix by modifying with CTAB.

No known work so far has been reported to make photoactive geopolymer matrices containing Cu_2O and Cu_2O/TiO_2 nanoparticles, which indicates the innovative nature of this research. Although some publications have reported making photoactive geopolymers using metakaolin and TiO_2 (e.g., Cerny *et al*. 2009, Tirado *et al*. 2013), this work presents the first effort to explore and validate a new potential application of metakaolin-based geopolymers, which are used as photocatalysts for decomposition of organic pollutants. Thus, the motivation of this dissertation can be summarized as follows:

- Innovation
  - Produce geopolymer matrices using oxide nanoparticles that have never been reported in the existing literature
  - Present the first effort to validate the possibility of a new photoactive geopolymer composite.

- Potential applications of the synthesized geopolymers

- Construction materials

- Materials for photodecomposition of organic and some inorganic pollutants

1.4 Thesis Layout

This thesis consists of eight chapters, which papers have been published, or submitted to peer-reviewed journals or conferences.

Chapter 2 provides a literature review, which focuses on the raw materials used to make geopolymers and the oxide nanoparticles, the mechanism of geopolymer technology, the photocatalytic process, and the mechanism of photo-oxidation processes.

Chapter 3 demonstrates a methodology that describes experimental details, chemicals, materials and analysis techniques for characterization of the synthesised materials. This chapter explains several methods for synthesis of Cu_2O nanoparticles and combination of the nano oxide particles with the geopolymer matrix.

Chapter 4 studies the effect of incorporation of Cu_2O nanoparticles in a geopolymer matrix evaluated by XRD, SEM, TEM, BET, NMR and NQR. The photocatalytic properties of the composites were studied by the photodegradation of MB dye, which is commonly used for such degradation studies.

Chapter 5 examines a new geopolymer composite which consists of Cu_2O/TiO_2 nanoparticles, characterized with XRD, SEM, TEM, BET, NMR and NQR. This product shows even better photocatalyst properties than geopolymers containing Cu_2O and TiO_2 alone.

Chapters 6 and 7 describe a new method for modifying the geopolymer matrix by using a large cation surfactant (CTAB). The modified geopolymer was combined with the oxide nanoparticles and the photocatalytic activities of the composites were investigated.

Chapter 8 presents a summary of all of the studies performed as part of this thesis and lists suggestions for future work.

Chapter 2

Literature Review

2.1 Fundamentals of the photocatalytic process

Currently one focus of global concern is the presence of harmful organic compounds in water supplies and the discharge of wastewater from chemical industries, power plants, landfills, and agricultural sources. Traditional water treatment processes are filtration, thermal and catalytic oxidation, chemical treatment and biological treatment.[15] Some of the materials used in this process are chlorine, potassium permanganate, ozone, hydrogen peroxide and high-energy UV light. However, there are some safety and economic restrictions on these water treatment processes. Phase transfer methods eliminate undesirable organic pollutants from wastewater, but they do not remove the pollutants entirely. Toxic organic compounds in water can be oxidized by powerful chemical treatment based on aqueous phase hydroxyl radical chemistry. This process uses either high-energy UV light or strong chemical oxidants whose hazardous nature is undesirable.[16,17] Moreover, during this process several, even more hazardous intermediates are formed. An advanced oxidation technology process (AOT) has been developed as an efficient method for removing organic pollutants from water streams, based on a heterogeneous photocatalysis process using metal oxide semiconductor particles.[17] Metal oxides, such as ZrO_2, Al_2O_3, Cu_2O, TiO_2 and SiO_2 are widely used catalyst supports. These oxides are active towards many reactions, including oxidation of CO, selective oxidation (alkenes, alcohols and even alkanes), water-gas shift, and removal of atmosphere pollutants (NO_X, VOCs).[18]

Varieties of air pollutants have been suspected to have harmful effects on human health and the environment. These pollutants are mainly the products of combustion from power generation, space heating or motor vehicle traffic.[19] Secondary pollutants such as acid rain or ozone arise from the products created in the immediate area of the pollutant sources by chemical reactions in the atmosphere. The principal pollutants released by vehicles are carbon monoxide, oxides of nitrogen (NO_X), volatile organic compounds (VOCs) and particulates. These pollutants are having an increasing influence on urban air quality. Photocatalytic materials can be added to the surface of pavements and building materials to oxidise the pollutants by the action of light irradiation and forming precipitates on the surface of the material, then these precipitates are eliminated from the surface by rain.[19]

Photocatalysis is a catalytic reaction including light absorption by a substrate containing a catalyst. Reactions involving the participation of catalysts are called catalytic. Photocatalysis is defined as a change in the rate of chemical reactions or their generation in the presence of substances that absorb light quanta that are then involved in the chemical transformations of the reaction participants.[20] Photocatalytic degradation of environmental contaminants has been studied in the past two or three decades. In 1972, Fujishima and Honda reported the photocatalytic splitting of water on TiO_2 electrodes, which was the first suitable photocatalyst for water splitting and the beginning of a new era of modern heterogeneous photocatalysis.[21] The use of photocatalytic oxidation to remove trace-level organic contaminants in air, energy renewal and energy storage has recently received considerable attention since this technology has a broad range of potential applications, including air purification in office buildings, factories, homes, cars, and spacecraft.[22]

The importance of semiconductor-based photocatalysts is their charge separation ability (Figure 2.1). When a semiconductor is irradiated with light of energy greater than the bandgap, the excitation of an electron occurs from the VBto the CBand leaves a hole in the valence band.[23] This separated hole has strong oxidizing power; this power comes from the electron of the absorbed species. The separated charge and hole can also recombine to release energy in the form of heat. The photocatalysis reaction is improved if the electron-hole pair recombination is inhibited. This can be achieved by trapping either the photogenerated electrons or the photogenerated holes at trapping sites in the structure.
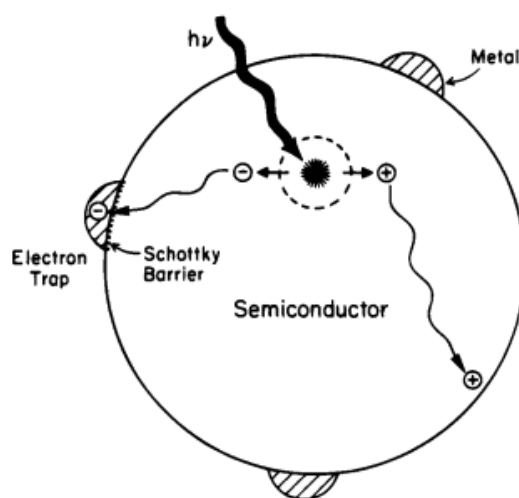
Figure 2.1. Metal-modified semiconductor photocatalyst particle.[19]

2.2 Heterogeneous photocatalysis

Photocatalytic reactions are divided into homogeneous and heterogeneous reactions. Heterogeneous photocatalysis has been far more intensively studied in recent years because it has potential applications in a variety of environmental and energy-related uses as well as in organic synthesis. Heterogeneous photocatalysis reaction systems involve the development of an interface between a solid photocatalyst (metal or semiconductor) and a fluid containing the reactants and products of the reaction.[24]

Heterogeneous photocatalysis can be carried out in different systems such as the gas phase, pure organic liquid phases or aqueous solutions. The overall process can be explained in several independent steps:

The reactants in the fluid phase are transferred to the surface of the photocatalyst, one or more of the reactants are absorbed to react with the absorbed phase; the released products are remove from the interface region. Thus, the photocatalytic reaction occurs in the adsorbed phase.[24]

In homogeneous photocatalysis the photocatalyst is in the same phase as the reactant, and typically will exist as a gas or contained in a single liquid phase. Usually, homogeneous photocatalysts are dissolved in a solvent together with the substrates. Most of the processes using homogeneous photocatalysis occur in the liquid phase whereas in heterogeneous catalysis the photocatalyst is usually in the solid form, and the reaction occurs either in the liquid or gaseous phase.

In these systems a distinction must be made between adsorption and absorption. Adsorption is a surface phenomenon and involves unequal distribution of the molecular species in the bulk and at the surface; it is rapid to begin with but slows down as the system approaches equilibrium. By contrast, absorption involves uniform distribution of the molecular species throughout the body of material at a uniform rate.

Depending upon the nature of forces between the adsorbate molecules and the adsorbent, the adsorption can be classified into two types:

- Physical adsorption or physisorption
- Chemical adsorption or chemisorption

Where the forces between the adsorbate and adsorbent are van der Waals, the adsorption is called physisorption. Since the forces of this type are very weak, physisorption can be easily reversed by heating or decreasing the pressure.

If the forces between the adsorbate particles and the adsorbent are of similar strength as chemical bonds, the adsorption is called chemisorption. Since these forces are very strong, this type of adsorption cannot be easily reversed.[25]

The major advantages/disadvantages of heterogeneous and homogeneous photocatalysis summarised in Table 2.1.[26]

Table 2.1. Comparison of main advantages/disadvantages of heterogeneous and homogenous photocatalysis.[26]

Property	Homogenous	Heterogeneous
Catalyst recovery	Difficult and expensive	Easy and cheap
Thermal Stability	Poor	good
Selectivity	Excellent/good-single active site	Good/Poor -multiple active site

2.3 Fundamental Concepts

2.3.1 Insulators, conductors, and semiconductors

Figure 2.2 shows the band structures of the three main classes of electrical materials, insulators, semiconductors and conductors. Due to the large band gaps in insulators, the valence band (VB) is full, and the conduction band (CB) is empty. There are two possibilities for conductors. One is that the valance band is not filled, so an electron in the VBcan be parted from its atom by simply being raised to a higher energy level within the same band. Another situation is that there is no energy gap between the VB and conduction band, and so electrons can easily make transitions from the valence to the CBe.g. metals. The energy gaps between the VB and CB are very small and different for different materials. Figure 2.2 (c) indicates in red the overlap of the VB and CB in some conductors.[27]

In semiconductors; (Figure 2.2d) the band gap is small enough to be navigated once an electron is sufficiently energized but the bandgap is still large enough to obstruct the conduction. This unique property makes semiconductors useful for many applications, such as circuit elements, computer chips, chemical catalysts, and photovoltaic devices. Changing the physical properties of semiconductors allows alteration of the width of the gap, as well as the position of the band, edges.[28]
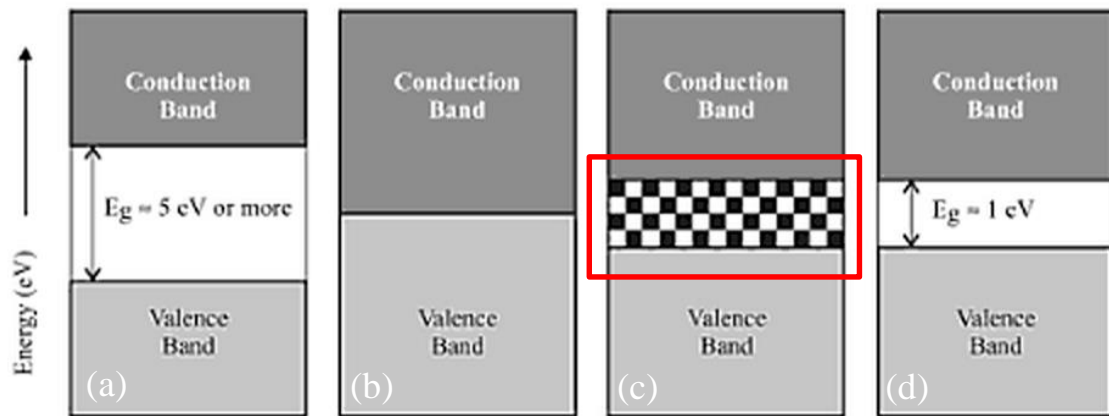
Figure 2.2. Energy band diagrams for (a) Insulators; (b) and (c) conductors, and (d) semiconductors.[27]

Semiconductors can be classified into two types, intrinsic and extrinsic. An intrinsic semiconductor is pure enough for impurities not to have an effect on its electrical behaviour. Elements (e.g. Si, Ge) and compounds (e.g. InSb, GaAs, SiC) are intrinsic semiconductors that possess poor conductivity. At a temperature of absolute zero an intrinsic semiconductor does not have any charge carriers and consequently, the material behaves as an insulator. In energy band terms, the CB is empty of electrons and the VB is fully occupied by the valence electrons. At a temperature above absolute zero, a VB electron (e⁻) may be thermally excited into the CB, leaving an unoccupied state in the VBthat is called a hole (h⁺). Electrons and holes flow in opposite directions in the presence of an electric field but contribute to a current in the same direction since they are oppositely charged. Holes and electrons created in this way known as intrinsic charge carriers. In intrinsic semiconductors, for each electron in CB the corresponding hole exists in the valance band.[29]
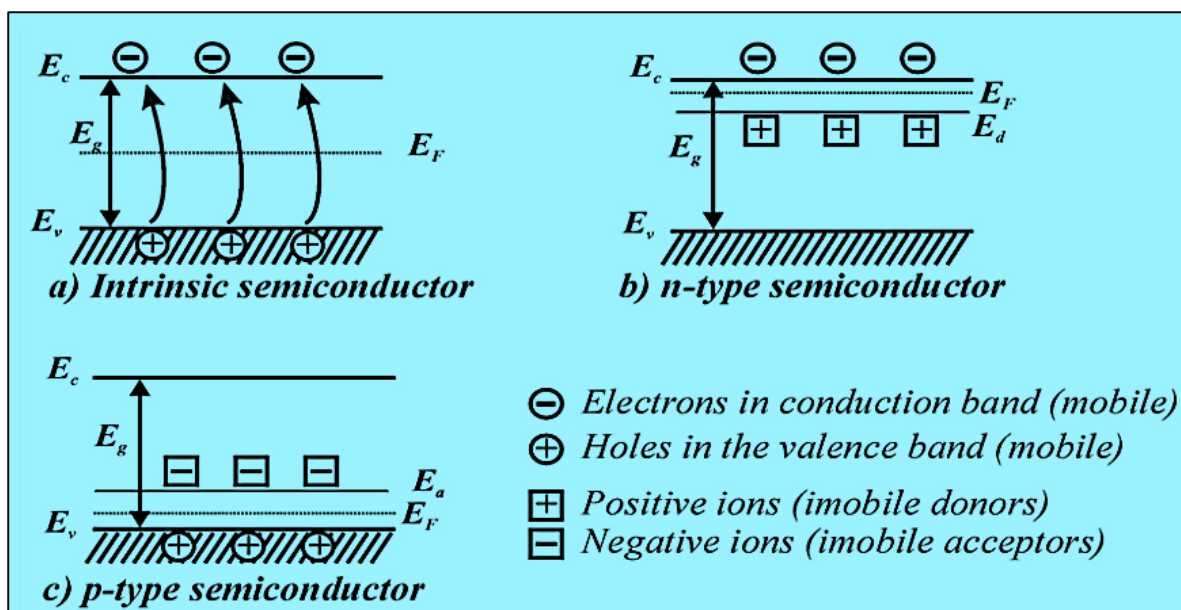
Figure 2.3. Three types of semiconductors: a) intrinsic semiconductors, b) n-type semiconductors, and c) p-type semiconductors.[29]

Extrinsic semiconductors can be formed by addition of impurity atoms into the intrinsic semiconductor, in a doping process. Alteration of the relative concentrations of electrons and holes in the material depends on the type and concentration of the dopant atom. The *N*-type semiconductors are doped with donors. The acceptors can remove an electron from the semiconductors and produce *p*-type semiconductors (p stands for positive holes). The majority carriers in an *n*-type semiconductor are electrons and their concentration is equal to the donor impurity concentration. Holes are minority carriers in *n*-type semiconductors. Electrons are minority carriers in *p*-type semiconductors.[29] (See Figure 2.3)

2.4 Semiconductor Physics

2.4.1 Band gaps

Electrons are locally bound to their corresponding atoms at the ground or lowest energy state and do not travel through the bulk of the solid. These low-energy electronic states determine the valance band, and if the electrons are energized sufficiently, they can leave the valance band and transfer through the solid. Figure 2.4 explains photon absorption. In this figure, a VBelectron (e_{vb}) absorbs light with energy $h\nu > E_g$ and then jumps to the conduction band. This situation creates a free roaming pair of charge carriers, namely a CBelectron (e_{cb}^-) and a VBhole (h_{vb}^+). These charge carriers, e_{cb}^- and h_{vb}^+ are of fundamental importance in semiconductor physics and photocatalysis.[30]
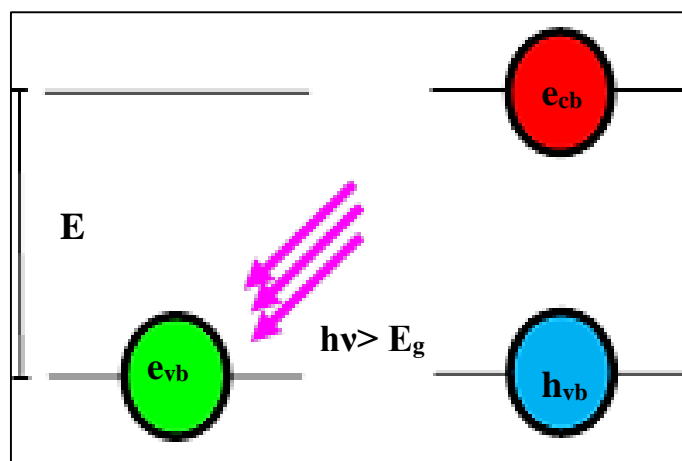
Figure 2.4. Photon absorption and charge carrier pair generation.[31]

2.4.2 Band Theory

Each band has a different energy, and the bands are filled with electrons from the lowest energy to the highest, in the same way as electrons occupy the orbitals in a single atom. The valance band (VB) is the filled band of highest energy, which is equivalent to the highest occupied molecular orbital (HOMO) in a molecule. The next highest energy band is called the CB which corresponds to the lowest unoccupied molecular orbital (LUMO) in a molecule. The energy gap called the bandgap (E_g) separates the VB and the CB. Figure 2.5 shows band formation with increasing atom population.[32] A greater number of atoms results in a larger number of possible electronic states collapsing the energy levels into a continuous band.
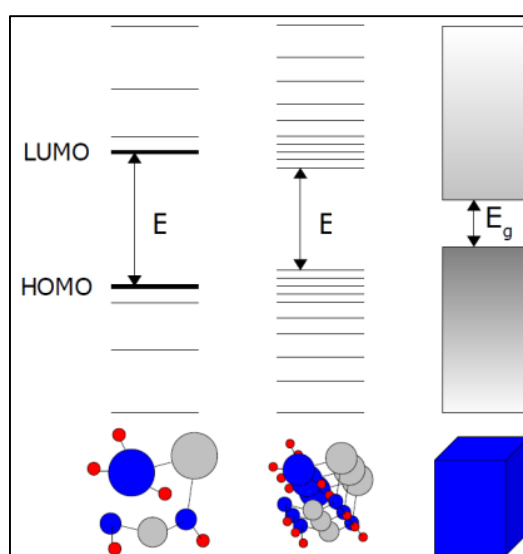
Figure 2.5. Formation of bands in a semiconductor.[33]
(blue = metal, red = oxygen, grey = hydrogen)

2.5 Basic principles and mechanism for photocatalyzed dye degradation

2.5.1 Indirect dye degradation mechanism

The mechanism of indirect heterogeneous photocatalytic oxidation using semiconducting materials can be summarized by four basic processes as follows:

I. Photoexcitation

The photocatalytic reaction is started by promotion of a photoelectron from the semiconductor (Figure 2.6) photocatalyst filled VB to the vacant CB as a result of irradiation. The energy (hυ) of the absorbed photon is either equal to or greater than the band gap of the semiconductor photocatalyst. This excitation process leaves a hole in the VB (h_{VB}^+). Accordingly electron and hole pairs (e^-/h^+) are generated as specified by eq. (1) below[31, 33-36]

$$Photocatalyst + h\nu(UV) \rightarrow Photocatalyst(e^-(CB) + (h^+VB)) \tag{1}$$
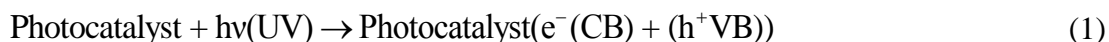
II. Ionization of water

OH$^•$ radicals are produced by reaction of the photogenerated holes in the VBwith water (eq. 2). (Figure 2.6)

$$H_2O(ads) + h^+(VB) \rightarrow OH^•(ads) + H^+(ads) \tag{2}$$

The HO$^•$ radicals are extremely powerful oxidizing agents, and are produced on the surface of the irradiated semiconductor. They have the ability to attack adsorbed organic molecules, and also those located very close to the catalyst surface, non-selectively degrading these molecules to an extent depending on their structure and stability. These powerful radicals not only attack organic pollutants but can also attack and destroy microorganisms.[37]

III. Oxygen ion sorption

Anionic superoxide radicals (O_2^-) are generated from oxygen *via* the electrons in the CB(e_{CB}); this occurs simultaneously with the creation of hydroxyl radicals by the reaction of photogenerated holes (h_{VB}^+) with surface bound water or OH$^-$ (eq. 3). (Figure 2.6)

$$O_2 + e^-(CB) \rightarrow O_2^-(ads) \tag{3}$$

Typically, this superoxide ion not only participates in the further oxidation process but also prevents electron-hole recombination, thereby maintaining electron neutrality within the photocatalyst molecule.

IV. Protonation of the superoxide

The created superoxide (O^{2-}) becomes protonated and forms hydroperoxyl radicals, (HO_2^-), followed by the separation of H_2O_2 into highly reactive hydroxyl radicals (OH^-). Both oxidation and reduction processes commonly occur on the surface of the photoexcited semiconductor photocatalyst. The complete process is shown in Figure 2.7 and equations (4) to (9):

$$O_2^{-\bullet}(ads) + H^+ \rightarrow HOO^{\bullet}(ads) \tag{4}$$

$$2HOO^{\bullet}(ads) \rightarrow H_2O_2(ads) + O_2 \tag{5}$$

$$H_2O_2(ads) \rightarrow 2OH^{\bullet}(ads) \tag{6}$$

$$Dye + OH^{\bullet} \rightarrow CO_2 + H_2O(intermediates) \tag{7}$$

$$Dye + h^+(VB) \rightarrow \text{ oxidation products} \tag{8}$$

$$Dye + e^-(CB) \rightarrow \text{ reduction products} \tag{9}$$
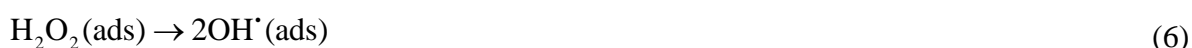
2.5.2 Direct mechanism for dye degradation

Another photocatalyst mechanism of photocatalytic dye degradation is the excitation of the dye under visible light ($\lambda > 400$ nm) from the ground state (Dye) to the triplet excited state (Dye*). The excited state dye species are converted into semi-oxidized radical cations (Dye$^+$) by electron injection into the CBof photocatalyst material. The superoxide radical anions (O_2^-) are created by reaction between dissolved oxygen and trapped electrons and are then converted to hydroxyl radicals ($OH^{\bullet}$). The $OH^{\bullet}$ is responsible for the oxidation of the organic compounds. Figure 2.7 represents this mechanism.[38-43]

$$Dye + h\nu \rightarrow dye^* \tag{10}$$

$$Dye^* + Photocatalyst \rightarrow dye^+ + Photocatalyst \tag{11}$$
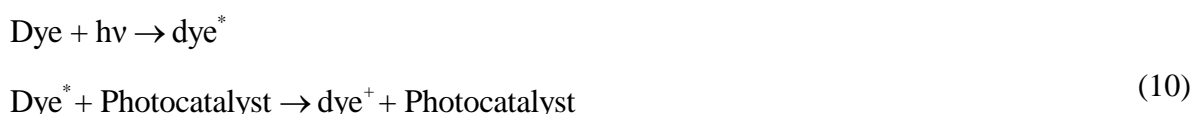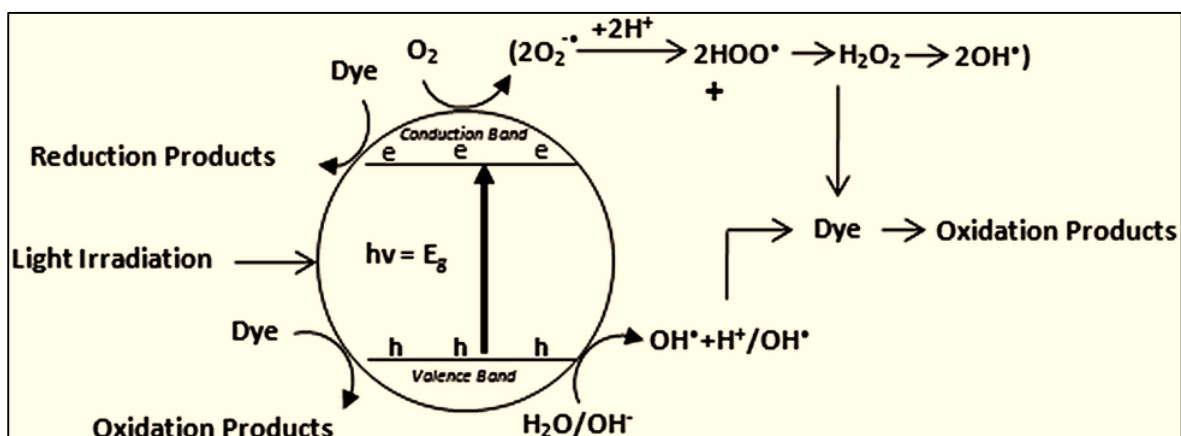
Figure 2.6. Pictorial representation of direct dye degradation process.[44]

The oxidative pathway leads in many cases, to complete conversion of an organic entity to CO_2, H_2O, and in some instances, an inorganic acid. Table 2.2 gives the band energies and band gaps of these catalysts.

Table 2.2. Bandgap energy of various photocatalysts.[41]

Photocatalyst	Band Gap Energy (eV)	Photocatalyst	Band Gap Energy (eV)
Diamond	5.4	WO_3	2.76
CdS	2.42	Si	1.17
ZnS	3.6	Ge	0.744
ZnO	3.436	Fe_2O_3	2.3
TiO₂	3.03	PbS	0.286
CdS	2.582	PbSe	0.165
SnO₂	3.54	ZrO_2	3.87
CdSe	1.7	Cu_2O	2.172

2.6 Cu₂O Photocatalyst

A good photocatalyst should be photoreactive, capable of utilizing visible or near UV radiation, biologically and chemically inert, photostable (i.e. not disposed to photo corrosion), inexpensive and non-toxic.[16] In the conversion of solar energy, it is essential to have a photocatalyst that works under visible light irradiation ($\lambda > 400$ nm); however such a photocatalyst has not yet been created. Cuprous oxide has been investigated for decades for its unique semiconductor and optical properties.[45] Cu_2O, a well-known p-type semiconductor acts as a photocatalyst under visible light irradiation (≤ 600 nm) and has shown great potential for applications in electronics, communication, gas sensors, energy and environmental protection because of its useful electronic and optical properties.[46] In addition, the conduction and VBedges of Cu_2O are separated by a band gap energy of 2.0–2.2 eV and the oxide has a considerable absorption coefficient (up to ~10^4 cm^{-1}) in the visible-light region of the solar spectrum.[45-49] Cu_2O is a brownish-red colour and crystallizes in a high-symmetry cubic structure.[50] In cuprite-structured Cu_2O, each oxygen is surrounded by a tetrahedron of Cu, and each Cu has two oxygen neighbours, as shown by its unit cell model (Figure 2.6a).[51] Table 2.3. summarises the physical and chemical properties of Cu_2O.[52]
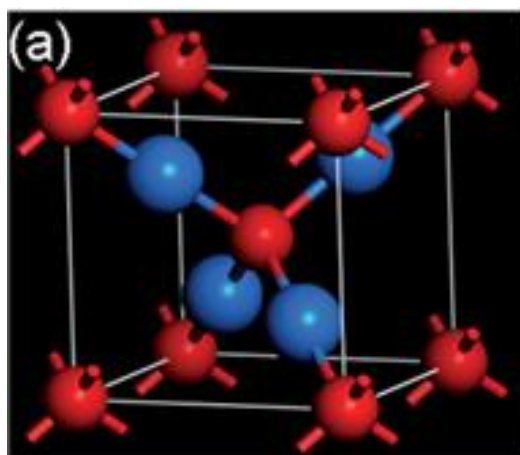
Figure 2.7. The unit cell of the cuprite Cu_2O[53] blue = copper, red = oxygen

Table2.3. Physical and chemical properties of Cu_2O [52]

IUPAC name	Copper (I) oxide
Synonyms Copper	Copper oxide; cuprous oxide; dicopper oxide
CAS number	1317-39-1
Molecular Formula	Cu_2O
Molecular weight(g/mol)	143.09
Appearance	Yellow, red, or brown crystalline powder
Odor	None
Boiling point STP^a(∘C)	1800
Melting STP^a(∘C)	1235
Density (g/cm^3)	6
Refractive index	2.705
Vapour Pressure	Negligible
Solubility	Soluble in dilute mineral acid to form copper (I) salt or copper (II) salt plus metallic copper; aqueous ammonia and its salts
Insoluble	Insoluble in water and organic solvents
Stability	Stable in dry air; in moist air oxidizes to cupric oxide

The reactivity and selectivity of a nanocatalyst can be tailored by controlling the shape, which defines the number of atoms located at the edges or corners. Shape control can determine the properties of a nanocrystal with great flexibility.[54] The common shapes of face-centred cubic (fcc) metals are surrounded by (111) and (100) facets and include a small percentage of corner and edge sites (Figure 2.8). Surface energies corresponding to different crystallographic facets usually increase in the order $\gamma_{(111)} < \gamma_{(100)} \leq \gamma_{(110)} \leq \gamma_{(hkl)}$, where (hkl) signifies high-index facets, with at least one h, k, and l value equal to two or greater.[54] In the case of crystal growth, it is suggested that the primary driver for the development of the morphology is the reduction of surface energy. In principle, tuning the shape could be achieved by modifying the relative order of the surface energy of the different crystallographic facets.[53] The rare occurrence of O−Cu−O 180° in linear coordination in Cu_2O gives its crystalline facets (111), (100), and (110) a unique chemical activity.[55]
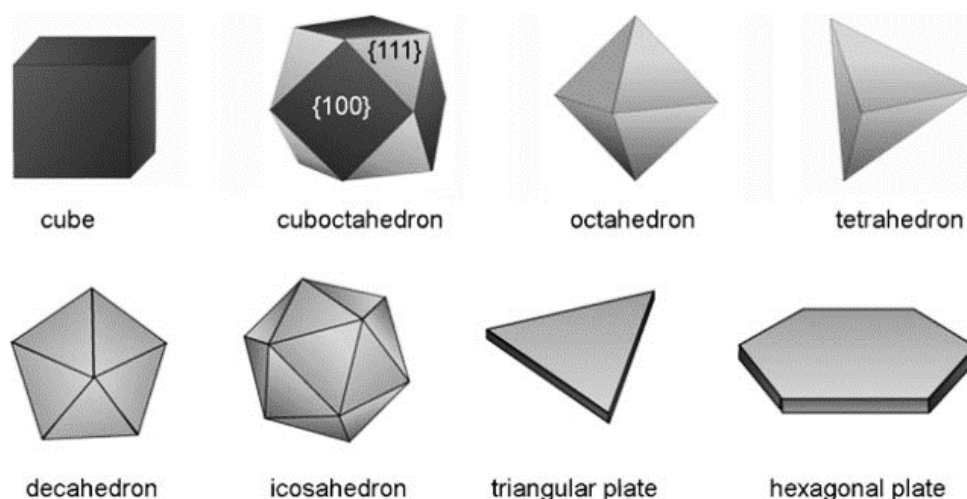
Figure 2.8. Conventional shapes of face-centered cubic (fcc) metals, surface is enclosed by (100) and (111) facets. Black and gray colors represent the (100) and (111) facets, correspondingly.[54]

Michael *et al.,* (2009) have reported the synthesis of sub-micrometer-sized Cu_2O crystals with morphological evolution from cubic to hexapod structures using $CuCl_2$ as the precursor and sodium dodecyl sulphate (SDS) as a surfactant and hydroxylamine (NH$_2$OH●HCl) reductant.[56] (Figure 2.9)
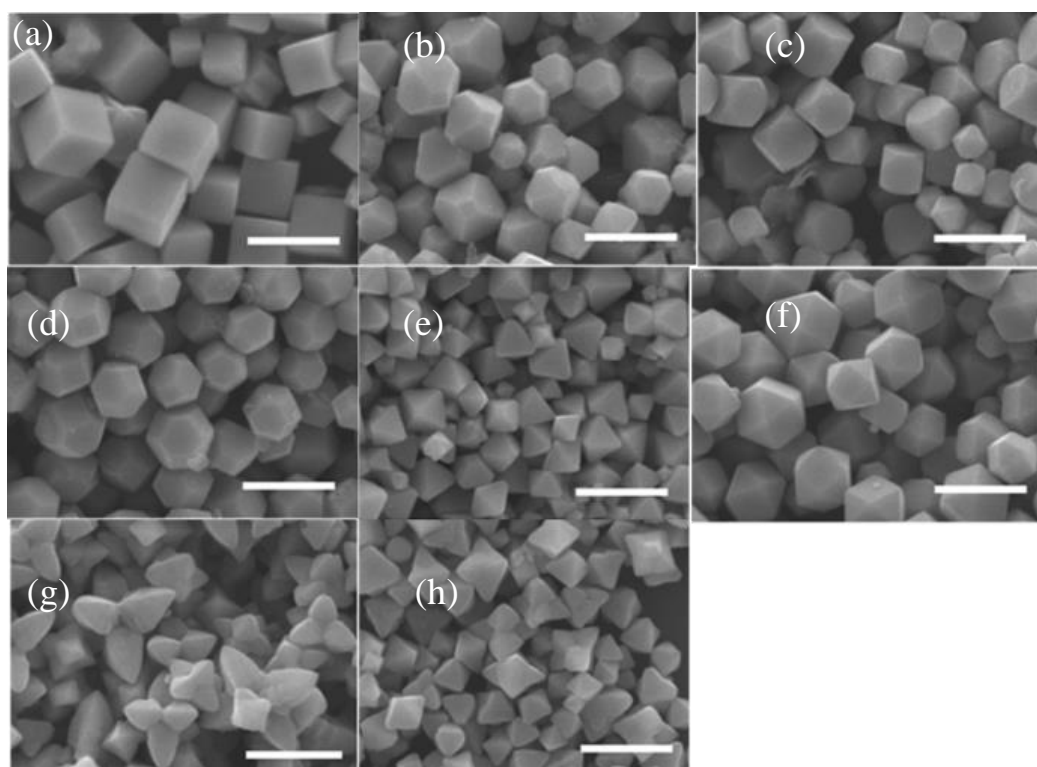
Figure 2.9. SEM images of the Cu_2O crystals with various morphologies: (a) cubes, (b) type II truncated octahedra, (c) truncated cubes, (d) type I truncated octahedra, (e) octahedra, (f) cuboctahedra, (g) extended hexapods, and (h) short hexapods (scale bar) 1 μm.[54]

Figure 2.10 shows the XRD patterns of the different morphologies of Cu_2O crystals reported by Michael *et al.,* (2009). The diffraction patterns clearly display a change in the relative intensities of the (111) and the (200) peaks in relation to the morphology. As expected, cubes show an extremely strong (200) reflection peak and a weak (111) reflection peak.[56]
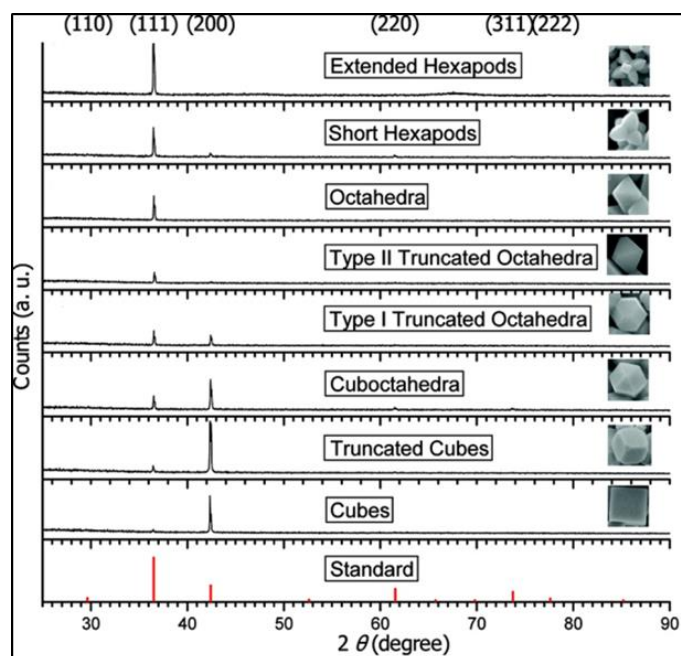
Figure 2.10. Powder XRD patterns of the different morphologies of Cu_2O crystals. A standard diffraction pattern of Cu_2O is also given.[55]

Recently, many researchers[57,58,59,60] have studied Cu_2O as a photocatalytic material because of its following advantages:

a) Low toxicity, environmentally acceptable, inexpensive, plentiful, readily available, and have antifouling properties when used in paints; these are the major attractions of Cu_2O.[61]

b) Cu_2O can directly utilize visible light in the photocatalytic process, even though it is commonly used as a sensitized semiconductor material for a solar cell fabrication.[39] These properties are related to the band gap tuning of the Cu_2O by factors such as particle size.[14, 62-65]

c) Cu_2O effectively adsorbs oxygen molecules[66] that scavenge the photogenerated electrons to restrict the recombination of electron–hole pairs, subsequently improving the efficiency of photocatalytic processes.

Furthermore, Cu_2O can act as a stable photocatalyst for the photochemical decomposition of H_2O and generation of O_2 and H_2 under visible light irradiation.[13] Therefore, it is of great

interest to investigate the stability of Cu_2O. In the field of photovoltaics, copper and copper oxide (a metallic semiconductor) were some of the first photovoltaic cells, invented by Pollack and Trivich in 1975.[11] It has been reported that photocatalytic splitting water on Cu_2O powder proceeded without any noticeable deactivation for more than 1900 h.[48] Huang *et al.* also reported that Cu_2O particles with different sizes were used as photocatalysts to directly degrade methyl orange. The results showed that the stability of Cu_2O was different under ambient atmosphere and photocatalytic conditions in solution. Cu_2O nanoparticles can readily be deactivated during the photocatalytic reaction because their photocorrosion rate is very rapid. Therefore, it is great importance to investigate the stability of Cu_2O[50] and clarify the mechanism of deactivation of Cu_2O.[48]

Cu_2O not only makes good use of visible light in the photolysis process but is also used as a sensitized semiconductor material for solar cell fabrication; this is related to its band gap tuning by factors such as its particle size and surface area.[63,14,12] Large surface areas can provide more surface sites for the adsorption of reactant molecules and render the adsorption process more efficient. Thus, porous structures with large surface areas have prospective applications as photocatalysts.[67] The band gap of a semiconductor determines its working wavelength. Semiconductors with bandgaps that are either too large or too small are not suitable for practical use. The reason is larger band gaps will not produce any photoreaction while narrow band gap materials will have problems with light corrosion. Figure 2.11 shows the band-edge positions of several semiconductors, along with the redox potentials of water.[68]
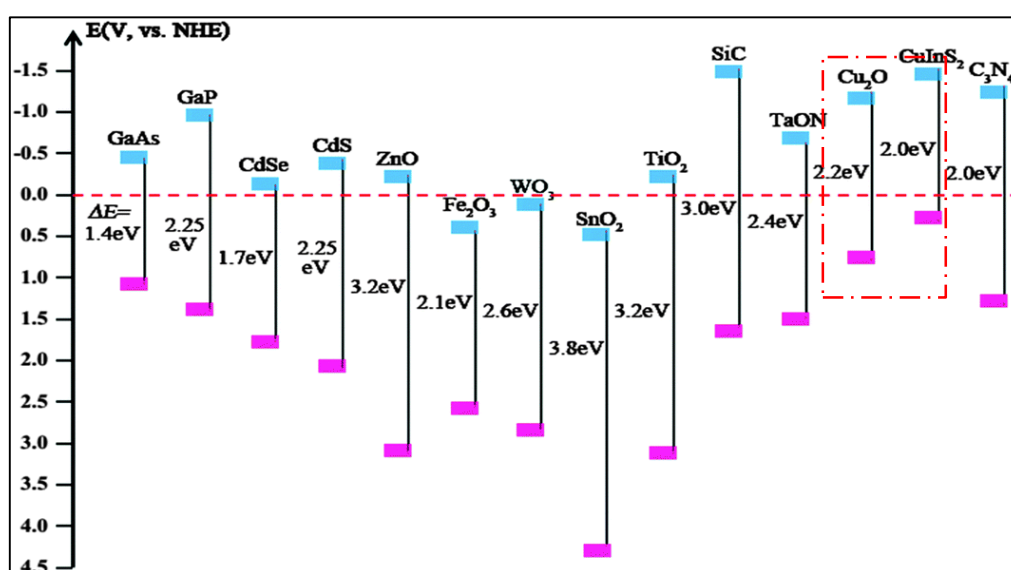
Figure 2.11. Eg values (in eV) and position of CB (blue) and VB (pink) for various semiconductors.[69]

TiO_2 (3.0–3.2 eV) has a suitable band edge but its solar light consumption is limited by its large band gap.[70] WO_3 has a small band gap of 2.6 eV, and can utilize ~12% solar light but for the reduction of water it needs a more negative CB.[71] Fe_2O_3 has a smaller band gap of 2.1 eV, which has the ability to absorb longer wavelengths, but one of its major drawbacks is that its CB edge position is not negative enough for solar water splitting, and it needs a large external bias to perform this function.[72] Much work has been done during the past decades to overcome these limitations in semiconductor photocatalysts, and significant progress has been achieved.

One of the developments has been to increase the visible light photoactivity of metal oxides with elemental doping and sensitization with small band gap semiconductors. Hoang *et al.* created a CdS/TiO_2 electrode that exhibited good visible light photoactivity and excellent stability without showing any CdS photodegradation.[73] Another improvement was the development of a nanostructured electrode, since the nanostructure can offer a better surface contact with the electrolyte and a smaller diffusion distance for photogenerated minority carriers.[69] Cu_2O is one of the semiconductors that has a small enough band gap of ~ 2.2 eV and a CB that is negative enough for water splitting.

Additionally, Cu_2O can effectively adsorb molecular oxygen, which can scavenge the photogenerated electrons to maintain the recombination of electron-hole pairs, and consequently facilitate the photocatalytic efficiency.[66] Cu_2O can generate electrons and holes when irradiated by visible light.

The microstructure and morphology of Cu_2O nanoparticles varies depending on the copper source and the additives used to produce them. Zheng *et al.,* (2009) reported the use of $Cu(CH_3COO)_2.H_2O$ and CH_3COOH as precursors to synthesise Cu_2O particles.[74] After one hour irradiation with visible light, the Cu_2O (100) and (110) facets gradually transform into nanosheets and after 16 hour, the Cu_2O microcrystals had completely changed into nanosheets (Figure 2.12).[74]
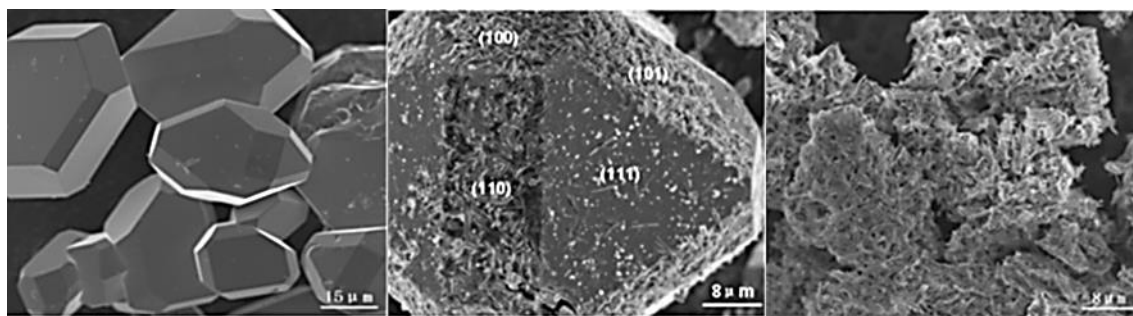
Figure 2.12. SEM images of Cu$_2$O samples after irradiation for (a) 0, (b) 1, and (c) 16 hour.[74]

XRD analysis confirmed that Cu$_2$O nanosheets are formed after 16 hour irradiation under visible light (Figure 2.13).[74] Cu$_2$O (100) and (110) facets steadily convert into nanosheets during the photodegradation of methyl orange (MO) under visible light irradiation. The electrons and holes are generated when the intermediate CuO is irradiated by the visible light, and the MO may capture the photogenerated holes. As the holes are consumed, CuO formed on the (100) and (110) facets is reduced back to Cu$_2$O, ultimately forming Cu$_2$O nanosheets. With increased irradiation time, Cu$_2$O microcrystals are completely transformed into nanosheets.[74]
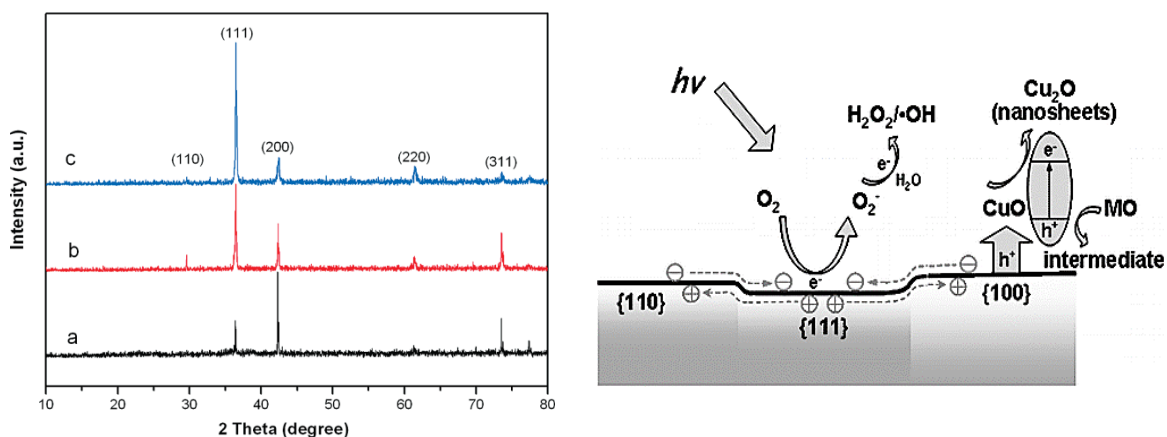
Figure 2.13. (Left), XRD patterns of Cu$_2$O irradiated for (a) 0 h, (b) 1 h, (c) 16 h in MO solution. (Right) schematic diagram showing charge separation among the different crystal faces and regeneration of Cu$_2$O nanosheets.[74]

By contrast with Cu$_2$O, a drawback to the use of TiO$_2$ as a photocatalyst is its comparatively large band gap energy (3.0–3.2 eV), allowing it to be activated only by UV radiation ($\lambda <$ 387nm); this greatly limits its efficiency in coupling with solar radiation, of which less than 4% occurs in the UV region. On the other hand, cuprous oxide (Cu$_2$O) is a p-type

semiconductor [75, 76] with a direct band gap of 2.2 eV and a high optical absorption coefficient compared with TiO_2, allowing it to make direct use of visible light.[77, 78]

Recently, Cu_2O has shown promise as a visible light-driven photocatalyst for splitting water and degrading organic contaminants.[59, 79, 80] Low toxicity, inexpensive and its environmental-friendliness are some of the properties of Cu_2O which make it a potential alternative to the other photocatalysts such as TiO_2 in photocatalytic degradation of organic contaminants[81]. Different approaches are frequently used to overcome these disadvantages, including elemental doping of large and small band gap semiconductors to produce the most efficient photocatalysts. One possibility is to couple Cu_2O with n-type semiconductors such as TiO_2 since the two semiconductors possess matching band potentials.[82] Han *et al.* reported TiO_2/Cu_2O composite films demonstrated better photocatalytic efficiencies than TiO_2 and Cu_2O alone under visible light irradiation.[83] Bessekhouad and co-workers prepared Cu_2O/TiO_2 heterojunctions *via* physical mixing that exhibited a higher activity for the degradation of MB as a dye than Cu_2O alone.[84] Huang *et al.* also described Cu_2O/TiO_2 nano-heterostructures based on a chemical precipitation method and reported these to show better photocatalytic efficiencies than pure TiO_2 (P25).[85] Xue and co-workers produced core–shell TiO_2/Cu_2O heterostructures by an electrochemical method and reported that these had excellent photoelectrochemical performances under visible light.[86]

2.6.1 The mechanism of photo-oxidation in Cu_2O

Wang *et al.* discussed the mechanism of deactivation of Cu_2O during the photocatalyst reactions. The thermodynamic possibility of both reduction and oxidation processes in the photocatalyst sample is essential, and this phenomenon for Cu_2O has been verified.[13] The photo-generated electrons can readily transfer to another semiconductor or be taken up by molecular oxygen O_2 and H_2O. According to Figure 2.14 a type of overpotential occurs for this reduction reaction, as shown in Eqs. (13), (15) and (17). In reaction (13) the Cu_2O is reduced to Cu by electrons and the reduction reaction (15) of water to hydrogen seems to be insignificant due to the competing reaction. On the other hand, the quantity of holes on the Cu_2O increases when the electrons are transferred and scavenged.

$$Cu_2O + h\nu \rightarrow e^-(CBCu_2O) + h^+(VBCu_2O) \tag{12}$$

$$Cu_2O + H_2O + 2e^- \rightarrow 2Cu + 2OH^- \tag{13}$$

$$Cu_2O + 2OH^- \rightarrow 2CuO + H_2O + 2e^- \tag{14}$$

$$2H_2O + 2e^- \rightarrow H_2 + 2OH^- \tag{15}$$

$$2H_2O \rightarrow O_2 + 4H^+ + 4e^- \tag{16}$$

$$O_2 + e^- \rightarrow O_2^{\bullet} \tag{17}$$

However, the holes are difficult to eliminate in the absence of other redox species, and therefore reaction (14) will take place preferentially. On the other hand, Cu_2O can also be oxidized by the oxidizing potentials of $OH^{\bullet}$ or H_2O_2 that are more positive than those of holes. Remarkably, in the photocatalysis of TiO_2, $OH^{\bullet}$ is produced while the holes oxidize H_2O. It is clear that the TiO_2 VBedge level is higher than the oxidation potential of water, so both TiO_2 holes and $OH^{\bullet}$ are referred to "holes" without distinction.[87]

$$O_2 + 2H_2O + 2e^- \rightarrow H_2O_2 + 2OH^- \tag{18}$$

$$O_2 + 2H_2O + 4e^- \rightarrow 4OH^- \tag{19}$$

$$H_2O_2 + O_2^{\bullet} \rightarrow OH^{\bullet} + OH^- + O_2 \tag{20}$$

$$OH^{\bullet} + MO \rightarrow Degradation \tag{21}$$

Whereas in the photocatalysis of Cu_2O, the hole cannot be transferred to $OH^{\bullet}$ because it cannot oxidize H_2O and the Cu_2O VBedge level is lower than the oxidation potential of water, more and more holes accumulate on the surface of the Cu_2O so that the concentration of holes is far greater than that of $OH^{\bullet}$.
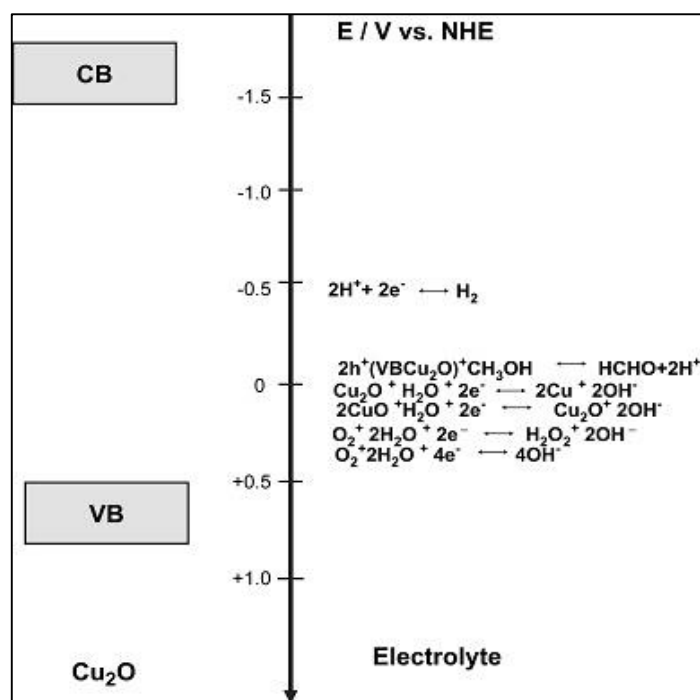
Figure 2.14. Overview of the redox potentials of the relevant reactions with respect to the estimated position of the Cu_2O band edges.[87]

2.7 The geopolymer matrix of the proposed new photocatalytic materials: Raw materials used to make geopolymers

2.7.1 Metakaolin (dehydroxylated kaolinite)

Kaolinite is a 1:1 clay mineral which means each structural unit has one tetrahedral silica layer and one octahedral alumina layer with the chemical composition $Al_2Si_2O_5(OH)_4$, (Figure 2.15). Individual particles of kaolinite form layers held together by hydrogen bonds and Van der Waals forces. The strength of these bonds prevents water from entering the interlayer spaces and cause swelling.[88] The dehydroxylated form of the clay mineral kaolinite is metakaolin, formed by the reaction $Al_2Si_2O_5(OH)_4 \rightarrow Al_2O_3.2SiO_2 + 2\ H_2O$. Halloysite $(Al_2Si_2O_5(OH)_4)$, a hydrated form of kaolinite, loses most of its adsorbed water in the temperature range 100-200 °C. Between 500-800 °C, kaolinite-type minerals lose their hydroxyl water by dehydroxylation. A large amount of energy is required to remove the chemically bonded hydroxyl ions, breaking down the crystal structure and producing an X-ray amorphous transition phase consisting of silica and amorphous alumina in a reactive form;[89] this has a high surface area, so the dehydroxylation of kaolinite to form metakaolin is an endothermic process. Heating at a higher temperature will cause recrystallization into

cristobalite (SiO_2) and mullite ($3Al_2O_3.2SiO_2$, the higher temperature form which is more thermodynamically stable than the lower-temperature form $2Al_2O_3.SiO_2$).
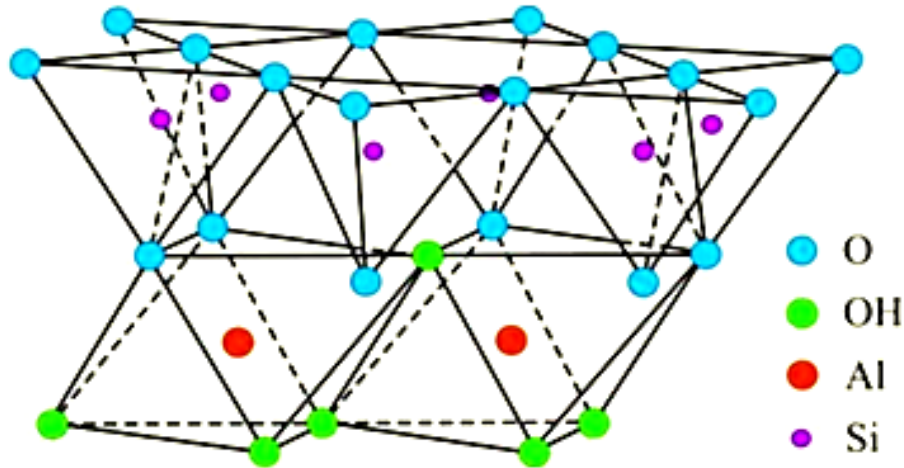
Fig 2.15. Structure of the kaolinite unit [90]

2.8 Geopolymers

Geopolymers are alumino-silicate materials formed by the reaction of alumina and silicate sources with an alkali metal activator. The solid source materials (typically aluminosilicates) should be rich in Si and Al and may be by-products or waste materials such as fly ash, silica fume, slag, rice husk ash, red mud, *etc*.[91] Geopolymers are unique by comparison with other aluminosilicates (e.g. aluminosilicate gels, glasses, and zeolites), since the concentration of solids in the geopolymerization reaction is higher than in aluminosilicate gel or zeolite synthesis.[92] Geopolymers are amorphous three-dimensional aluminosilicate binder materials, which were first discovered by Glukhovsky in the former Soviet Union in the 1950s.[92] In 1979 Davidovits, a French scientist, created similar materials, giving them the name "geopolymers"; these are a type of geopolymer containing SiO_4 and AlO_4 tetrahedra as the structural units. In general, geopolymers are typically formed by reaction between an alkaline solution (e.g., sodium hydroxide and sodium silicate) and a solid aluminosilicate source (e.g., metakaolin, fly ash or slag). Currently, geopolymers are receiving increasing attention from researchers because of their useful properties such as their strength and low environmental impact. An important property is that geopolymer materials can be made at room temperature

without firing; thus, an important reason for taking an interest in these materials is their low-temperature formation and hence low energy requirement.[93] Four essentials features have been proposed for distinguishing geopolymers from other aluminosilicate systems (i.e. zeolites, clays, etc.):[94]

i. They are prepared by alkali activation of an aluminosilicate source.

ii. They formed at temperatures between ambient and ~90 °C.

iii. They consist of cross-linked tetrahedral Si and Al units with charge compensation provided by alkali ions.

iv. They are X-ray amorphous materials that display a lack of long range ordering.

In addition, due to their exceptionally high thermal and chemical stability, excellent mechanical strength, adhesive behaviour and long-term durability, they may be used as a viable economical alternative to organic polymers and inorganic cements in diverse applications such as military,[95] aircraft,[96, 97,98] high-tech ceramics, thermal insulating foams,[99] fire-proof building materials,[94] protective coatings,[98] refractory adhesives[100] and hybrid inorganic-organic composites.[101,102] Furthermore, early researchers have demonstrated that geopolymers are cheap to produce and can be made from a vast number of minerals and industrial by-products, including pozzolans,[103,104] natural aluminosilicate minerals, metakaolin,[105,106] fly ash and kaolinite mixtures.[107,108] Geopolymers are resistant to fire and thermal shock and are used as a binder for the immobilisation of hazardous heavy metals and radioactive wastes.[109] They also have very low corrosion properties compared to other materials. Geopolymers may be modified or functionalized for applications as catalysts,[110] for purifying water[109] or removing CO_2, ammonia, or NO_X gases from the atmosphere.[111] They have attracted considerable attention as new, low CO_2 emission replacements for Portland cement.[109] Moreover, they are environmentally friendly materials from the point of view of reducing the greenhouse effects caused by CO_2 emission from the manufacture of Portland cement.

The chemical compositions of geopolymers are similar to natural zeolitic materials, but the microstructure is amorphous rather than crystalline.[112,32] According to Davidovits,[113] geopolymers possess amorphous to semi-crystalline three-dimensional silico-aluminate structures consisting of SiO_4 and AlO_4 tetrahedra linked by sharing all the oxygen atoms, giving units that can be designated as poly-sialate (-Si-O-Al-O-) (Si:Al = 1), poly-sialate-siloxo (-Si-O-Al-O-Si-O-) (Si:Al = 2), poly-sialate-disiloxo (-Si-O-Al-O-Si-O-Si-O-) (Si:Al

= 3), and sialate units (Si:Al > 3). Sialate is an abbreviation for silicon-oxo-aluminate. The empirical formula for the geopolymer matrix is:

$$M_n^+ \left\{ -(SiO_2)_z - AlO_2 - \right\}_n$$
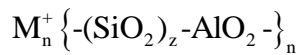
where M^+ = an alkali cation (K^+, Na^+) to balance the negative charge of Al^{3+} in IV-fold coordination, n = the degree of polymerization and z = the Si/Al ratio. By varying the Si/Al ratios (i.e. z = 1 to 300),[114] geopolymers exhibit different properties; low ratios (i.e., Si/Al ≤ 3) result in three-dimensional cross-linked rigid networks and stiff and brittle properties (as in cements and ceramics), while high ratios (i.e., Si/Al >3) result in 2-D networks and linearly linked polymeric structures with adhesive and rubbery properties, respectively.

Geopolymers appear to be good candidates as binders for ecologically friendly concrete, because of their durability. Furthermore, geopolymers can be used in concrete instead of Portland cement to give "green" concrete. Geopolymer cement concretes (GPCC) are geopolymer composites with the potential to form a substantial element of environmentally sustainable construction, by replacing or supplementing conventional concretes. GPCCs have high strength, with good resistance to chloride penetration, acid attack, etc.[1] Geopolymer concrete has emerged as a new technology in construction materials.[115]

2.8.1 Mechanism of Geopolymer Formation (Geopolymerization)

Geopolymerization is an exothermic process that proceeds *via* oligomers (dimers, trimmers) which are the fundamental unit structures in the three-dimensional macromolecular structure.[116] Davidovits suggested that geopolymerization could be regarded as the analogue of synthesis of zeolites.[117] In other words, the geopolymer microstructure is amorphous or semi-crystalline rather than crystalline.[117] The process of geopolymerization, represented schematically in Figure 2.16,[51] is proposed to occur by a complex series of concurrent and coupled reactions, the mechanism of which is thought to involve several key processes.[62, 106, 117]

I.   The generation of reactive species by alkali activation; this is the dissolution of amorphous phases (e.g., aluminosilicates) by alkali to produce small units of reactive silica and alumina.

II. Reorientation, which is the transportation or orientation or condensation of precursor ions into oligomers, and

III. The actual setting reaction, which is the polycondensation process leading to the formation of amorphous to semi-crystalline aluminosilicate polymers.

However, these three steps can overlap with each other and occur almost simultaneously, thus making it difficult to isolate and examine each of them separately.[112] The following two reactions can illustrate the schematic formation of geopolymer materials.

$$n(OH)_3\text{-Si-O-Al}^-\text{-O-Si-}(OH)_3 + NaOH \text{ or } (KOH) \rightarrow (Na^+,K^+)\text{-}(\text{-Si-O-Al}^-\text{-O-Si-O-}) + 4nH_2O \quad (I)$$

(OH)$_2$

(Geopolymer backbone)

$$n(Si_2O_5,Al_2O_2) + 2nSiO_2 + 4nH_2O + NaOH \text{ or } (KOH) \rightarrow Na^+,K^+ + n(OH)_3\text{-Si-O-Al}^-\text{-O-Si-}(OH)_3 \quad (II)$$

(Si-Al materials)

(OH)$_2$

(Geopolymer precursor)
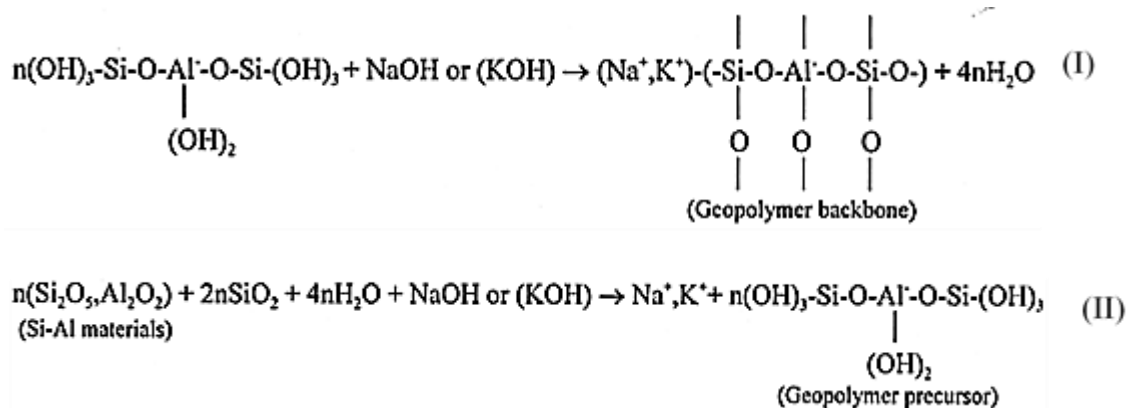
The two above reactions suggest that any material that contains mostly silica and alumina in an amorphous form is a possible source for the production of geopolymers.
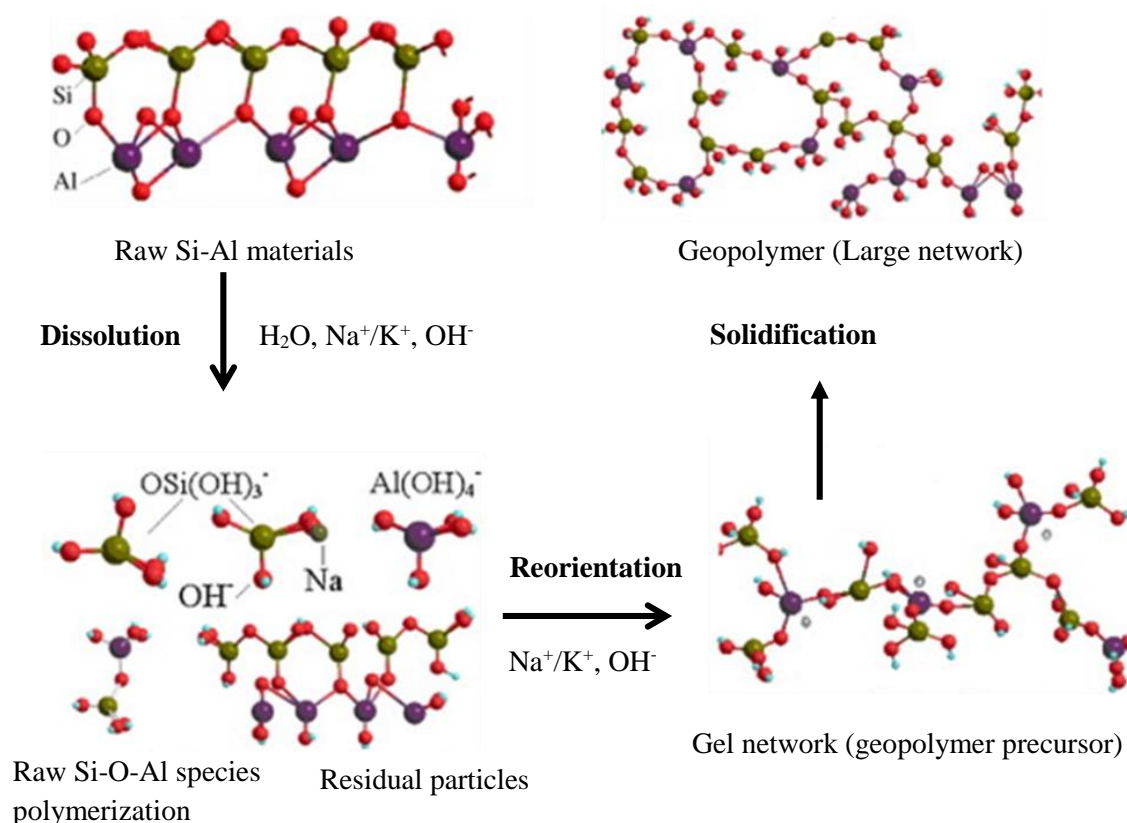
Figure 2.16. Sketch of the typical reaction mechanism of geopolymerization.[51]

During the dissolution step, both Si and Al species are produced when Si-Al raw materials come into contact with the alkaline solution.[118] The concentration of the alkaline solution, the alkali metal cation (e.g., Na^+, K^+), the mixing rate and time, and the intrinsic structure and composition of the Si-Al raw materials are the main factors controlling the generation of the Si and Al species. It has been suggested that the concentration of the alkaline solution and the intrinsic properties of the Si-Al raw materials are the dominant factors in this reaction step.[118] The reorientation step involves the dispersion of dissolved Si and Al species (e.g., Al^{3+}, Si^{4+}) into the oligomers, followed by the formation of a gel from the oligomers in the aqueous phase, producing relatively large networks by condensation.[32, 119] Once the dissolved Al^{3+} and Si^{4+} species on the surface of the source Si-Al materials are removed, further leaching of reactive Al and Si species from the raw materials occurs.

Throughout the solidification step, the gelation process continues to rearrange and reorganize the product, increasing the connectivity of the gel network and resulting in the amorphous or semi-crystalline three-dimensional aluminosilicate network commonly attributed to the geopolymer. At this stage, the temperature and air circulation are two major factors determining the properties of the final geopolymeric products.[118] These three major steps

occur simultaneously; for instance, during the solidification step, both dissolution and reorientation are also occurring.[112]

The resulting monolithic solids consist of cross-linked polymeric sialate chains of tetrahedrally coordinated Si and Al units linked by O. These tetrahedral SiO_4 and AlO_4 units have well-defined coordination geometries but form an extremely disordered network, shown in Figure 2.17.[120]

The alkali cations remain in the structure in irregular sites within the networks cavities. They take a range of hydrated states and provide the charge balance to the AlO_4^- or Si-O-Si bridges depending on the amount of free OH in the geopolymer structure.[120] Although a significant quantity of the initial water content is lost during gelation and hardening due to evaporation, large quantities are also retained as free and exchangeable water within the porous microstructure of the monolith.
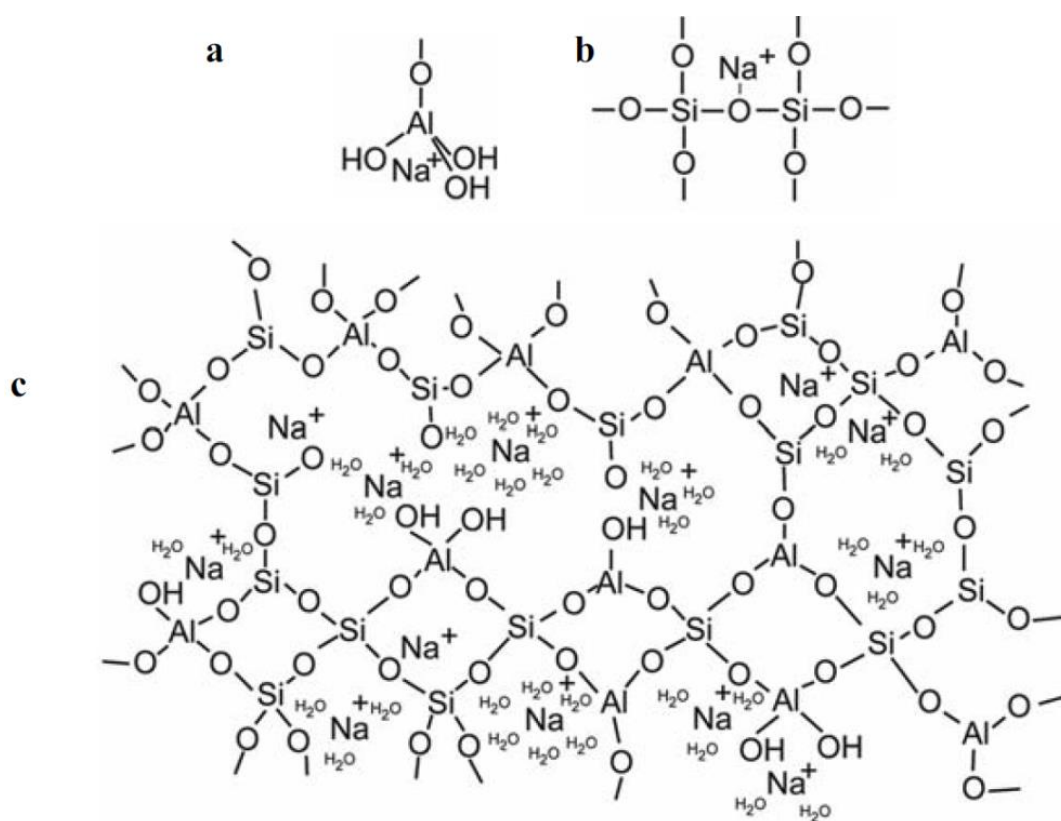
Figure 2.17. (a) Proposed model for the location of the charge balancing Na+ cation that assumes the form of a semi attached Na aluminate species. (b) Proposed model for the site of the charge balancing Na+ cation that assumes the form of a modified bridging network. (c) proposed a schematic structural model of AIP structure based on an original model by Barbosa *et al.*[121]

2.8.2 Characteristics of geopolymers

A principal characteristic of geopolymers cured at ambient temperatures is that they are x-ray amorphous. The XRD patterns of well-cured geopolymers do not normally show sharp peaks but present a large hump in the background at around 30 $^{\circ}2\theta$. A typical pattern is shown in Figure 2.18. The peak labelled "Q" is a quartz peak, from an impurity in the clay reactant.
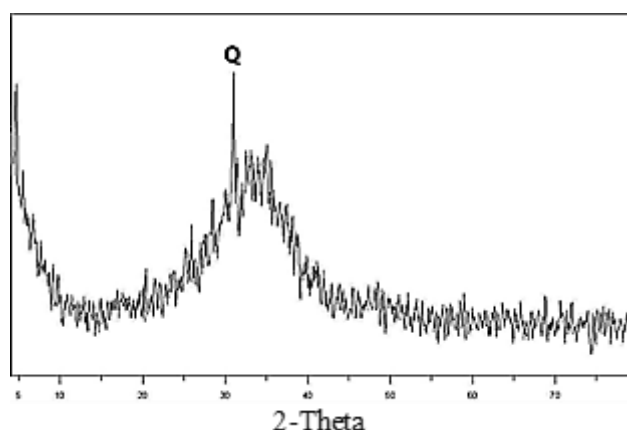
Figure 2.18. Typical XRD spectrum of a GP.[122] Q = quartz (PDF no.33-1161)

Geopolymers can be produced with various microstructures depending on the Al: Si ratio; two and three-dimensional cross-linked geopolymer structures are formed in compositions of high aluminium and silicon contents respectively. Because of the various microstructures, different mechanical and physical properties can be achieved.[123] Since XRD cannot determine the coordination state of atoms in amorphous materials, ^{27}Al and ^{29}Si solid state nuclear magnetic resonance spectroscopy with magic angle spinning (MAS NMR) must be used to provide this information.[124]

2.8.3 Application of geopolymers as photocatalytic materials

Geopolymers derived from clay minerals can maintain elements of the layered structures and large surface areas of the precursor with the ability to absorb organic substances on both their external surfaces or within their internal spaces.[125]

In a potential application to decompose hazardous atmospheric pollutants, Tirado *et al.* [126,127] have used an ion exchange procedure to incorporate photoactive TiO_2 into an aluminosilicate

geopolymer (geopolymer). TiO_2 and TiO_2-based nanomaterials are noted photocatalysts for effective treatment of wastewater polluted with toxic organic compounds. In another study, Cerney et al. [128] have reported a simple method for the preparation of photocatalytically active layers of metakaolinite-based geopolymer composites containing TiO_2 powders deposited on steel plate substrates. In both these studies the photoactive element was TiO_2 and the geopolymer acted as the supporting matrix. In addition to geopolymers, other porous matrices that have been used for supporting TiO_2 particles include silica [129, 130], alumina [131, 132], activated carbon [133, 134], clays and zeolites [135-137]. The use of high surface area supports in conjunction with nanoparticle oxides provides more efficient adsorption sites by comparison with bare TiO_2.[138]

Tirado et al. prepared metakaolin-based geopolymers at different temperatures and ion-exchanged them with solutions of $(NH_4)_2TiO(C_2O_4)_2.H_2O$. This ion-exchange method incorporated the anatase form of TiO_2 particles inside the geopolymers.[110] The EDS of these materials (Figure 2.19) showed that the exchanged surfaces prepared at 90 °C from the NH_4-geopolymer contained a greater percentage of titanium than samples prepared from the Na form of the geopolymer at same temperature.

Elem	Wt %	At %
O	27.67	56.45
Na	1.83	2.6
Al	4.81	5.82
Si	9.34	10.85
Au	27.38	4.54
Ti	28.96	19.73

Elem	Wt %	At %
O	43.72	67.37
Al	12.34	11.27
Si	18.43	16.17
Au	20.55	2.57
K	0.46	0.29
Ti	4.51	2.32
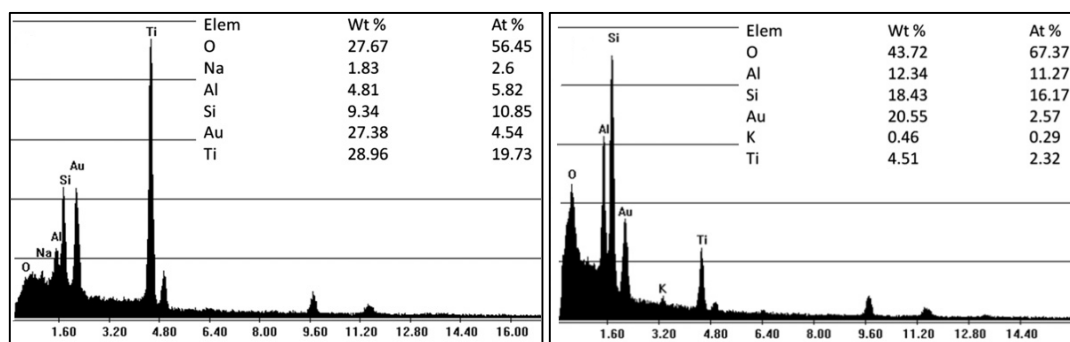
Figure 2.19. EDS element quantification of Ti ion-exchanged GPs: (right) 90 °C Na GP, (left) 90 °C NH_4.[110]

Figure 2.20(a) shows that TiO_2 is present as anatase in the composites, in different amounts as reflected in the XRD peak intensities. The UV–Vis reflectance spectra reported by Tirado et al. (Figure 2.20(b, c)) show differences between the reference and ion-exchanged geopolymers. The blue shifts in UV-visible spectra demonstrated the growth of TiO_2 nanoparticles inside the micropores of the geopolymer which is related to quantum size effects of the TiO_2 particles. The presence of micropores and mesopores of <5 nm size in the

geopolymers formed at 90ºC restricts the TiO_2 particles growing inside them to nanoscale dimensions.

The rate of degradation of MB by the sample with the highest amount of TiO_2 compared with the blank geopolymer highlighted the photoactivity of the TiO_2 particles inside the pores of the ion-exchanged geopolymer.[110]
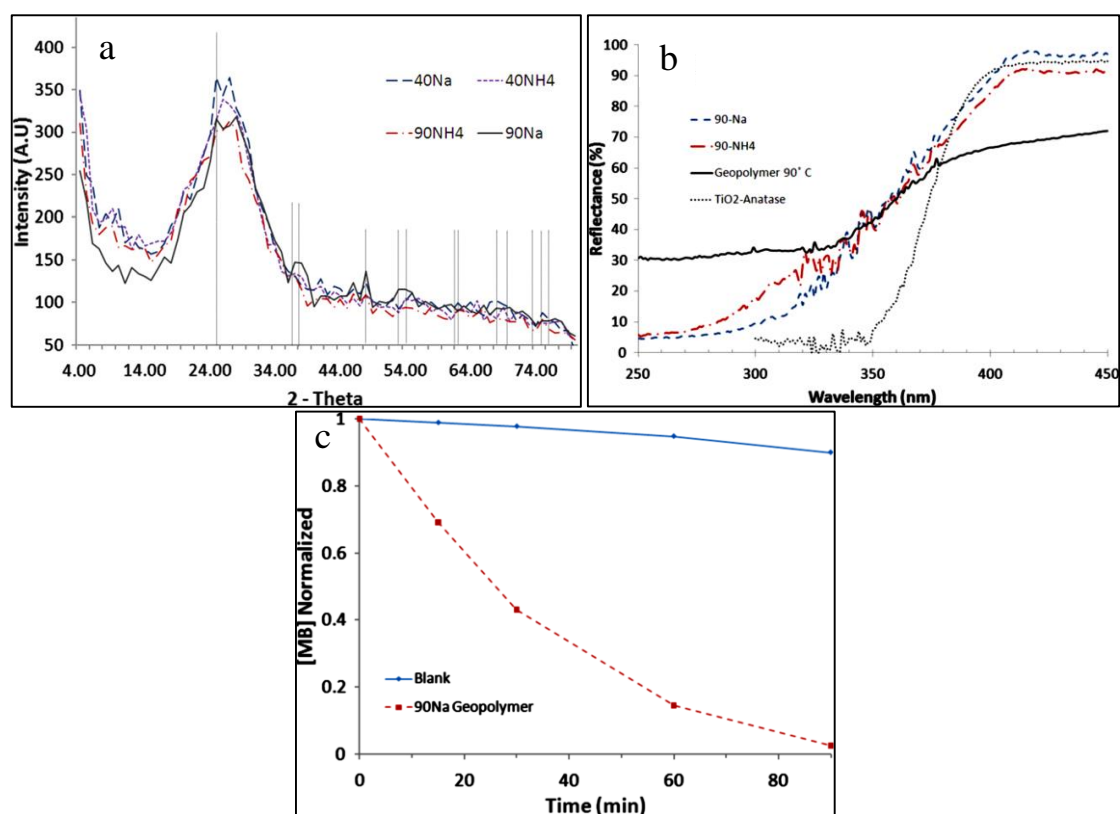
Figure 2.20. (a) XRD pattern of powdered ion-exchanged GPs, (b) UV–Vis reflectance spectra of 90 ºC Na-derived GP and 90 ºC NH₄–derived GP, (c) Photoactive bleaching of MB by TiO_2 particles in Na-derived GP.[110]

On the basis of the effectiveness of these geopolymer-TiO_2 composites, it is thought that by inserting Cu_2O particles into a geopolymer matrix, the resulting composite photocatalyst with a direct band gap of 2.17 eV should have the ability to show good photocatalytic activity in visible light and result in a material suitable for efficiently degrading toxic organic compounds.

2.9 Modification of the geopolymer matrix

Recently, clays such as kaolinite, montmorillonite, sepiolite, and mica have attracted much interest due to their high surface area and porosity, layered structure and high adsorption

ability [139]. Kaolinite is a clay with strong interactions between the layers, with both cationic and anionic charge on the upper and the lower surfaces of the layers[140]. Moreover, dehydroxylated kaolinite reacts with alkali silicate solution under highly alkaline conditions to produce geopolymers (geopolymers) that are X-ray amorphous and consist of a random three-dimensional tetrahedral network of aluminate and silicate units[141] as described in Section 2.8. Immobilization of nanoparticles on the inner and outer surfaces of these geopolymer matrices has the potential to produce improved heterogeneous photocatalysts. The role of these nanocomposite matrices is of great interest in the study of photocatalytic reactions for the removal of organic pollutants.[142] Nano-composite matrices can adsorb organic substances either on their external surfaces or within their layer spaces *via* interactions or exchange reactions.[76] One possible method for increasing the porosity and surface area of the composites by the use of a surfactant such as a large quaternary ammonium ion in the synthesis process. The modification of clays with quaternary ammonium ions has been reported by many research groups since the 1950's (de Paiva *et al*.,[143] Jordan *et al*.,[144]). Organic compounds in aqueous solution are inserted in the interlayer of the clay mineral during cation exchange. The amount of exchange is specified by the hydrocarbon chain length and can be equal to or greater than the cation exchange capacity (CEC) of the clay.[143, 144] In general, synthesis and characterization of photocatalytic TiO_2 pillared clays, especially of montmorillonite type, by the use of small amounts of a quaternary ammonium ion has been reported extensively. The clay modification process not only expands the layers and controls the size of the clays but also can produce a hydrophobic photocatalyst composite.[9, 76, 145-150]

In 1986, TiO_2 pillars (anatase) were formed between the montmorillonite layers by Johan Sterte.[151] The TiO_2-cross-linked montmorillonite was prepared by dispersion of the montmorillonite powder into the distilled water, with a cross-linking agent of $TiCl_4$ in HCl. The mixture was then aged for 16 h and separated by centrifuging. The surface areas were in the range of 200-350 m^2/g and pore volumes were about 0.2 cm^3/g, as determined by N_2-desorption pore size analysis. The surface area increased, and the pore volume decreased with increasing HCl-concentration in the Ti-solution. A further increase of Ti added resulted in a reduction in surface area, but the pore volume and the uptake of TiO_2 remained almost constant.[151]

Later in 1999 Ooka *et al*.[152] prepared a novel pillared montmorillonite with crystallized TiO_2 that showed effective photocatalytic activity. The synthesis was hydrothermal and the

porosity of the pillared clay was retained. The pillared montmorillonites exhibited higher catalytic activity by decreasing the TiO_2 pillar size.[152]

In 2002, Zhu *et al.*[153] reported the formation of bentonite pillared with a mixed solution of silicon and titanium hydroxides treated with quaternary ammonium surfactants. They found that titanium in these samples was highly dispersed in the silica matrix rather than existing in the form of small particles of pure titania. Excellent activity for catalytic oxidation reactions, increased porosity and improvement in thermal stability were reported to result from this surfactant treatment.[153]

Miao *et al.* successfully prepared titanium tetrabutyloxide by impregnating the interlayers of montmorillonite (MMT), followed by hydrolysis of the precursor in water and calcination at 500 °C. XRD and electron microscopy showed that the layered structure of MMT was destroyed in the composites. High-resolution transmission electron microscopy revealed the loading of TiO_2 particles in the exfoliated layers of the MMT. The samples also exhibited highly efficient removal of MB due to the adsorptive capacity of MMT and the catalytic degradation ability of TiO_2 for MB.[139]

Yan *et al.* reported the adsorption of benzoic acid from water on CTAB-exchanged montmorillonite. The largest adsorption was achieved at pH 9, and the adsorption kinetic data were fitted by a pseudo-second-order equation. The results confirmed that CTAB-montmorillonite is a potential adsorbent for benzoic acid.[154]

Kibanova *et al.* reported a new method for the synthesis of photocatalytically active small-sized TiO_2 supported on hectorite and kaolinite. This method deposited the TiO_2 on the clay mineral surface by a sol–gel process using titanium isopropoxide as a precursor. The synthesized clay–TiO_2 composites were compared with pure commercial TiO_2 (Degussa P25). The results showed that the photocatalytic activity of the anatase phase TiO_2 composite was similar to that of commercial P25 TiO_2.[155]

Recently, Wang *et al.* developed a new method for immobilizing nano scaled TiO_2 on the surface of montmorillonite clay. The CTAB cationic surfactant was inserted into the montmorillonite clay by ion exchange and physical adsorption processes, then the as-prepared TiO_2 solution was dispersed on the external and internal surface of the product after removal of the surfactant. These authors suggested that the cationic surfactant has a templating role, and can control the contents of the composite. The photocatalytic activities of these TiO_2 composites were higher than that of P25. The method consists of the modification of the montmorillonite with the surfactant and then the formation of the TiO_2 particles. According to their schematic model, as shown in Figure 2.21, montmorillonite has

two siloxane tetrahedral sheets sandwiching an aluminum octahedral sheet with a negative surface charge on the clay. The cationic surfactants increase the surface area of the clay and the TiO_2 particles hydrolyze and condense around or on the surface of the surfactant.[156] Nano scaled TiO_2 particles were created both on the surfaces and in between the montmorillonite layers, as shown by the high-resolution TEM image (Figure 2.22) of the intercalation of the titanium species between the layers of the clay. TiO_2 is present both in the internal and external surfaces of the clay.[76]
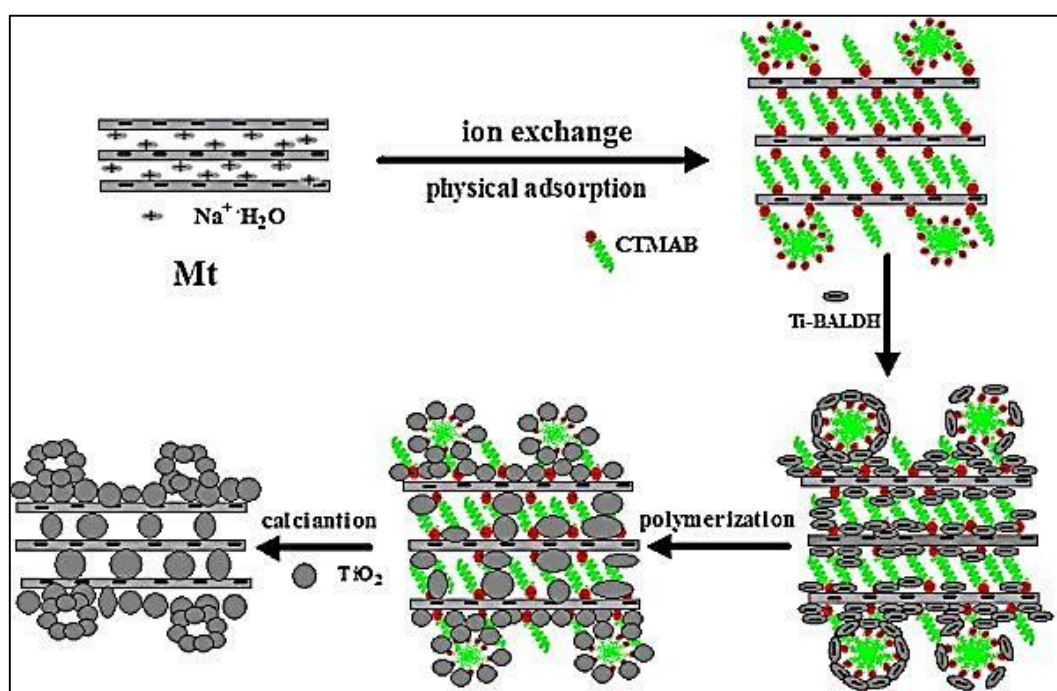
Figure 2.21. Schematic for the preparation of Ti(*x*)C$_{16}$(*y*)-Mt.[76]
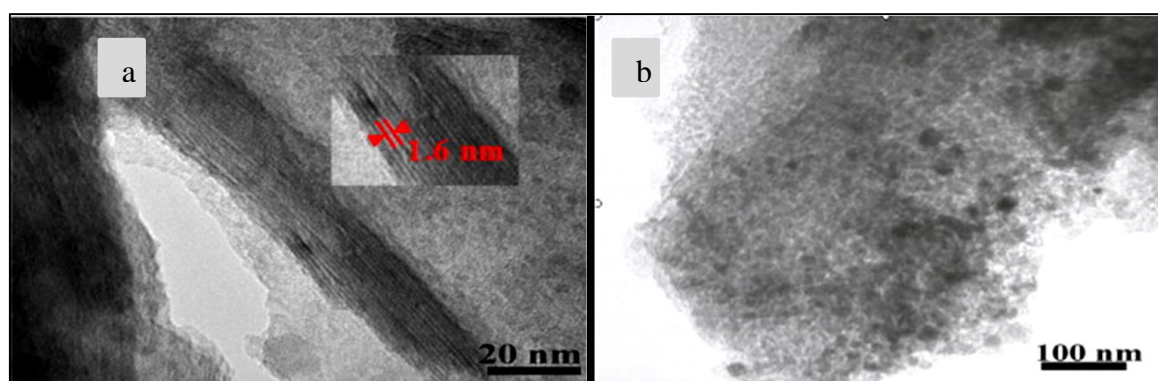
Figure 2.22. (a,b) TEM images of Ti(25)C$_{16}$(1.0)-MMT sample calcined at 600 °C.[76]

All these applications involve the formation or modification of a crystalline structure, but to our knowledge, CTAB has never previously been used to modify an X-ray amorphous

material such as an aluminosilicate geopolymer. One part of this work was intended to exploit the ion-exchange properties of geopolymers by replacing the monovalent charge-compensating ion by the much larger CTAB, thereby expanding the pore structure and facilitating the entry of the photoactive Cu_2O and/or P25 titania deeper into the structure. It was also hoped that the presence of the CTAB might modify the mechanism by which the photoactive oxides are attached to the geopolymer matrix, and help to stabilize the pH of the solution, allowing the dye removal processes containing adsorption and photodegradation to be separately measured.

Chapter 3
Methodology

This chapter describes the experimental details, chemicals, materials and characterization techniques used for this research.

3.1 Preparation of Sodium-Geopolymer (Na-GP)

The geopolymer matrix was prepared from New Zealand kaolinite-type halloysite clay (Imerys Premium Grade) dehydroxylated at 600 °C for 24 hour, sodium hydroxide (BDH reagent grade) and sodium silicate solution (FERNZ Chemical Co, NZ, Type "D", Na_2O/SiO_2 = 0.48, solids content=41.1 mass %). These constituents, formulated to the molar oxide ratio SiO_2/Al_2O_3=2.91, Na_2O/SiO_2=0.34, Na_2O/Al_2O_3=1.01 and H_2O/Na_2O=10.12 were mechanically mixed for 15 min. before transferring to cylindrical plastic molds and vibrating for 15 min. to remove entrained air. The sealed composites were then cured for 12 hour at 40 °C and after unsealing, dried for another 12 hour. The prepared geopolymers matrix was finely ground and stored in sealed plastic bags for characterization. This molar composition has been reported[121] by Clelio *et al.* to produce geopolymers with optimal mechanical properties.

3.2 Synthesis of Cu_2O nanoparticles

Three published synthesis methods for Cu_2O were investigated as outlined below: these were the precipitation method of Bai *et.al* [157] which produces cubic crystallites, the method of Luo *et.al* [64] which gives octahedral crystallites, and the method of Shah *et.al*.[158] which gives spherical crystals. Although all three syntheses are reported to produce nanosized crystals, only the the method of Bai *et al.* was found to give nanoparticles with an average size of ~ 80-150 nm; for this reason, this method was adopted because it was the only one that produced nanosized particles, and was a facile synthesis involving a lower synthesis temperature.

3.2.1 Synthesis of cubic Cu_2O particles

An aqueous solution of copper acetate, $Cu(CH_3COO)_2.H_2O$ (May and Baker) and polyvinylpyrrolidone (PVP, K30, MW 10,000, Sigma-Aldrich) was stirred vigorously, producing a blue suspension after dropwise addition of NaOH solution. The colour of this

suspension progressively changed from blue to green, and after stirring for 30 min., to orange upon dropwise addition of a solution of ascorbic acid, $C_6H_8O_6$ (Fisher, AR grade). The precipitate was then centrifuged, washed three times with deionized water and dried in air. The PVP surfactant is used to kinetically control the growth of the single crystal nanocubes, since surfactants play an important role in the development of the average size and morphology of nano crystals. When added to the solution, the active surfactant molecules are adsorbed on to specific crystal planes of the developing nano crystals. The shape of the crystal and the growth habit of the crystal planes are related to the type and amount of surfactant used.[157]

3.2.2 Synthesis of octahedral Cu_2O particles

The synthesis was carried out by a simple solution-phase reduction system in which $CuCl_2.2H_2O$ (Alfa), is reduced by AR grade glucose and $NaHCO_3$. The non-ionic surfactant octylphenyl ether Triton X-100, (x =100, Pure Science) was used as a capping agent to form the hybrid building blocks. Uniform octahedral polycrystals precipitated from the resulting blue–green mixture after heating at 60 °C for 4 hour under constant magnetic stirring. The solution was centrifuged at 4000 rpm for 15 min., and the orange precipitate was rinsed several times with distilled water and dried at room temperature for 12 hour.

3.2.3 Synthesis of spherical Cu_2O particles

Polycrystalline spherical Cu_2O particles were synthesized at 140 °C without any surfactant or additives. Copper metal powder was added to distilled water, sonicated for about 25 min. and transferred to a stainless steel bomb that was sealed under ambient conditions. The bomb was then placed inside a preheated furnace at 140 °C for 15 hour. The resulting suspension was centrifuged, washed and dried at room temperature.

Since the spherical and octahedral Cu_2O products were found by SEM analysis to be in the sub-micron size range, whereas the cubic oxide nanoparticles were of nanometer size, the latter were chosen for incorporation into the geopolymer matrix. Another advantage of the cubic Cu_2O is its room- temperature synthesis, making it more ecologically friendly.

3.2.4 Another Method for Synthesising Cu₂O Nanoparticles: The Gas Reduction Method

3.2.4.1 Preparation of brochantite (Cu₄SO₄(OH)₆)

The first step in this synthesis was the preparation of brochantite (Cu₄SO₄(OH)₆), as follows: 1.0 M NaOH solution was very slowly (~1 drop every 3 s) added to a 1.0 M aqueous of copper sulphate solution. The solution was stirred magnetically throughout the titration and the stirring continued for an additional 30 min. The reactant was heated to 60 ºC on a hotplate throughout the titration and stirring period. The product was filtered and air-dried.

3.2.4.2 One-step synthesis of tenorite (CuO) nanoparticles from Cu₄(SO₄)(OH)₆ by a direct thermal-decomposition method

The product from the above step was calcined in air in a muffle furnace for 6 hour during which time the temperature was raised from 120-750 °C to form CuO nanoparticles. The reaction pathway of the thermal decomposition of brochantite to CuO includes thermal dehydration and desulfuration processes (Eqs. 22–24).[159]

$$Cu(SO)_4(OH)_6 \cdot xH_2O \xrightarrow{80-170\ ℃} CuSO_4 \cdot 3Cu(OH)_2 + xH_2O \qquad (22)$$

$$CuSO_4 \cdot 3Cu(OH)_2 \xrightarrow{250-400\ ℃} CuSO_4 \cdot 2Cu(OH)_2 + CuO + H_2O \qquad (23)$$

$$CuSO_4 \cdot 2Cu(OH)_2 \xrightarrow{610-700\ ℃} 3CuO + 2H_2O + SO_2 + \frac{1}{2}O_2 \qquad (24)$$
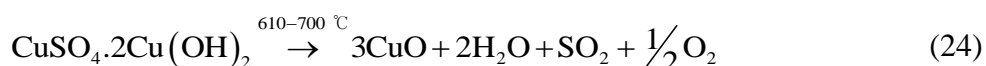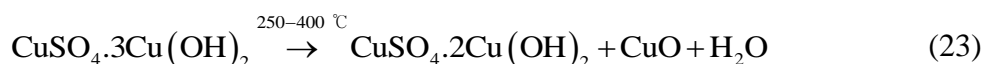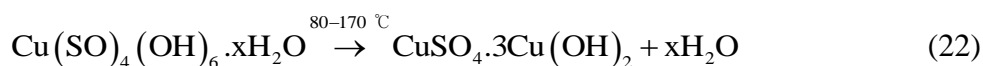
3.2.4.3 Formation of stable Cu₂O by reduction of CuO nanoparticles

The loose CuO powder was loaded into an open tube with an inner diameter of 2 cm. One end of the tube was connected to an inlet with a gas mixture of 5% H₂ and 95% N₂ (99.999% purity) while the other end was connected to a flow meter. The powder was heated in the tube furnace from room temperature to 250 °C for 135 min. Every 45 min. a small fraction of the produced precursor was collected for analysis.

The Cu_2O particles prepared by this method was not chosen for the continuing experiment because the preparation method was time-consuming and requires a temperature of about 750 °C, militating against one of the main objectives of this research which was to prepare eco-friendly materials.

3.3 Synthesis of spherical Cu_2O/TiO_2 nano-heterostructures

Representative Cu_2O/TiO_2 nano-heterostructures were prepared by an alcohol-aqueous based chemical precipitation method reported by Huang *et al.*:[85]

A calculated amount of copper acetate (May and Baker AR grade) was dissolved in 100 ml absolute ethanol to form a deep green solution and stirred for around 30 min. sufficient TiO_2 (Degussa P25) was added to this solution such that the mass composition of the heterostructure was 50/50 Cu_2O:TiO_2 and the solution was sonicated to achieve a uniform suspension. 100 ml aqueous glucose solution was then added drop wise to the suspension heated at 60°C in a water bath, followed by the drop wise addition of NaOH dissolved in 70 ml absolute ethanol and 50 ml distilled water. The resulting yellow precipitate was centrifuged from the solvent and washed several times with distilled water to remove residual acetate, glucose and NaOH. The light orange product was then oven-dried at 50 °C overnight.

3.4 Preparation of Na-Geopolymer Composites Containing Cu_2O

The photocatalytic geopolymer/Cu_2O composites were prepared by blending the uncured geopolymer mixture, prepared as described in Section 3.1, with 10, 20 and 30 wt% of cubic nano crystalline Cu_2O powder prepared as described in Section 3.2.1, stirring for 15 min. before transferring to cylindrical plastic moulds and vibrating for 15 min. to remove entrained air. The composites were then cured for 12 hour at ambient temperature, finely ground and stored in sealed plastic bags. In an alternative approach, an attempt was made to synthesize the geopolymer/Cu_2O composites by mixing the matrix and Cu_2O-forming reagents *in situ* in a single step; this was abandoned however because of the high water content which militated against the formation of a well-reacted geopolymer as determined by ^{27}Al and ^{29}Si MAS NMR spectroscopy.

3.5 Preparation of Na-Geopolymer Composites Containing Cu_2O/TiO_2

The photocatalytic geopolymer/Cu_2O/TiO_2 was prepared as described in section 3.4 except that the 10, 20 and 30 wt% nanoparticle oxide additions were of Cu_2O/TiO_2 nano-

heterostructures synthesised as described in Section 3.3. For comparison, a corresponding set of composites containing only P25 titania was synthesized and tested.

3.6 Preparation of CTAB-Modified Na-Geopolymer Matrix

The CTAB-modified geopolymer matrix was synthesised by mixing together New Zealand kaolinite-type halloysite clay (Imerys Premium Grade) dehydroxylated at 600 °C for 24 hour, sodium hydroxide (BDH reagent grade) and sodium silicate solution (FERNZ Chemical Co, NZ, Type "D", $Na_2O/SiO_2 = 0.48$, solids content = 41.1 mass %), in proportions such that the molar oxide ratio was $SiO_2/Al_2O_3 = 2.91$, $Na_2O/SiO_2 = 0.34$, $Na_2O/Al_2O_3 = 1.01$, $H_2O/Na_2O = 10.18$. A calculated amount of cetyltrimethylammonium bromide (CTAB) (Merck) based on the cation exchange capacity of the starting clay was added and the resulting paste mixed for 15 min. before transferring to cylindrical plastic moulds and vibrating for 15 min. to remove entrained air. The moulds were then sealed and their contents cured for 12 hour at 40 ^{0}C, unsealed and dried for 12 hour.

The quantity of CTAB added to the geopolymer matrix was determined by:

$$f = \frac{M_{Cation}}{CECM_{clay}GMW_{Cation}X} \qquad (25)$$

where f is the fraction cation exchange capacity (dimensionless), M_{cation} the mass organic cation required to achieve desired fraction of CEC (mass), CEC the cation exchange capacity of clay (equivalents/mass), M_{clay} the mass clay (mass), GMW_{cation} the gram molecular weight of organic cation (mass/mol) and X is the moles of charge per equivalent = 1 mol/equiv. for the cations used in this study (mol/equiv.).[160]

3.7 Preparation of CTAB-modified Na-Geopolymer Composites Containing Cu_2O

The CTAB-modified geopolymer-Cu_2O photocatalyst composite was prepared by powdering the matrix geopolymer and dispersing it as a 1% suspension in distilled water. To this suspension, after stirring for 2 hour at ~ 50 ^{0}C, was added 10, 20 and 30 wt% of cubic nano crystalline Cu_2O powder prepared as described in Section 3.2.1, stirring for 15 min. before transferring to cylindrical plastic moulds and vibrating for 15 min. to remove entrained air. The composites were then cured for 12 hour at ambient temperature, finely ground and stored in sealed plastic bags.

3.8 Preparation of CTAB-modified Na-Geopolymer Composites Containing Cu₂O/TiO₂

The procedure for preparing the photocatalyst composite of CTAB-modified geopolymer with Cu_2O/TiO_2 followed the method described in the section 3.7 except that the 10, 20 and 30 wt% nanoparticle oxide additions were of Cu_2O/TiO_2 nano-heterostructures synthesised as described in Section 3.3. For comparison, a corresponding set of composites containing only P25 titania was synthesized and tested.

3.9 Sample Characterization Techniques

A number of techniques were used to characterise the crystalline phases, surface morphologies, and molecular structure and photocatalytic properties of composites. The instruments employed in this research are shown in Table 3.1.

Table 3.1. List of instruments used in this work.

Test	Model
X-ray diffraction (XRD)	PANalytical X'Pert
Scanning Electron Microscopy (SEM)	JEOL 6500 F, JEOL JSM-6610 LA
Transition Electron Microscopy (TEM)	JEOL 2010, JEOL 2100 F
Fourier Transform Infrared Spectroscopy (FTIR)	Perkin-Elmer model 2000
Nuclear Magnetic Resonance Spectroscopy (MAS NMR)	Bruker Avance 500
UV-Visible spectroscopy	Agilent 8453
Brunauer–Emmett–Teller (BET)	Micromeritics ASAP 2010
Nuclear quadrupole resonance (NQR)	Chemagnetics CMX

3.10 Powder XRD Analysis (PXRD)

XRD is an important method used for structural studies including crystal imperfections, preferred orientation in polycrystalline sheets and the network of atoms in solids. X-rays are

electromagnetic waves, but have smaller wavelengths (10^{-10} m) that are of the same magnitude as the interatomic spacing in crystals. Using XRD, crystallographic phases can be identified and quantitatively determined in materials such as metals, clays, ceramics or mineral mixtures.[161]

XRD is based on the diffraction of x-rays from crystalline phases containing long-range order, hence characterization of amorphous phases with diffuse scattering patterns is not possible. Amorphous phases in such materials appear as broad humps and a raised background rather than well-defined peaks. However, the presence of a broad amorphous hump allows this technique to indicate the presence of the amorphous geopolymers. Any partially reacted crystalline phases still present in geopolymers will also be detected as sharp peaks, or as peaks related to the mineral phases present as impurities in the reactants.

3.10.1 Basic Principles

The x-ray beam interacts with a crystalline substance and the reflection of the beam results in a characteristic diffraction pattern of intensities at particular diffraction angles. Subsequently each crystalline material produces its unique diffraction pattern; each crystalline phase can be identified or determined within a substance containing multiple crystalline phases. X-ray patterns of pure substances are therefore like fingerprints. The resulting pattern is characteristic of the sample material and thus can be used for the identification by comparison with a pattern database. By measuring the spacing of the lines in the diffraction pattern, identification of the size and shape of the unit cell are achieved. The Bragg equation (eq. 26) is the central equation in analysing the results for a powder diffraction experiment.[162] X-rays are effective for analysis of crystal structures because their wave lengths of about 1Å are of the same order as the spacing of atomic planes in crystalline materials. One of the most commonly used interpretations of XRD is the Bragg Reflection Analogy, which describes the uniqueness of XRD in terms of the reflection of X-rays by planes of atoms in minerals.
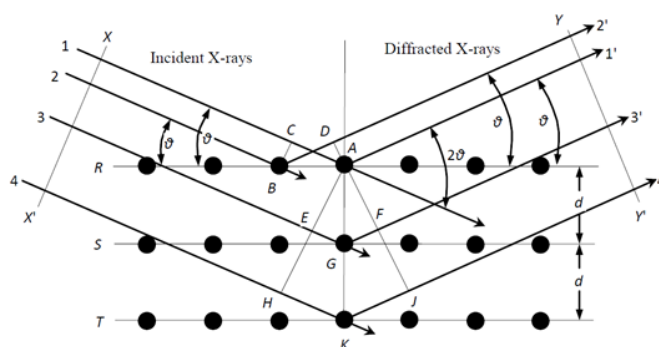
Figure 3.1. XRD by lattice planes. Schematic illustration of Bragg's Law.[163]

XRD analysis is based on the principles of XRD by a diffraction grating. Suitable "gratings" for x-ray beams are the planes of atoms in the crystal structures of crystalline phases. Without any diffraction effects, the incidence of a primary x-ray beam onto a sample volume would produce scattering in all directions. The directions in which the reflections can be observed depend on the intervals between the lattice planes scattering x-ray beams and interference of the scattering by scattering from neighbouring lattice planes.[161]

The most common expression of Bragg's Law is given by:

$$n \lambda = 2d \sin \theta \tag{26}$$

Where λ is the wave length of the X-rays, d is the distance between parallel atomic planes, θ is the angle between the incident rays and parallel atomic planes, and n is an integer. The values of d and the number and types of atoms in each plane are unique for every mineral. Since each mineral has its specific spacing of interatomic planes in three dimensions, the angles at which diffraction occurs can be used for identification.[161]

3.10.2 Preparation of the XRD Sample

Phase analysis of powders using XRD requires sample preparation. To prevent contamination of the samples and give deceptive results, it is necessary to work in a clean environment. The solid pieces of starting material must be powdered using a mortar. Ideally the particles should not be larger than about 5μm; a good indication of sufficient fineness is when the powder feels floury. The sample holder is filled with a slight excess of powder which is then compressed using a clean glass microscope slide. It is important that the powder is only pushed down; sliding or turning the glass slide across the powder bed should be avoided to

prevent preferred orientation of crystals. To check if the powder is attached to the holder, it can be gently tipped.

Amorphous phases in geopolymer materials appear as broad humps in the background. However, the presence of such a broad amorphous hump allows this technique to indicate the presence of the amorphous geopolymers. Data were collected from powdered samples using a Panalytical Pro MPD diffractometer with CuKα-radiation and a PIXcel detector. Scans were determined in the region 10–80 °2θ with a 0.013 °step operated at 45 kV and 40 mA. The details of the identified crystalline phases and reflection data for the principal components encountered in the present samples are summarized in Table 3.2.

Table 3.2. Assigned crystalline phases and measured reflections

Crystalline Phase	JCPDS File No.	Measured 2θ degrees for Cu Kalpha	(hkl)	d-Spacing nm
Cristobalite	01-075-0923	21.96	(101)	0.28
Quartz	01-078-2076	26.75	(100)	0.34
Cu_2O (Cubic)	01-073-6237	29.41	(110)	0.30
		36.28	(111)	0.24
		42.18	(200)	0.21
		52.39	(211)	0.17
		61.30	(220)	0.15
		73.49	(311)	0.13
		77.35	(222)	0.12
TiO_2 (Rutile)	04-006-1919	27.51	(110)	0.33
		36.15	(101)	0.25
		41.31	(111)	0.22
		44.13	(211)	0.20
		54.01	(210)	0.16
		54.34	(211)	0.17
		56.68	(220)	0.16
		62.78	(002)	0.15
		64.09	(310)	0.15
TiO_2 (Anatase)	00-021-1272	25.37	(101)	0.35
		37.02	(103)	0.24
		37.89	(004)	0.24
		38.62	(112)	0.23
		48.13	(200)	0.19
		55.05	(211)	0.17
		55.15	(211)	0.17
		68.76	(116)	0.14
		70.31	(220)	0.13

3.11 Scanning Electron Microscopy (SEM)

SEM is electron microscopy that images the sample surface by scanning it with a high-energy beam of electrons. The electrons interact with sample, producing various signals including secondary electrons, and back-scattered electrons, characteristic X-ray signals that contain information about the sample surface topography (e.g. microstructure or a composition).

From these signals we can image the sample and determine atomic composition. The SEM can produce images with a resolution up to 1 nm.[164] ENREF_120

3.11.1 Energy-dispersive X-ray Spectroscopy (EDXS)

Highly energetic electrons re-emitted from the sample surface after being scattered within the specimen. In backscattered imaging mode regions with higher average atomic number appears brighter than regions with lower average atomic number.

EDXS is a type of X-ray detector used for quantitative elemental microanalysis.[164] Areas of interest of a sample are exposed to the atoms in the sample have unexcited electrons (or electrons in ground state) in their electron shells. The highly energetic beam excites these electrons and forces them into a higher energy level (higher shell) which causes an electron gap. This gap is filled by another electron from a higher energy level (higher shell). The energy difference between these two shells is expressed by the emission of specific x-ray radiation characteristic of the energy difference. Every element has a specific x-ray radiation energy if its electrons are excited in this way which can therefore be used as a "fingerprint" or unique identifier.

SEM images of the geopolymer composites and oxide nanoparticles were acquired under high vacuum using high and low resolution analytical SEM. The probe current was 15 kV, and the working distance was 10 mm. The sample powders were placed on carbon tape attached to an aluminium stub and coated with 7–9 nm carbon using high-vacuum carbon coater. Elemental analysis was achieved by the EDXS unit operating in the backscattered mode.

3.12 Transition Electron Microscopy (TEM)

TEM images were obtained using a JEOL 2010 or JEOL 2100 F electron microscope with an integrated EDXS detector and operated at 200 keV. For sample preparation the powdered sample was suspended in 5 ml absolute ethanol, and the suspension was dropped onto 400

mesh ProSciTech copper grids and 200 mesh ProSciTech gold grids with a holey carbon film. Lattice fringes and selected area electron diffraction (SAED) measurements were performed and analysed using Digital Micrograph software.

3.13 Fourier Transform Infrared Spectroscopy (FTIR)

Infra-red spectroscopy exploits the interaction of infrared radiation with matter, whereupon absorption takes place, which then causes the chemical bonds in the material to vibrate. The functional groups present in the constituent molecules absorb infrared radiation at diagnostic frequencies. Thus, the structure of an unknown molecule can be determined by its infra-red spectrum.[166] Infra-red spectroscopy provides molecular structural information by determining the frequency of the vibrational modes of a compound.

3.13.1 FTIR Principle

When IR radiation interacts with a compound at the proper frequency, it results in the transfer of energy to the molecule.[166] When the frequency of the IR radiation matches the vibrational frequency of a functional group in a compound, absorption occurs. Absorbing of this energy causes the molecule to transition between two vibrational energy levels.

IR spectroscopy has three typical spectral regions based on wavelength. The infrared region is subdivided into the near infra- red, infrared and far- infrared spectrum.[167]

The IR spectrum records absorbed light which tells how energy was absorbed at each wavelength when the IR radiation passes through the sample. The fingerprint region is 1450 to 600 cm^{-1} and is unique to a given molecule. Absorption bands in the region 4000 to 1450 cm^{-1} are known as the group frequency region.[168] ENREF_123

3.13.2 FTIR instrumentation

An FTIR spectrophotometer has four main components, namely, a radiation source, analyser, detector and electronics for signal processing which can change according to the instrument type and application.[169]
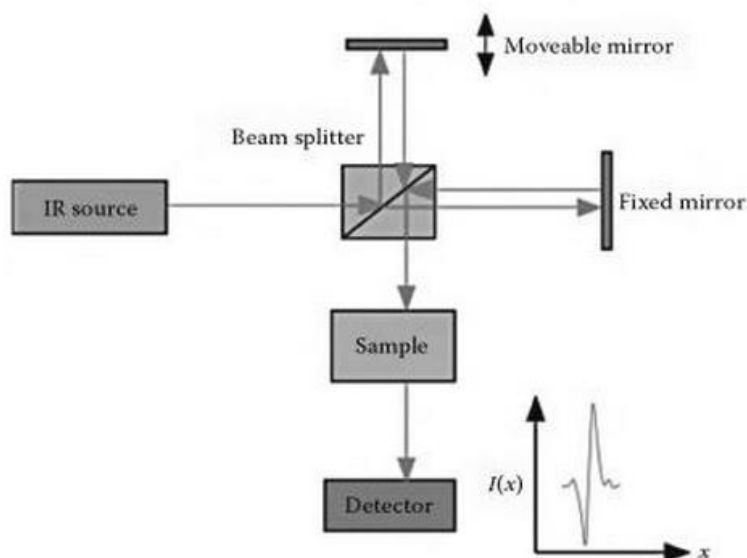
Figure 3.2. Diagram of an FTIR spectrophotometer. [168]

The IR radiation source consists of a Nernst glower or a Glowbar unit (silicon carbide rod). The interferometer combines the separate waves together. The monochromatic light, after being split into two beams, is then recombined to form a visible pattern of areas of constructive and destructive interference of bright and dark fingers. The signal is fed to a computer where the data are Fourier transformed and a spectrum having a transmission versus wavenumber is obtained. The IR spectrum records transmitted light which shows how energy was absorbed at each wavelength when the IR radiation passes through the sample. The fingerprint region is 1450 to 600 cm^{-1} and is unique to any given molecule. Absorption bands in the region 4000 to 1450 cm^{-1} are known as the group frequency region.[168]

Powdered samples are suspended in 1.000 ± 0.003 g of potassium bromide in approximately $0.1 – 0.3$ wt% concentration. The sample is prepared by grinding with the KBr powder using a mortar and a pestle. The mixture is then placed between a punch and die and compacted into a translucent film using a mechanical die press. Spectra were collected in the range 4000 – 400 cm^{-1} in the absorbance mode. The main IR characteristic peaks corresponding to metakaolin and geopolymeric matrices are summarised in Table 3.3.

Table 3.3. IR characteristic bands and corresponding species of metakaolin and geopolymeric matrices

Assignment	Wavenumber(cm^{-1})	Characteristic band
–OH	3700–3600	Stretching vibration (–OH)
–OH, HOH	3600-2200	Stretching vibration (–OH, HOH)
HOH	1700-1600	Bending vibration (HOH)
Si–O–Si & Al–O–Si	1200-950	Asymmetric stretching (Si–O–Si and Al–O–Si)
Si–O	1086	(symmetrical vibration)
Si(Al)–O	1008	(asymmetrical vibration)
Al–OH	914	(six-coordinated Al–OH stretching vibration)
Si–OH	840	(bending vibration)
Al–O	798	(six-coordinated Al–O stretching vibration)
Si–O	694	(symmetrically stretching vibration)
Si–O–Al	540	(bending vibration)
Si–O	469	(in-plane bending vibration)

Note: The assignments of the IR characteristic bands are based on references.[123, 170, 171]

3.14 Nuclear Magnetic Resonance Spectroscopy (MAS NMR)

Solid state nuclear magnetic resonance spectroscopy (NMR) is a relatively new method for exploring solid materials. As comparison between XRD and NMR analysis, NMR provides structural information that is not available from x-ray diffractometry especially for amorphous materials, for specific NMR-active elements.[172]

NMR is a radio frequency spectroscopy and exploits the nuclear spin of specific nuclei to determine factors such as their bonding to surrounding atoms and coordination state. When nuclei with a nuclear spin are located in a strong magnetic field, the energy levels of the different spin states separate. In the strong magnetic field, the nuclear spin has an associated magnetic moment and therefore the nucleus spins around an axis of the magnetic field at a specific frequency (the Larmor frequency). The sample is then irradiated with a pulse of plane polarised rf radiation at the Larmor frequency, causing a tipping of the spin system with respect to the magnetic field axis. At the end of the pulse, the spin system returns to its original axis with a characteristic time constant and the emission of a decaying pulse. Since the nucleus of an atom is shielded from the applied magnetic field by its surrounding electrons, this changes the emitted frequency slightly by an amount called the chemical shift.
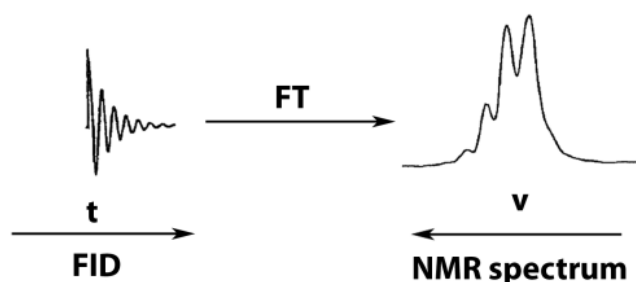
Figure 3.3. Fourier transformation of free induction decay (FID) in the time domain to an NMR spectrum in the frequency domain.[173]

This emitted frequency is detected by a coil surrounding the sample as a decaying voltage and is called free induction decay (FID) which is transformed from the time domain to the frequency domain using Fourier transformation.[173]

Solid state NMR spectra are broadened due to a number of interactions including dipole moments and, in quadrupolar nuclides, quadrupole moments.[124] Some of these broadening effects can be cancelled out by spinning the sample at high speeds (up to 20000 revolutions s^{-1}) The sample is spun at the specific angle of 54.7 ° to the magnetic field axis (called the "magic angle") to reduce the broadening of the NMR peaks and give a sharp spectrum. This technique is known as magic angle spinning (MAS) and produces sharp peaks in the spectra of solids. However, not all elements possess nuclei suitable for NMR spectroscopy. The NMR- active nuclei in the present system are ^{27}Al and ^{29}Si in various environments[124].

3.14.1 Solid-state NMR sample preparation

NMR spectra are acquired using similar powder samples as are used for x-ray diffraction. It is most important that the powders are finely ground and oven dried. High spinning speeds and residual water cause the sample to solidify in the rotor. The powder is gently tamped into the rotor in layers and the rotor cap fitted.

Solid-state ^{27}Al and ^{29}Si MAS NMR spectroscopy were used to study the chemical environment of these elements in the system before and after their use as photocatalysts. The NMR spectra were acquired using similar powdered samples as are used for XRD. The spectra were acquired at a magnetic field of 11.7 T using a Bruker Avance III 500 spectrometer operating at a ^{27}Al frequency of 130.24 MHz and a ^{29}Si frequency of 99.29 MHz. The ^{27}Al solid-state spectra were acquired using a 4 mm Doty MAS probe with a

silicon nitride rotor spun at 10-12 kHz, a 1 μs pulse and a 1 s recycle time, the spectra referenced with respect to $Al(H_2O)_6^{3+}$. The ^{29}Si spectra were acquired with a 5 mm Doty MAS probe and a zirconia rotor spun at ~6 kHz. The excitation pulse for ^{29}Si was 7 μs with a recycle time of 30 s and the spectra were referenced with respect to tetramethyl silane (TMS).

3.15 Nuclear quadrupole resonance (NQR)
3.15.1 Principle of NQR

Unlike NMR, in which the nuclei have spins of ≥ 1 with energy levels split by an external magnetic field, NQR is used to study nuclei with spins ≤ 1 such as ^{63}Cu, which have an electric quadrupole moment so that their energies are split by the electric field gradient associated with the immediate environment of the nucleus. As in the case of NMR, the nuclear spin states are perturbed by the application of a radio frequency pulse of appropriate energy to excite the particular nucleus under investigation, but unlike NMR, the NQR experiment is conducted in the absence of an external magnetic field.

The state of the copper (Cu) in the present samples before and after their use as photocatalysts was studied by ^{63}Cu NQR spectroscopy. ^{63}Cu (and ^{65}Cu) quadrupole frequencies (v_Q) were obtained at ambient temperature through the use of a Chemagnetics CMX console pulsing into a probe arrangement that was well-removed from the magnet (>5 m) and shielded from extraneous magnetic and radio frequency interference by a mumetal container. The quadrupole frequency range scanned was determined from previous $^{63,65}Cu$ NQR and NMR studies of two, three and four coordinate Cu (I) systems.[174-177] The location of both ^{63}Cu and ^{65}Cu isotope resonances (related by the ratio $v_{Q(63Cu)}/v_{Q(65Cu)}) = 1.081$) verified that true copper NQR frequencies were being observed. A scan of ~±500 kHz around the central Cu_2O frequency was undertaken for each sample by stepping the spectrometer frequency in 100 kHz increments through this range and retuning the probe at each frequency. A Hahn echo (θ-τ-2θ-τ-acquire) sequence with extended phase cycling was employed to obtain undistorted echoes,[178] where the recycle delay was 0.5 s and hard θ/2θ pulses of 2/4 μs duration, respectively, were implemented.

3.16 UV-Visible spectroscopy

Ultraviolet-visible (UV-vis) spectroscopy was used to acquire the absorbance spectra of compounds in solution. UV-visible adsorption of the solutions were acquired using an Agilent 8453 spectrophotometer operated in single beam mode using 1 cm quartz cuvettes

(frosted opposite faces) of 1 cm thickness (path length) and the spectra were recorded between 200 and 800 nm. This technique measures the absorbance of light energy or electromagnetic radiation, which excites electrons from the ground state to the first singlet excited state of the compound. The UV-vis region of energy for the electromagnetic spectrum covers the range 1.5 - 6.2 eV, which relates to a wavelength range of 200-800 nm.

The Beer-Lambert equation is the principle behind absorbance spectroscopy:

$$A = \varepsilon bc \qquad\qquad (27)$$

For a single wavelength, A is the absorbance, ε is the molar absorptivity of the compound or molecule in solution ($M^{-1}cm^{-1}$), b is the path length of the cuvette or sample holder (usually 1 cm), and c is the concentration of the solution (M).[179]
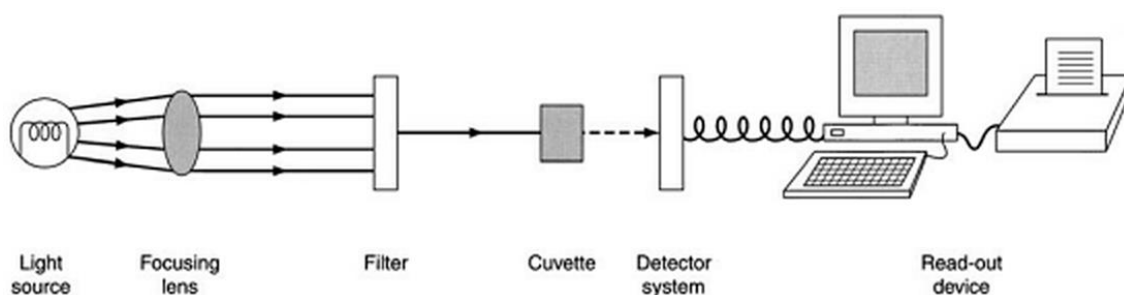
Figure 3.4. Illustration of a single beam UV-visible instrument.[180]

3.16.1 Photodegradation measurements

The photoactivity of the composites was evaluated by measuring the bleaching of a model organic compound (MB dye) under dark and UV illumination by UV-visible spectroscopy. MB (MB) was preferred for these experiments since its colour is stable at the high pH of the geopolymer matrix.

The interaction of the composites with the MB was carried out by the batch method in which 100 mg of the powdered sample was mixed with 100 ml of 0.1 mM aqueous MB solution in a round bottom flask and magnetically stirred throughout the experiment. The experiments were carried out both in the dark and under UV illumination using a 150 W xenon lamp as the light source.

Photodegradation experiments are normally carried out by allowing the photocatalyst sample in contact with the solution to be degraded (in this case MB dye) under dark conditions, then exposing the system to UV irradiation and monitoring the removal of the dye colour by spectrophotometry. This approach proved not to be possible with the present samples based on an unmodified geopolymer matrix, since equilibrium under dark conditions was never reached because the pH of the system never stabilized, but the geopolymer continued to remove the dye by adsorption. For this reason, two sets of experiments were carried out in attempt to separate the two processes occurring with these samples, namely adsorption of the dye and its photodecomposition. In one set of experiments the adsorption of the dye by photocomposites of the unmodified geopolymer with the oxide nanoparticles was measured in the dark and the adsorption characteristic (kinetics and adsorption isotherms) were determined from these data. In a second set of experiments, new samples were exposed to fresh MB dye and immediately irradiated with UV radiation; the decolouration of the dye in this case was due to a combination of adsorption by the geopolymer composite and the photodegradation process. The situation was found to be different in the composites based on the modified geopolymer matrices, in which a stable pH was achieved under dark conditions, allowing the system to come to equilibrium, and photodegradation measurements to be made in the usual manner. In these experiments, the photocatalys/MB system was equilibrated overnight in the dark, and then exposed to UV irradiation.

After varying reaction periods, 5 mL aliquots of the sample were taken, the suspension centrifuged off and the concentration of the dye remaining in the solution determined by measuring the height of the absorbance maximum at 664 nm in the UV-visible spectrum using a spectrometer between 200 and 800 nm. The amount of dye uptake (q) and the removal efficiency (η) of the dye were then calculated by eq. 28 and 29:

$$q = \frac{C_0 - C_t}{m} \times V \tag{28}$$

$$\eta = \frac{\left(C_0 - C_t\right)}{C_0} \times 100 \tag{29}$$

V is the volume of dye solution (mL), and m is the mass (g) of the adsorbent, C_0 and C_t are the concentration of the dye solution at the initial time and after time t of absorption respectively.

3.16.2 Dye adsorption kinetics under dark conditions

The kinetics of dye adsorption on the geopolymer composites measured under dark conditions were analysed using two kinetic models previously proposed, namely, pseudo-first-order (eq. 30) and pseudo-second-order models (eq. 31)[181]

$$q = q_e \left(1 - \exp\left(-k_1 t\right)\right) \qquad (30)$$

$$q = \frac{\left(k_2 q_e^2 t\right)}{\left(1 + k_2 q_e t\right)} \qquad (31)$$

Where q is the amount of dye adsorbed (mg/g) at time t (min), q_e is the amount of dye adsorbed at equilibrium (mg g^{-1}), k_1 is the equilibrium rate constant for pseudo-first-order kinetics (min^{-1}) and k_2 is the equilibrium rate constant for pseudo-second-order kinetics (g. mg^{-1} min^{-1}). The adsorption data were fitted to these two equations by a nonlinear method with successive interactions calculated by the Levenberg-Marquardt algorithm[182] using OriginPro 2015 software.

3.16.3 Dye adsorption isotherms under dark conditions

The relationship between the amount of solute adsorbed and the concentration of the solution in the liquid phase at a given constant temperature can be described by an adsorption isotherm. The present experimental data for dye adsorption on the geopolymer composites were fitted to three equations commonly used to describe adsorption isotherms, namely, the Langmuir isotherm, which assumes that the adsorption process occurs at specific homogeneous sites within the adsorbent,[178] the Freundlich isotherm which is an empirical equation used to describe heterogeneous systems, and the Langmuir-Freundlich isotherm which provides a more flexible analytical modelling framework by use of a three-parameter equation that can give a better fit to the data.

The Langmuir isotherm takes the form:

$$q = \frac{\left(Q_s kC\right)}{1 + kC} \qquad (32)$$

where q is the adsorbed amount of the dye (mg/g), C is the equilibrium concentration of the dye in solution (mg/L), Q_s is the adsorption capacity (mg/g) and k is a constant related to the free energy of adsorption (L/mg).

The Freundlich isotherm can be written:

$$q = kC^n \tag{33}$$

where k and n are constants specifying the extent of the adsorption and the degree of nonlinearity between the solution concentration and q the adsorption.

The Langmuir-Freundlich equation takes the form:

$$q = \frac{\left(Q_s kC^n\right)}{\left(1 + kC^n\right)} \tag{34}$$

3.17 Brunauer-Emmett-Teller (BET) Surface Area Analysis

Nitrogen adsorption/desorption isotherms were recorded for powdered samples using a Micrometrics model ASAP2010 analyzer at 77 K. The samples were degassed at ~ 100 °C overnight prior to the measurement. The surface area was obtained by the Brunauer–Emmett–Teller (BET) method, and pore size distribution was calculated from the adsorption branch of the isotherm by the Barret–Joyner–Halenda (BJH) model.

Chapter 4

Synthesis and characterization of new photoactive inorganic polymer composites with Cu$_2$O nanoparticles

Introduction

This chapter describes the synthesis of geopolymer composites produced by incorporating Cu$_2$O nanoparticles and the characterization of these novel composites. It should be noted the use of ecologically-friendly geopolymers in conjunction with nanocrystalline Cu$_2$O for photo-degradation of harmful organic substances has not previously been reported. The synthesis method was outlined in chapter 3, section 3.4 and the morphology of the product composites was assessed using SEM and TEM. The crystallinity and structure of the samples was evaluated using XRD and FTIR. MAS NMR and NQR spectroscopy confirm the formation of well-reacted geopolymer composites containing Cu$_2$O nanoparticles. The specific surface areas were determined by the adsorption and desorption of nitrogen gas on the composites, and their important photocatalytic properties and degradation processes of MB dye were determined using UV- visible absorption spectra.

4.1 Results and Discussion

4.1.1 XRD Analysis

XRD was used to confirm the crystallinity of the Cu$_2$O and the structure of the geopolymer matrix and Cu$_2$O/geopolymer composites. A selection of typical powder XRD patterns of the geopolymer matrix and composites with different Cu$_2$O loadings are shown in Figure 4.1. Geopolymers are usually described as x-ray amorphous, with an XRD pattern consisting of a largely featureless hump at about 20-35º 2θ (Figure 4.1, (black line). Impurities in the clay starting material are responsible for the sharp peaks at 26.75° 2θ (quartz) and 21.96º 2θ (cristobalite). The as-synthesized cubic Cu$_2$O (Figure 4.1, yellow line) and the geopolymer-Cu$_2$O composites 10-30 wt% (Figure 4.1. red, blue, and green line) contain all the expected peaks from cubic bcc Cu$_2$O (PDF no. 01-073-6237), (Table 3.1) confirming the successful synthesis of Cu$_2$O, with no peaks from CuO, Cu or other impurities.

The intensities of the Cu$_2$O reflections increase with the addition of 30 wt% and with the 10 wt% addition of Cu$_2$O showing the lowest Cu$_2$O intensity. As expected, the intensities of the

geopolymer quartz reflections decrease with increasing oxide content of the composite (Figure 4.1).
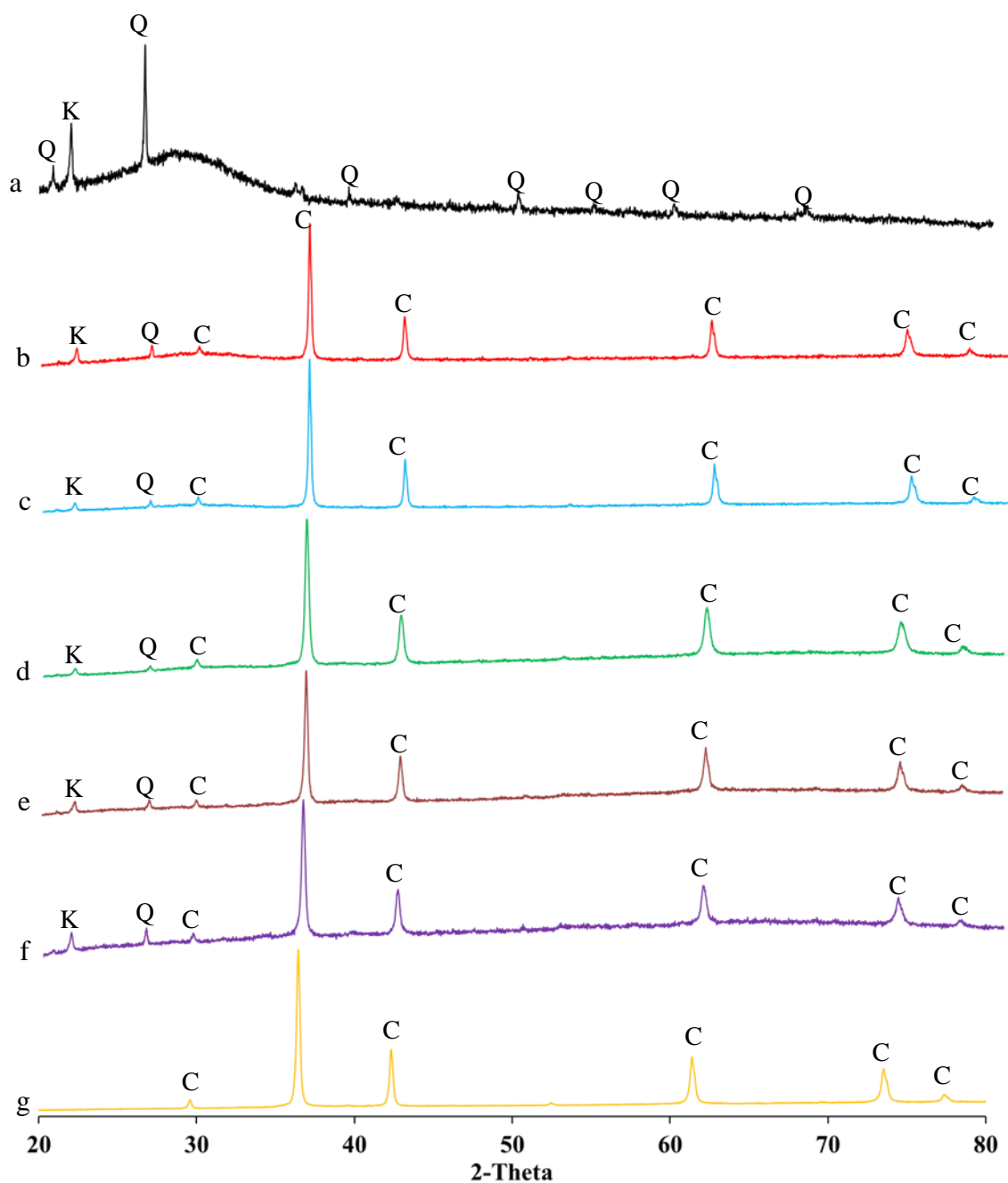
Figure 4.1. Normalized XRD patterns of GP and Cu_2O and Cu_2O supported by GP with different loading contents; (a) GP, (b) GP-10 wt% Cu_2O, ((c) GP-20 wt% Cu_2O, (d) GP-30 wt% Cu_2O, (e) GP-30 wt% Cu_2O-under UV with MB, (f) GP-20 wt% Cu_2O-under UV with MB, (g) Cu_2O. Q = quartz, K = cristobalite, C = cuprous oxide.

4.2 Scanning electron microscopy

SEM micrographs (Figure 4.2) confirm the success of the Cu$_2$O synthesis methods of Luo *et al.*[64] and Shah *et al.*[158]. Cu$_2$O crystals with uniform octahedral shape are shown in Figure 4.2. a,b, the average particle size of 200-500 nm. The uniform spherical Cu$_2$O crystals are shown by SEM in Figure 4.2c and d with an average size of ~600 nm. Cu$_2$O crystals synthesized by the method of Bai *et al.*[157] are shown by SEM (Figure 4.3) to be nanocrystals of uniform cubic morphology with an edge length of 80-150 nm. This unique morphology is a result of ripening and surface reconstruction processes in the Cu^{2+} solution capped with PVP. The addition of OH$^-$ forms a blue insoluble Cu(OH)$_2$ precipitate which changes through light yellow to orange with increasing particle size. [183] The nanometer size of the cubic crystals confirms the decision to use these in the subsequent experiments.
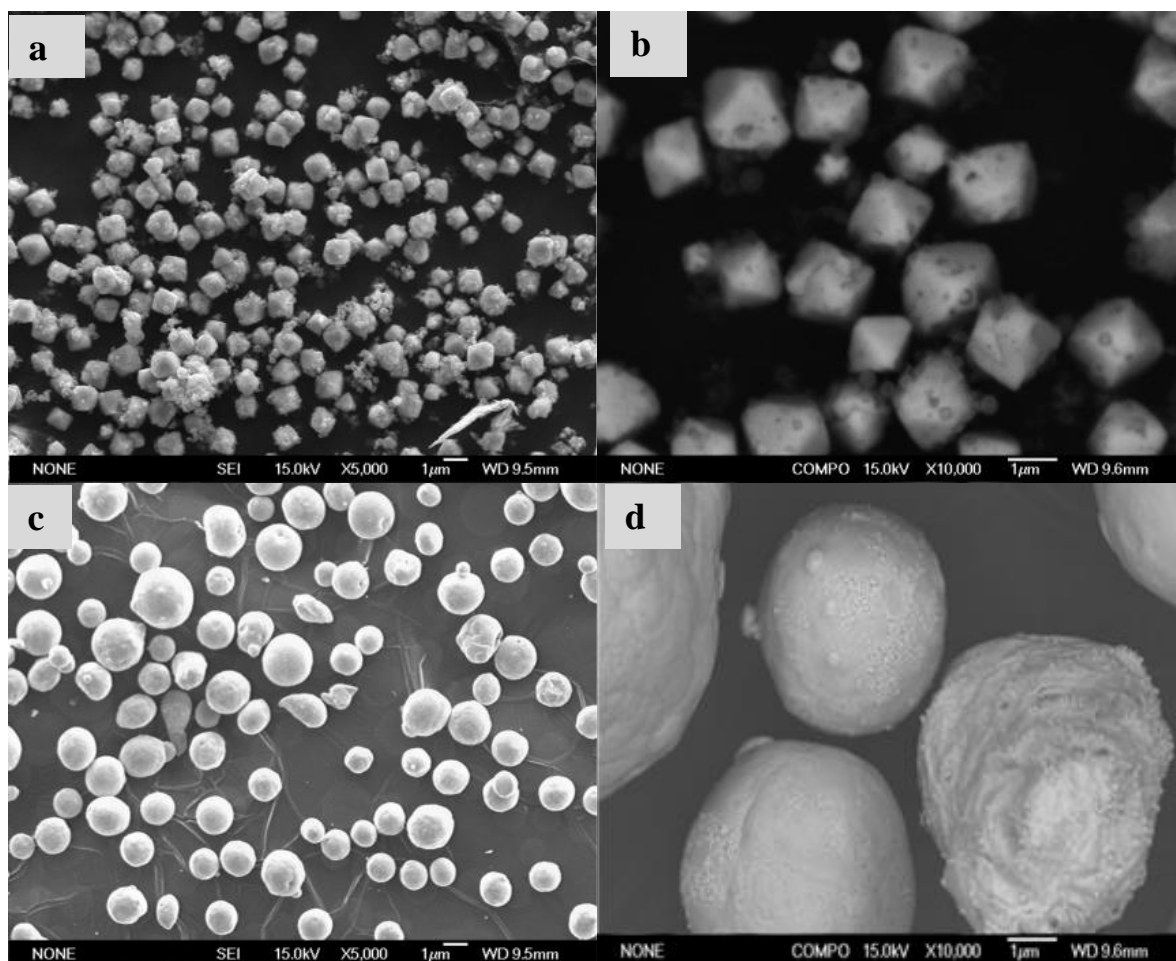
Figure 4.2. SEM micrographs of Cu$_2$O octahedral (a, b) and spherical (c, d) synthesized *via* a typical procedure described in the experimental section 3.2.2 and 3.2.3.
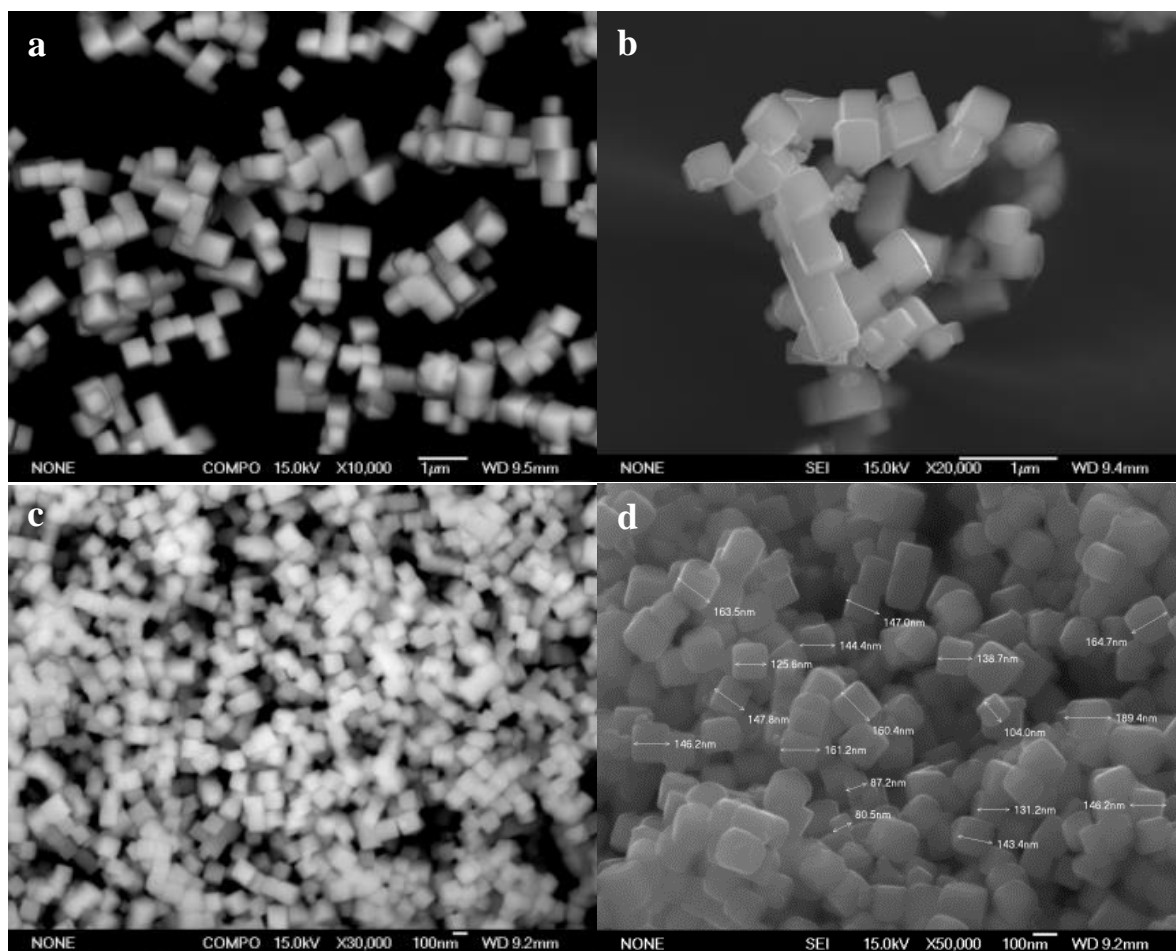
Figure 4.3. (a-d) SEM micrographs of Cu_2O nanocubes at different magnifications synthesized *via* a typical procedure described in the experimental section 3.2.1.

Figure 4.4 (a-c) shows high resolution TEM micrographs of the Cu_2O nanocubes synthesized by the method of Bai *et al.*[159] The HRTEM image of Cu_2O area (Figure 4.4e) confirmed its crystalline structure (region I) in which lattice planes could be detected with a d-spacing of 0.21 nm corresponding to the (200) plane of the cubic Cu_2O phase. Figure 4.4(g,i) shows the corresponding Fast Fourier Transformation (FFT) patterns of regions I,II in Figure 4.4e. These FFT patterns verified that region I consisted of crystalline Cu_2O. Selected Area Diffraction patterns (SAED) (Figure 4.4d) show principally three rings which are attributed to the (111), (200) and (110) of the cubic Cu_2O. These lattice spacing are in agreement with the (cubic) structure of Cu_2O (JCPDS file 01-073-6237). This HRTEM analysis provides a reliable confirmation of the XRD analysis.(Figure 4.5)
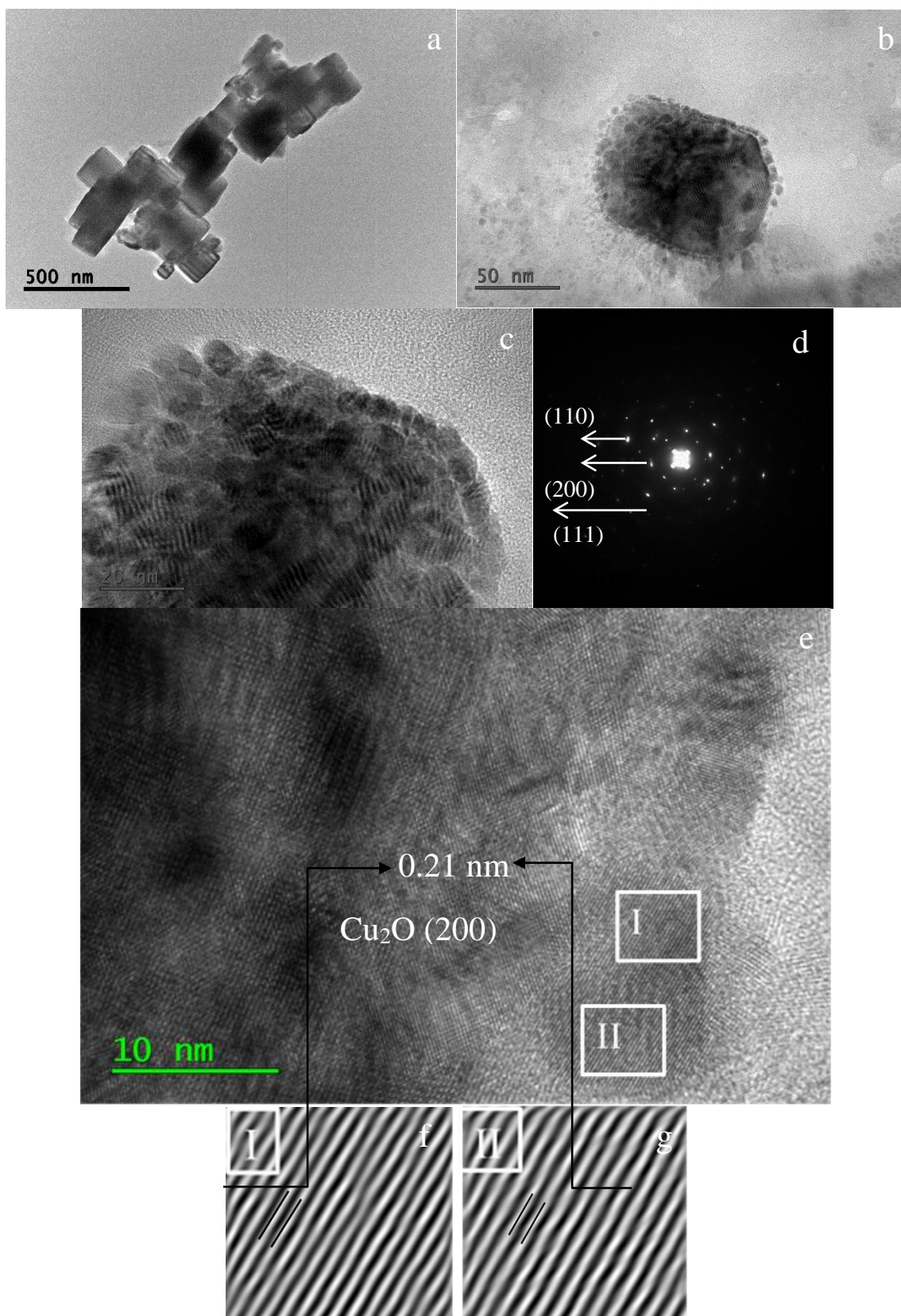
Figure 4.4. (a-c) TEM micrographs of the Cu_2O nanocubes, (d) SAED pattern, (e) HRTEM image of Cu_2O, (f, g) corresponding Fast Fourier Transformation (FFT) patterns of region I and II in panel e.
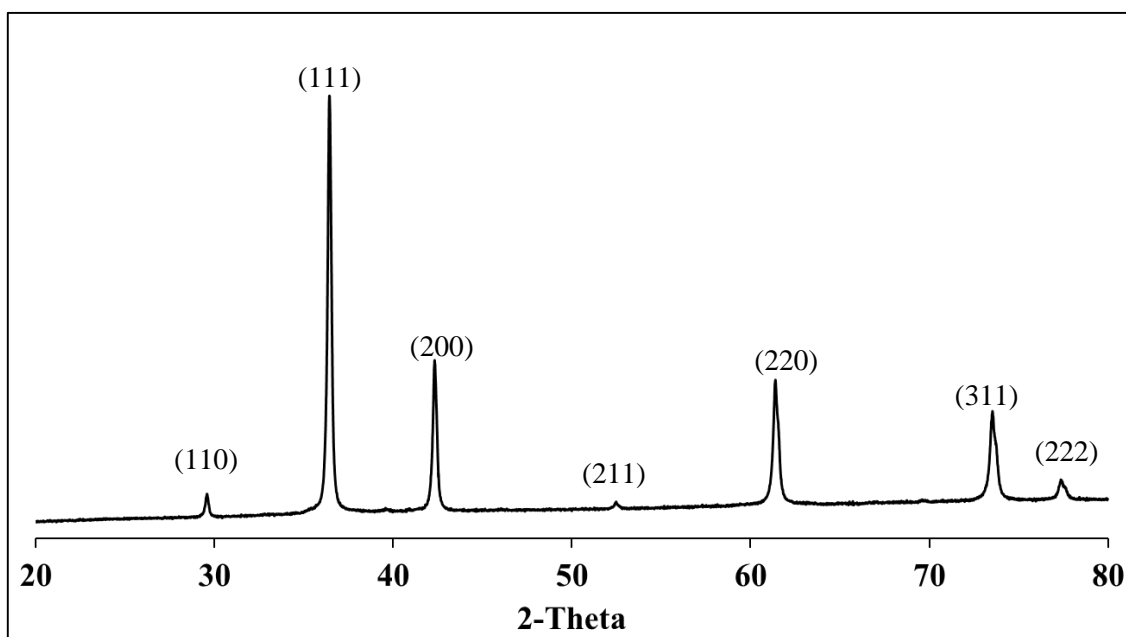
Figure 4.5. XRD pattern of as-prepared Cu_2O nanocubes synthesised by the method of Bai *et al.*[159]

The morphology of the as-synthesized Na-geopolymer without Cu_2O (Figure 4.6a) shows a homogenous microstructure of particles with a few voids, which suggests a high degree of gel reorganization during the geopolymerization processes.

The SEM images of the Na-geopolymer composites with a Cu_2O loading of 10, 20 and 30 wt% (Figure 4.6 (b-d) respectively) reveal well-dispersed Cu_2O nanocubes throughout the geopolymer matrix. SEM micrographs of the 10 wt% of Cu_2O/geopolymer composite (Figure 4.6) confirm the entry of ~100 nm Cu_2O nanocubes into the pore structure of the geopolymer matrix even at 10 wt% Cu_2O concentration.
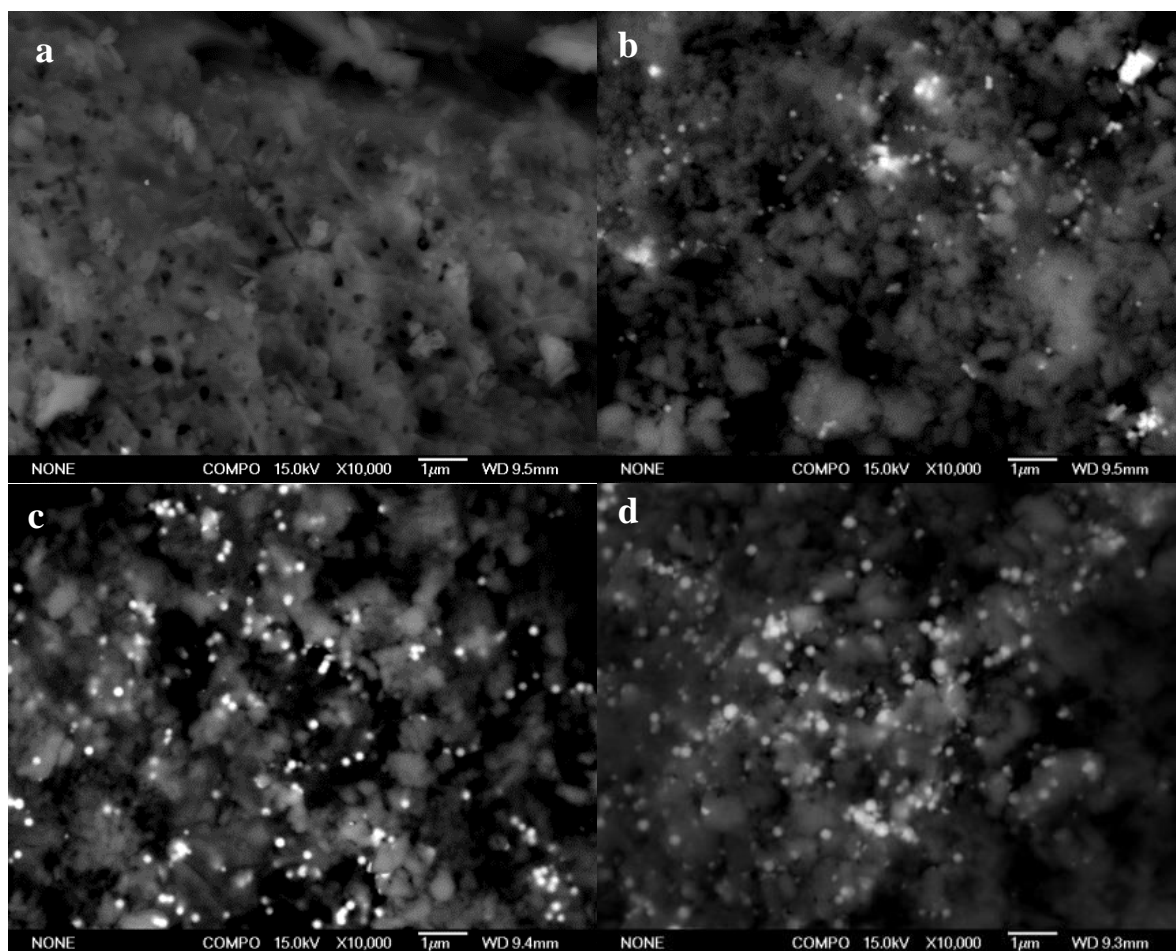
Figure 4.6. SEM micrographs of (a) GP matrix, (b) GP-10 wt% Cu$_2$O, (c) GP-20 wt% Cu$_2$O, (d) GP-30 wt% Cu$_2$O.

EDS analysis of the surface of the geopolymer-Cu$_2$O composites reveals the presence of Si, Al, Na, and Cu atoms (Figure 4.8), with no change in the surface morphology after incorporation of Cu$_2$O but an increase in the height of the Cu peak with increased loadings. The Cu$_2$O particles of 90-150 nm average size appear to cover most of the geopolymer surfaces, especially at the highest loading of 30 wt%. This homogenous distribution of Cu$_2$O particles on the composite surface should facilitate the photocatalytic activity. The average atomic number of Cu$_2$O and the geopolymer composite is approximately 22 and 8 respectively. As shows in the BSE map, the Cu$_2$O will appear as bright spots on the darker geopolymer matrix.
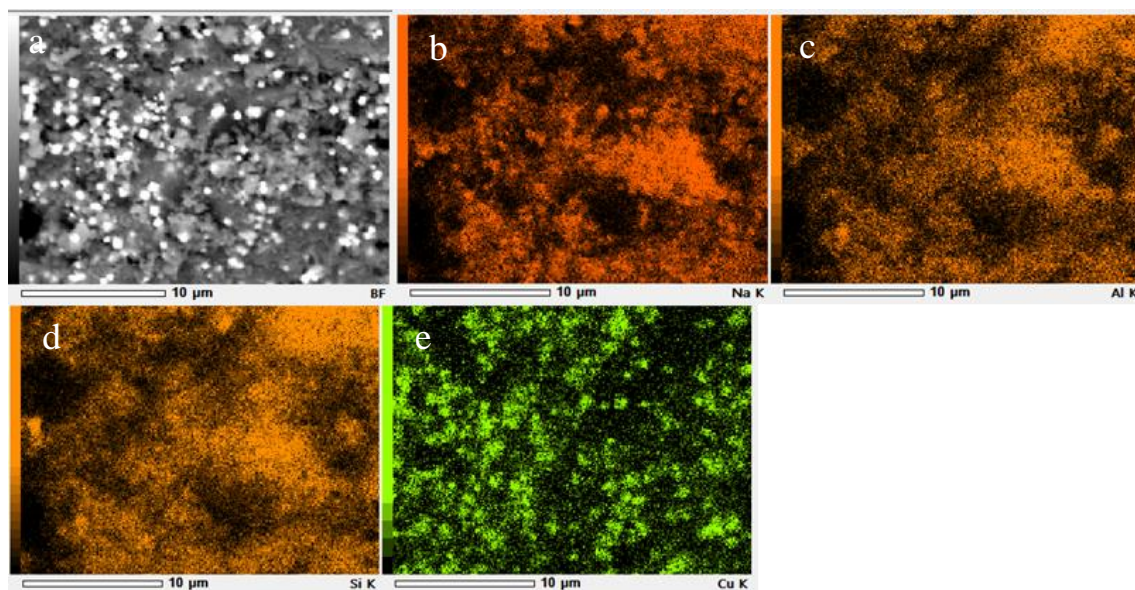
Figure 4.7. (a) Backscattered SEM image of ground GP- 30 wt% Cu_2O with corresponding, (b) Na, (c) Al, (d) Si, (e) Cu elemental map.

Figure 4.8 shows the EDS spectra and the percentage of Cu particles spread over the geopolymer matrix. It is clear that increasing the percentage of Cu_2O loading into the matrix, the height of the Cu peak increases as expected.
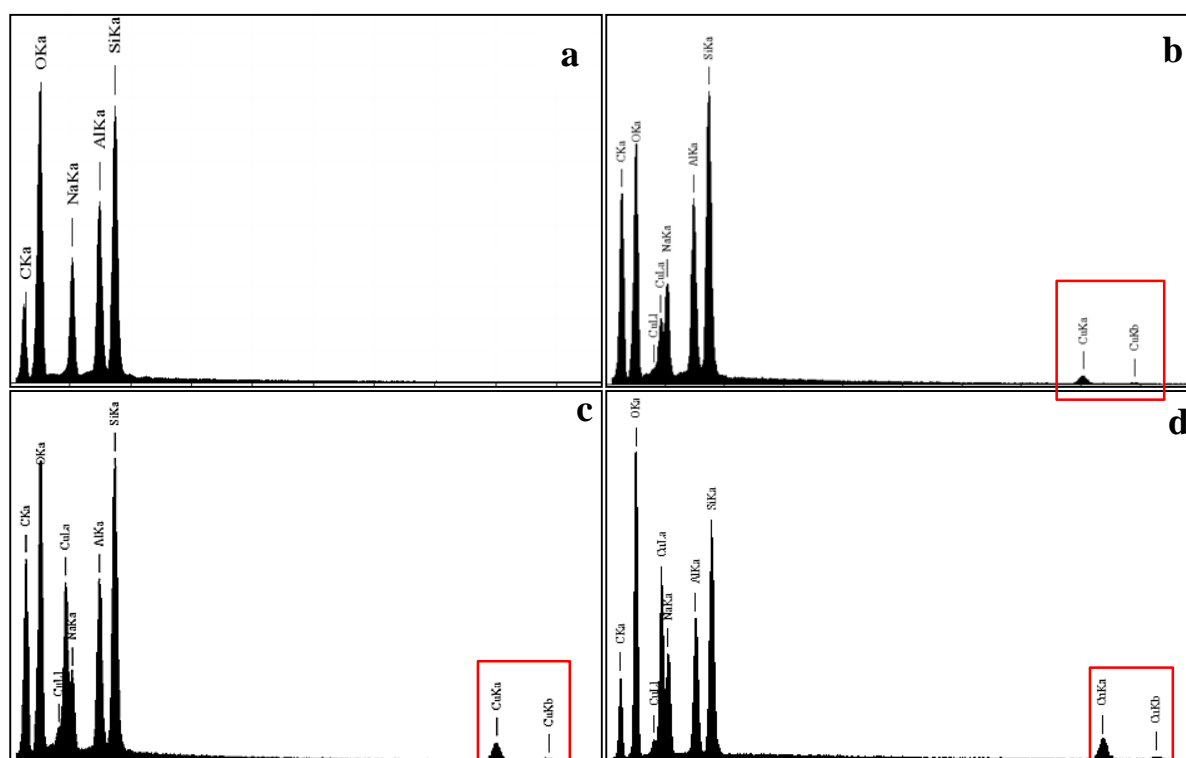
Figure 4.8. EDS data of (a) GP, (b) GP- 10 wt% Cu_2O (c) GP- 20 wt% Cu_2O (d) GP- 30 wt% Cu_2O.

4.3 FTIR spectra of these samples

In order to investigate the structure of the as-prepared materials the FTIR spectra were acquired in the range 400-4000 cm^{-1}. Representative FTIR spectra of these samples are shown in Figure 4.9. The positions of the main IR bands and corresponding species are listed in Chapter 3, Table 3.3.
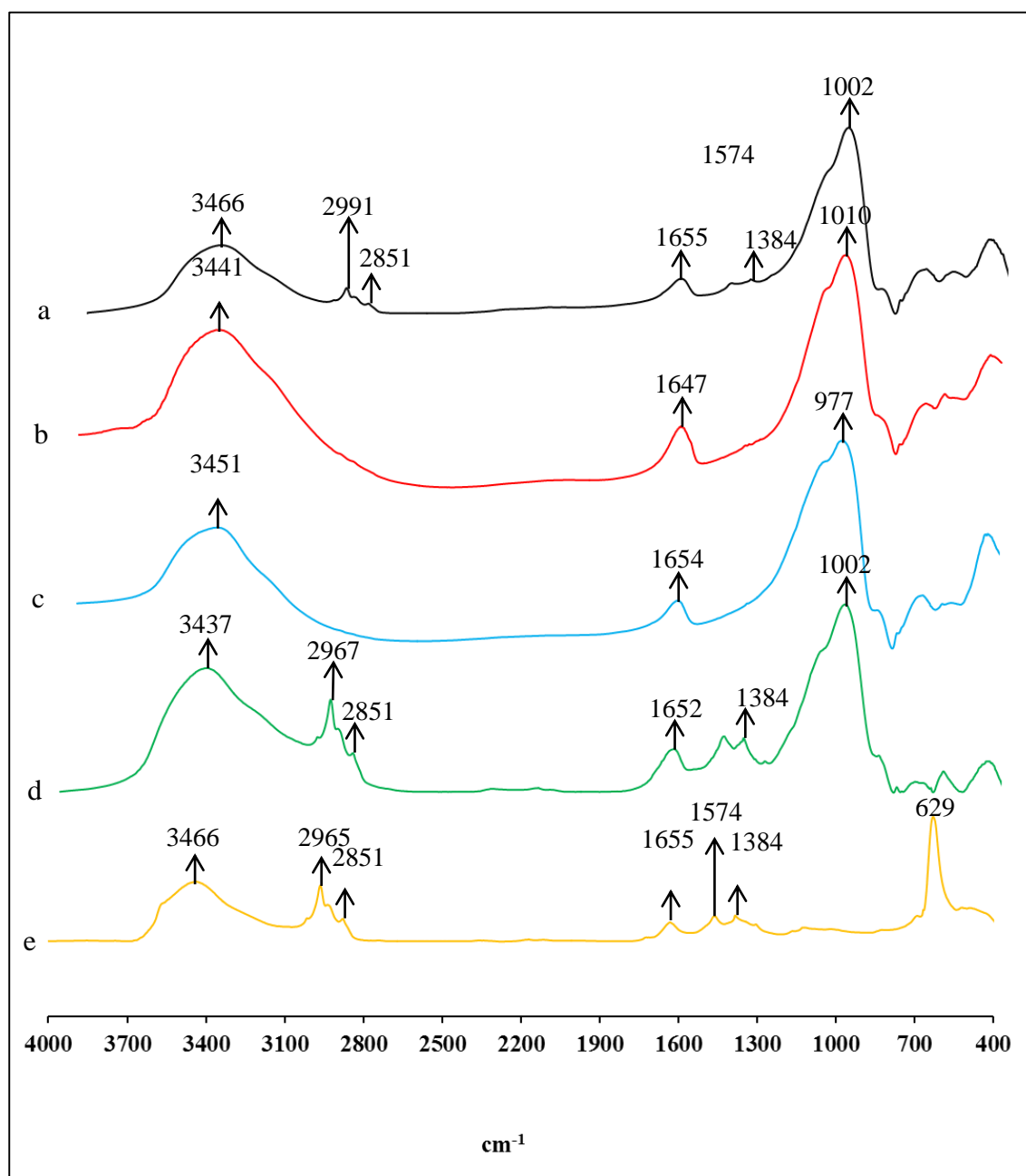
Figure 4.9. FTIR spectra of (a) GP, (b) GP- 10 wt% Cu_2O, (c) GP- 20 wt% Cu_2O, (d) GP- 30 wt% Cu_2O, (e) Cu_2O.

The peaks at about 1000 cm^{-1} are typical of the geopolymer matrix, with the presence of both Al-O and Si-O asymmetric stretch[184] (Figure 4.9). This peak appeared at 1002 cm^{-1} in the reference geopolymer and with 10 wt% addition of Cu_2O it was shifted to 1010 and 977 cm^{-1} for 20 and 30 wt% addition of Cu_2O respectively, indicating that the presence of the oxide particles does affect the structure. Three fundamental vibration modes indicate the presence of water molecules; the spectral regions are the OH stretching region, H-O-H bending region of H_2O, and the structural OH-bending region of the structural OH groups.[185] The absorption bands related to the H-O-H bending vibration of water appears at 1645 cm^{-1}, and are all very similar, resulting from the slight differences in water content in these geopolymer preparations.

The FTIR spectra also display a band at 3440 cm^{-1} in the geopolymer matrix due to the symmetric O-H stretching vibration of H-bonded water.[185] This wave number shifted to 3441, 3451, and 3437 cm^{-1} for different percentages Cu_2O addition from 10 to 3 wt% which corresponds to the hydroxyl group involved in water-water hydrogen band.[186] The absorption band at 629 cm^{-1} appearing in pure Cu_2O is assigned to the phase bending vibration of surface OH group. The OH_2 stretching band at 2967 cm^{-1} is assigned to asymmetric stretching of OH_2 groups and this peak disappears in the samples with 10 and 20 wt% additions of Cu_2O and was shifted to 2965 cm^{-1} in the 30 wt% Cu_2O sample.

4.4 ^{63}Cu NQR Spectroscopy

^{63}Cu NQR spectra of the Cu_2O and Cu_2O/geopolymer composites (Figure 4.10) show the expected single line in the reported position for the pure oxide[187] (Figure 4.10a) which is unchanged by its incorporation in the geopolymer matrix (Figure 4.10c), indicating that the Cu_2O has not been incorporated into the geopolymer matrix.
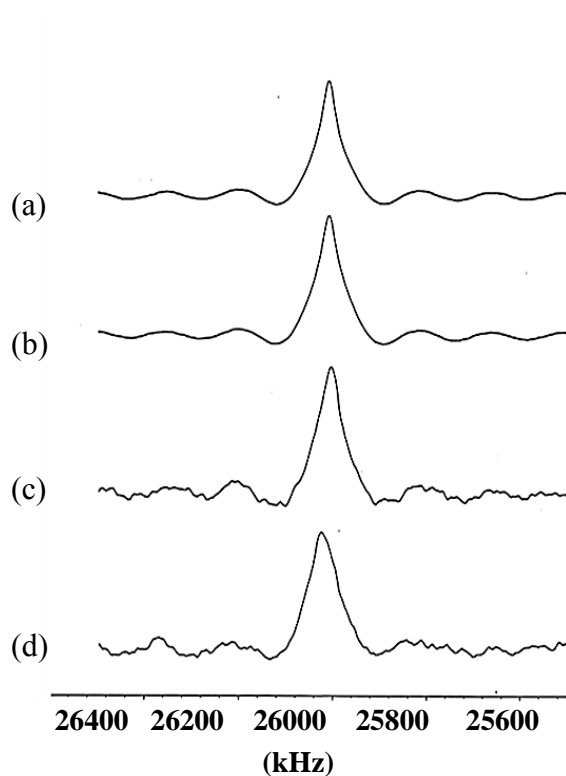
Figure 4.10. ^{63}Cu NQR spectra of nanoparticle Cu_2O and Cu_2O/GP composites. (a) as-synthesized Cu_2O, (b) Cu_2O after UV irradiation, (c) Cu_2O/GP composite before UV irradiation, (d) Cu_2O/GP composite after UV irradiation.

4.5 ^{29}Si and ^{27}Al solid state MAS NMR

Representative ^{27}Si MAS NMR spectra of the geopolymer and geopolymer composites (Figure 4.11.) show that these are all well-formed geopolymers with a broad principal resonance at about -85 to -87 ppm, corresponding to a framework structure significantly saturated in Al, but broadened by the presence of several slightly different Si-O-Al environments.[121]
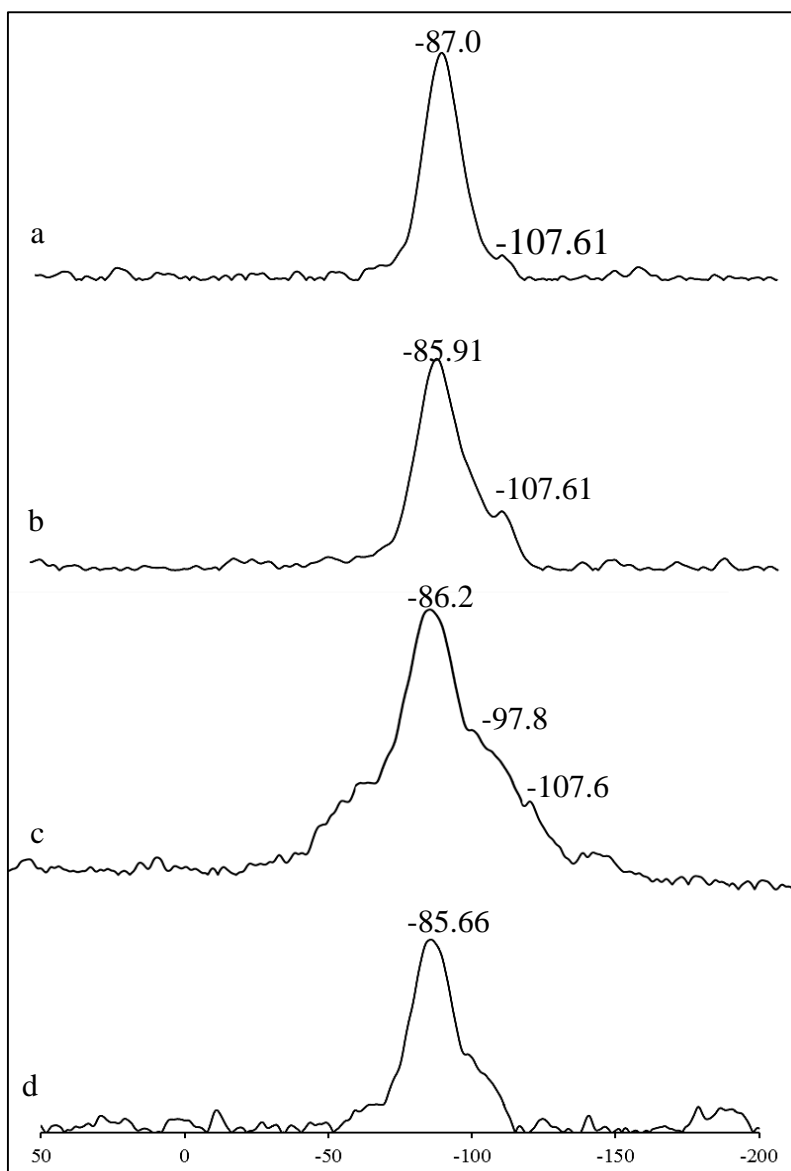
Figure 4.11. 11.7 T ^{29}Si MAS NMR spectra. (a) GP, (b) GP-10 wt% Cu_2O, (c) GP-20 wt% Cu_2O, (d) GP-30 wt% Cu_2O

A feature at about -100 to -107 ppm which broadens into a shoulder in the composites with higher Cu_2O content (Figure 4.11) denotes the presence of a greater number of sites in which the silicon atoms are bonded through oxygen to other silicon.[188]

The corresponding ^{27}Al MAS NMR spectra (Figure 4.12) all contain a predominant sharp resonance at about 59 ppm corresponding to the tetrahedral Al-O units of a well-developed geopolymer structure.[121] The small broad feature in some of the samples arises from Al-O in octahedral coordination,[188] as a residual trace of unreacted metakaolin.[121]
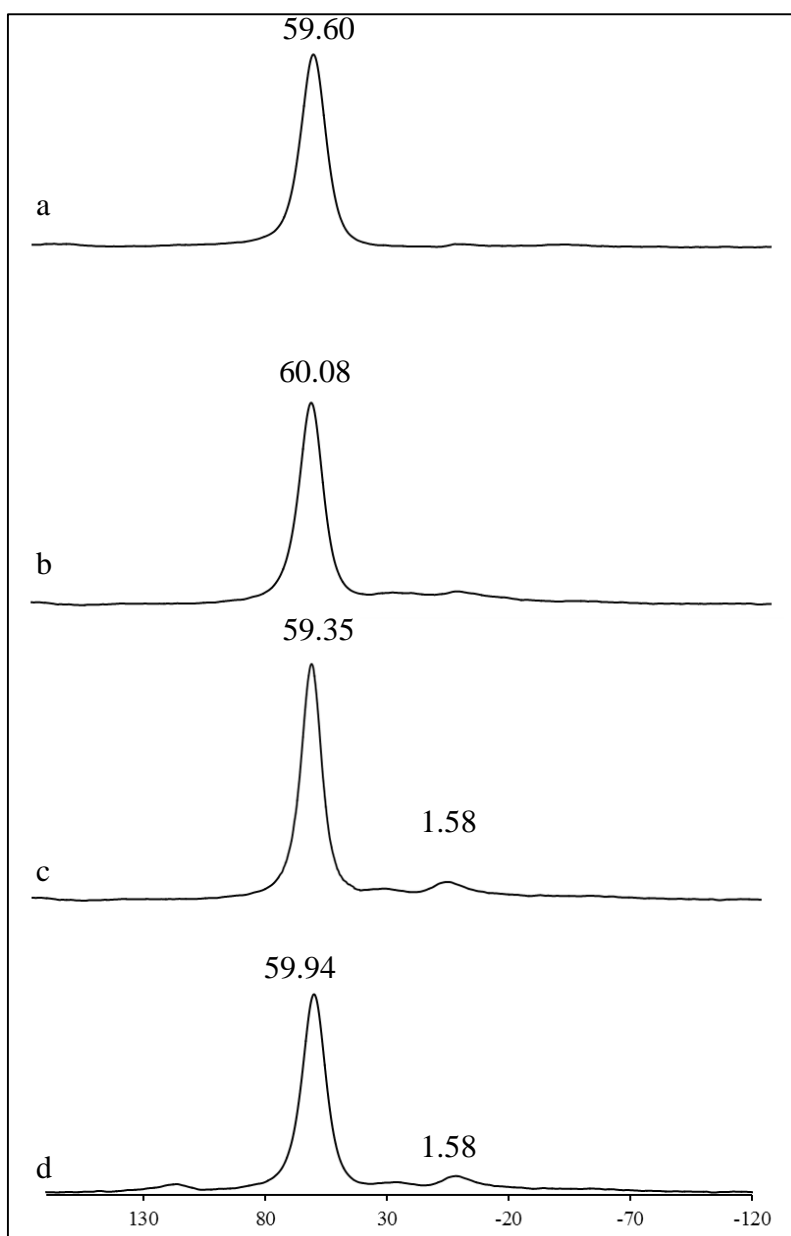
Figure 4.12. 11.7 T ^{27}Al MAS NMR spectra. (a) GP, (b) GP-10 wt% Cu_2O, (c) GP-20 wt% Cu_2O, (d) GP-30 wt% Cu_2O

To summarize, these results confirm the successful formation of aluminosilicate geopolymer composites containing homogeneously distributed nanosized cubic Cu_2O particles.

4.6 Dye Adsorption experiments

Reference geopolymers which do not contain Cu_2O can remove MB from aqueous solution by adsorption. This suggests a dual mechanism for the present geopolymer composites,

whereby the geopolymer matrix removes the dye by adsorption under dark conditions, whereas under UV illumination, photodegradation also occurs concomitantly with the adsorption process.[139] Thus, in the present experiments an initial attempt was made to distinguish the two processes by carrying out separate experiments under dark conditions and UV illumination. As noted in Chapter 3, section 3.16.1, it did not prove possible to bring the samples to equilibrium under dark conditions in order to measure the photodegradation step, so the experiments under UV illumination were carried out on fresh samples and dye solutions without equilibration in the dark, and therefore represent a combination of the two dye removal processes.

Adsorption of MB by the composites and geopolymers alone was investigated under dark conditions by the batch method. The results for the MB complex of geopolymer and Cu_2O-GEOPOLYMER at an initial MB concentration of 0.1 mM solution are plotted as a function of adsorption time in Figure 4.13. The absorption spectra show a maximum absorption band at approximately 664 nm. A shoulder at 620 nm which indicates a blue shift after 4 hour stirring in the dark is more obvious in the geopolymer containing 20 wt% Cu_2O. At this stage dye penetrates into the pores of the geopolymer composite and causes this spectral shift. Since the solution pH remains in the range of 9-11 during the sorption experiments, it appears that the positively charged surface hydroxyl groups on the edges of the geopolymer may repel the similarly charged MB cations, which can then enter the pores of the composite where there are no outer exchange sites.[189] The adsorption mechanism of a cationic dye such as MB is related to its point of zero charge (PZC) with respect to that of the adsorbent. No PZC values for geopolymers are available in the literature, but those of zeolites, with which geopolymers are closely related, are known to vary widely with the Al/Si ratio. At higher pH values corresponding to the alkaline geopolymers, electrostatic adsorption of cationic species is likely to occur on the silanol groups present, and these are probably the adsorption sites in the present composites.

The absorption spectrum shape remains unchanged for the first 2 hour but its intensity decreases as adsorption occurs. The percentage removal of dye is fast at the beginning but steadily diminishes with time. Rapid adsorption of the dye at the initial contact time may be due to the initial availability of the active surface of the adsorbents. In the later stages, the slower rate of adsorption is a result of less accessibility of the active sites of the adsorbent, accompanied by the slow diffusion of the dye molecules into the porous structure of the adsorbent. After 120 min. 83, 86, 77 and 96% of the dye is removed in the dark by the

geopolymer matrix, geopolymer-Cu_2O 10 wt%, geopolymer-Cu_2O 20 wt% and geopolymer-Cu_2O 30 wt%.
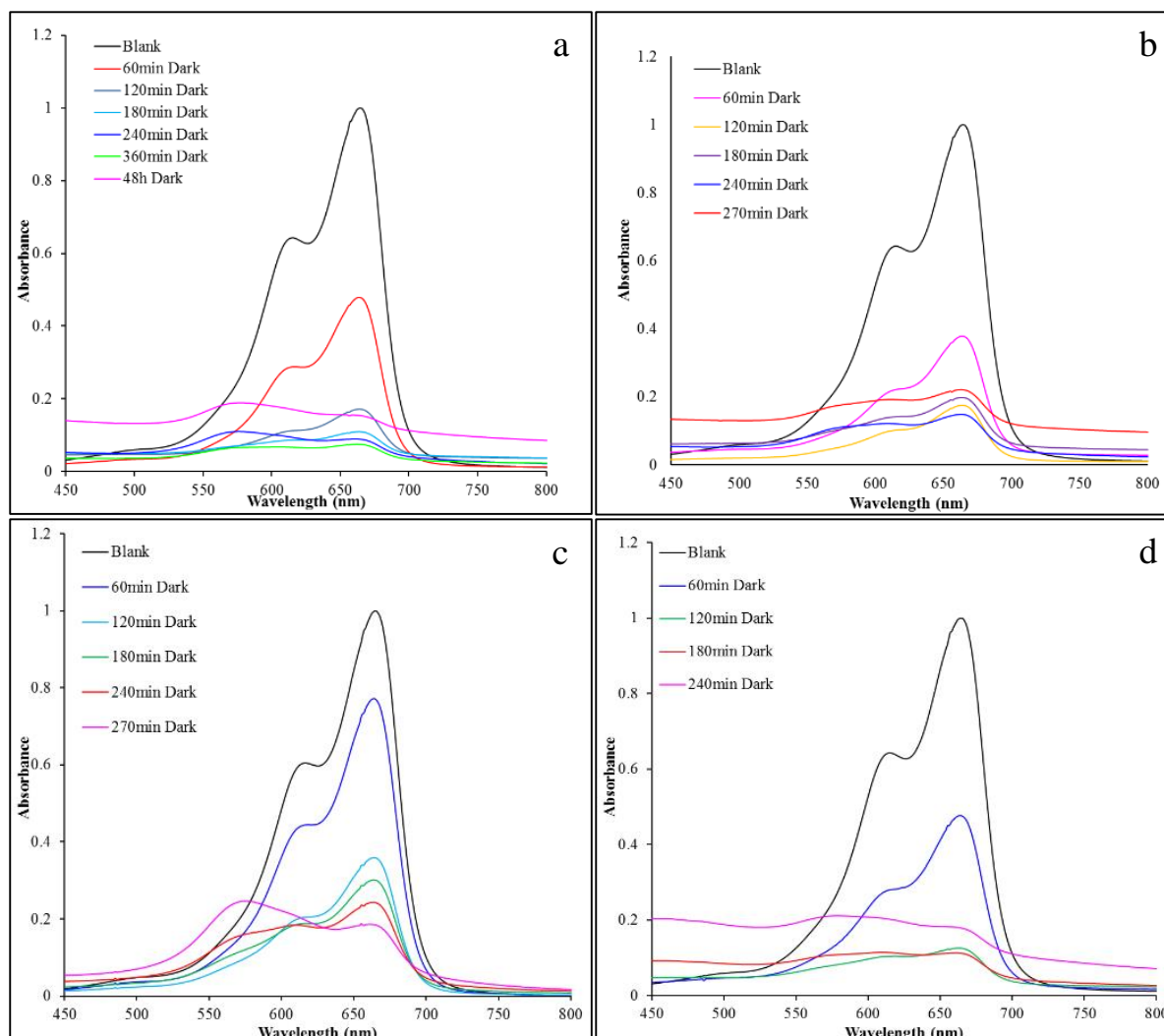
Figure 4.13. UV–vis absorption spectra of the MB solution during adsorption in the dark by (a) GP, (b) GP-10 wt% Cu_2O, (c) GP-20 wt% Cu_2O, (d) GP-30 wt% Cu_2O.

All adsorbents have a limited number of active sites which become saturated at a certain concentration of adsorbate. Dark adsorption experiments involving all the catalysts indicate that the effective surface area and adsorption capacity of the supported Cu_2O were much higher than that of the bare Cu_2O. Figure 4.14. shows the variation in the relative concentration (C/C_0) of MB dye solution with time for the geopolymer matrix, geopolymer-Cu_2O 10 wt%, geopolymer-Cu_2O 20 wt% and geopolymer-Cu_2O 30 wt%. This indicates that the composite containing 20 wt% Cu_2O shows the most rapid adsorption of MB; the decreased adsorption rate resulting from the inclusion of further Cu_2O may be due to blocking of the active adsorption sites by the additional oxide.
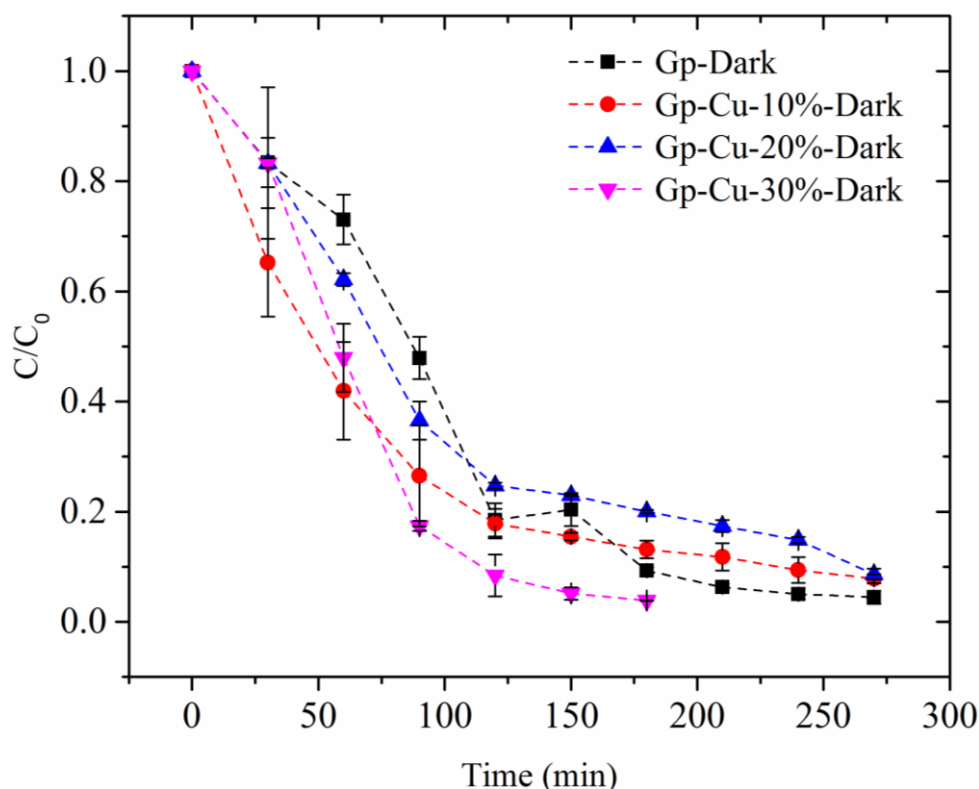
Figure 4.14. Plots of the residual concentration (C/C$_0$) *vs.* time (t) onto the GP matrix, GP-Cu$_2$O 10, 20, and 30 wt%. (monitored at 664 nm in the dark)

4.6.1 Dye adsorption kinetics under dark conditions

The adsorption data (Figure 4.15) were fitted to pseudo-first-order (eq. 27) and pseudo-second-order (eq. 28) kinetic equations by a nonlinear method with successive interactions calculated by the Levenberg-Marquardt algorithm[182] using OriginPro 2015 software. The resulting plots of the data fitted to these two equations are shown in Figure 4.15, with the resulting pseudo-first and pseudo-second order rate constants, the q$_e$ values, and the correlation coefficients R^2 shown in Table 4.1. Comparison of the q$_e$ values calculated from these equations with the experimental values q$_{exp}$ (Table 4.1) shows that in all samples the pseudo-first order model provides a better fit to the experimental data; this is also supported by the superior fit of the experimental and calculated curve shapes (Figure 4.15a). The first-order rate constants (Table 4.1) increase slightly with increasing Cu$_2$O content of the geopolymer/Cu$_2$O composites, reflecting the improved adsorption by the composites.
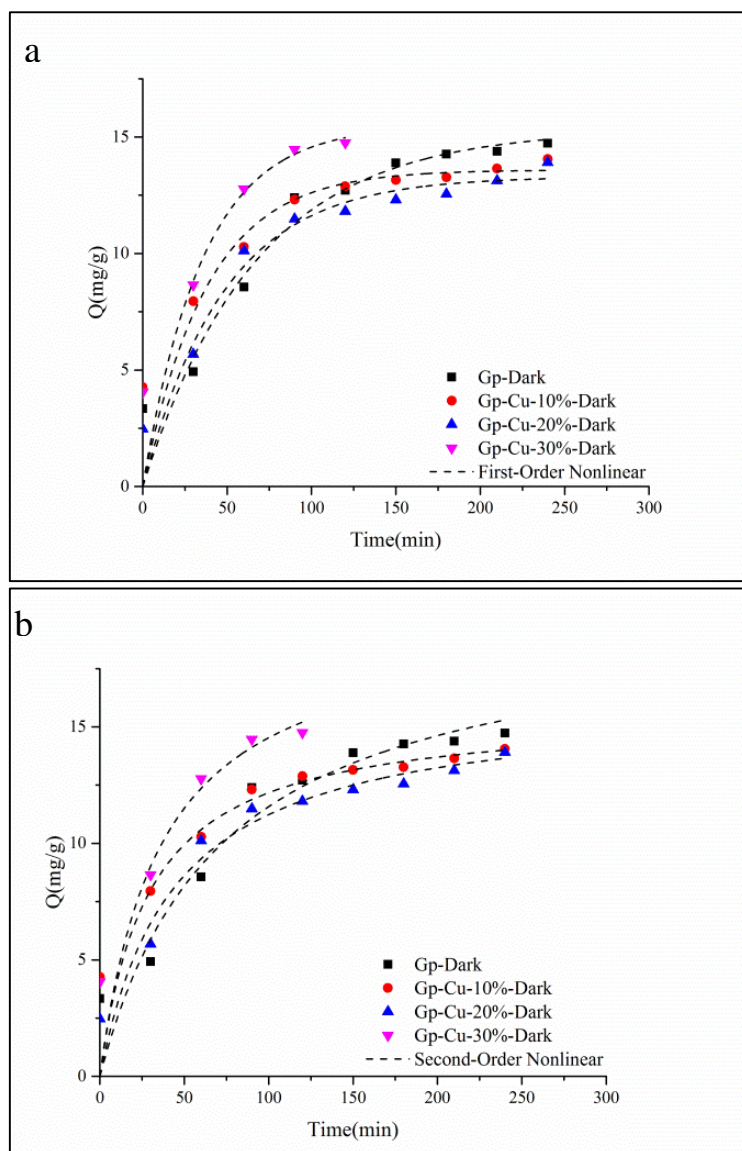
Figure 4.15. (a) Pseudo first-order kinetics, (b) Pseudo second-order kinetics by the nonlinear method and experimental kinetics for the adsorption of MB onto the GP matrix and GP composites.

Table 4.1. Parameters for kinetic models of MB adsorption on samples

Sample	Kinetic model	q_{exp} (mg/g)	q_{e} (mg/g)	k
GP	1st-order	14.74	15.33	0.015
"	2nd-order	"	19.85	7.05e^{-04}
GP/10%Cu$_2$O	1st-order	14.05	13.59	0.026
" "	2nd-order	"	15.69	0.002
GP/20%Cu$_2$O	1st-order	13.91	13.10	0.021
" "	2nd-order	"	16.14	0.001
GP/30%Cu$_2$O	1st-order	14.76	15.51	0.028
" "	2nd-order	"	17.73	0.001

4.6.2 Dye adsorption isotherms under dark conditions

The relationship between the amount of solute adsorbed and the concentration of the solution in the liquid phase at a given constant temperature can be described by an adsorption isotherm. As described in Section 3.16.3, three isotherm equations commonly used to describe adsorption isotherms are the Langmuir isotherm (eq. 31), which assumes that the adsorption process occurs at specific homogeneous sites within the adsorbent,[178] the Freundlich isotherm (eq. 32) which is an empirical equation used to describe heterogeneous systems, and the Langmuir-Freundlich isotherm (eq. 33) which provides a more flexible analytical modelling framework by use of a three-parameter equation that can give a better fit to the data.

Figure 4.16 (a-c) shows the experimental MB adsorption data for the geopolymer matrix, and all the geopolymer/Cu$_2$O composites fitted to the Langmuir and Langmuir-Freundlich equations. When the present dye adsorption data were fitted to these three isotherm equations, the goodness of fit, evidenced by the R^2 values, varies with the amount of Cu$_2$O in the composite (Table 4.2), those composites containing 20 and 30 wt % Cu$_2$O being well described by all three isotherms. The fit of these composite compositions to the Langmuir isotherm suggests that at these high Cu$_2$O contents, adsorption of the dye is occurring on

specific sites which are associated with the oxide itself. At lower concentrations of Cu_2O, the Freundlich isotherm does not fit the data as well as the empirical Langmuir and Langmuir-Freundlich isotherms, suggesting that adsorption in these composites is not occurring by a single identifiable mechanism. The plots of the data (Figure 4.16) indicate that the more empirical Langmuir-type isotherms are in general the most appropriate to describe the absorption of the dye on the geopolymer and geopolymer composites.

Table 4.2. Calculated isotherm parameters for MB adsorption on samples

Freundlich equation ($q=kC^n$)			
		n	R^2
GP-Dark		2.9	0.85
GP-Cu-10%-Dark		1.22	0.80
GP-Cu-20%-Dark		2.40	0.95
GP-Cu-30%-Dark		2.52	0.97
Langmuir-Freundlich Equation ($q=(Q_skC^n/(1+kC^n))$)			
	Qs(mg/g)	n	R^2
GP-Dark	0.94	3.68	0.97
GP-Cu-10%-Dark	0.97	2.29	0.98
GP-Cu-20%-Dark	1.08	2.94	0.96
GP-Cu-30%-Dark	1.02	1.42	0.99
Langmuir Equation ($q=(Q_skC/(1+kC))$)			
	Qs(mg/g)		R^2
GP-Dark	1.18		0.90
GP-Cu-10%-Dark	1.27		0.79
GP-Cu-20%-Dark	1.77		0.91
GP-Cu-30%-Dark	1.06		0.99
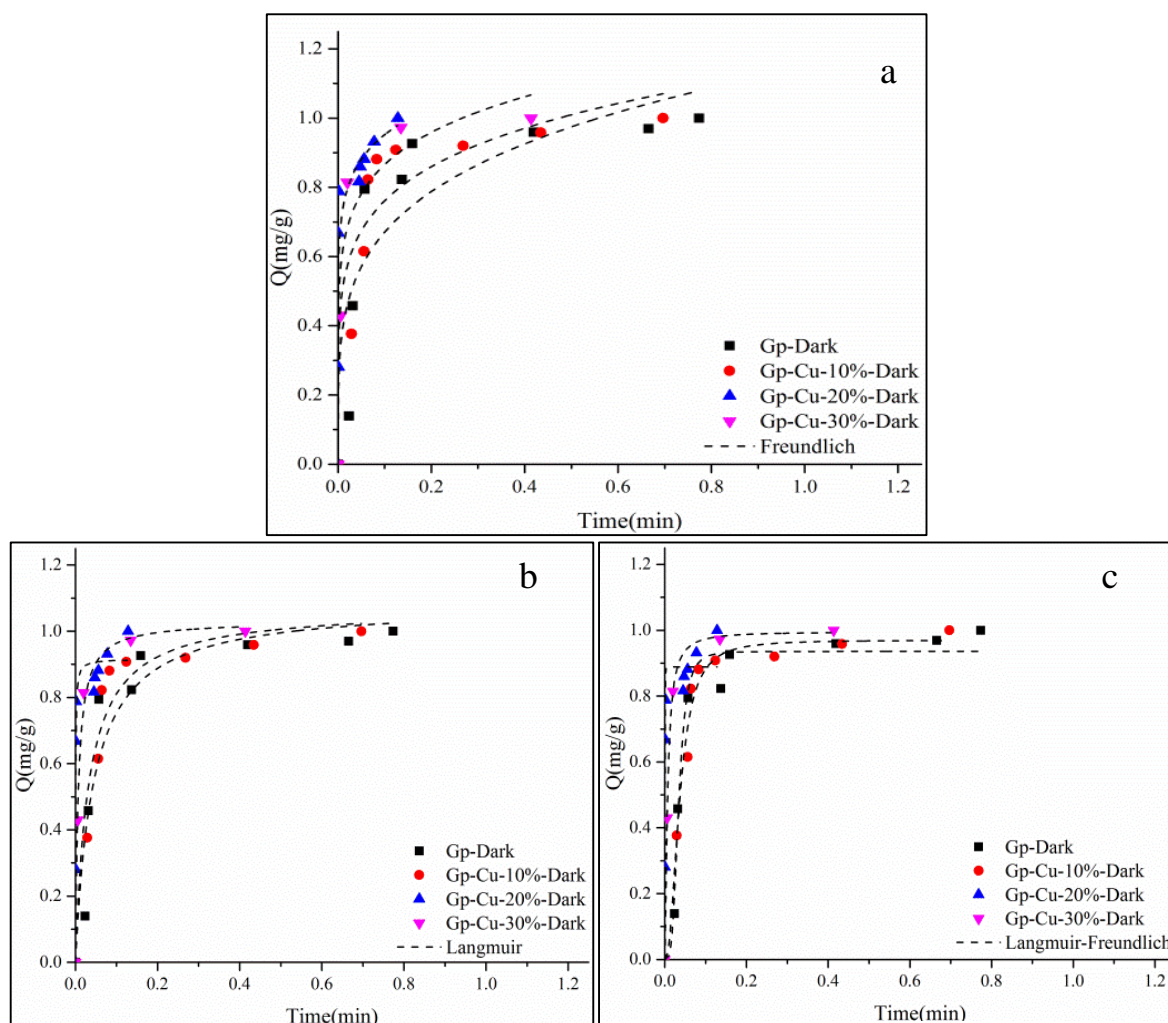
Figure 4.16. (a) adsorption isotherms for MB adsorption and the corresponding Langmuir, (b-c) adsorption isotherms for MB adsorption and the corresponding Freundlich and Langmuir-Freundlich models fits (dashed lines)

4.6.3 Reactions under UV irradiation

Figure 4.17 shows MB removal under UV irradiation by the geopolymer containing different amounts of added Cu_2O. Changes in the UV−vis spectra of the dye solutions at different reaction times are presented in Figure 4.17(a-d).
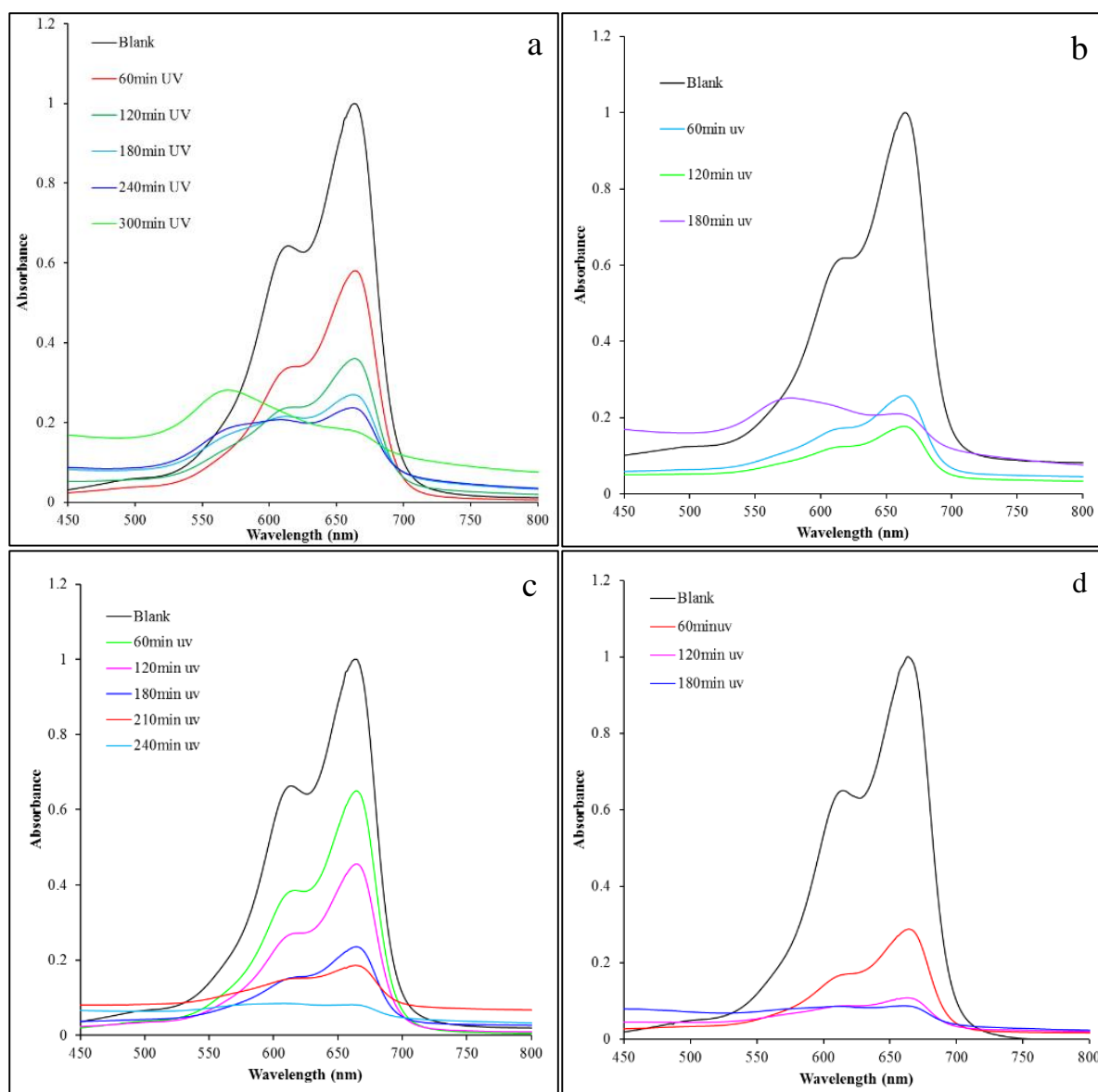
Figure 4.17. The UV–vis absorption spectra of the MB solution during the photocatalytic degradation in the presence of (a) GP, (b) GP-10 wt% Cu_2O, (c) GP-20 wt% Cu_2O, (d) GP-30 wt% Cu_2O under UV light irradiation.

As shown in Figure 4.17, when the dye solution in the presence of the photocatalyst materials was exposed to UV irradiation, it was degraded within 120 min. with a maximum degradation rate of 100% in the presence of the geopolymer containing 10% Cu_2O. The color of the MB dye changed from dark blue to colorless, confirming its photodestruction. The degree of degradation was 77%, 79% and 98% for the geopolymer matrix, and the geopolymer containing 20% and 30% Cu_2O respectively. In the reference geopolymer the UV peak was not completely removed but with increasing the reaction time it shifted to a lower wavelength.

The two processes operating in the decoloration of the MB dye under UV irradiation can be seen in Figure4.18. which illustrates the difference between the behavior of the geopolymer matrix and the composite containing 30 wt% Cu_2O in the dark and under UV illumination. The geopolymer matrix behaves essentially similarly in dark and UV conditions, showing the adsorption of the dye but no evidence of photoactive properties, as would be expected. By contrast, the Cu_2O-containing composite is more efficient in removing the dye, due to a combination of the adsorption and photodegradation processes.
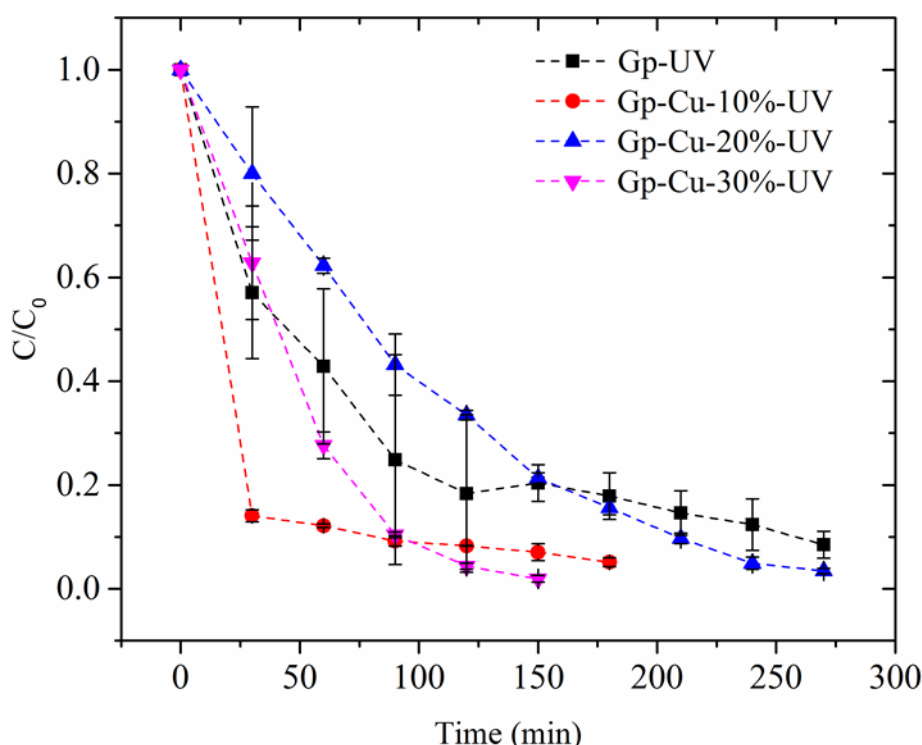
Figure 4.18. Plots of the residual concentration (C/C_0) *vs.* time (t) onto the GP, Cu_2O-GP-10, 20, 30 wt%. (monitored at 664 nm under UV)

After adsorption or photodegradation of the MB, the structures of the geopolymer matrix and the Cu_2O/geopolymer composites are essentially unchanged, according to their XRD patterns (Figure 4.1, purple line). The photoactive Cu_2O itself is unaffected by exposure to the MB, either in the dark or under UV irradiation, as evidenced by ^{63}Cu NQR spectroscopy (Figure 4.10 b,d). Thus, these composites should continue to remove organic substances from their immediate environment by a combination of adsorption and photodegradation without deterioration of their structure or of the photoactive component. Figure 4.19 shows the

combined adsorption and photodegradation processes of the MB dye under UV irradiation in the composite containing 30 wt% Cu_2O. The geopolymer matrix should behave essentially similarly in dark and UV conditions, adsorbing the dye but should show no evidence of photoactive degradation. By contrast, the Cu_2O-containing composite is more efficient in removing the dye due to the combination of adsorption and photodegradation processes.
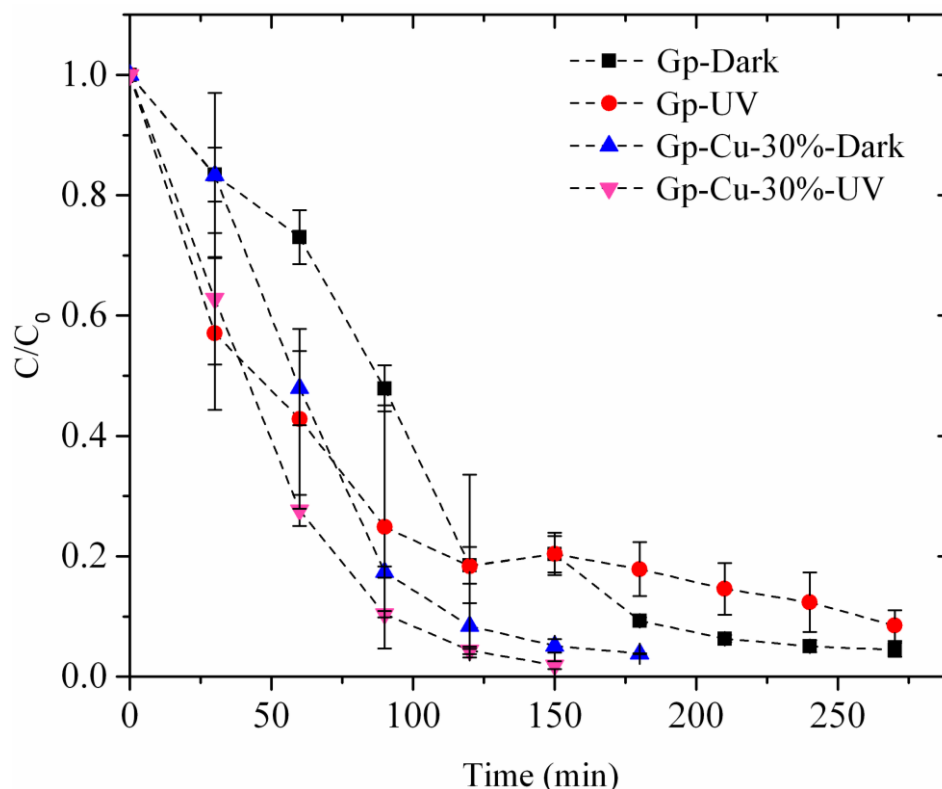
Figure 4.19. Residual concentration (C/C_0) of MB upon exposure to the GP matrix (GP) and the 30 wt% Cu_2O GP composite versus time in the dark and under UV illumination.

Figure 4.20 compares the removal of MB by the composites after 60 min. The geopolymer matrix and Cu_2O itself in the dark and under UV irradiation, showing the ability of the samples to eliminate MB from the aqueous solution under UV irradiation by a combination of adsorption and photodegradation.[150] It was found that only about 10% MB is removed in the dark by Cu_2O alone, indicating that Cu_2O by itself only weakly adsorbs MB, by comparison with the geopolymer matrix alone, which removes about 40% MB within 30 min. More than 54% of the MB was removed within 60 min. with the addition of 10% Cu_2O to the geopolymer, this number changing to 66% and 83% for composites containing 20% and 30 wt% Cu_2O respectively. This confirms the result that the MB is strongly adsorbed from its

aqueous solution by the geopolymer matrix, and is then degraded by the Cu_2O photoactive component in the composites.

Under both dark conditions and UV irradiation, the colour of the geopolymer matrix becomes progressively bluer due to adsorption of the MB. However, a similar observation was not recorded for the geopolymer composites, since their yellowish-brown color obscured any other changes in colour due to the presence of MB.
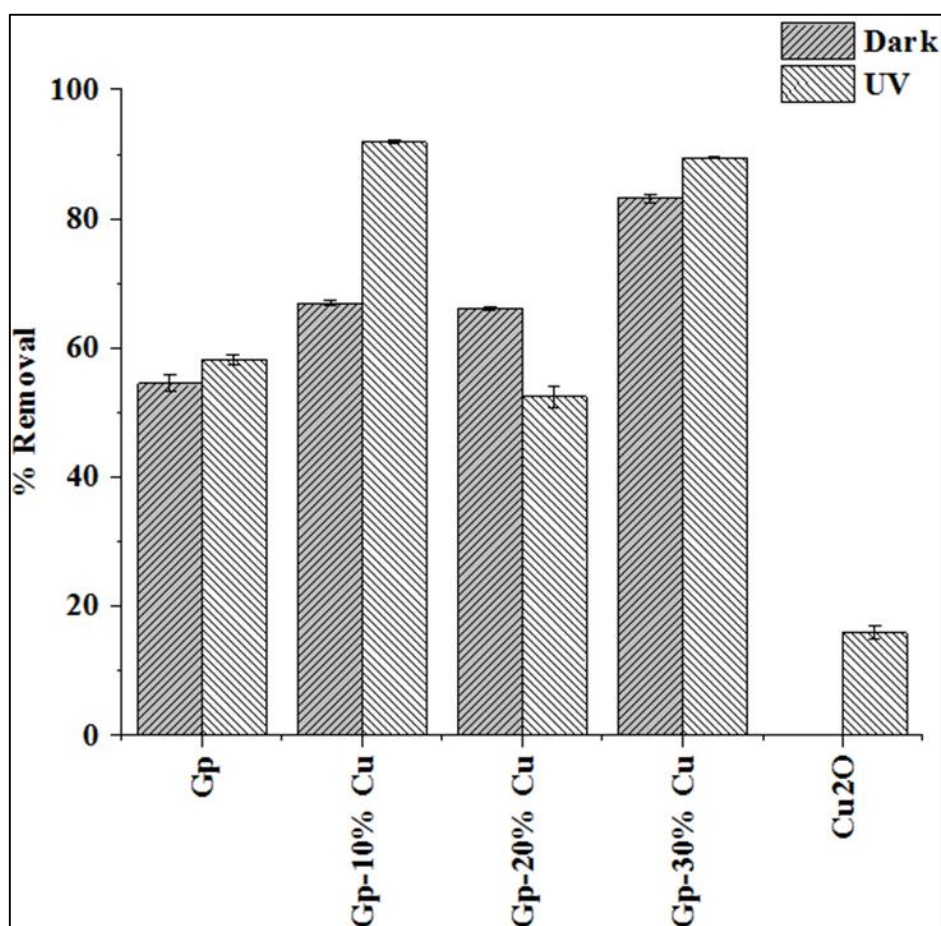
Figure 4.20. Comparison of MB removal in the dark and under UV irradiation by the GP matrix, GP-(10-30 wt%) Cu_2O composites and Cu_2O after 60 min. reaction.

Conclusions

This chapter describes the successful synthesis of cubic Cu_2O nanoparticles and their incorporation into aluminosilicate geopolymer matrices. The homogeneity of the oxide nanoparticle dispersion within the geopolymer matrix was demonstrated by SEM/EDS and TEM. Other experimental techniques (XRD, FTIR, ^{27}Al and ^{29}Si MAS NMR and ^{63}Cu NQR spectroscopy) confirmed the formation of a well-reacted geopolymer matrix with a structure that was unaffected by the insertion of the Cu_2O nanoparticles, or by the adsorption or

photodegradation of a model organic compound (MB, chosen for its color stability at high pH).

Experiments to determine the photodegradation of MB dye by these composites showed that the solid/dye interaction occurs by two processes, namely, adsorption by the matrix (in the dark) and photodegradation (under UV irradiation). Since the adsorption process in the dark did not come to equilibrium, conventional photodegradation experiments were not possible, but the dye adsorption step, monitored by experiments in the dark, were found to follow pseudo first-order kinetics. The adsorption data were fitted to adsorption isotherms which depended on the concentration of Cu_2O present; at higher concentrations (20-30 wt%) the data were described by Langmuir-type isotherms, whereas at lower concentrations, the empirical Langmuir-Freundlich isotherms were more appropriate. Although the nano-Cu_2O particles themselves do not adsorb the MB dye, their incorporation of up to 20 wt% into the geopolymer composites increases their adsorption ability, probably by increasing the porosity of the matrix. At concentrations >20 wt%, the oxide decreases the adsorption by blocking the active adsorption sites of the geopolymer. Under UV radiation, the composites remove the MB by a combination of adsorption and photodegradation, evidenced by a more rapid dye removal by comparison with the adsorption process alone. The combined adsorption/photodegradation process occurs without deterioration of the geopolymer structure or the photoactive Cu_2O component, confirming the original premise that these geopolymer composites should function as efficient new materials for the removal of organic pollutants from water or the atmosphere.

Chapter 5

Synthesis, characterization and photoactive properties of geopolymercomposites with Cu_2O/TiO_2 nano-heterostructures and P25 titania

Introduction

In the previous chapter, the feasibility of producing viable composites of geopolymers with Cu_2O was established and the structures and photoactivity of these products was determined. In this chapter, attention is turned towards improving the photocatalytic performance of the photoactive component by combining the Cu_2O with another well-known photoactive compound, TiO_2. The form of TiO_2 that has been found to perform most efficiently as a photocatalyst is a mixture of the anatase and rutile poymorphs, synthesized by an Aerosil process and known commercially as P25. This material consists of a mixture of 80% anatase and 20% rutile, present as a thin layer covering the anatase particles.[190] The enhanced photocatalytic effect has been suggested to arise from the enhanced space-charge potential resulting from the contact between the two phases; the resulting electron transfer from the anatase to lower-energy electron trapping sites in the rutile reduces the recombination rate in the anatase, improving the efficiency of the electron-hole separation and thus the catalytic activity.[190] A more recent study using electron paramagnetic resonance spectroscopy suggests that the presence of nanoclusters of rutile crystallites act as transition points for the rapid exchange of electrons to the anatase,[191] but a study in which the anatase and rutile components of P25 were separated and their individual photocatalytic behavior determined has cast doubt on the role of anatase-rutile interactions.[192] In the present work we prepared a series of composites of Cu_2O/TiO_2 nano-heterostructures incorporated into an aluminosilicate geopolymer host. The Cu_2O/TiO_2 heterostructures were synthesized as spherical nanocrystals combined with commercial P25 titania as described in chapter 3, Section 3.3. The Cu_2O particles in this part of the study result from the synthesis method used to prepare the TiO_2/Cu_2O nano-heterostructures, as described in Chapter 3. The structures of the resulting nanocomposites were characterized by XRD, FTIR, SEM/EDS and HRTEM and the photocatalytic properties of the composites for the destruction of MB were determined as in the previous chapter both in the dark and under UV radiation. For comparison, a corresponding series of samples containing P25 titania only were prepared and studied.

5 Results and Discussion

5.1 XRD Analysis

Figure 5.1 shows representative XRD patterns of the starting Cu_2O/TiO_2 and geopolymer composites with different Cu_2O/TiO_2 contents. The geopolymer matrix is typically x-ray amorphous, with superimposed sharp peaks at 26.75° 2θ (quartz) and 21.96° 2θ (cristobalite) arise from as-prepared impurities in the clay starting materials. Figure 5.1 (Purple line) shows that the as-synthesised Cu_2O contains no other peaks related to Cu or CuO. The diffraction peaks for P25 TiO_2 correspond to anatase and rutile. The Cu_2O/TiO_2 heterostructure (Figure 5.1, yellow line) shows the presence of both Cu_2O and TiO_2 with no other impurities. Geopolymer-Cu_2O/TiO_2 composites 10-30 wt% (Figure 5.1. (Red, blue, and green line) contain all the expected peaks from cubic bcc Cu_2O (PDF no. 01-073-6237) and the anatase and rutile phases of P25 TiO_2 confirming the synthesis of Cu_2O/TiO_2. The intensities of the geopolymer quartz reflections decrease with increasing oxide content of the composite but the Cu_2O and TiO_2 intensities remain constant.
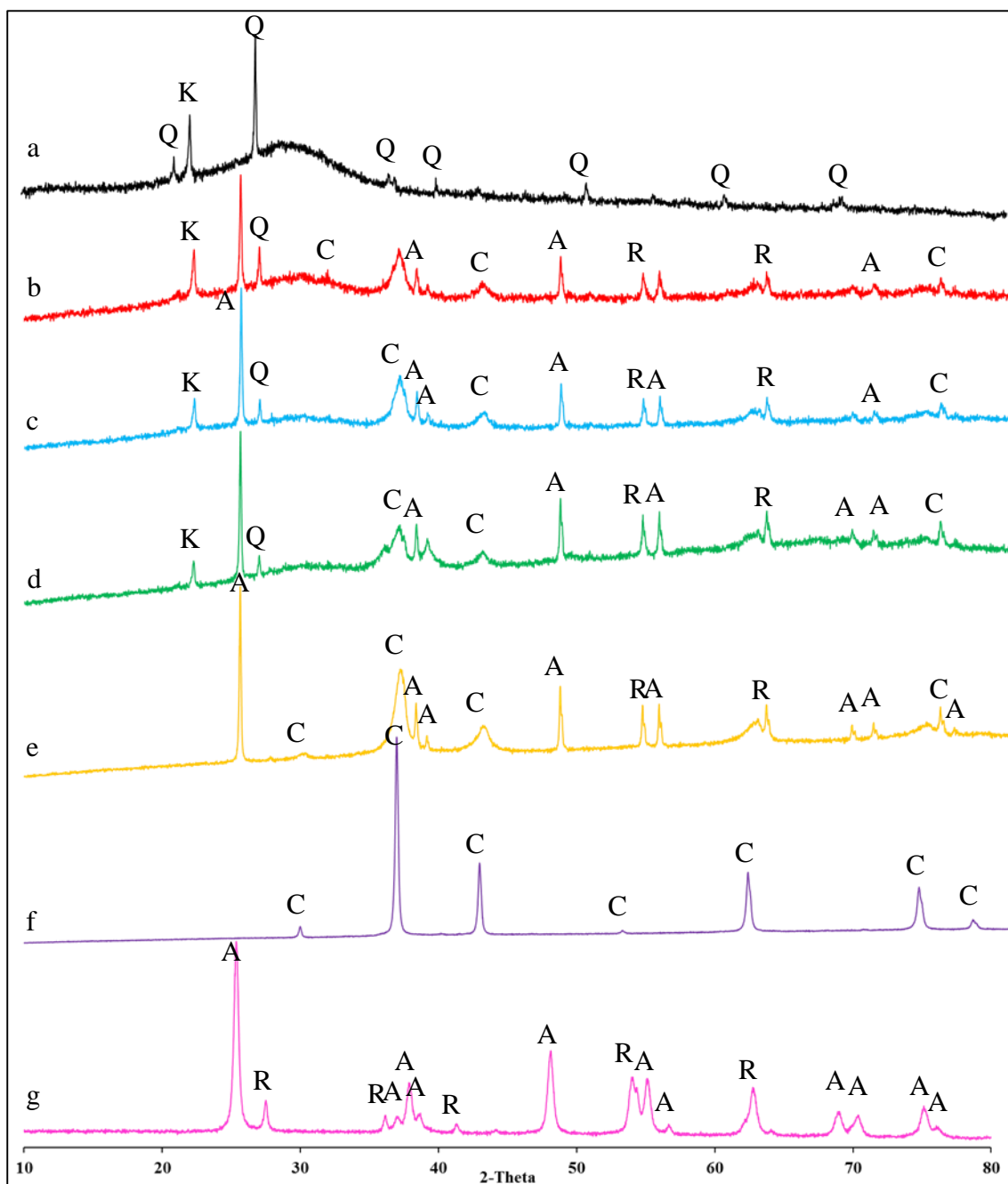
Figure 5.1. XRD patterns of GP and GP composites with different loading contents; (a) GP, (b) Cu_2O/TiO_2-GP (10 wt %), (c) Cu_2O/TiO_2-GP (20 wt %), (d) Cu_2O/TiO_2-GP (30 wt %), (e) Cu_2O/TiO_2, (f) Cu_2O, (g)TiO_2(P25).
Key: Q = quartz , K = cristobalite and A = (TiO_2-anatase) and R = (TiO_2-rutile).

5.2. Scanning electron microscopy

The morphology of the Cu_2O/TiO_2 heterostructure (Figure 5.2) shows small interconnected sub-micron spherical Cu_2O and TiO_2 particles (bright spots), the Cu_2O particles of 200-300 nm size and the TiO_2 particles 25-50 nm in size (Figure 5.2 (a-c). No obvious aggregation of TiO_2 or Cu_2O is seen in the Cu_2O/TiO_2 sample, suggesting that the TiO_2 and Cu_2O are

homogenously deposited through the heterostructure. This is confirmed by Cu and Ti EDXS maps, indicating that both elements are present in the sample with a homogenous distribution. The XRD pattern of the sub-micron Cu_2O/TiO_2 heterostructure (Figure 5.4e) confirms the coexistence of Cu_2O and the two polymorphs of TiO_2 present in P25.
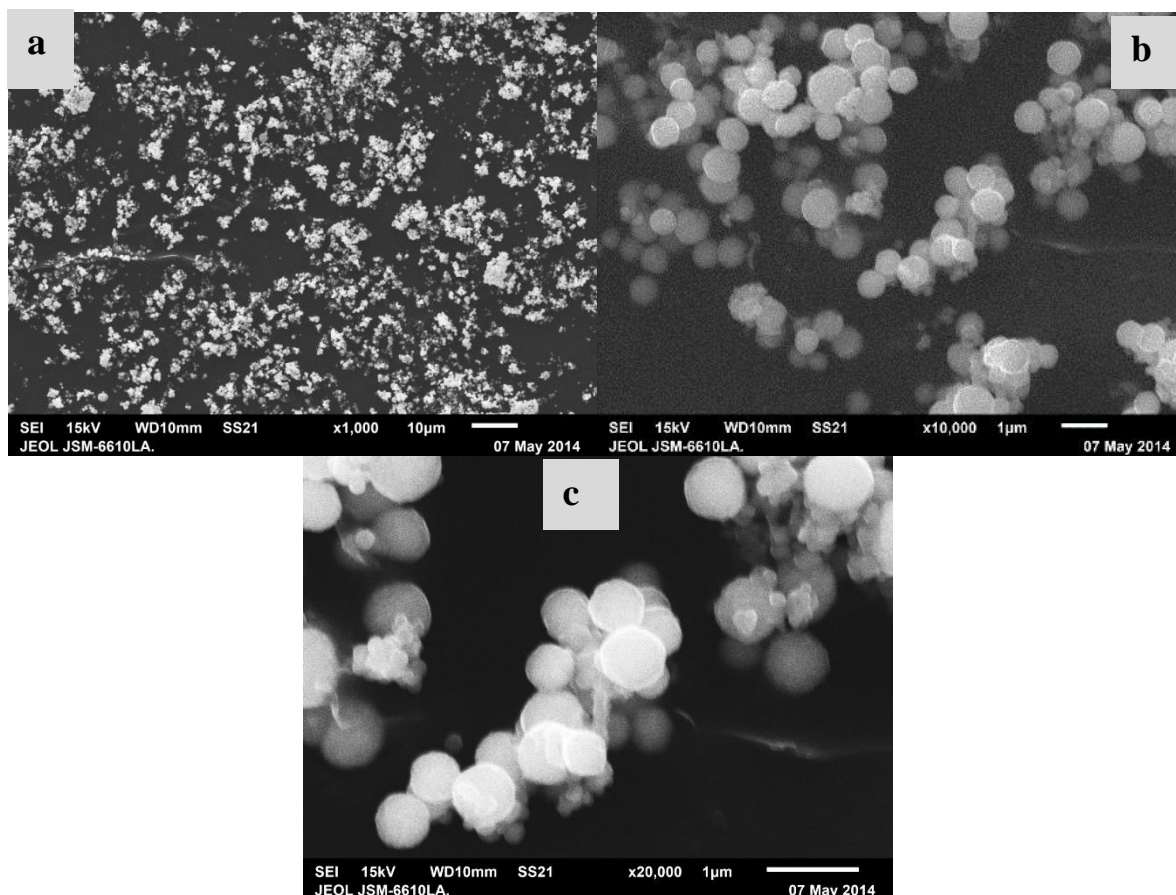
Figure 5.2. (a-c) SEM micrographs of spherical Cu_2O/TiO_2 at different magnifications, synthesized *via* the procedure described in Chapter 3.
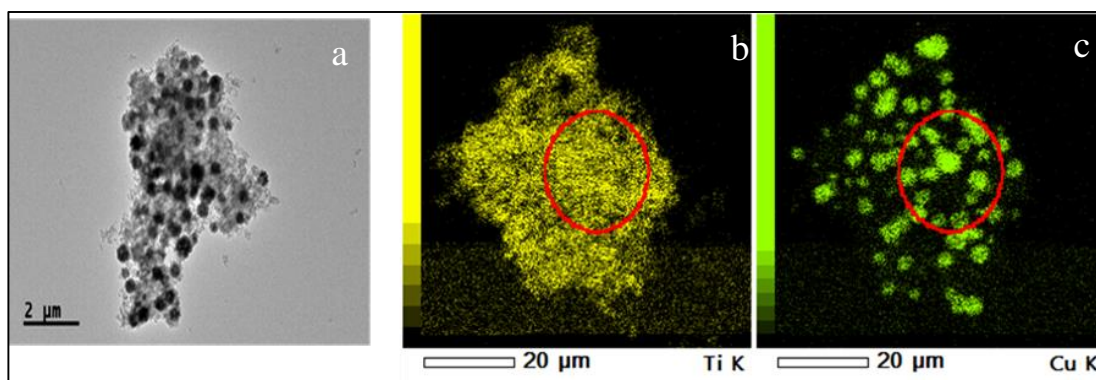
Figure 5.3. (a) STEM image of Cu_2O/TiO_2, with (b, c) corresponding Cu, Ti elemental maps.
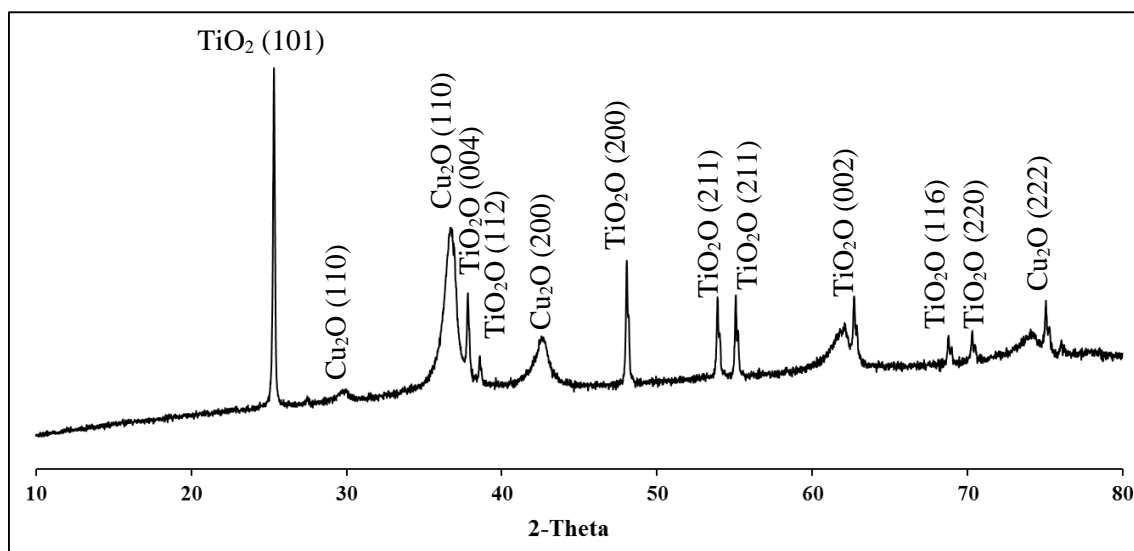
Figure 5.4. XRD pattern of Cu_2O/TiO_2.

The SEM images of the GP composites with a Cu_2O/TiO_2 loading of 10, 20 and 30 wt% (Figure 5.5 (a-c) respectively) show Cu_2O/TiO_2 nanoparticles deposited mainly on the geopolymer surface of the geopolymer matrix.
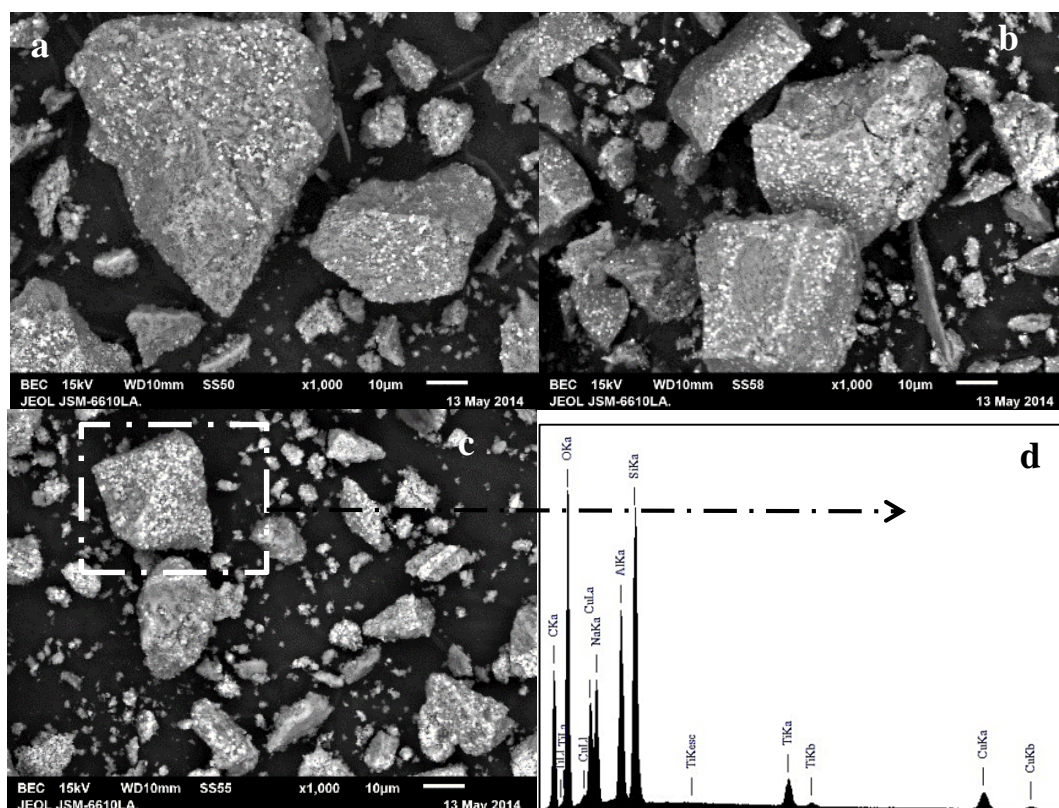
Figure 5.5. Backscattered SEM micrographs of (a) GP-10 wt% Cu_2O/TiO_2 composite, (b) GP-20 wt% Cu_2O/TiO_2 composite, (c) GP-30 wt% Cu_2O/TiO_2 composite, (d) EDS element spectra of the indicated area of image.

EDS elemental map of the GP- 30 wt% Cu_2O/TiO_2 composite (Figure 5.6) shows the expected presence of Si, Al, Na, Ti and Cu. The lighter spherical regions signify the presence of Cu_2O/TiO_2 throughout the geopolymer matrix and which is evidenced by the Cu and Ti elemental maps.
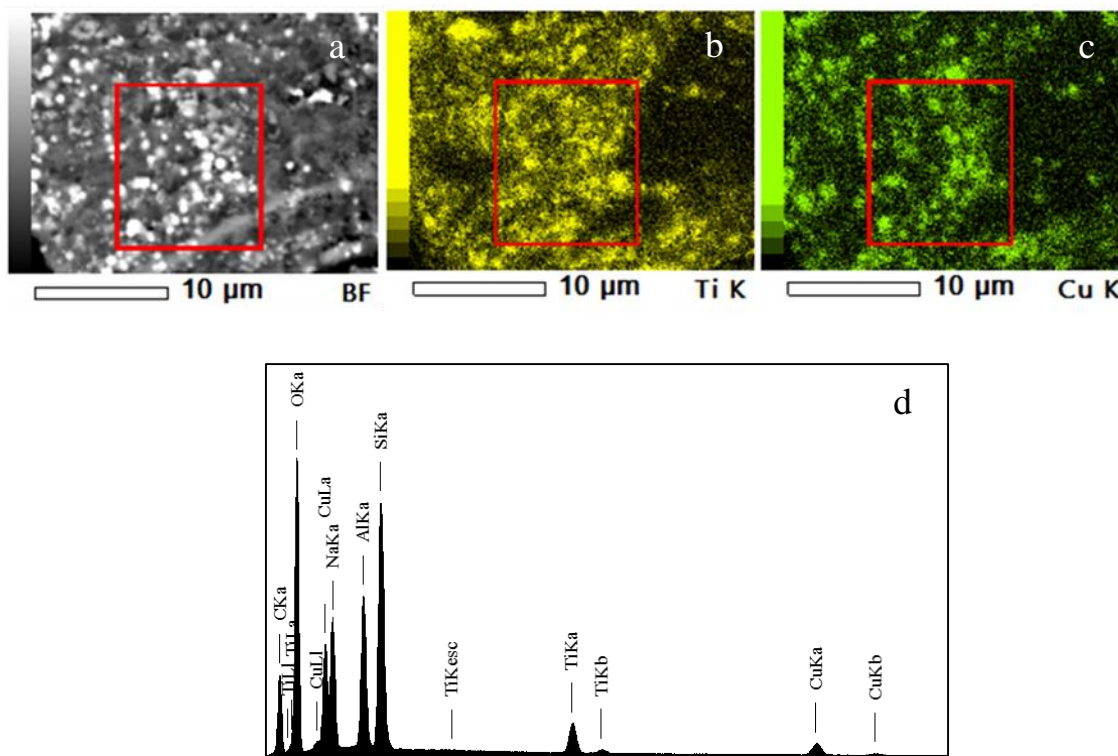
Figure 5.6. (a) Backscattered SEM image of ground GP-30 wt% Cu_2O/TiO_2 and (b) Ti, (c) Cu, EDS maps, (d) EDS element spectra of the indicated area of image.

5.3 High-Resolution Transmission Electron Microscopy

Figure 5.7 is a series of lower magnification and higher magnification TEM micrographs of the GP-10%Cu_2O/TiO_2 sample. In the low magnification image (Figure 5.7a) small dark spots are observed evenly dispersed though a lighter matrix. It is assumed that the lighter matrix is the GP and the small grains are either the TiO_2 or the Cu_2O. From initial grain size analysis (Figure 5.2) there appears to be a bimodal grain size distribution, the TiO_2 being considerably smaller than the Cu_2O grains (200 – 300 nm).

To confirm that both TiO_2 and Cu_2O are present, HRTEM images were acquired (Figure 5.7 b). Image analysis from this HRTEM confirms a d-spacing of 0.22 and 0.45 nm in two different regions which corresponds to the Cu_2O (200) and TiO_2 (110) respectively. Both these grains are smaller than 20 nm in size. As these grains are small, and as the GP is reacted

after the nanoparticles have been added, it is proposed that the nanoparticles are not only present on the sample surface (as observed in SEM), but also dispersed throughout the GP bulk.
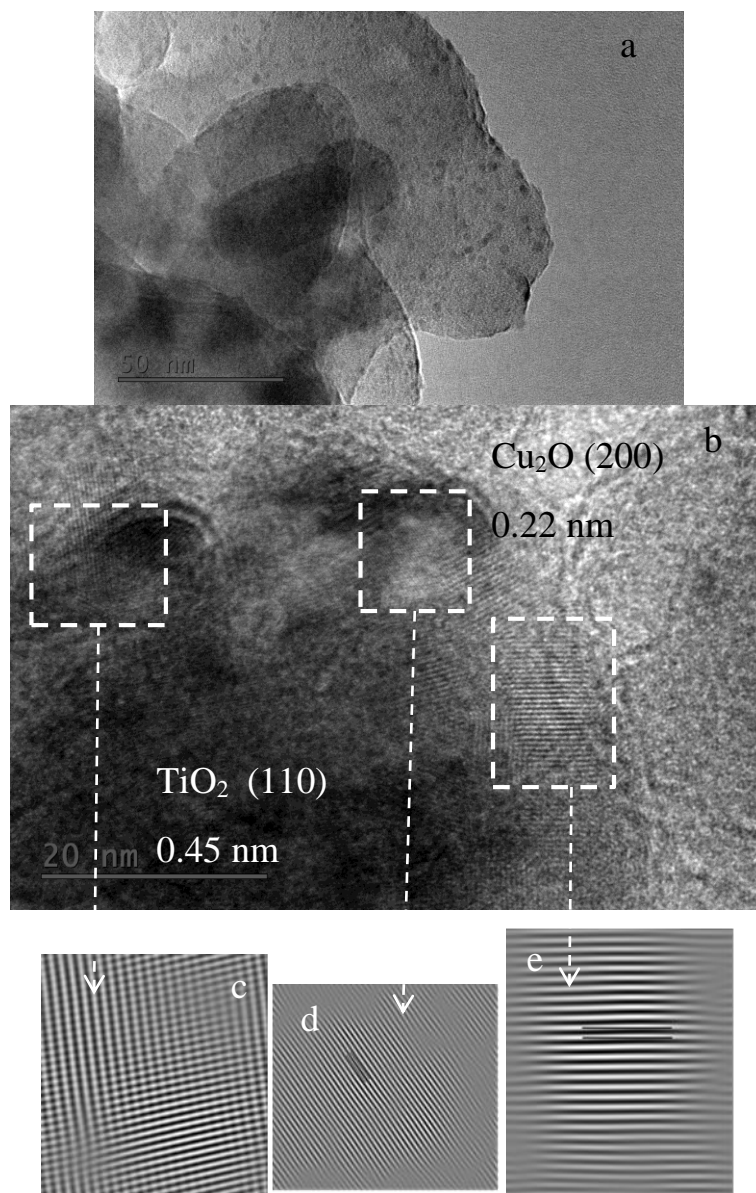
Figure 5.7. (a,b) TEM images of GP-10%-Cu_2O/TiO_2 composite, (c-e) HRTEM image of a selected area in (b).

5.4 FTIR spectroscopy
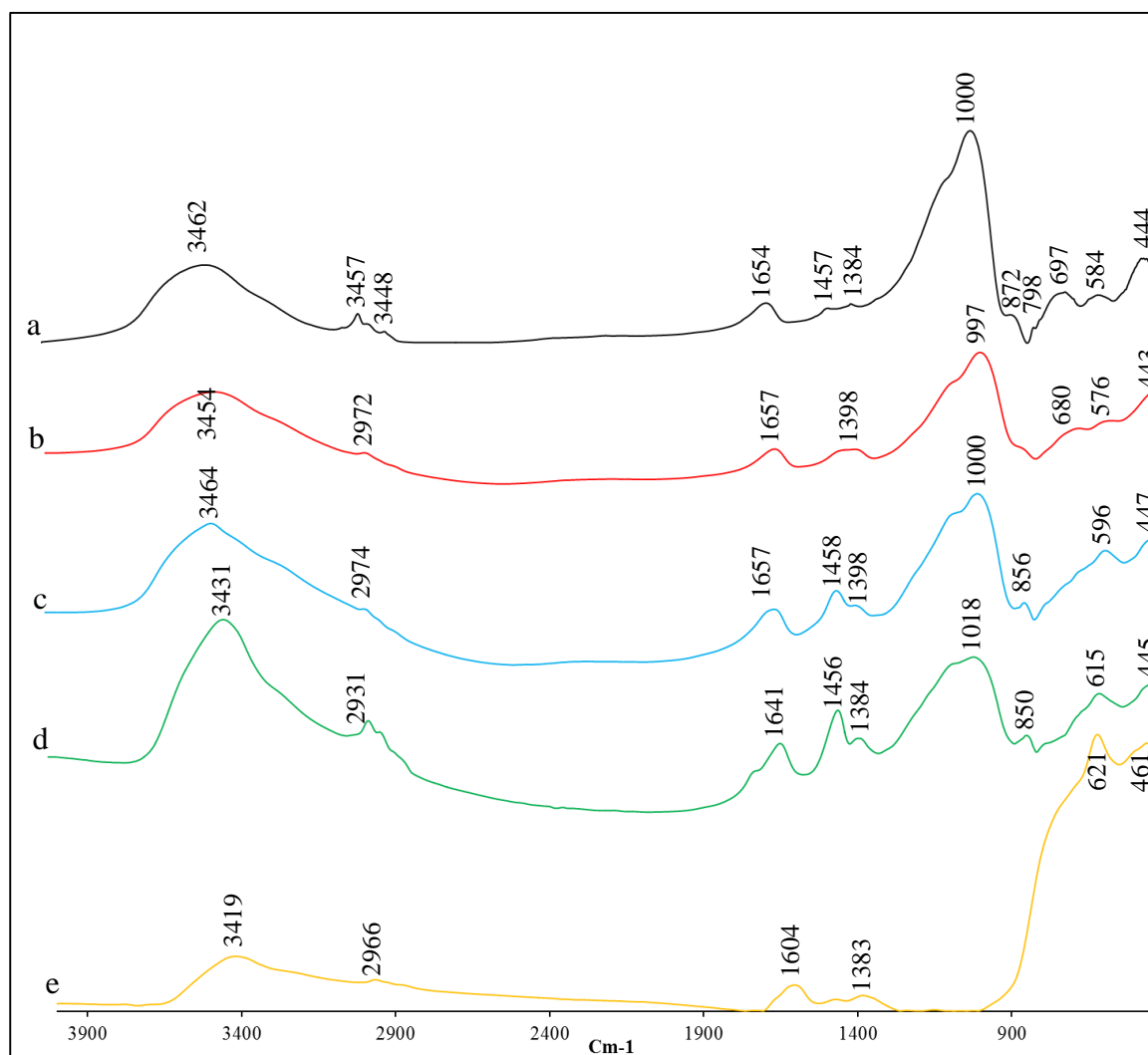
Figure 5.8. FTIR spectra of (a) GP matrix, (b) GP-10 wt % Cu_2O/TiO_2, (c) GP-20 wt % Cu_2O/TiO_2, (d) GP-30 wt % Cu_2O/TiO_2, (e) Cu_2O/TiO_2

The FTIR spectra of these samples (Figure 5.8) show a principal band in the region 997-1018 cm^{-1} arising from the Si-O-Si and Si-O-Al asymmetric stretching vibrations.[123] The (H-O-H) bending and (OH) stretching bands at 1641-1657 and 3431-3462 cm^{-1} respectively indicate that the geopolymer retains absorbed water following polycondensation of the (OH) groups.[185] Addition of 10 and 20 wt% Cu_2O/TiO_2 to the geopolymer causes a small shift in the position of the asymmetric Si–O–Si stretching vibration at 1000 cm^{-1} and a reduction in the intensity of this band. At lower wave numbers, the Si-O-Si bands of the geopolymer matrix are observed at 444 cm^{-1} and 798 cm^{-1} (Si–O–Si symmetric stretching mode), while other significant asymmetric bands appear at 576-615 cm^{-1} in the Cu_2O/TiO_2 composites; these probably arise from the superposition of Cu/Ti–O–Cu/Ti, since they progressively shift

from 576 to 615 cm^{-1} with the addition of 10 wt% to 30 wt% of Cu/Ti to the nanocomposites. These spectra are consistent with a conventional geopolymer matrix in which the Cu$_2$O/TiO$_2$ heterostructure has not significantly distorted the matrix structure.

5.5 Adsorption of MB

5.5.1 Reactions under dark conditions (adsorption on the matrix)

As described in the previous chapter, an identical series of experiments on the removal of MB dye was carried out using these Cu$_2$O/TiO$_2$ composites. As concluded from the results of the previous chapter, the geopolymer matrix should be an efficient absorbers of organic dyes in its own right since its surface hydroxyl groups can attract and hold cationic organic species.[178] As in the experiments of chapter 4, the adsorption of MB on the composites was monitored by measuring the decolorization of the MB dye under dark conditions (Figure 5.9). Incorporation of 10 wt% Cu$_2$O/TiO$_2$ nanoparticles into the geopolymer matrix results in a significant slowing of the rate of dye adsorption (Figure 5.9), probably because of blocking of the adsorption sites by the non-adsorbing oxide particles as was the case with Cu$_2$O alone. However, this effect is reversed by the addition of larger concentrations of Cu$_2$O/TiO$_2$ (Figure5.9), suggesting that the Cu$_2$O/TiO$_2$ heterostructures are now acting to open up the geopolymer matrix structure, facilitating access of the dye to the internal adsorption sites.
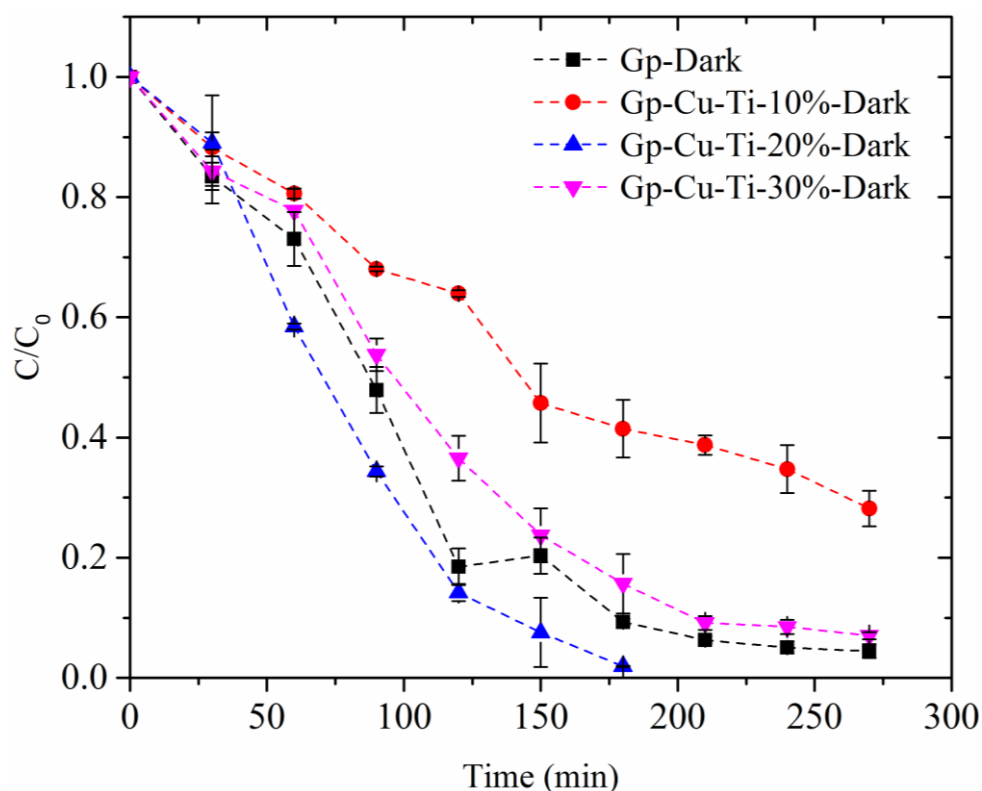
Figure 5.9. Plot of the residual concentration (C/C$_0$) *vs*. time (t) on the GP, Cu$_2$O/TiO$_2$-GP 10, 20, and 30 wt% (monitored at 664 nm) under dark conditions.

Following the procedure outlined in the previous chapter, the MB adsorption data were fitted to pseudo-first order and pseudo-second-order models (equations 29 and 30 respectively in chapter 3).[181, 182] The resulting plots of q versus time (t) for the adsorption of MB on these adsorbents are presented in Figure 5.10 (a, b). Comparison of the q$_e$ values calculated from these equations with the experimental values of q$_{exp}$ (Table 5.1) shows that for all the samples the pseudo-first order model provides a better fit to the experimental data. Apart from the 10 % Cu$_2$O/TiO$_2$ geopolymer composite, which has already been noted as being less absorptive for MB dye, the first-order rate constants (Table 5.1) are very similar, as are the correlation coefficients R^2 for both the pseudo-first order and pseudo-second order models.
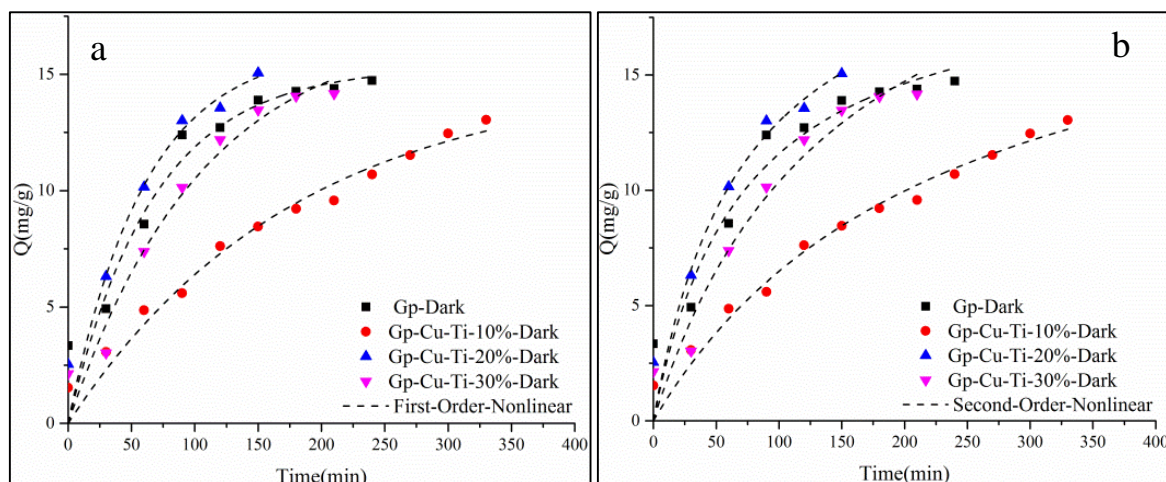
Figure 5.10. (a) Pseudo first-order kinetics and (b) Pseudo second-order kinetics by the nonlinear method and experimental kinetics for the adsorption of MB on the geopolymer matrix and geopolymer composites containing Cu_2O/TiO_2 heterostructures.

Table 5.1. Kinetic parameters for adsorption of MB under dark conditions by geopolymer composites with Cu_2O/TiO_2

Sample	Kinetic model	q_{exp} (mg/g)	q_e (mg/g)	k	R^2
GP	1st-order	14.74	15.33	0.015	0.90
"	2nd-order	"	19.85	$7.05e^{-04}$	0.89
GP/10%Cu_2O/TiO_2	1st-order	14.76	14.92	0.006	0.97
" "	2nd-order	"	21.56	$2.00e^{-04}$	0.97
GP/20%Cu_2O/TiO_2	1st-order	14.76	16.23	0.016	0.93
" "	2nd-order	"	22.31	$6.24e^{-04}$	0.93
GP/30%Cu_2O/TiO_2	1st-order	14.76	17.13	0.010	0.95
" "	2nd-order	"	25.43	$2.71e^{-04}$	0.94

5.5.2 MB dye adsorption isotherms under dark conditions

As in the previous chapter, the experimental MB adsorption data determined under dark conditions were fitted to the Freundlich, Langmuir and Langmuir-Freundlich isotherms (equations 31-33 in chapter 3).[17, 178] The resulting plots of the data are shown in Figure 5.11 a, b and c respectively. The correlation coefficient (R^2) of all these fits for the geopolymer-

10% Cu_2O/TiO_2 composite is >0.98, indicating that the adsorption of MB by this composite can be described equally well by all three isotherms; however, the R^2 values for all the composites fitted by all three isotherms are satisfactorily high (0.90-0.99), suggesting that the most appropriate isotherm cannot be identified from a consideration of the R^2 values alone. The slightly better adsorption characteristics of the geopolymer-10% Cu_2O/TiO_2 composite are consistent with the differences already noted between the adsorption behaviour of the geopolymer-10% Cu_2O/TiO_2 composite and those containing higher Cu_2O/TiO_2 concentrations.
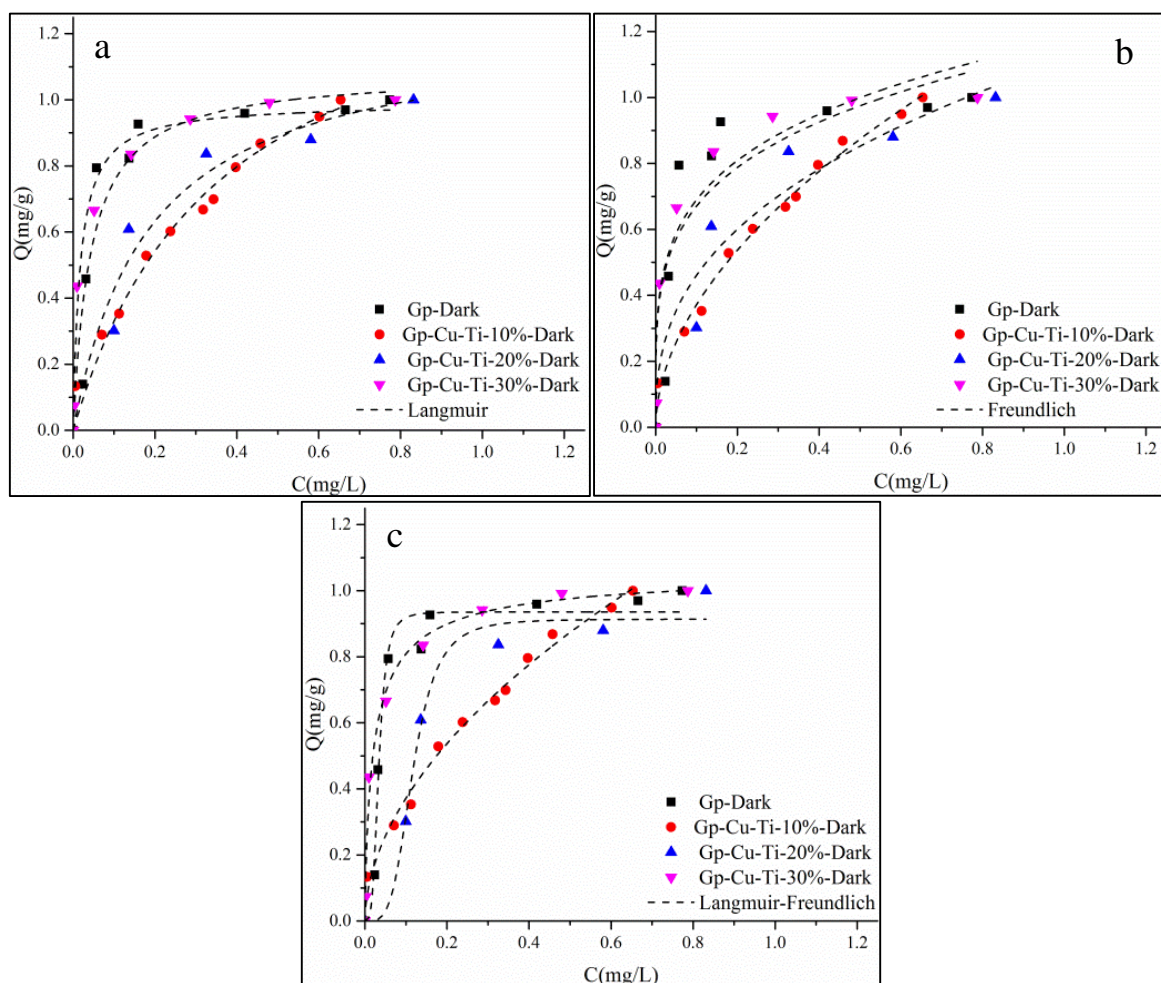
Figure 5.11. (a-c). Adsorption isotherms for MB adsorption and the corresponding Langmuir, Freundlich and Langmuir-Freundlich models fit (dashed lines).

5.5.3 Reactions under UV radiation

As discussed in Chapter 4, the decolouration of MB dye under UV radiation shown in Figure 5.12 was determined in a separate series of experiments in which fresh MB solutions were mixed with fresh composite samples and immediately exposed to UV irradiation. As with the composites containing only Cu_2O (Chapter 4), removal of the dye is due to a combination of adsorption and photodegradation processes and should therefore be more rapid than in the dark. Comparison of Figure 5.12 with the process in the dark (Figure 5.9) shows this to be the case, particularly in the geopolymer-20% Cu_2O/TiO_2 composite, in which the destruction of the MB is markedly faster than in the dark.
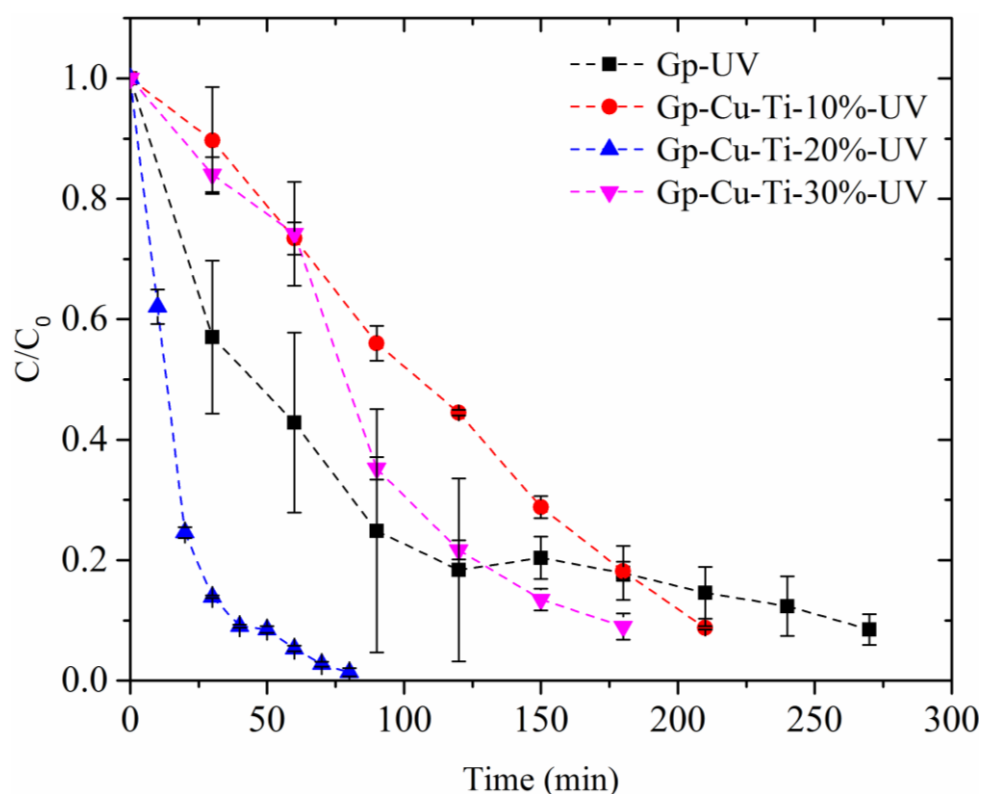
Figure 5.12. Plots of the residual concentration (C/C_0) *vs.* time (t) on the GP matrix and Cu_2O/TiO_2-GP 10, 20, and 30 wt% composites (monitored at 664 nm) under UV irradiation.

Figure 5.13, which compares the behavior of the all the materials towards MB in the dark and under UV radiation after 60 min., clearly shows the expected increase in photodegradation with increasing Cu_2O/TiO_2 content of the composites, with 98% dye removal achieved by the geopolymer-20% Cu_2O/TiO_2 composite in this time interval. The photodegradation properties of the Cu_2O/TiO_2 component alone are not as marked as those of the composites, since these results represent a combination of adsorption and photodegradation, and this component of the composites does not adsorb the dye (Figure 5.13). The response of the geopolymer

matrix to the MB is similar under both dark conditions and UV radiation, suggesting that irradiation has little effect on the dye adsorption characteristics of the geopolymer.
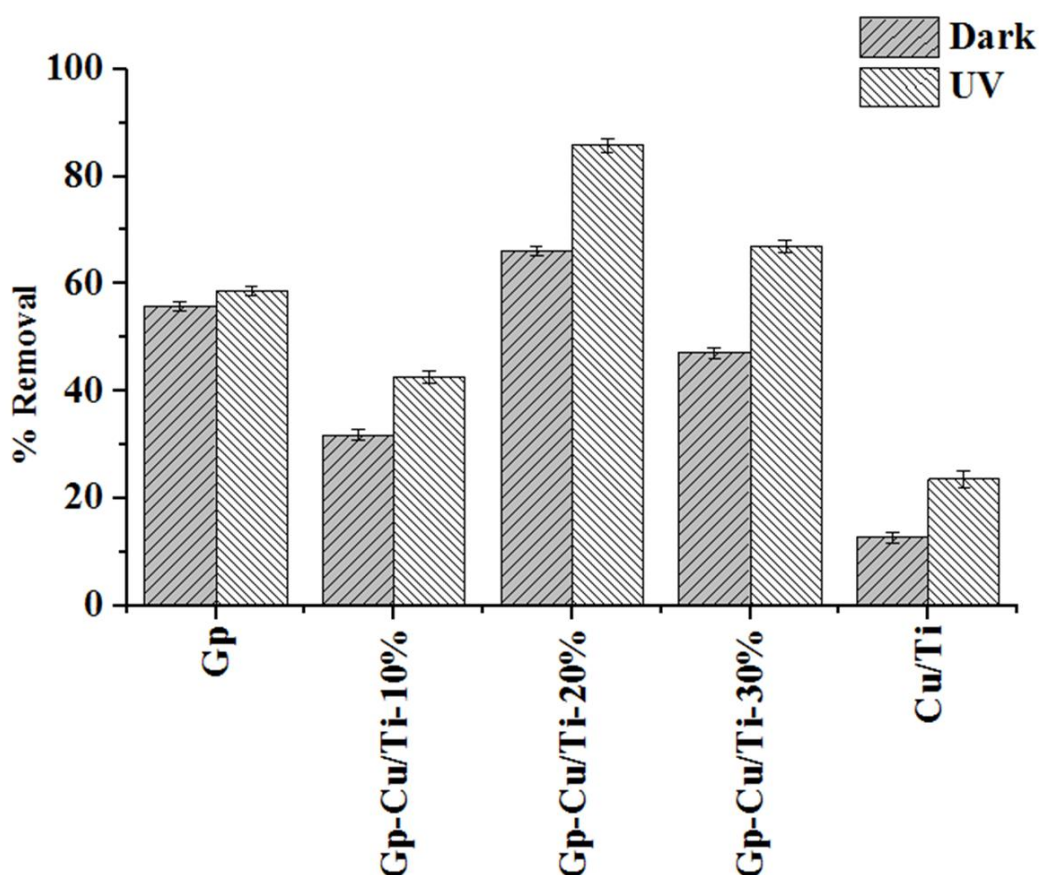
Figure 5.13. MB removal after 60 min. by the GP matrix, (10-30 wt%) GP-Cu_2O/TiO_2 composites and the Cu_2O/TiO_2 nano-heterostructure.

5.5.4 Adsorption and degradation of MB dye by P25 titania, Cu_2O and their geopolymer composites

For comparison with the Cu_2O/TiO_2 nanocomposites, the behaviour of P25 titania alone and in conjunction with the geopolymers matrix was measured under dark conditions and UV radiation and compared with and the Cu_2O results of the previous chapter (Figure 5.14). Under dark conditions, neither TiO_2 nor Cu_2O alone nor their mixture removes MB from solution, indicating that the nanostructure and surface properties of these oxides is not effective in absorbing the dye. However, in combination with the geopolymer matrix, adsorption occurs on the geopolymer (Figure 5.13a). When fitted to pseudo- first and pseudo-second order kinetic equations, the data of Figure 5.13a behave similarly to the geopolymer Cu_2O/TiO_2 composites, being best described by the pseudo first-order equation (Table 5.1).

Likewise, these data are well fitted by Freundlich-type isotherms, confirming that the behaviour of these geopolymer composites under dark conditions represent adsorption of the dye on the matrix.

Under UV irradiation (Figure 5.14b) both the TiO_2 and Cu_2O alone, and their nano-heterostructure exhibit the expected photodegradation of the MB dye, the Cu_2O being markedly less efficient that the P25 titania. However, combination of Cu_2O with P25 titania greatly improves its performance (Figure 5.14b), but the incorporation of this nano oxide combination into the geopolymer matrix produces an even greater effect than with the Cu_2O/TiO_2 combination by itself, particularly in composites containing 20 wt% Cu_2O/TiO_2. Since it was shown in Figure 5.14 that the photoactive oxides Cu_2O and TiO_2 separately and in combination do not have any significant absorption characteristics compared with the geopolymer matrix, their removal of MB under UV irradiation is solely due to photodegradation.

The excellent performance of the geopolymer-Cu_2O/TiO_2 composites in destroying the model organic compound result is probably due to the ability of the matrix to trap and hold the dye during the photocatalysis process. The facilitating effect of the matrix, in terms of its pore size and structure will be addressed in the following chapters. The present results suggest however that composites of nanosized Cu_2O particles and photoreactive P25 titania in an aluminosilicate geopolymer matrix have been successfully synthesised, and have an improved potential as materials for environmental protection applications to efficiently remove organic pollutants from water or the atmosphere.
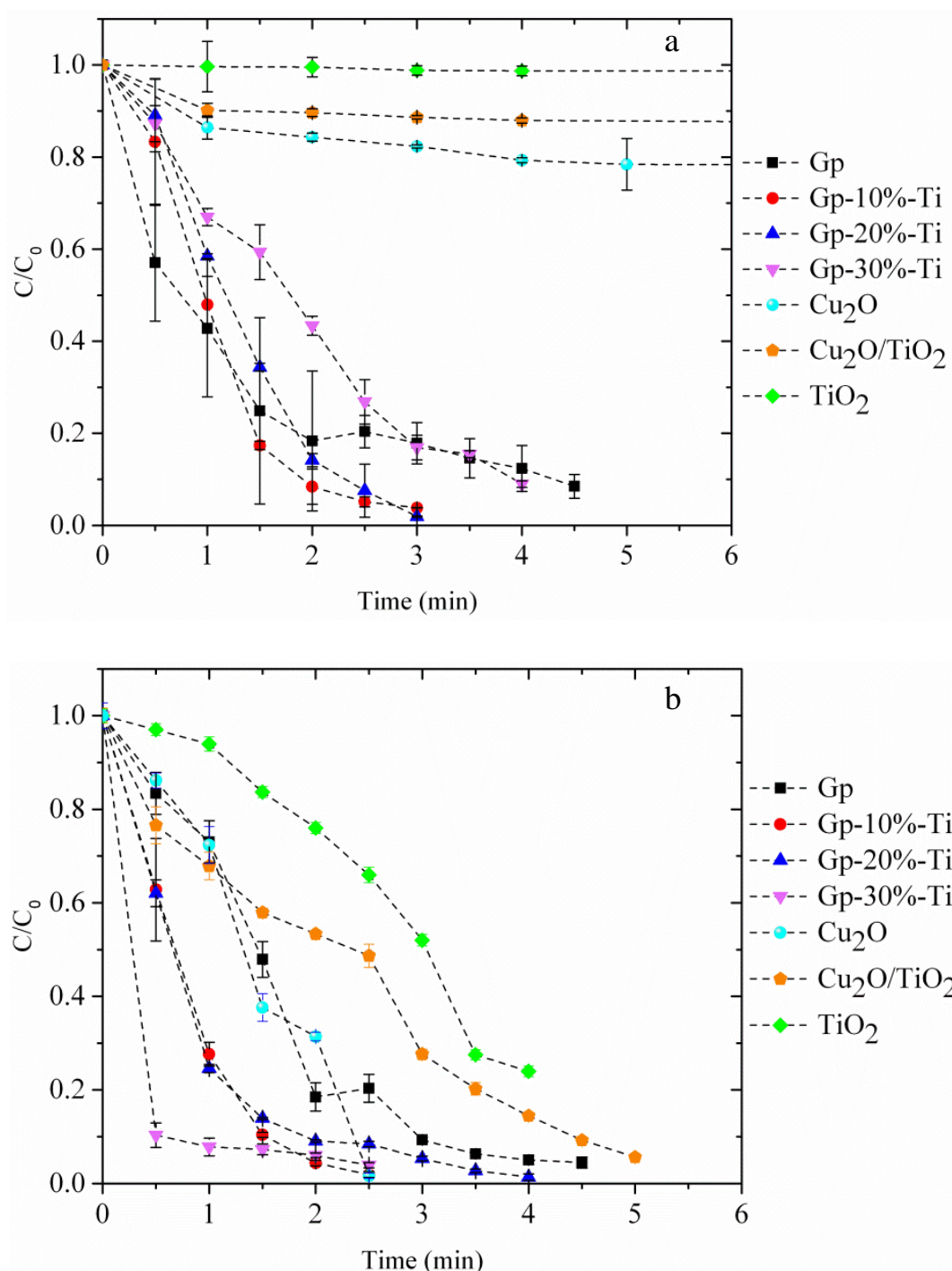
Figure 5.14. Residual concentration (C/C_0) *vs*. time (t) of MB dye adsorbed and photodegraded on the TiO_2, Cu_2O and Cu_2O/TiO_2, compared with the GP-Cu_2O/TiO_2 composites under (a) dark conditions, (b) UV radiation.

5.6 Geopolymer composites of P25 titania alone

5.6.1 XRD Analysis

The XRD traces of geopolymer composites containing only P25 titania (Figure 5.15) are as expected, containing only the broad X-ray amorphous feature overlaid by the sharp peaks of the anatase and rutile forms of titania.
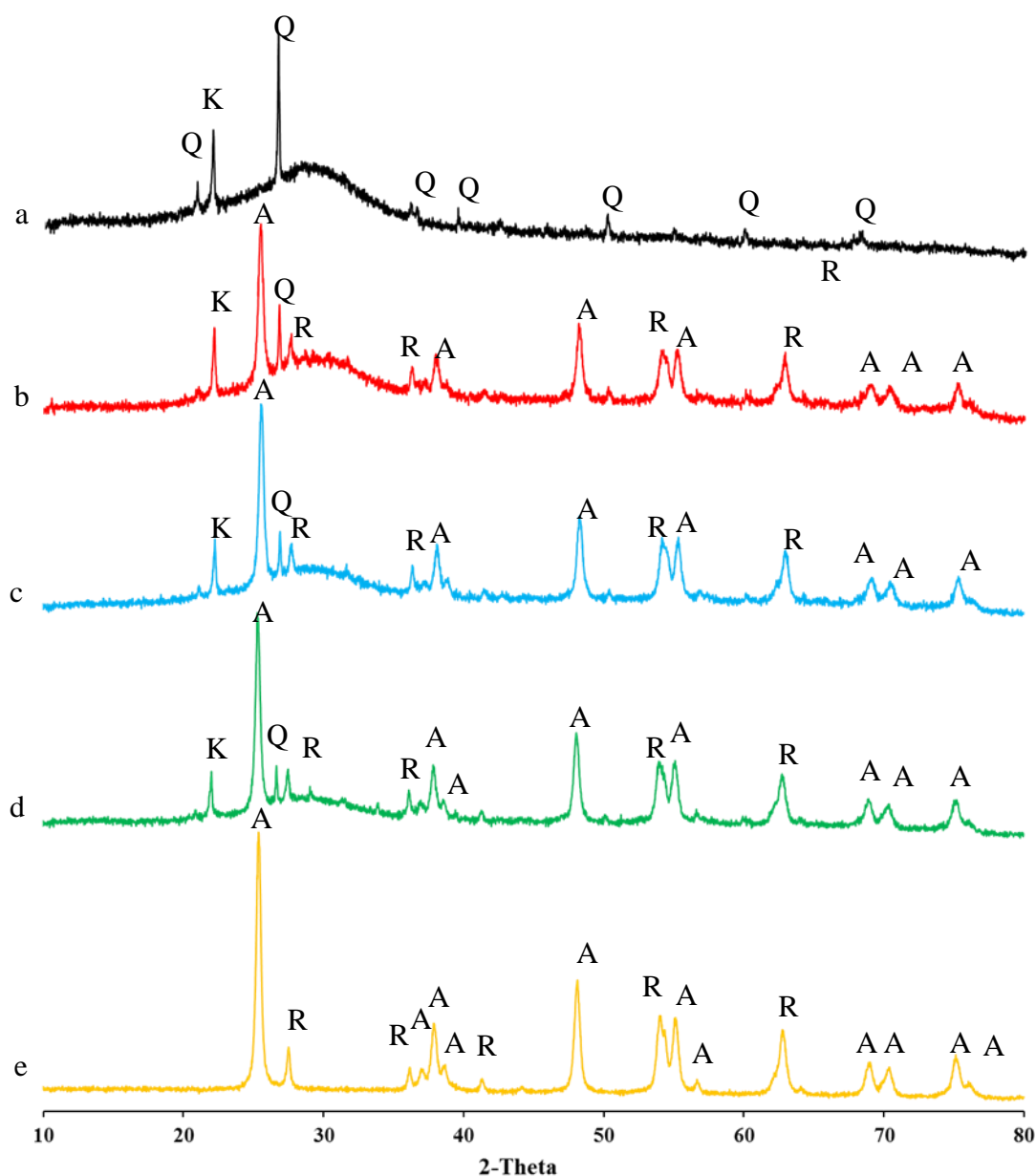
Figure 5.15. XRD patterns of GP and TiO_2 and TiO_2 supported by GP with different loading contents; (a) GP, (b) GP-10 wt % TiO_2, (c) GP-20 wt % TiO_2, (d) GP-30 wt % TiO_2, (e) TiO_2. Q = quartz, K = cristobalite, A = TiO_2 anatase, R = TiO_2 Rutile

5.6.2 Scanning electron microscopy

SEM micrographs (Figure 5.16) confirm the homogeneous dispersion of the P25 TiO_2 particles on the surface of the geopolymer composites with no obvious particle aggregation (Figure 5.16). As expected, increasing the oxide concentration part is evidenced by a greater concentration of TiO_2 particles, especially on the surface of the composite matrix, as shown by the backscattered images (Figure 5.16 b,d,f).
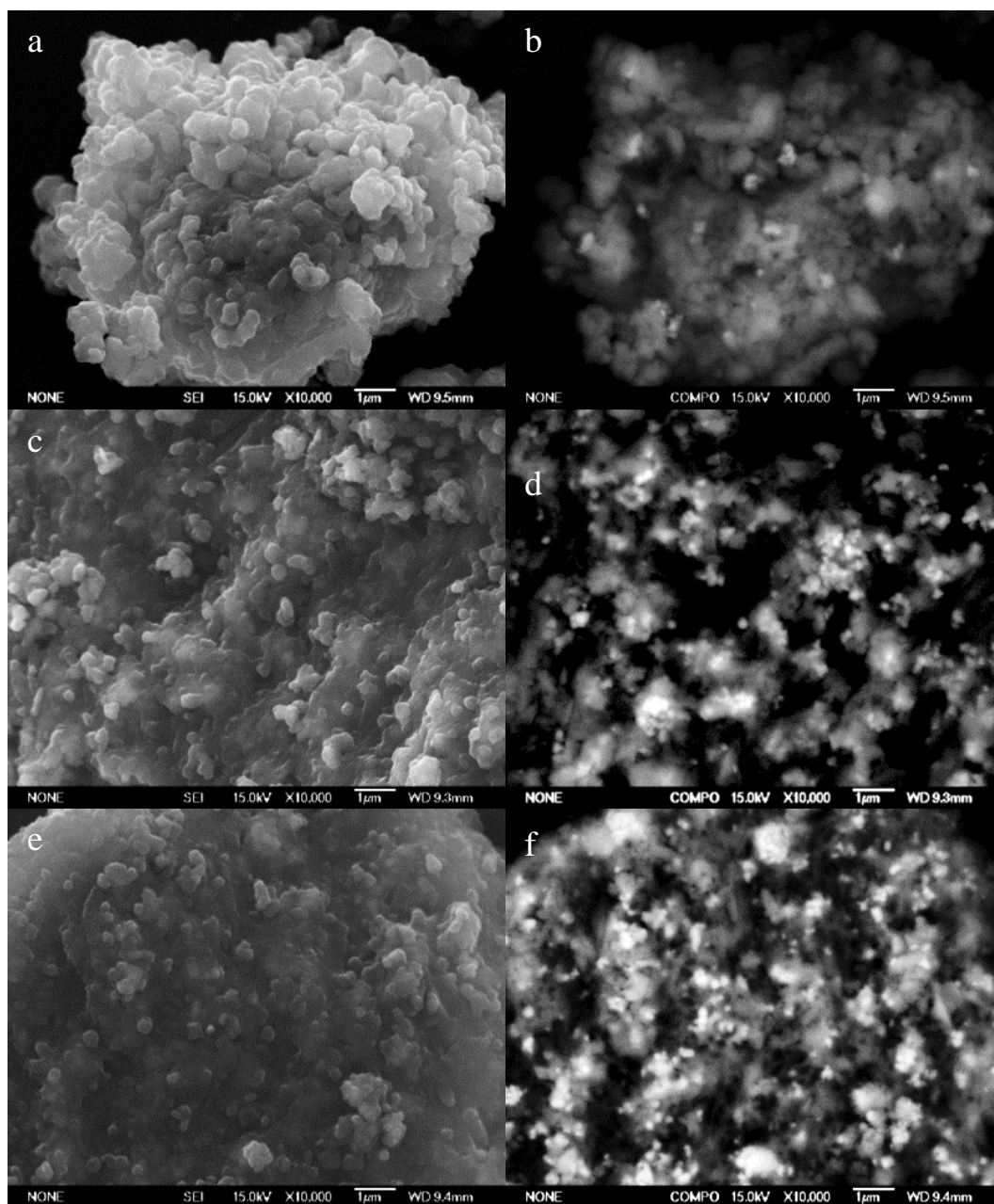
Figure 5.16. SEM micrograph of (a) GP-10 wt % TiO_2, (b) BSE of GP-10 wt % TiO_2, (c) SEM micrograph of GP-20 wt % TiO_2, (d) BSE of GP-20 wt % TiO_2, (e) SEM micrograph of GP-30 wt % TiO_2, (f) BSE of GP-30 wt % TiO_2, showing TiO_2 nanoparticles deposited mainly on the GP surface.

Figure 5.17a is a BSE micrograph of the GP-30% TiO_2 sample. The bright regions in the BSE image correspond to the TiO_2 rich regions, which have a higher average atomic number than the GP matrix. Figure 5.17 b – e are the corresponding EDS elemental maps from Na, Al, Si and Ti. There are some higher concentration regions in the Na, Al, Si EDS maps, which may be attributed to the sample morphology or to phase segregation yielding the observed quartz and cristobalite XRD peaks. The TiO_2 grains look evenly distributed on the sample surface, but it is interesting to note that the Ti EDS maps do not always directly correspond with the bright regions in the BSE image. As the BSE interaction volume region is larger than the EDS interaction volume, it is proposed that the TiO_2 grains are embedded to some extent in the GP matrix.
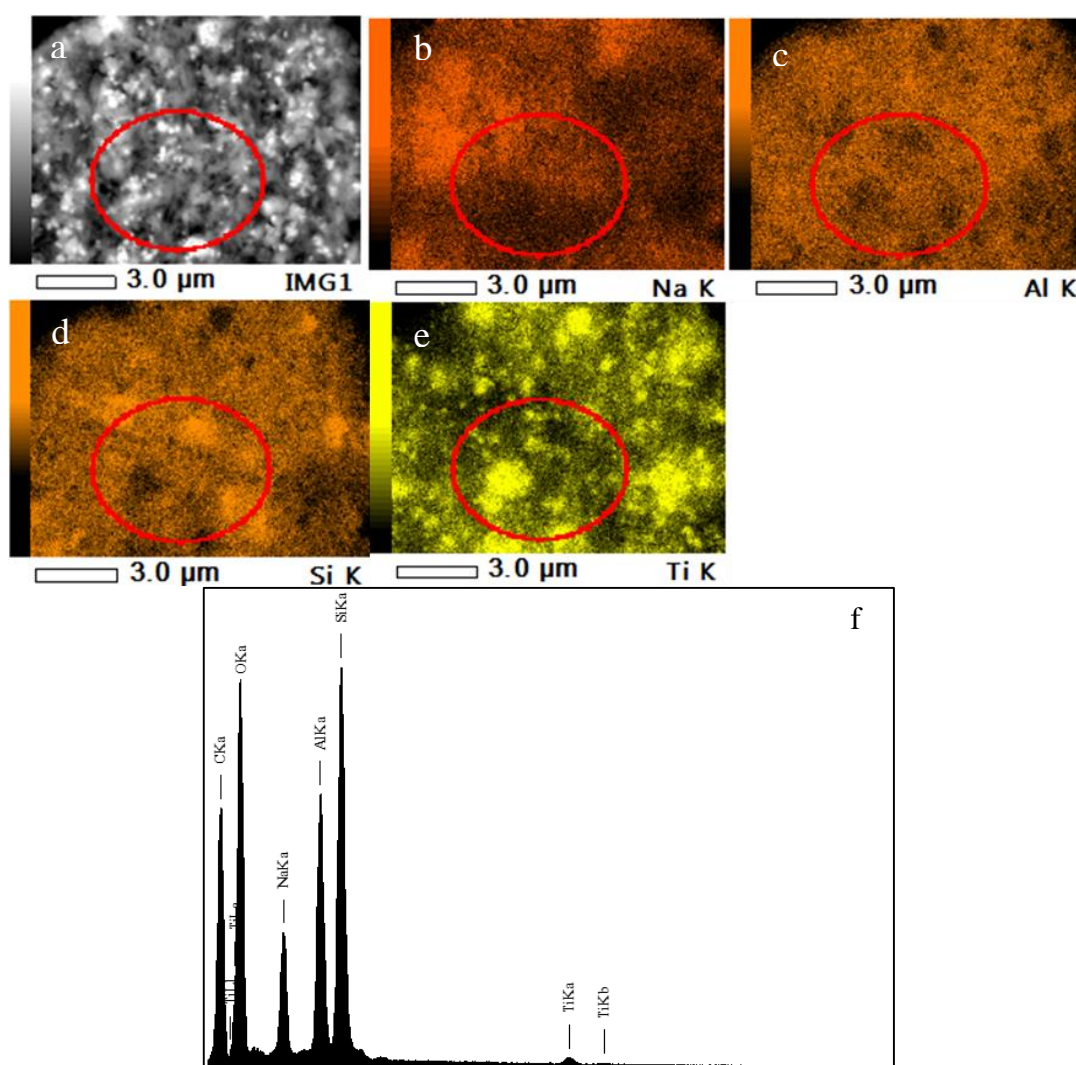
Figure 5.17. (a) Backscattered electron image of GP composite containing 30 wt%TiO_2 and (b) sodium, (c) aluminium, (d) silicon, (e) titanium EDS maps, (f) EDS element spectra of the indicated area of image.

5.6.3 High-Resolution Transmission Electron Microscopy

Figure 5.18 shows a series of low magnification and high magnification TEM micrographs. Figure 5.18 shows dark ca. $10 - 20$ nm sized grains embedded within a lighter matrix. It is proposed that the lighter matrix is the GP, whereas the dark particles are the TiO_2 grains. This is confirmed in Figure 5.18 b which shows lattice fringes with a *d*-spacing of $0.42 - 0.45$ corresponding to the TiO_2 {110} plane. The GP pore size has experimentally been determined to range from $24 - 55$ nm. As such, it is possible that the $10 - 20$ nm sized TiO_2 could be incorporated into the GP matrix.
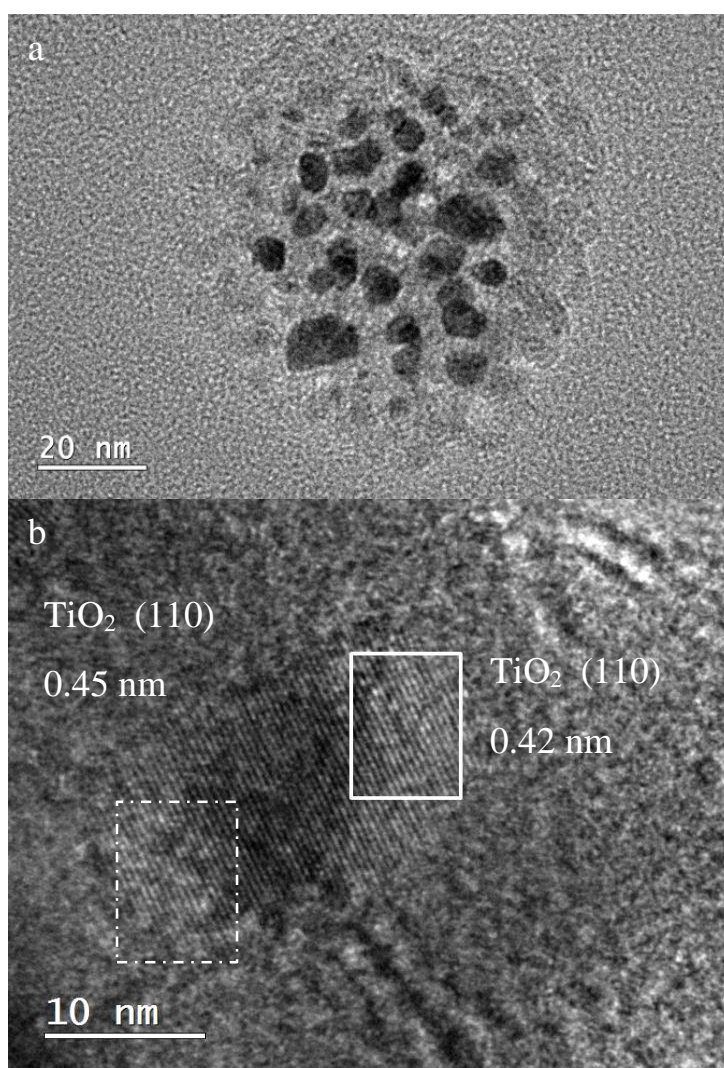
Figure 5.18. (a,b) TEM images of GP-10%-TiO_2 composite

5.6.4 Nitrogen Adsorption/Desorption Isotherms

Information about the pore structures of the composites was obtained by measuring the N_2 adsorption-desorption isotherms of the composites containing 10 wt% Cu_2O and 10 wt% TiO_2 (Figure 5.19). The specific surface areas were obtained by several different methods: single point BET, multiple-point BET, Langmuir, BJH adsorption and BJH desorption measurements (Table 5.3). All these techniques show similar trends, with a significant increase in area from the geopolymer matrix alone to the composite containing 10 wt% TiO_2 and a significant decrease in the area of the composite containing 10 wt% Cu_2O, the latter possibly due to blocking the pores by the Cu_2O particles as previously suggested. This observation is also consistent with the much smaller pore volumes recorded for the Cu_2O composites, and the decreased adsorption of MB dye under dark conditions in this composite (Figure 4.14). The increased surface area of the titania-geopolymer composite (Table 5.3) suggests that in this composite the titania nanoparticles are more readily able to enter into and expand the internal structures of the geopolymer matrix, or that the surface area of the titania itself is contributing to this result. The present experiments do not allow these possibilities to be distinguished.
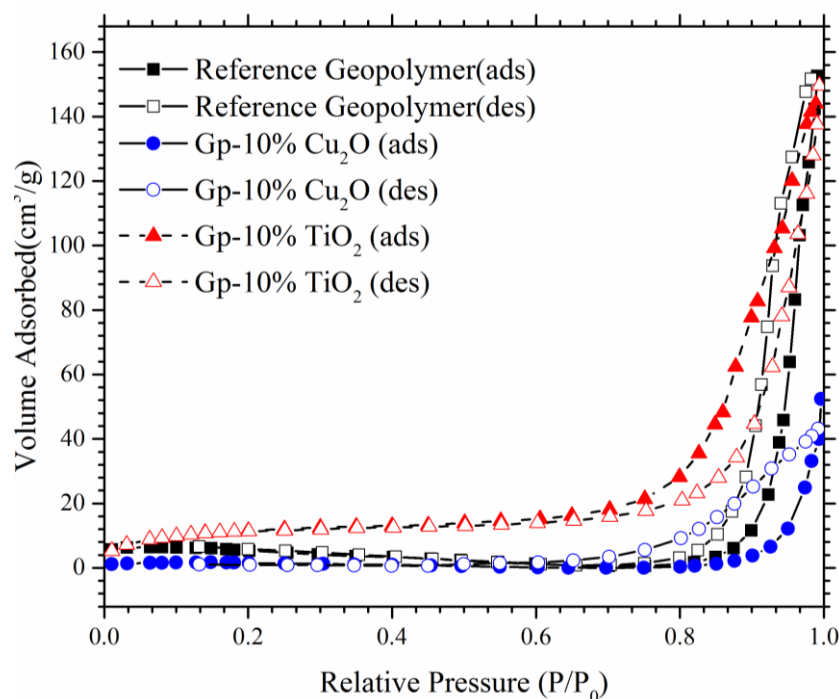
Figure 5.19. Nitrogen sorption isotherms of the GP matrix (■, adsorption □, desorption), GP-10 wt% Cu_2O- (●, adsorption ○, desorption) and GP-10 wt% TiO_2- (▲, adsorption △, desorption)

Table 5.2. Specific surface areas and pore parameters of geopolymer and geopolymer composites

	GP-Reference	GP-10%-TiO$_2$	GP-10%-Cu$_2$O
Single Point Surface Area	18.44 m²/g	39.60 m²/g	5.14 m²/g
S $_{BET}$	17.23 m²/g	41.75 m²/g	5.21 m²/g
S $_{Langmuir}$	21.92 m²/g	57.98 m²/g	6.82 m²/g
S $_{BJH\ Adsorption\ Cumulative}$	23.06 m²/g	30.87 m²/g	5.79 m²/g
S $_{BJH\ Desorption\ Cumulative}$	38.94 m²/g	46.55 m²/g	17.76 m²/g
Volume			
Single Point Adsorption	0.24 cm³/g	0.23 cm³/g	0.081 cm³/g
V $_{pore\ BJH\ Adsorption\ Cumulative}$	0.236 cm³/g	0.23 cm³/g	0.061 cm³/g
V $_{pore\ BJH\ Desorption\ Cumulative}$	0.236 cm³/g	0.23 cm³/g	0.081 cm³/g
Pore Size			
D $_{Adsorption}$	55 nm	22 nm	62 nm
D $_{BJH\ Adsorption}$	41 nm	30 nm	42 nm
D $_{BJH\ Desorption}$	24 nm	20 nm	18 nm

Conclusions

This chapter demonstrates that composites of spherical nanoparticle Cu$_2$O with P25 titania homogeneously distributed within a well-formed aluminosilicate geopolymer matrix can successfully be prepared, as shown by SEM/EDS and HRTEM. XRD and FTIR confirmed the formation of a well-reacted geopolymer matrix that was unaffected by the insertion of the Cu$_2$O/TiO$_2$ heterostructures or by the adsorption or photodegradation of MB dye. The entry of the Cu$_2$O/TiO$_2$ heterostructures into the geopolymer matrix is shown to facilitate the removal of MB dye from solution under dark conditions, but P25 titania or Cu$_2$O alone do not show this facility for dye adsorption. Under dark conditions, the geopolymer matrix, and, in particular, the Cu$_2$O/TiO$_2$ geopolymer composites, remove the dye by an adsorption process which can best be described by pseudo first-order kinetics and Freundlich-type isotherms, as

was shown in the previous chapter to be the case for Cu_2O/geopolymer composites. Nitrogen adsorption/desorption isotherms of the composites containing 10 wt% TiO_2 show a significantly larger specific surface area than the geopolymer matrix alone, possibly due to expansion of the pore structure by the titania, whereas the specific surface area of the composite containing 10 wt% Cu_2O is significantly decreased, possibly due to blocking of the pores by the Cu_2O nanoparticles. These observations provide a qualitative explanation for the differences in dye absorption behaviour of the different composites.

Under UV irradiation, the composites remove the MB dye by a combination of adsorption and photodegradation, as was found for Cu_2O/geopolymer composites (chapter 4). The combination of a nano-heterostructure composed of Cu_2O particles and photoreactive P25 titania in an aluminosilicate geopolymer matrix was found to be a more efficient photocatalyst under UV irradiation than geopolymer composites of the individual oxides alone, and represents an improvement in the performance of these composite photocatalysts over those containing Cu_2O alone.

Chapter 6
Composites containing Cu₂O nanoparticles supported on an expanded geopolymer matrix

Introduction

In previous chapters it was shown that composites of geopolymers with nanoparticles of Cu_2O can efficiently remove MB dye from solution by a combination of adsorption (in the dark) and photodegradation (under UV irradiation), and the efficiency of this process is considerably improved by combining the Cu_2O with a photoreactive form of titania (P25). In this chapter, attention is turned to the role of the geopolymer matrix, to determine whether by modifying its pore structure, the efficiency of the photoactive component might be improved further.

Although geopolymers, are X-ray amorphous, the negative charges on the aluminate units which are compensated by the presence of cations leads to similarities with zeolite structures, particularly with respect to cation exchange behaviour, which in turn suggests a possible procedure for expanding the pore structure of the geopolymer by the use of a large quaternary ammonium cation such as the cetyltrimethylammonium ion (CTAB), normally used as the bromide salt. CTAB is extensively used to expand the basal spacings of layer-lattice clay minerals such as montmorillonite,[125, 140] rectorite[76] and kaolinite.[9] Okada *et al*. synthesised TiO_2/mesoporous silica composites using the surfactant properties of CTAB as a structure directing agent under alkaline hydrothermal conditions,[150] and it is commonly used in a similar role in the hydrothermal synthesis of zeolites.[185] All these applications involve the formation or modification of a crystalline structure, but to our knowledge, CTAB has never previously been used to modify an X-tray amorphous material such as an aluminosilicate geopolymer which does not possess a layer structure, but contains pores which might be modified by yje inclusion of a large quaternary ammonium cation. The work presented in this chapter exploits the ion-exchange properties of geopolymers by replacing the monovalent charge-compensating ion by the much larger CTAB, thereby expanding the pore structure and facilitating the entry of the photoactive Cu_2O deeper into the structure. It was also hoped that the presence of the CTAB might modify the pore surfaces of the geopolymer and thus the mechanism by which the photoactive oxide is attached to the geopolymer matrix, resulting in

a geopolymer matrix of stable pH which would act as a pH buffer, allowing the two dye removal processes to be separately measured.

Immobilization of oxide nanoparticles on the inner and outer surfaces of these inorganic materials has been shown in previous chapters to produce efficient photocatalysts. Nano composite matrices adsorb organic substances either on their external surfaces or within their internal spaces *via* interactions or exchange.[193] Reports in the literature show that small amounts of surfactant such as CTAB can expand the layers of a clay mineral and control their separation, producing hydrophobic photocatalyst composites.[184, 194] Such a modified nano Cu_2O-geopolymer-composite is expected to show better photocatalyst properties than the unmodified Cu_2O-geopolymer composites developed in chapters 4 and 5, due to the improved dispersion of the metal oxide nanoparticles at external and interlayers of the geopolymer matrix.

The CTAB-expanded geopolymer matrices were synthesised as described in Chapter 3, and the structure and properties of the resulting composites of Cu_2O with the modified matrix were determined as described in chapters 4 and 5.

6 Result and Discussion

6.1 Elemental Analysis

The major element analyses by XRF (Table 6.1) show similar matrix compositions of the CTAB-modified geopolymer and, for comparison, a unmodified Na-geopolymer, apart from the Br content of the modified geopolymer; this decreases to almost zero upon formation of the oxide composite, indicating the effectiveness of the washing procedure followed in this part of the synthesis. Composite formation is also accompanied by a reduction in the Na content, again a result of the washing step. The Cu and Ti contents show the expected increase with increasing Cu_2O/TiO_2 contents of the composites.

Table 6.1. XRF analysis (wt%) of major elements of geopolymer samples with different compositions

	GP	M-GP	M-GP-10 wt% Cu_2O	M-GP-15 wt% Cu_2O
Na_2O	15.2	16.8	12.0	10.8
Al_2O_3	23.7	23.0	20.5	18.8
SiO_2	46.2	44.8	40.8	37.8
TiO_2	0.043	0.048	0.050	0.047
Fe_2O_3	0.193	0.194	0.183	0.169
Cu_2O	0.005	-	6.24	8.01
Br	-	0.342	0.006	0.005
ZrO_2	0.007	0.005	0.007	0.005
LOI	14.46	14.68	20.14	24.25
SiO_2/Al_2O_3	1.95	1.95	1.98	2.01

6.2 XRD Analysis

The XRD patterns of the starting Cu_2O, CTAB-modified geopolymer and corresponding Cu_2O composites (Figure 6.1) show that the modified geopolymer matrix is typically X-ray amorphous and similar to the unmodified matrix (chapters 4 and 5). The Cu_2O reflections and the absence of peaks of CuO or Cu confirm the successful synthesis of the Cu_2O.
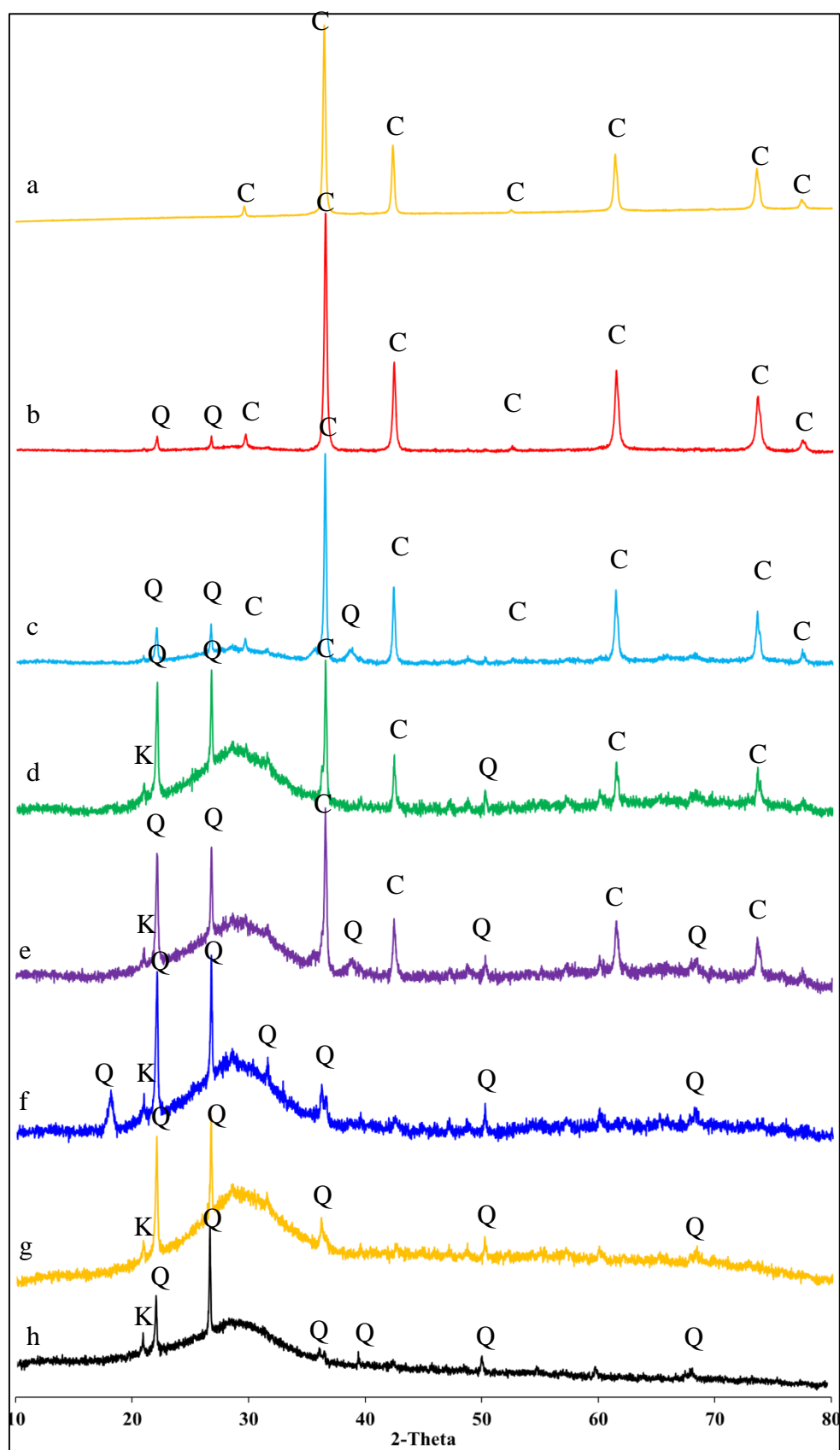
Figure 6.1. XRD patterns of (a) Cu_2O, (b) M-GP-50 wt% Cu_2O, (c) M-GP-30 wt% Cu_2O, (d) M-GP-15 wt% Cu_2O, (e) M-GP-10 wt% Cu_2O, (f) M-GP-5 wt% Cu_2O, (g) M-GP, (h) GP. Q = quartz, K = cristobalite, C = cuprous oxide.

6.3 Scanning electron microscopy

Figure 6.2a shows a BSE image of the CTAB-modified geopolymer. EDS mapping and point analysis (Figure 6.2 b-c) confirm the presence of sodium (Na), silicon (Si), aluminum (Al) without any other impurities.
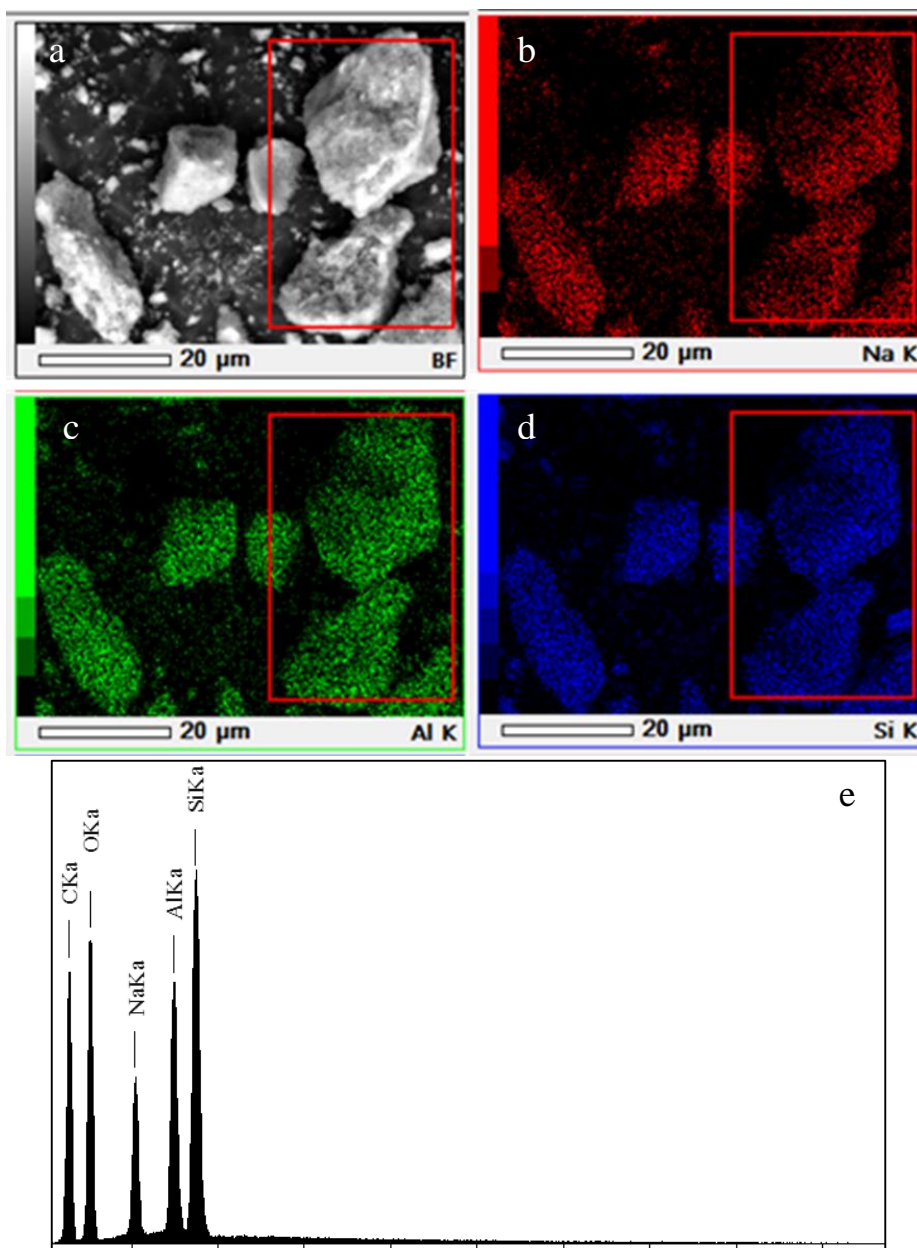
Figure 6.2. (a) Backscattered SEM image of M-GP and elemental maps of (b) Na, (c) Al, (d) si, (e) EDS element spectrum. Red rectangular areas in the elemental maps correspond to the EDS spectrum (e)
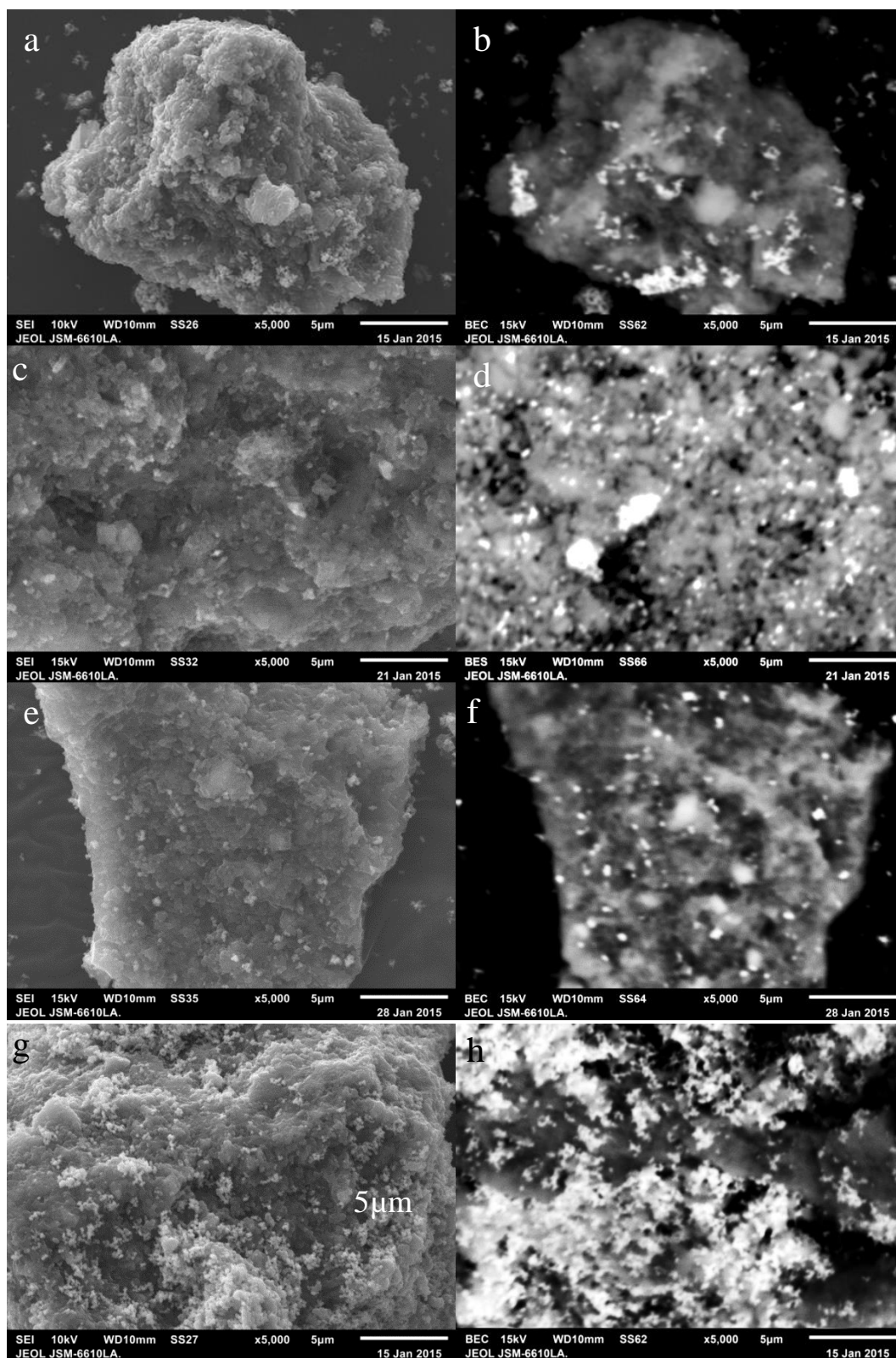
Figure 6.3. (a,b) M-GP-5 wt% Cu_2O composite, (c,d) M-GP-10 wt% Cu_2O composite, (e,f) M-GP-15 wt% Cu_2O composite, (g,h) M-GP-50 wt% Cu_2O composite. Micrographs b,d,f,h are BSE images, micrographs a,c,e,g are SE images.

Figure 6.3 is a series of SE and BSE micrographs of CTAB-GP with 5, 10, 15, 50 wt % Cu_2O. The left hand micrographs are SE micrographs and the right hand micrographs are the corresponding BSE micrographs. As Cu_2O has a higher average atomic number than the GP, the Cu_2O particles appear bright in comparison to the GP matrix.

Figure 6.4a is a BSE micrograph of the CTAB-GP- 50 wt% Cu_2O sample. Very bright regions are observed in the BSE image, suggesting Cu_2O phase aggregation. This is confirmed from the EDS mapping, where strong Cu-rich regions (Figure 6.4e) are seen. The Na, Al and Si elemental maps (Figure 6.4 (b-d)), show no strong phase segregation. From EDS elemental analysis no impurity phases are observed (Figure 6.4 f).
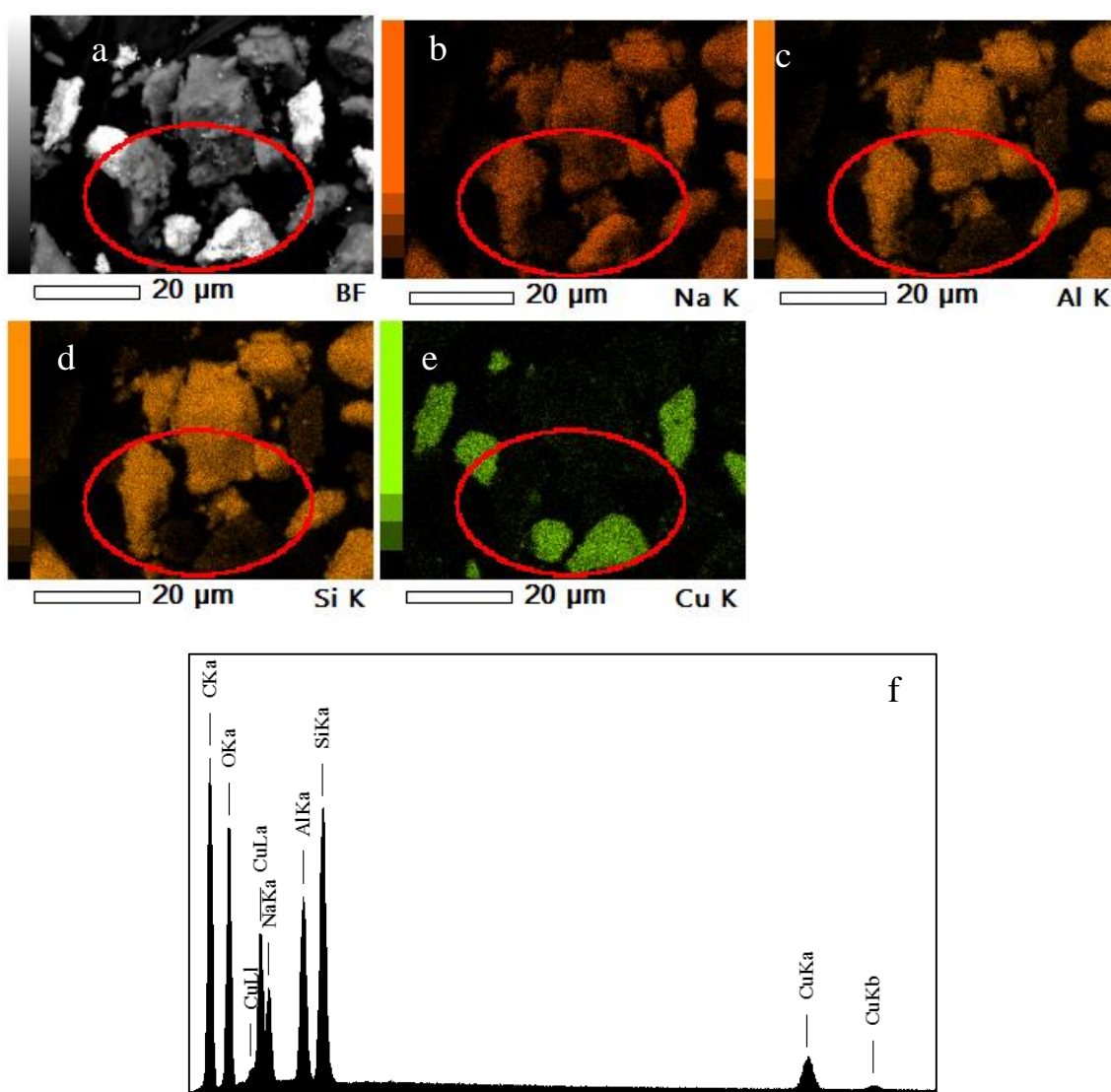
Figure 6.4. (a) Backscattered SEM image of ground M-GP-50% Cu_2O and elemental maps of (b) Na, (c) Al, (d) Si, (e) Cu, (f) EDS element spectrum of M-GP-50 wt% Cu_2O.

6.4 High-Resolution Transmission Electron Microscopy

The TEM image of the geopolymer-CTAB10%-Cu_2O composite (Figure 6.5a) shows the presence of dark nanocubes corresponding to Cu_2O nanoparticles. That the dark black dots represent the Cu_2O nanoparticles is confirmed by measurement of the lattice fringes in the HRTEM images (Figure 6.5).

Figure 6.5a is a low magnification TEM micrograph of the GP-CTAB10%-Cu_2O sample. The image is characterised by dark cubic regions in a lighter GP matrix. From HRTEM work these cubic regions are confirmed to be Cu_2O (Figure 6.5c and inset). The inset in Figure 6.5c is an inverse Fourier transform (IFFT) with a d-spacing of 0.24 nm which corresponds to the Cu_2O (111) plane. The Cu_2O are approximately 100 nm in size which agrees with the initial synthesis work described in Section 4.2. The smaller spherical grains observed in Figure 6.5b are Cu_2O.
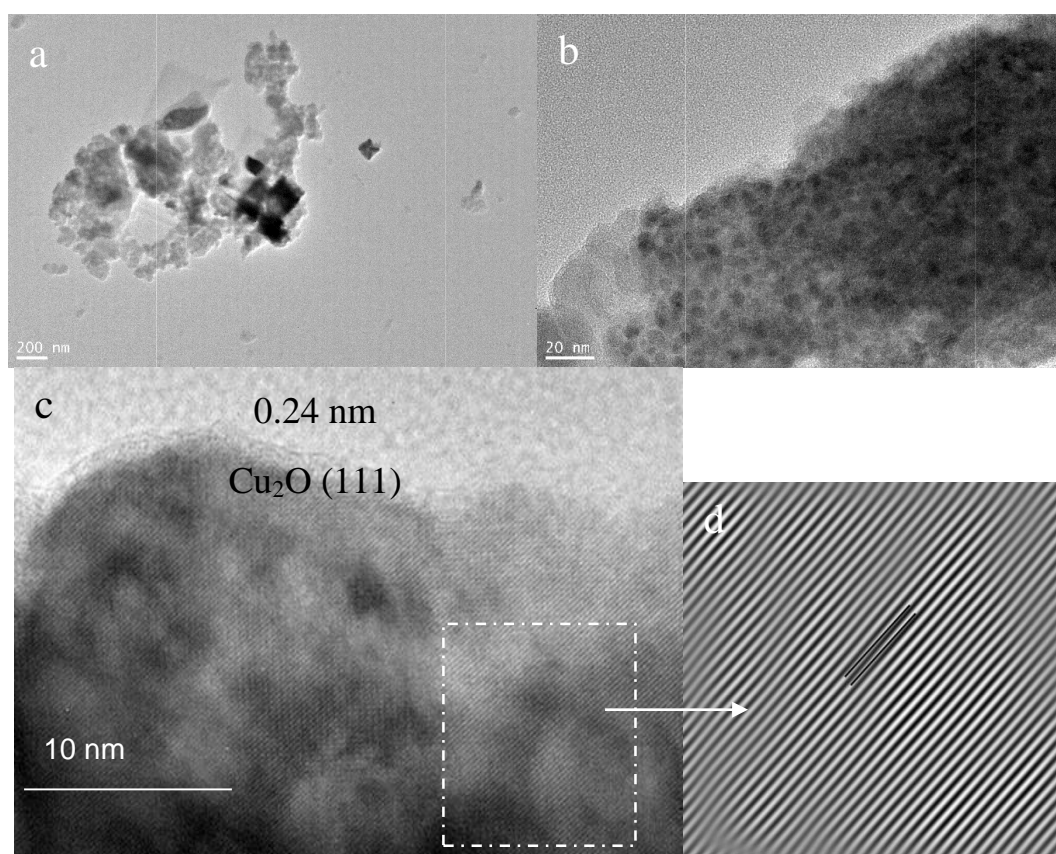
Figure 6.5. (a-c) TEM images of GP-CTAB10%-Cu_2O composite, (d) HTREM of selected area in (c).

The aligned lattice fringes of the Cu_2O nanoparticles are clearly illustrated in Figure 6.5. which shows adjacent fringe spacings of about 0.21 nm, measured by digital micrograph

software by calculating the average parameters between 10 lattice fringes. These lattice spacings are in agreement with the (cubic) structure of Cu_2O (JCPDS file 01-073-6237) and the HRTEM analysis thus provides a reliable confirmation of the XRD analysis.
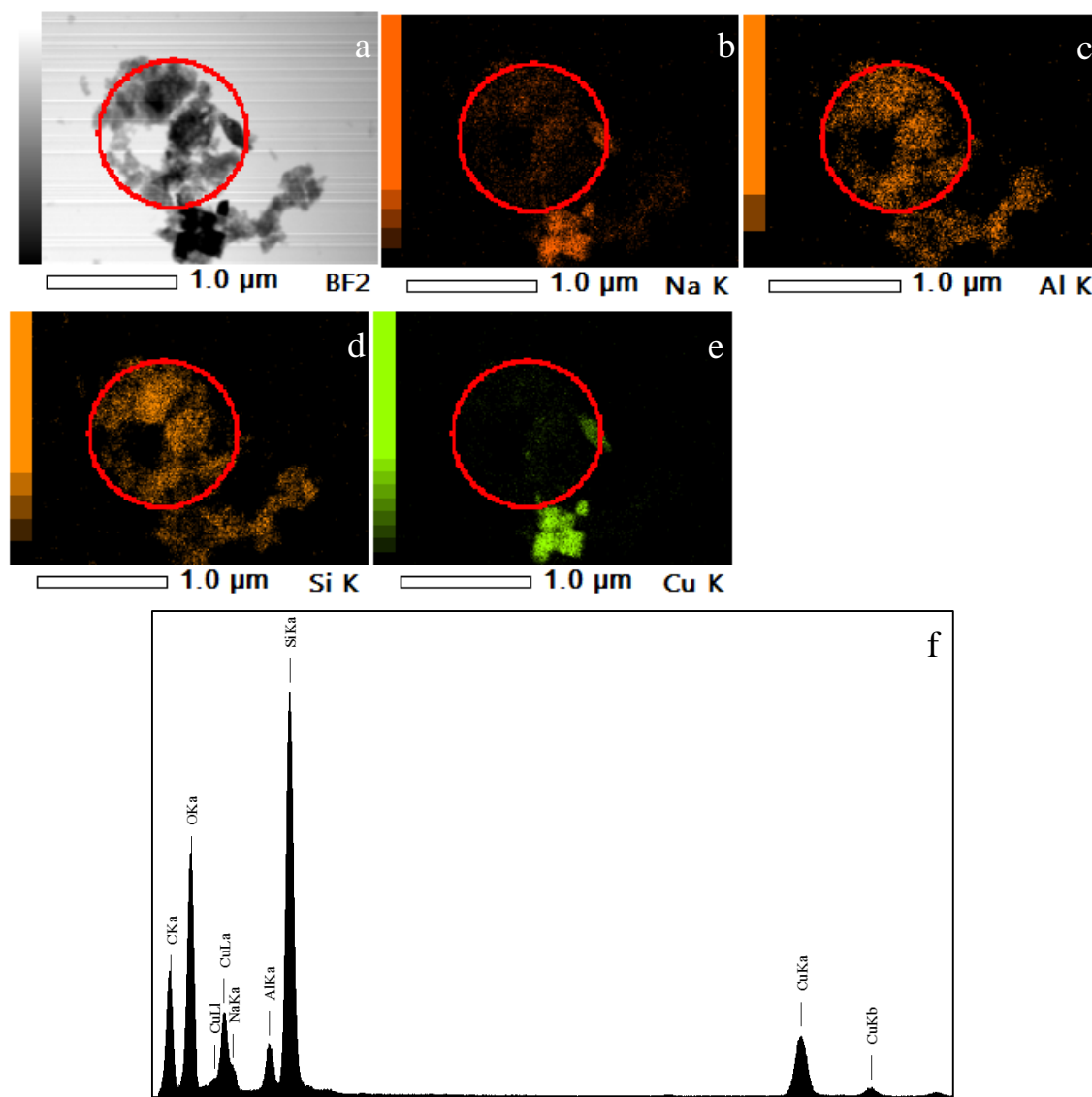
Figure 6.6. STEM and EDX elemental mapping images of M-GP-10 wt%-Cu_2O composite. Red circled areas in the elemental maps correspond to the EDS spectrum (f)

6.5 FTIR spectra of these samples

Figure 6.7 shows the FTIR spectra of unmodified geopolymer, CTAB-modified geopolymer and Cu_2O composites with CTAB-modified geopolymer (5-50 wt% Cu_2O). The band in the unmodified geopolymer at 1644 cm^{-1} is related to the H-O-H bending vibration of water molecules adsorbed on the geopolymer[10]. This vibration band is shifted to the higher number due to the presence of CTAB. The frequency shift trend indicates the hydrophobicity of the

resultant material by the surfactant loading.[10] However, all the FTIR frequencies of the composites decrease with increasing Cu_2O content, suggesting a reduction in the hydrophobicity of the Cu_2O composites by replacement of some surfactant. The adsorption band for the O-H stretching vibration of H-bonded water[10] appears in all the samples. This band occurs at 3439 cm^{-1} in the unmodified geopolymer and is shifted to higher frequencies for the composites containing CTAB and Cu_2O. The presence of the surfactant causes a decrease in the hydrogen bonding strength of the composite.[10]

Table 6.2. Positions and assignments of the IR vibration bands observed in the range of 400-4000 cm^{-1}

Unmodified GP	GP-CTAB	GP-CTAB-5%Cu_2O	GP-CTAB-10%Cu_2O	GP-CTAB-15%Cu_2O	GP-CTAB-50%Cu_2O	Cu_2O	CTAB
3834		3772	3774		3778	3560	
3439	3444	3479	3466	3464	3448	3433	
3015							3016
2967	2964	2966	2968	2968	2968		
	2929						2919
1644	1652	1653	1651	1649	1649		2848
1384	1384	1460			1462		1475
1002	1003	1009	1007	1007	1007		962
	872	874	874	874			910
694	700	700	698	698	698		725
			617	621	627	627	
578	588	586					
						521	
						482	
437	440	434	442	444	444	422	

−OH: 3700–3600, −OH, HOH: 3600-2200, HOH: 1700-1600, Si–O–Si &Al–O–Si: 1200-950

The CTAB surfactant replaces the hydrated cations and causes a reduction of the H_2O content, so the H-bonding is strongly reduced, and the surface of the composite is changed from hydrophilic to hydrophobic[10]. Furthermore, the pore structure of the geopolymer may be altered, allowing nano oxides such as Cu_2O greater access to the cavities. The CTAB cation can be coordinated to the oxygen of the geopolymer from one side and the water molecules on the other side, decreasing the polarising ability and weakening the H-bonds in the isolated hydrated species,[10] so the O-H stretching band is shifted to higher wavenumbers.The vibration corresponding to the CH_2 stretching mode of the amine is located at 2918 and 2929

cm^{-1} in CTAB and the M-GP respectively. The presence of this band indicates the presence of CTAB at the surface or inside the geopolymer matrix. The –CH– stretching vibration disappears in the M-GP-Cu_2O composites, due to the interaction between the surfactant and Cu_2O.

The most significant peak which confirms the formation of the geopolymer is related to the Al-O and Si-O asymmetric stretching vibration[11] at about 1000 cm^{-1} is located in the matrix and all the composites. This band is shifted to higher numbers by the addition of Cu_2O to the modified geopolymer composite, evidencing a small change in the geopolymer structure. The vibration associated with the Cu-O stretch is situated at 627 cm^{-1} in the reference Cu_2O. This vibration appears at almost the same position in the composites containing 10, 15 and 50 wt% Cu_2O.
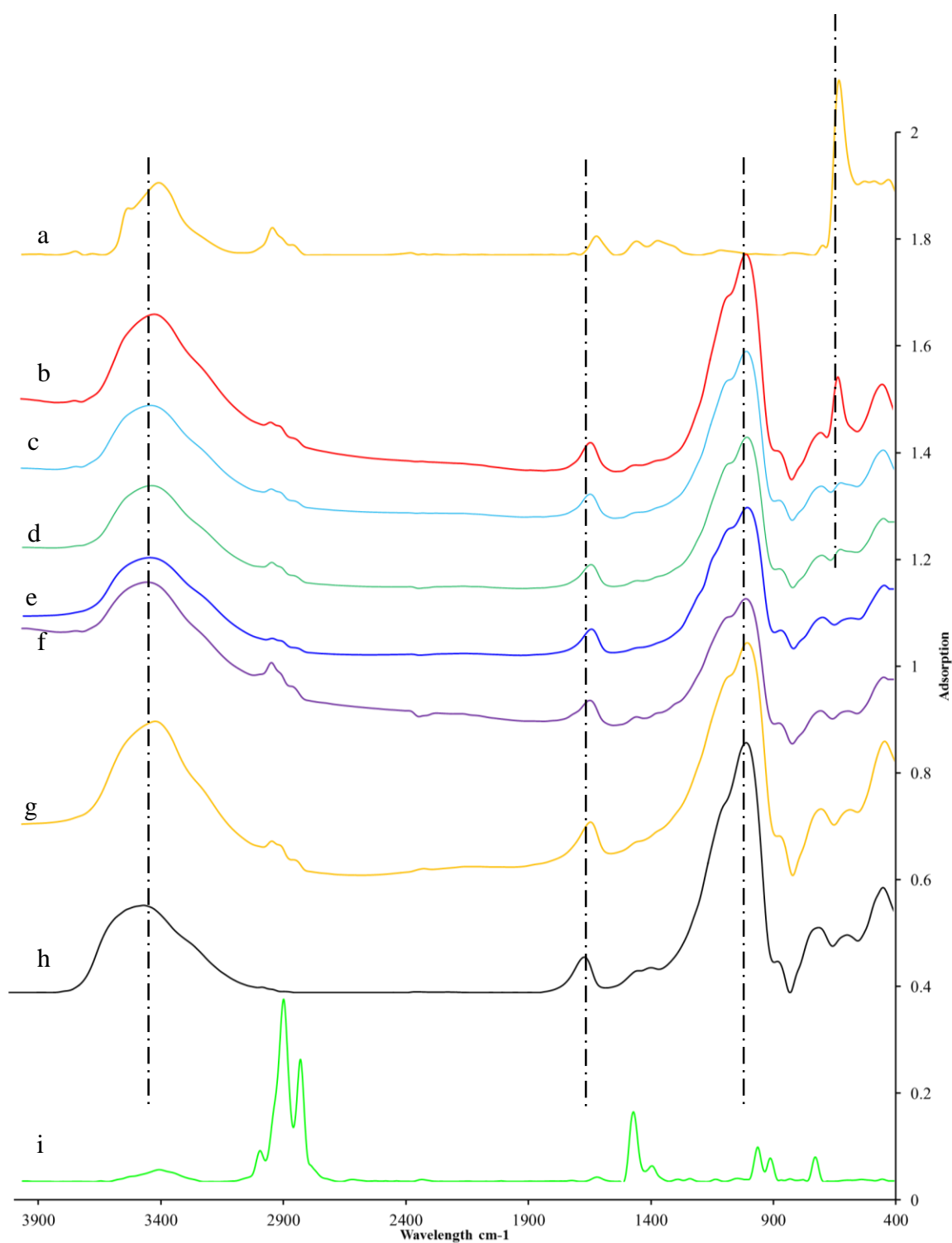
Figure 6.7. FTIR spectra of unmodified GP, M-GP, Cu_2O and Cu_2O supported by GP matrix with different loading contents; (a) Cu_2O, (b) M-GP-50 wt% Cu_2O, (c) M-GP-30 wt% Cu_2O, (d) M-GP-15 wt% Cu_2O, (e) M-GP-10 wt% Cu_2O, (f) M-GP-5 wt% Cu_2O, (g) M-GP, (h) GP, (i) CTAB .

6.6 ^{29}Si and ^{27}Al solid state MAS NMR

The ^{29}Si MAS NMR spectra of the geopolymer and geopolymer composites are shown in Figure 6.8. All the samples contain a principal resonance at about -87 ppm, confirming the considerable saturation of the framework structure in Al, but this peak is broadened due to the presence of several slightly different Si-O-Al environments.[121] This peak remains essentially unchanged after adding different percentages of Cu$_2$O nanoparticles. As was found for the Cu$_2$O composites in a unmodified geopolymer matrix (chapter 4), the general characteristics of these ^{29}Si MAS NMR spectra are similar, as are the ^{27}Al MAS NMR spectra of the CTAB-modified geopolymer composites (Figure 6.9). The ^{27}Al MAS NMR spectrum of the unmodified geopolymer matrix is noticeably narrower than those of the CTAB-modified matrix and corresponding composites; this probably reflects a progressive disruption of the structure by the insertion of the CTAB.
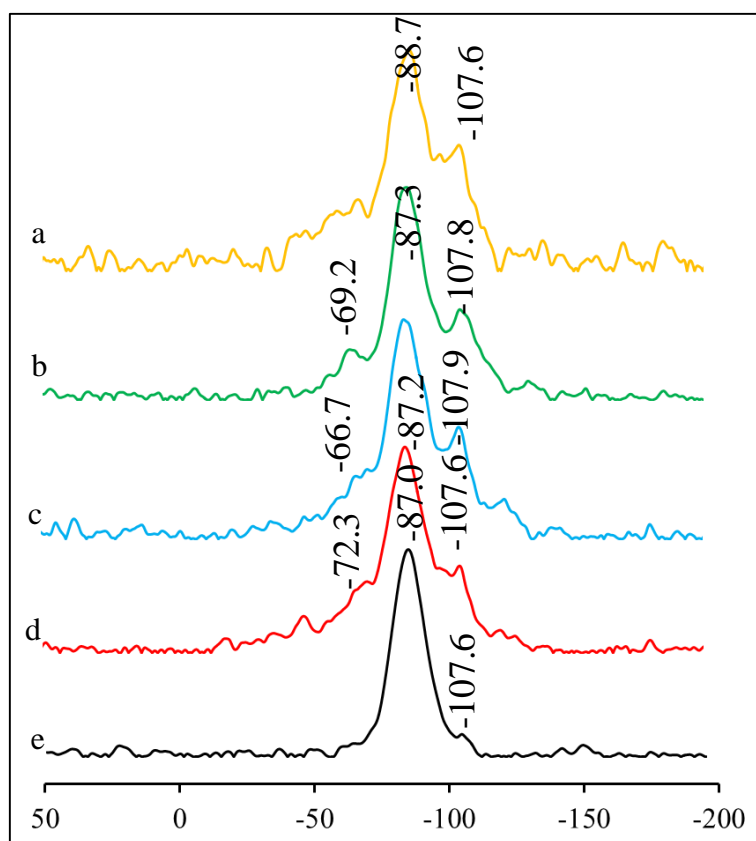
Figure 6.8. 11.7 T ^{29}Si MAS NMR spectra (a) GP, (b) M-GP, (c) M-GP-10 wt% Cu$_2$O, (d) M-GP-30 wt% Cu$_2$O, (e) M-GP-50 wt% Cu$_2$O

Thus, these spectra confirm the successful formation of aluminosilicate geopolymer composites in the presence of the CTAB surfactant.
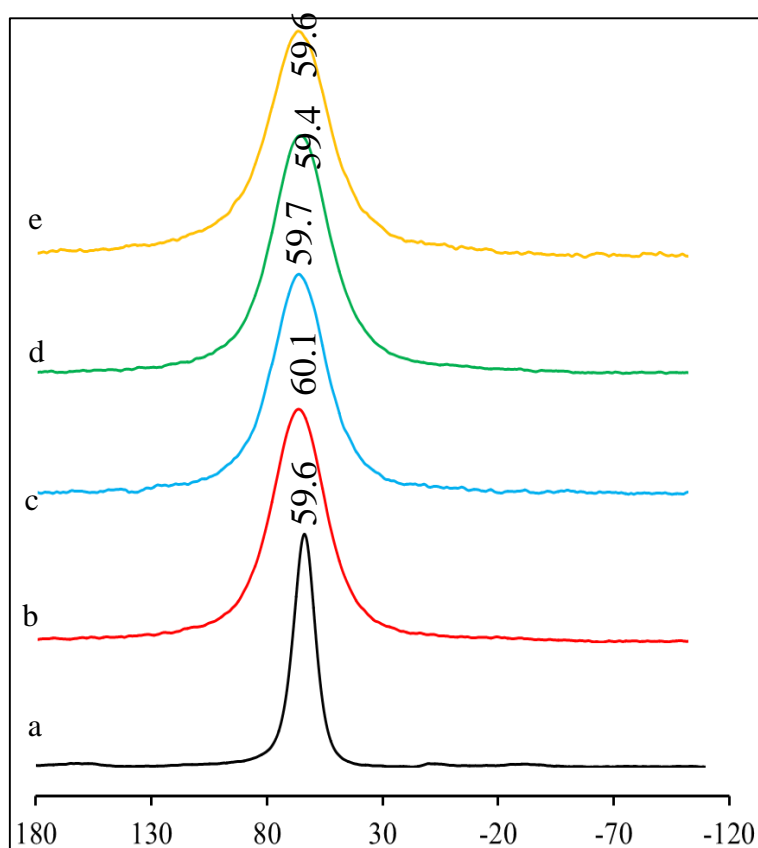
Figure 6.9. 11.7 T ^{27}Al MAS NMR spectra (a) GP, (b) M-GP, (c) M-GP-10 wt% Cu_2O, (d) M-GP-30 wt% Cu_2O, (e) M-GP-50 wt% Cu_2O.

6.7 Adsorption of MB

6.7.1 Reactions under dark conditions

As with the composites formed with the unmodified geopolymer matrix discussed in chapter 4, a corresponding set of experiments was conducted on the composites formed with the CTAB-modified geopolymer matrix. The CTAB-modified composites are expected to decolorize the MB dye by a combination of adsorption on the geopolymer matrix (in the dark), and by photodegradation (under UV irradiation). For this reason, the adsorption characteristics of these composites were first investigated in the dark. Figure 6.10 shows the change in the relative concentration (C/C_0) of MB dye solution with time in the dark for the CTAB-modified geopolymer matrix and the corresponding composites with 5, 10, 15 and 50 wt% Cu_2O. By contrast with the experiments using the unmodified geopolymer matrix which

did not reach equilibrium, but adsorbed the dye continuously (Chapter 4), the CTAB-matrix samples reached equilibrium after 12 hour. The most rapid decrease in MB colour and greatest degree of adsorption reached at equilibrium was observed in the composites containing 5-10 wt% Cu_2O. The slower adsorption rates and lower degree of adsorption at equilibrium in the samples containing higher concentrations of Cu_2O may be due to blocking of the active adsorption sites by the presence of the additional oxide and is particularly noticeable in the sample containing 50 wt% Cu_2O.
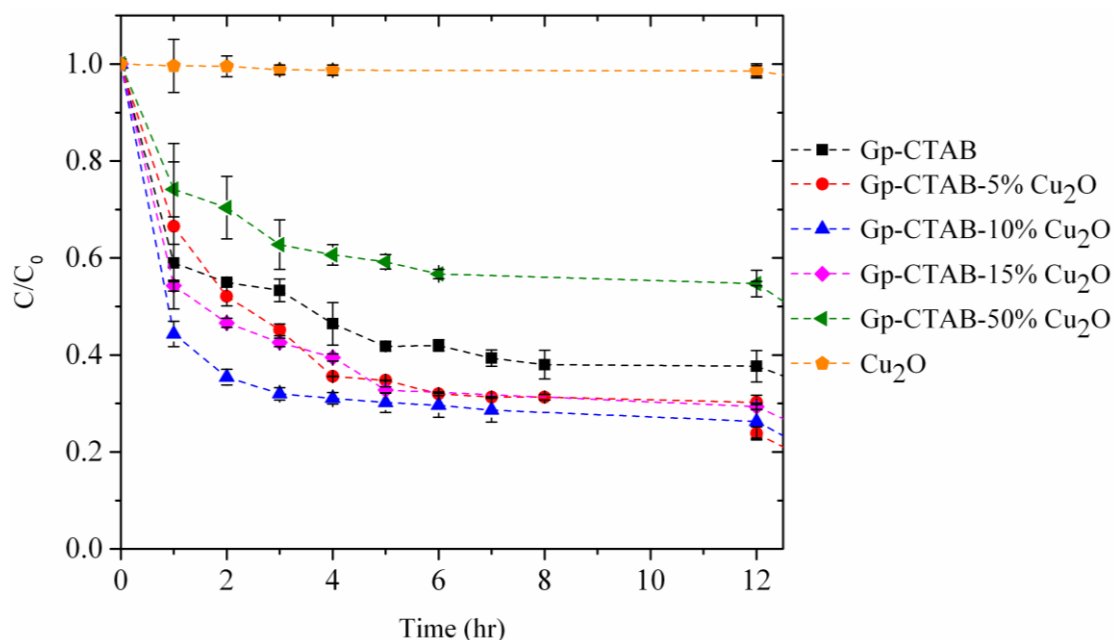
Figure 6.10. Plots of the residual concentration (C/C_0) *vs.* time (t) onto the GP matrix, M-GP 5, 10, 15 and 50 wt% Cu_2O (monitored at 664 nm in dark)

As with the composites of unmodified geopolymer, the adsorption data were fitted to both pseudo-first order and pseudo-second order kinetic equations,[181, 182] but the fits to the pseudo-first-order model were poorer, as suggested by comparison of the experimental values q_{exp} with the q_e values and the correlation coefficients R^2 (Table 6.3). In addition, the correlation coefficients for the second order kinetic model are >0.99 (Table 6.3) confirming the superior fit to the second order kinetic model. (see Figure 6.11.)

The difference between the adsorption kinetic model followed by the composites based on the unmodified geopolymer matrix (pseudo first-order) and the present CTAB-modified matrix is interesting, and arises from differences in the matrix itself. This is not unexpected; the kinetic order of adsorption is known to depend on the nature of the matrix since in the case of dye adsorption on a fly ash geopolymer matrix, second order kinetics were followed, reflecting the presence of impurities in the fly ash.[195]
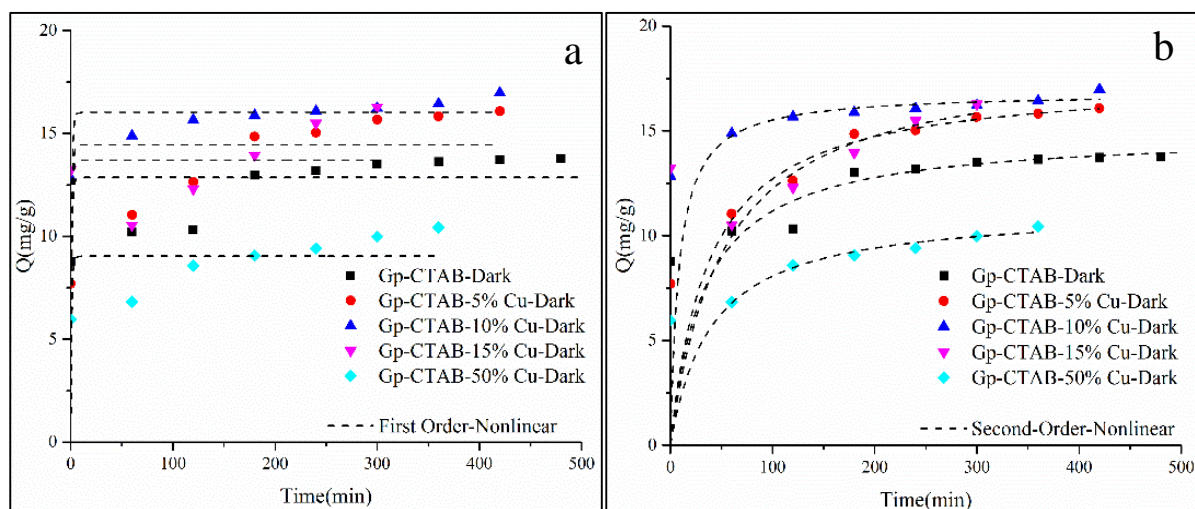
Figure 6.11. (a) Pseudo first-order kinetics, (b) Pseudo second-order kinetics by the nonlinear method and experimental kinetics for the adsorption of MB onto M-GP and GP composites.

Table 6.3. Parameters for kinetic models of MB adsorption on CTAB-based samples

Sample	Kinetic model	q_{exp} (mg/g)	q_e (mg/g)	k	R^2
M-GP	1st-order	14.40	12.86	240.78	0.97
"	2nd-order	"	14.91	0.52	0.97
M-GP-5 wt%Cu$_2$O	1st-order	16.08	14.45	163.43	0.92
" "	2nd-order	"	17.50	99.56	0.99
M-GP-10 wt%Cu$_2$O	1st-order	16.98	16.02	704.05	0.99
" "	2nd-order	"	16.84	3.39	0.92
M-GP-15 wt%Cu$_2$O	1st-order	16.28	13.71	984.54	0.96
" "	2nd-order	"	18.59	80.49	0.97
M-GP-50 wt%Cu$_2$O	1st-order	10.43	9.049	337.56	0.95
" "	2nd-order	"	11.28	1.38	0.99

6.7.2 MB dye adsorption isotherms under dark conditions

As for the previous composites (chapter 4) the equilibrium adsorption data were fitted to the three isotherms (Langmuir, Freundlich and Langmuir-Freundlich, eqs. 31-33)[17, 178] The results of the three models are displayed in Figure 6.12. The adsorption of MB dye in the dark on the CTAB-modified geopolymer matrix is well fitted by both the Langmuir and Freundlich models, with a high R^2 value (0.99). The CTAB-modified geopolymer composites containing 5, 10 and 50 wt% Cu_2O are fitted by the Langmuir-Freundlich model which gives the highest R^2 values (1.0, 0.99 and 0.99 respectively) but the 15%-Cu_2O-CTAB-modified geopolymer is better fitted to the Freundlich model ($R^2 = 0.97$). The similarity of all these fits as reflected by their R^2 values militates against distinguishing any one isotherm as being the most appropriate to describe the MB adsorption on these composite, but visual inspection of the plots of the isotherm data (Figure 6.12) suggests that the Langmuir-Freundlich may be the more appropriate description for all samples.
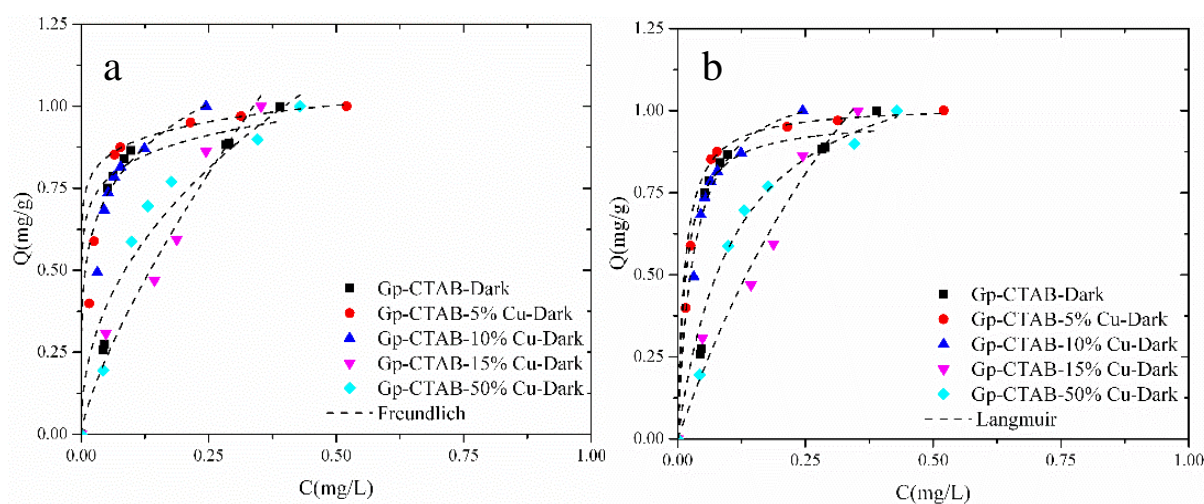
Figure 6.12. (a,b) adsorption isotherms for MB adsorption and the corresponding Freundlich and Langmuir models fit (dashed lines).
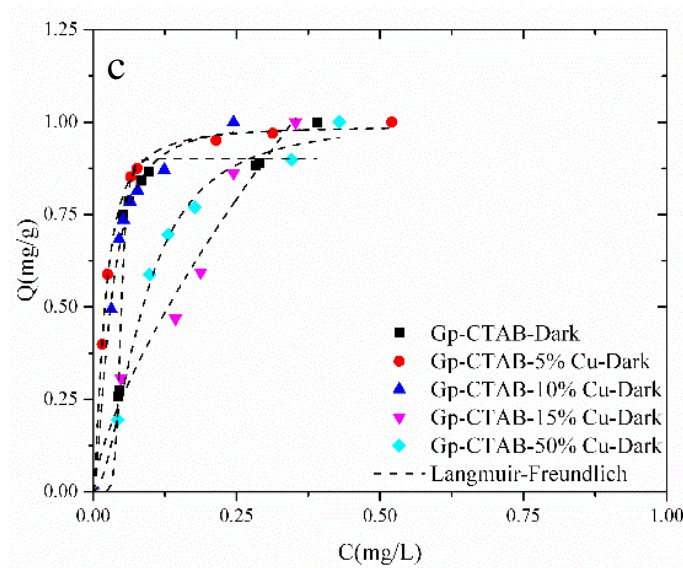
Figure 6.12. (Continued) (c) adsorption isotherms for MB adsorption and the corresponding Langmuir-Freundlich models fit (dashed lines).

6.7.3 Reactions under UV radiation

By contrast with the behaviour of composites based on the unmodified geopolymer matrix (Chapter 4) in which adsorption occurred continuously and never reached equilibrium, the composites based on CTAB-modified geopolymer matrices reached equilibrium under dark conditions, as demonstrated in section 6.7.1. This property of the matrix results from modification of the pore surfaces by the CTAB, producing a stable pH matrix which may act as a pH buffer and allow the two dye removal processes to be separated. The degradation of MB by the photocatalyst composites at room temperature was therefore determined in a separate set of experiments in which the fresh catalyst/dye solution was allowed to equilibrate in the dark for 12 hour to determine the amount of MB adsorbed onto the composites before photodegradation. After equilibration, the system was subjected to UV irradiation and the further change in MB concentration resulting from the photodegradation step was monitored by removing aliquots, centrifuging and measuring their absorbance. Each experiment was repeated a minimum of three times.

Figure 6.13 shows the results of MB degradation by these samples under both dark and UV conditions as a function of time. Under dark conditions, none of the metal oxide samples removes MB from solution, indicating that the nano structure and surface properties of these oxides is not effective in absorbing the dye.

Incorporation of 10 and 15 wt% Cu_2O nanoparticles into the CTAB-modified geopolymer produced much better photocatalytic activity than other samples, suggesting that the CTAB is

acting to open the geopolymer matrix structure, facilitating access of the dye to the internal adsorption sites. In addition, by being able to separate the two processes of adsorption and photodegradation, these results confirm the Cu_2O-geopolymer nano composites have significantly improved photocatalytic activity under UV irradiation compared with the Cu_2O nanoparticles alone.
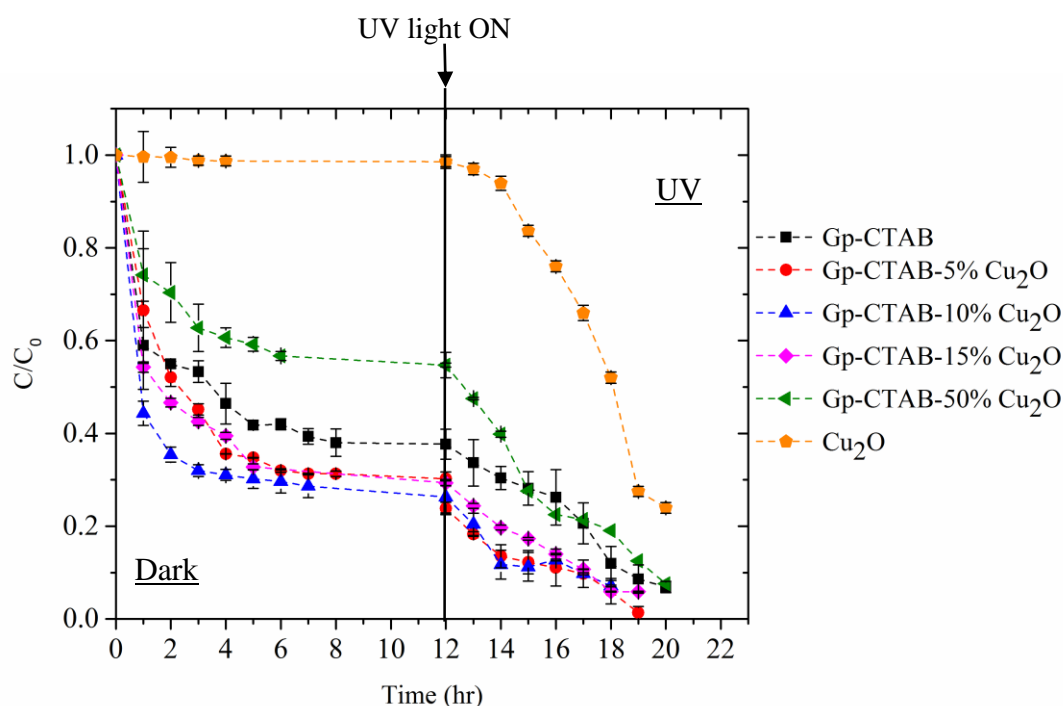
Figure 6.13. Plots of the residual concentration (C/C_0) *vs*. time (t) onto the M-GP, Cu_2O and M-GP-5, 10, 15, 50 wt% Cu_2O (monitored at 664 nm) under different conditions.

Figure 6.14 compares the removal of MB by the CTAB-modified geopolymer, the CTAB-modified geopolymer composite containing different amounts of Cu_2O, and Cu_2O itself after 60 min. in the dark and under UV irradiation. This figure shows that the elimination of MB from aqueous solution under UV irradiation by the composites of the CTAB-modified geopolymer with Cu_2O is more effective than by Cu_2O alone. It can be seen that only about 10% MB is removed in the dark by Cu_2O alone while in the geopolymer composites more than half the MB is removed by adsorption on the geopolymer. The adsorption process is more efficient in the composites containing lower Cu_2O contents (5-10 wt%) and decreases with increasing Cu_2O content. The highest degree of MB removal by both the adsorption and photodegradation processes occurs in the CTAB-modified geopolymer containing 10% Cu_2O. The poorer performance of the compounds containing higher Cu2O contents is probably due

to the blocking of the active sites for adsorption and photodegradation by the oxide nanoparticles.
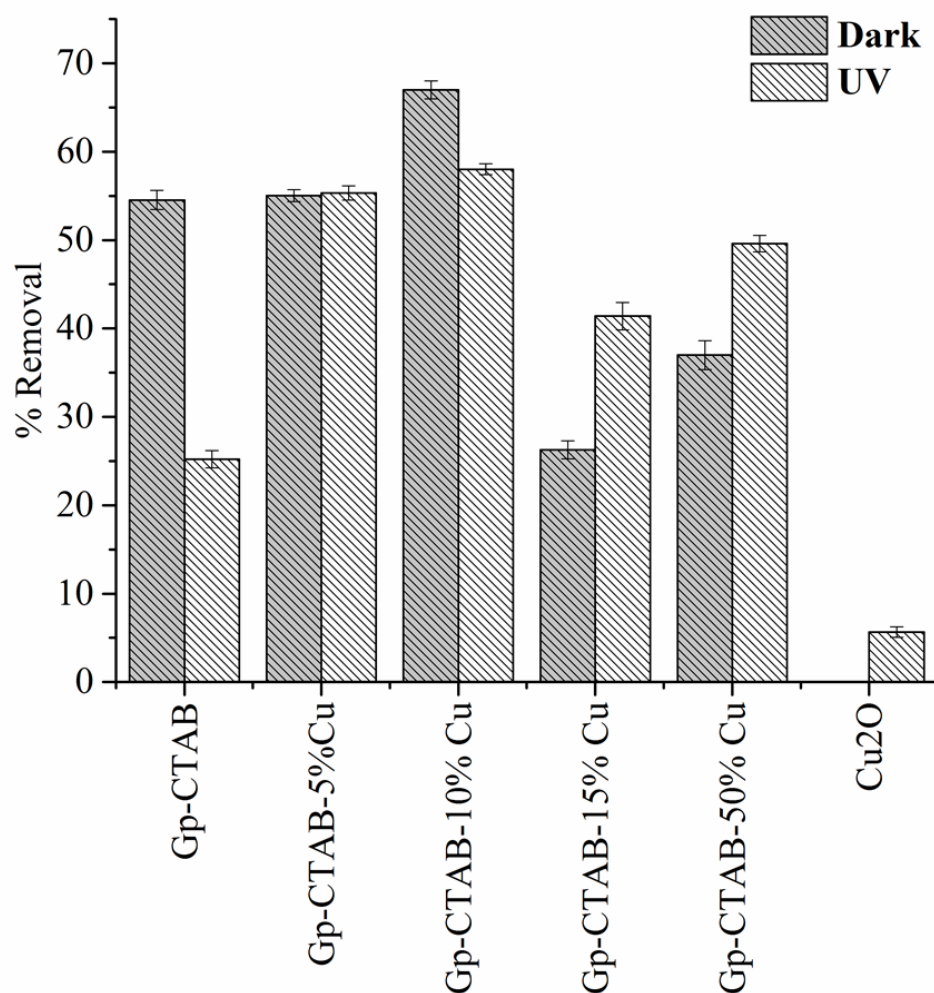
Figure 6.14. MB removal by the M-GP matrix, M-GP composites containing 5, 10, 15 and 50 wt% Cu_2O and Cu_2O alone after 60 min.

6.7.4 Nitrogen Adsorption/Desorption Isotherms

Possible explanations for the improved behaviour of the CTAB-modified geopolymer matrix were sought by making measurements of the surface area and porosity of the unmodified and CTAB-modified geopolymers and their Cu_2O-containing composites by determining their N_2 adsorption-desorption isotherms (Table 6.5).

The specific surface areas derived from these adsorption/desorption isotherms (Figure 6.15) indicate that these are relatively similar in the unmodified and CTAB-modified geopolymer matrices, whereas the inclusion of CTAB results in a decrease in the pore volume and pore size (Table 6.5). Incorporation of 10 and 15 wt% Cu_2O results in an increase in the BET surface area from 17.02 m²/g in the CTAB-modified geopolymer matrix to 27.27 m²/g and 23.73 m²/g in the composites containing 10 and 15 wt% Cu_2O respectively. Similar trends are seen in the Langmuir surface areas and the cumulative surface areas of the pores calculated by the BJH method (Table 6.5). This is accompanied by a corresponding decrease in the pore size from 43.09 nm in the CTAB-modified geopolymer matrix to 31.56 nm in the composite containing 10 wt% Cu_2O, remaining approximately constant at 32.67 nm in the composite containing 15 wt% Cu_2O. Thus, the superior performance of the composite containing 10 wt% Cu_2O under both dark and UV conditions, appears to be due to the improved ability ability of the oxide to enter the matrix pore structure, without causing too much constriction of the pore volume, as occurs at higher oxide concentrations.
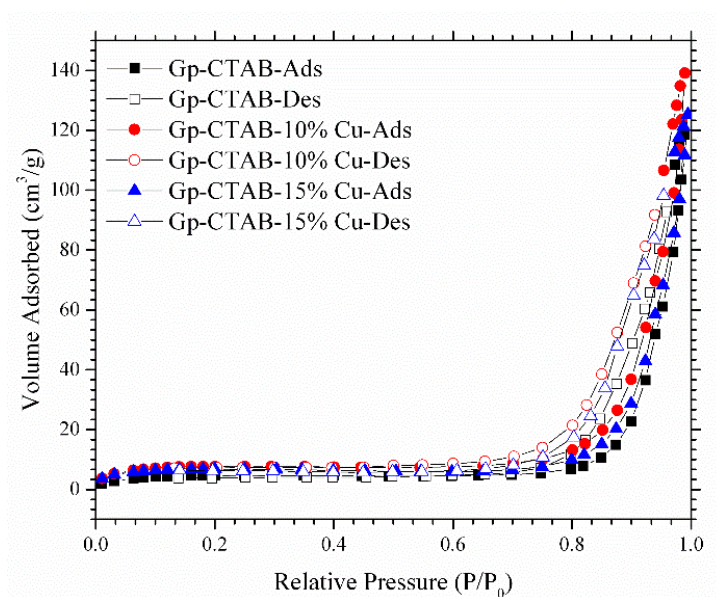
Figure 6.15. Nitrogen sorption isotherms of the M-GP (■, adsorption □, desorption), M-GP-10 wt% Cu_2O (●, adsorption ○, desorption) and M-GP-15 wt% Cu_2O (▲, adsorption △, desorption)

Table 6.4. Specific surface areas and pore parameters of geopolymer and geopolymer composites

	GP	M-GP	M-GP-10 wt%-Cu$_2$O	M-GP-15 wt%-Cu$_2$O
Single Point Surface Area	18.44 m²/g	16.14 m²/g	26.59 m²/g	23.52 m²/g
S $_{BET}$	17.23 m²/g	17.025 m²/g	27.27 m²/g	23.73 m²/g
S $_{Langmuir}$	21.92 m²/g	23.44 m²/g	37.07 m²/g	31.95 m²/g
S $_{BJH Adsorption Cumulative}$	23.06 m²/g	21.41 m²/g	28.72 m²/g	23.96 m²/g
S $_{BJH Desorption Cumulative}$	38.94 m²/g	33.63 m²/g	43.60 m²/g	39.70 m²/g
Volume				
Single Point Adsorption	0.24 cm³/g	0.18 cm³/g	0.22 cm³/g	0.19 cm³/g
V $_{pore BJH Adsorption Cumulative}$	0.24 cm³/g	0.18 cm³/g	0.22cm³/g	0.19 cm³/g
V $_{pore BJH Desorption Cumulative}$	0.24 cm³/g	0.18 cm³/g	0.22 cm³/g	0.19 cm³/g
Pore Size				
D $_{Adsorption}$	55 nm	43 nm	32 nm	33 nm
D $_{BJH Adsorption}$	41 nm	34 nm	30 nm	32 nm
D $_{BJH Desorption}$	24 nm	22 nm	20 nm	20 nm

Conclusions

This chapter confirms the successful preparation of a new geopolymer matrix with a pore structure expanded by the inclusion of the large quaternary ammonium ion CTAB. Composites of Cu$_2$O nanoparticles with this expanded matrix have an increased surface area facilitating the entry of Cu$_2$O nanoparticles into the internal pores of the geopolymer matrix. This phenomenon is also reflected by a decrease in the pore diameter after the addition of the nanoparticles. The uniform dispersion of the oxide nanoparticles in the composites was demonstrated by SEM/EDS and TEM. One major benefit of the use of this CTAB-modified matrix in MB dye removal experiments is its maintenance of a stable pH, enabling it to separate the two processes of adsorption and photodegradation in these composites. Unlike composites of unmodified geopolymers, the adsorption of MB dye on composites with CTAB-modified geopolymer matrices in the dark follow pseudo second-order kinetics, but are similar to composites with unmodified matrices in being described by Freundlich-

Langmuir type isotherms. Incorporation of 10 wt% Cu_2O into the geopolymer composites removes the highest percentage of MB under UV irradiation, and this is achieved by a combination of adsorption and photodegradation.

Chapter 7

Composites of CTAB-modified geopolymer matrices containing Cu$_2$O /TiO$_2$ nano-heterostructures and P25 titania

Introduction

The previous chapter demonstrated the previously unexplored possibility of producing a geopolymer matrix in which the pore structure is modified by the insertion of the large quaternary ammonium cation CTAB. Composites of this matrix with Cu$_2$O nanoparticles were synthesised and their structures and photoactive properties were investigated. A particular advantage of composites based on this modified matrix was shown to be its ability to act as a pH buffer, allowing the dual processes of MB dye adsorption and photodegradation to be distinguished. This chapter brings together the advantage of this new matrix with the improved photoactivity obtained by combining Cu$_2$O with P25 TiO$_2$ into a Cu$_2$O/TiO$_2$ nano-heterostructure, as demonstrated in chapter 5. The spherical nanocrystalline Cu$_2$O/TiO$_2$ heterostructures were synthesized as described in chapter 3, section 3.3 and the structural characteristics of the resulting composites were determined as previously by XRD, FTIR, SEM/EDS and HRTEM. The photocatalytic properties of the composites in the degradation of MB were determined as in chapter 6 by bringing the adsorption step to equilibrium in the dark, then initiating the photodegradation step by exposing the samples to UV radiation. For comparison, a corresponding set of samples containing P25 titania alone were prepared and studied.

7 Results and Discussion

7.1 Elemental Analysis

The chemical composition of all samples obtained by X-ray fluorescence (Table 7.1), confirmed the incorporation of Cu and Ti in different amounts in each composite. The Na content was dramatically decreased due to exchange by Cu$^+$ and Ti^{4+} ions. The increase in the Ti/Si and Cu/Si ratio confirmed the increase in the oxide elements and the presence of Cu-Ti oxides within the geopolymer matrix. The percentage of bromide decreased after addition of the nano oxide particles and confirmed the removal of bromide ions in the washing step accompanying the insertion of the metal oxide nanoparticles.

Table 7.1. XRF analysis (wt %) of the major elements in the geopolymer samples of different composition

	Halloysite clay	GP unmodified	M-GP	M-GP-10 wt% Cu/Ti	M-GP-15 wt% Cu/Ti
Na_2O	0.04	15.2	16.8	11.6	10.2
Al_2O_3	35.5	23.7	23.0	22.0	20.0
SiO_2	49.5	46.2	44.8	42.5	38.8
TiO_2	0.09	0.043	0.048	3.97	5.45
Fe_2O_3	0.29	0.193	0.194	0.194	0.192
Cu_2O	-	0.005	-	2.52	3.69
Br	-	-	0.342	0.014	0.007
ZrO_2		0.007	0.005	0.008	0.007
LOI	13.8	14.46	14.68	17.05	21.5
SiO_2/Al_2O_3	1.39	1.95	1.95	1.93	1.93
TiO_2SiO_2	-	-	-	0.09	0.14
Cu_2O/SiO_2	-	-	-	0.06	0.09

7.2 XRD Analysis

Figure 7.1 shows the XRD patterns of the CTAB-modified geopolymer composites with different Cu_2O/TiO_2 contents. As found for the CTAB-modified geopolymer containing Cu_2O (chapter 6), the XRD traces of the composites show that the modified geopolymer matrix is typically X-ray amorphous and similar to the unmodified matrix (chapters 4 and 5). The characteristic diffraction peaks for anatase at $2\theta = 25.29$, (111), Cu_2O at $2\theta = 36.50$ and the (310) reflection of rutile at $2\theta = 64.00$ are present in the XRD patterns of the composites containing the Cu_2O/TiO_2. However for the M-GP-Cu_2O/TiO_2 composites containing 5 and 10 wt% Cu_2O/TiO_2, there is insufficient nano-heterostructure present for these reflections to be observed by XRD.
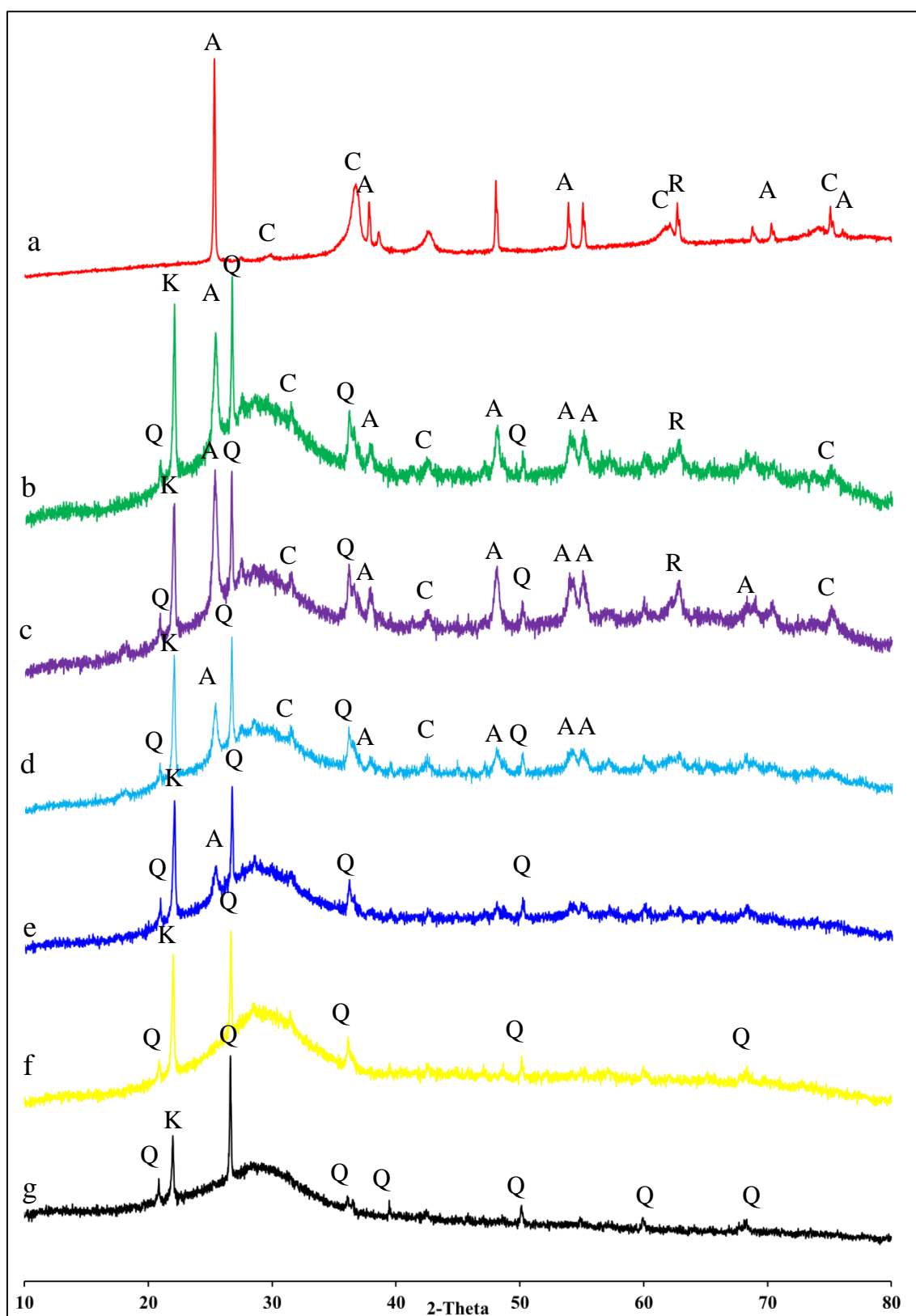
Figure 7.1. XRD patterns of M-GP, Cu_2O/TiO_2 and Cu_2O/TiO_2 supported by M-GP matrix with different loading contents; (a) Cu_2O/TiO_2, (b) M-GP-50 wt% Cu_2O/TiO_2, (c) M-GP-15 wt% Cu_2O/TiO_2, (d) M-GP-10 wt% Cu_2O/TiO_2 (e) M-GP-5 wt% Cu_2O/TiO_2, (f) M-GP, (g) GP. Q = quartz, K = cristobalite, C = cuprous oxide, A = anatase, R = rutile.

7.3 Scanning electron microscopy

Figure 7.2a is a BSE micrograph showing bright regions on a light grey background in sample M-GP-10 wt% Cu_2O/TiO_2. The lighter regions are from the higher atomic number TiO_2 and Cu_2O, which is confirmed by EDS elemental mapping (Figure 7.2e and f). The particles are homogenously dispersed on the GP surface with no obvious Cu or Ti aggregation. No additional impurities are found in the sample. As observed previously the Cu_2O grains (200 – 300 nm) are considerably larger than the TiO_2 grains (ca. 25 nm).
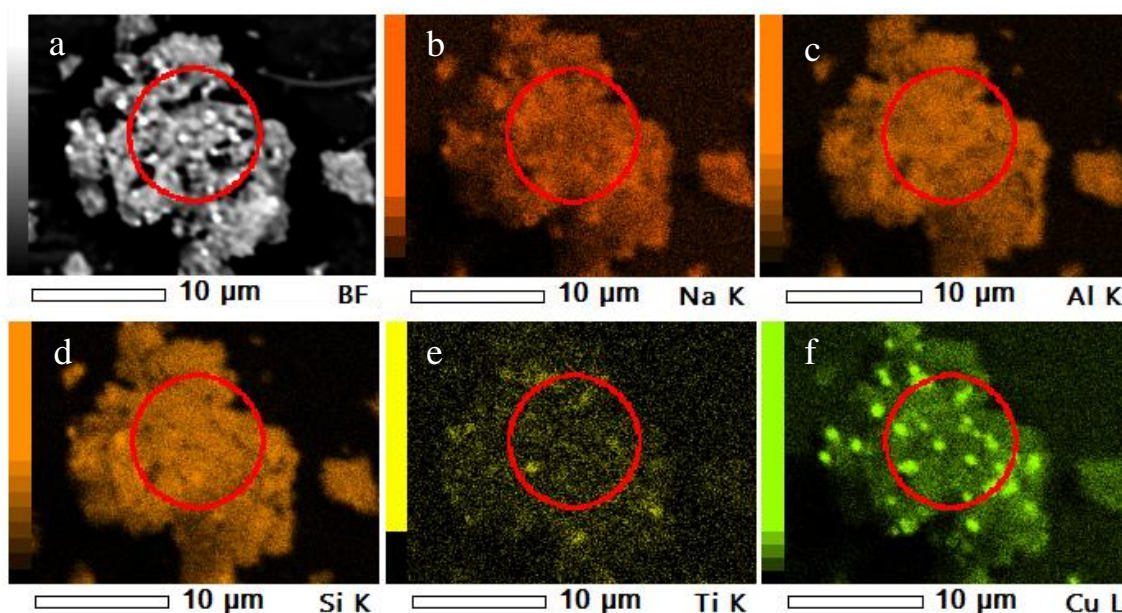
Figure 7.2. (a) BSE image of powdered M-GP-10 wt% Cu_2O/TiO_2, (b) Na, (c) Al, (d) Si, (e) Ti, (f) Cu.

Figure 7.3 is a series of SE and BSE micrographs of M-GP with 5, 10, 15, 50 wt % Cu_2O/TiO_2. The left hand micrographs are SE micrographs and the right hand micrographs are the corresponding BSE micrographs. As Cu_2O and TiO_2 have a higher average atomic number than the GP, these particles appear bright in comparison to the GP matrix. The surface morphology (Figure 7.3, SE micrographs) show a spongy-like structure.
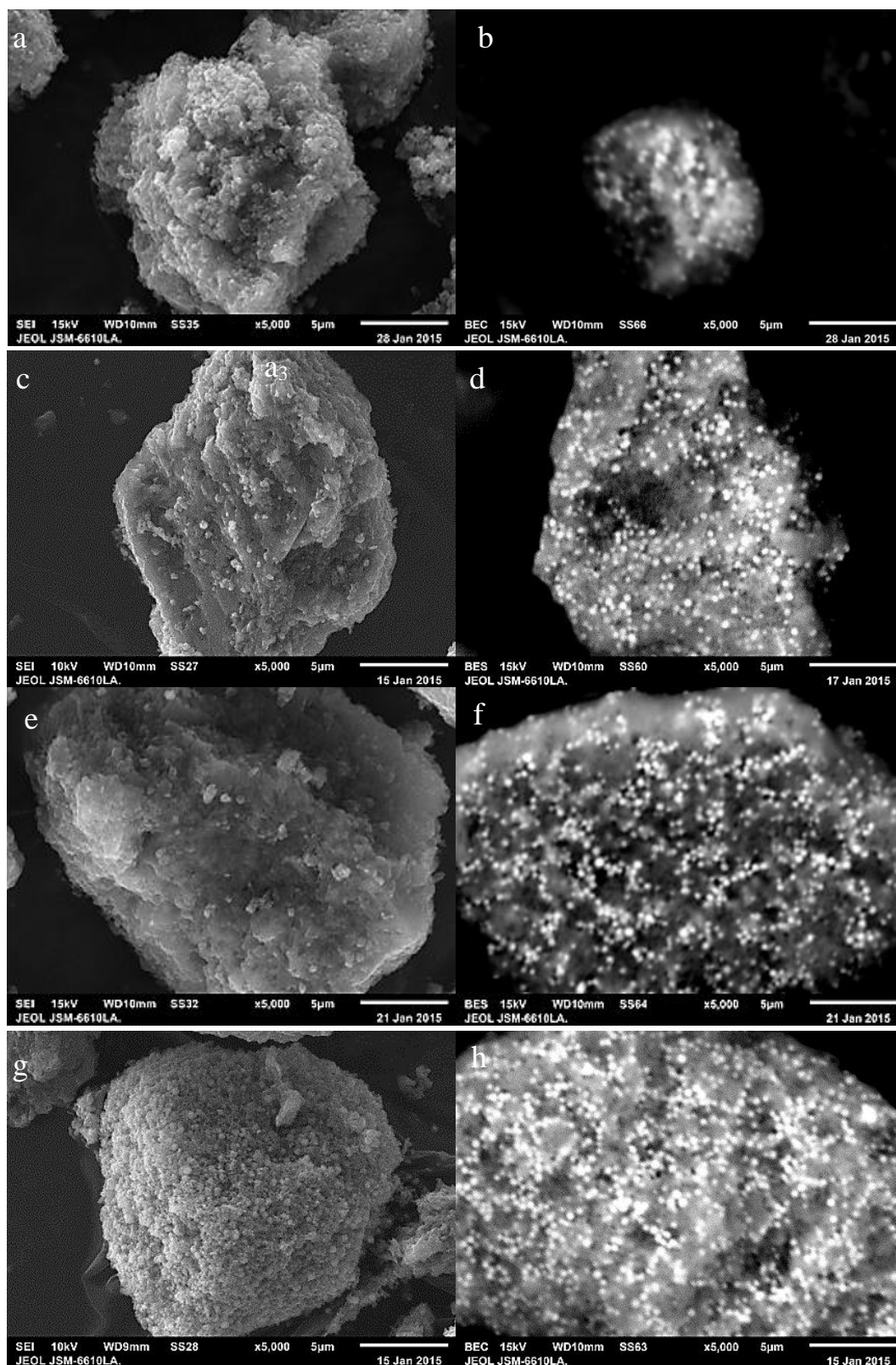
Figure 7.3. SEM micrographs of (a,b) M-GP-5 wt%Cu_2O/TiO_2, (c,d) M-GP-10 wt% Cu_2O/TiO_2, (e,f) M-GP-15 wt% Cu_2O/TiO_2, (g,h) M-GP-50 wt% Cu_2O/TiO_2. Micrographs on left-hand side of figure are SEM, those on the right hand side are BSE.

7.4 High Resolution Transmission Electron Microscopy

TEM images of the 10 % Cu_2O/TiO_2-modified geopolymer composite are shown in Figure 7.4 (a,b). These images show the penetration of the photoactive nano-hetrostructures into the geopolymer matrix, confirming that the preparation method achieved the desired photocatalyst morphology. The lattice fringes were measured by digital micrograph software by calculating the average parameters between 10 lattice fringes, resulting in lattice fringe spacings of 0.22 nm for the Cu_2O area and 0.18 nm for the TiO_2 area. These spacings correspond to the (312) lattice plane of TiO_2 and the (200) plane of Cu_2O. This HRTEM analysis provides a reliable confirmation of the XRD analysis. These lattice spacings are in agreement with the cubic structure of Cu_2O (JCPDS file no. 01-073-6237) and the tetragonal structure of the anatase and rutile phases of TiO_2 (JCPDS file no. 00-021-1272 and 04-006-1919 respectively).
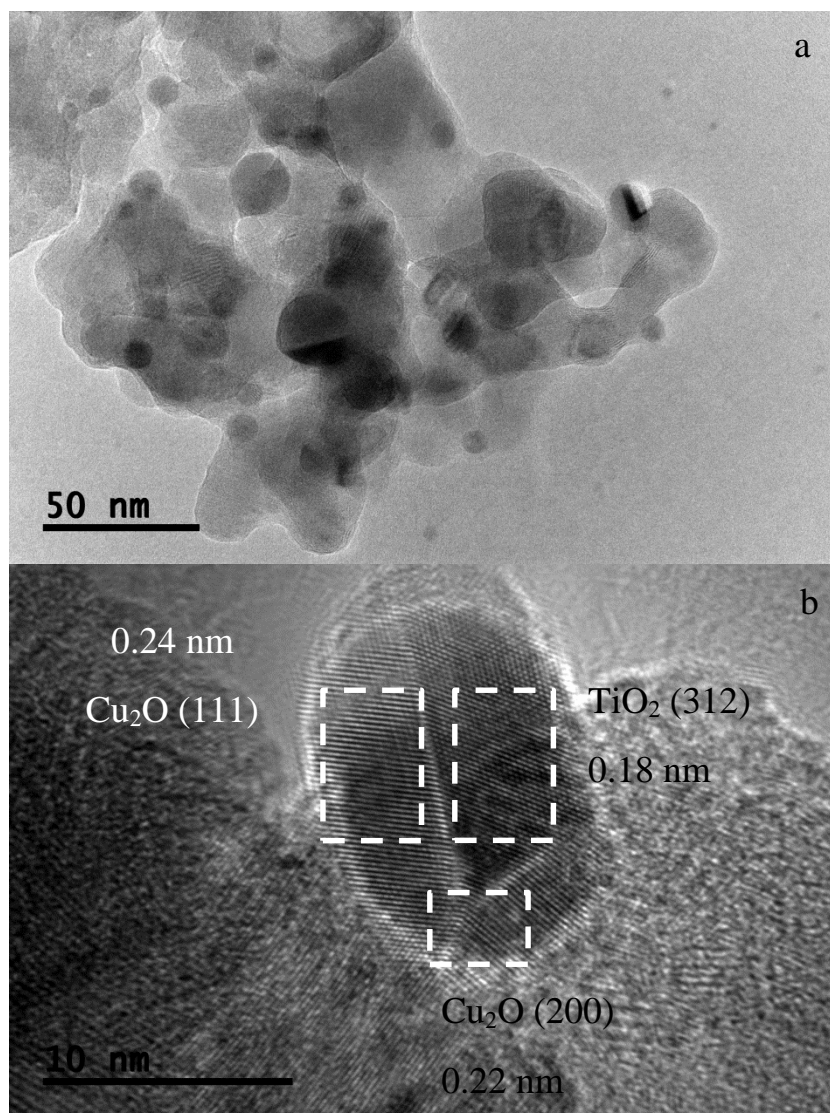
Figure 7.4. (a,b) TEM images of M-GP-10 wt% Cu_2O/TiO_2 composite

Further evidence for the successful synthesis of the Cu_2O/TiO_2 heterostructures is provided by STEM imaging in conjugation with EDS mapping (Fig. 7.5) which clearly shows that the composite contains a high concentration of Cu_2O/TiO_2 nanoparticles. EDX element mapping of the sample further shows the spatial distributions of Si, Al, Na, Cu and Ti in the composite. The Ti and Cu atoms are distributed within the geopolymer composite, but the Ti appears to be more closely associated with the Si elements of the geopolymer matrix, whereas the Cu is more homogeneously distributed over the complete matrix. The Si map suggests the presence of regions of the sample that are richer in Si, which are also associated with the Ti component, but there is no obvious explanation for this interesting observation.
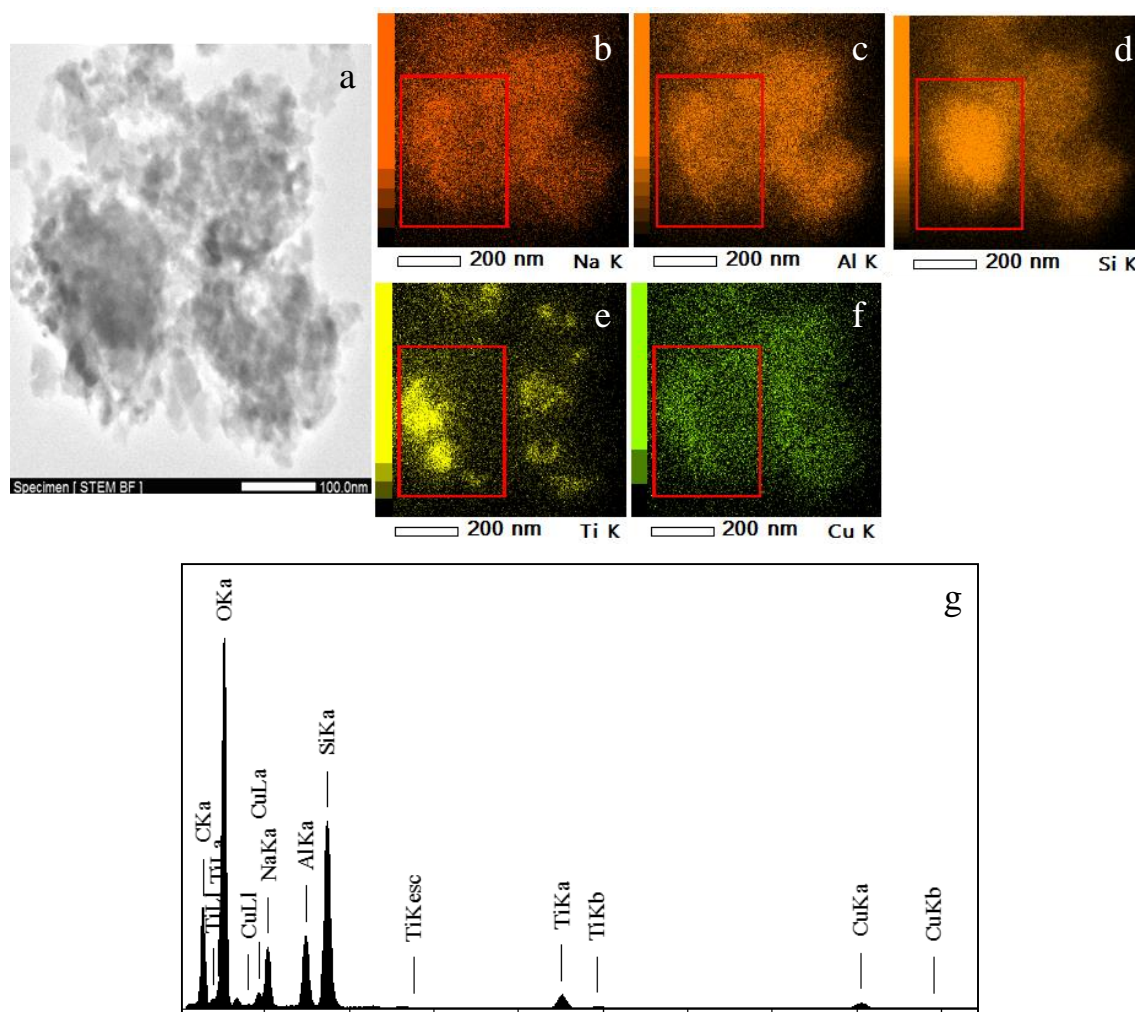
Figure 7.5. (a) STEM image of M-GP-10 wt%-Cu_2O/TiO_2 composite, (b-f) corresponding EDX elemental maps and (g) EDX spectrum of the area indicated in red.

7.5 FTIR spectroscopy

FTIR spectra of the unmodified geopolymer, CTAB-modified geopolymer and Cu_2O-TiO_2 M-GP composites (5-50 wt% Cu_2O) are presented in Figure 7.6. As with the previous samples prepared with CTAB-modified matrices, the FTIR spectra show three principal bands in the region (a) 3439-3463 cm^{-1}, (b) 1644-1652 cm^{-1} and (c) 1002-1008 cm^{-1} (Table 7.2). Region (a) arises from the (OH) stretching vibration of H-bonded water[193] and appears in all composites. This band is shifted to higher frequencies in most of the samples containing CTAB and Cu_2O/TiO_2. Loading with the surfactant causes a decrease of hydrogen bonding strength in the composite.[185, 193]
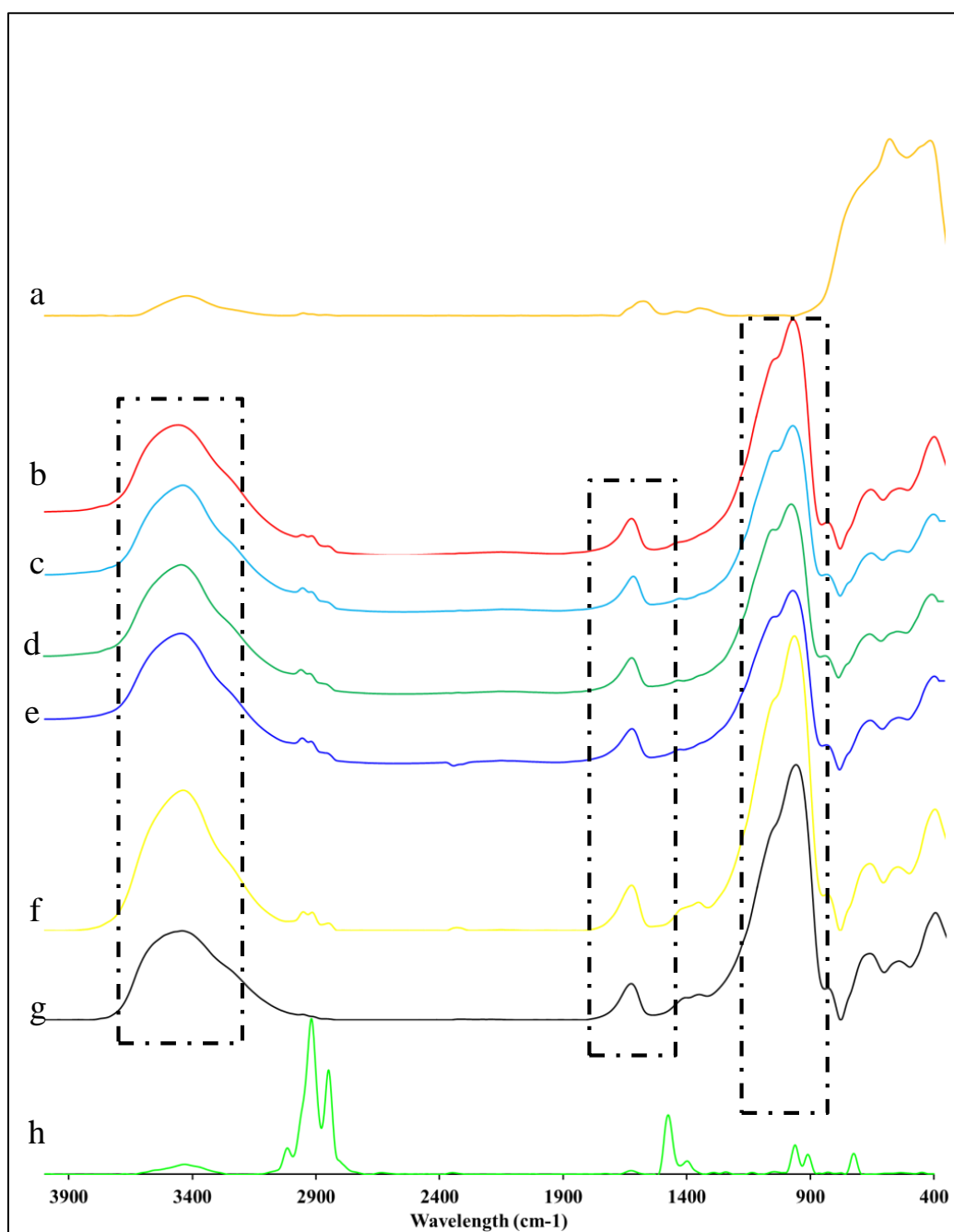
Figure 7.6. FTIR spectra of GP, M-GP, Cu_2O/TiO_2 and Cu_2O/TiO_2 supported by GP matrix with different loading contents; (a) Cu_2O, (b) M-GP 50 wt% Cu_2O, (c) M-GP 30 wt% Cu_2O, (d) M-GP 15 wt% Cu_2O, (e) M-GP 10 wt% Cu_2O, (f) M-GP 5 wt% Cu_2O, (g) M- GP, (h) CTAB.

The surfactant changes the composite surface from hydrophilic to hydrophobic by replacing the hydrated cations which are the cause of the reduction of H-bonding.[185] As previously noted in chapter 6, the photoactive constituents Cu_2O and TiO_2 can enter the cavities in geopolymer matrix and coordinate to the surface of the oxygen from one side and the water molecules on the other side, decreasing the polarising ability and weakening the H-bonds in the isolated hydrated band,[194] so that the O-H stretching band is shifted to higher wavenumbers.

Table 7.2. Positions and assignments of the IR vibration bands observed in the range of 400-4000 cm^{-1}

GP	M-GP	M-GP 5 wt% Cu_2O/TiO_2	M-GP 10 wt% Cu_2O/TiO_2	M-GP 15 wt% Cu_2O/TiO_2	M-GP 50 wt% Cu_2O/TiO_2	Cu_2O/TiO_2	CTAB
3834							
3439	3445	3450	3456	3447	3464	3429	
3015							3016
2967	2964	2968	2968	2968	29682	2964	
	2930	2932		2933	2932	2930	2918
1644	1653	1649	1651	1645	1653	1605	2849
1384	1385	1456				1381	1475
1002	1003	1007	1007	1009	1007		962
	872	872	870	874	870		910
694	700	696	694	694	696		725
						621	
578	588	582	581	582	581		
437	440	442	445	445	444	459	

–OH: 3700–3600, –OH, HOH: 3600-2200, HOH: 1700-1600, Si–O–Si &Al–O–Si: 1200-950

Area (b) (Figure 7.6) arises from H-O-H bending vibrations and indicates that the geopolymer retains absorbed water following polycondensation of the (OH) groups.[185] This vibration band is shifted to higher wave numbers due to the presence of CTAB. This frequency shift trend indicates the hydrophobicity of the materials resulting from the CTAB surfactant loading.[185]

Region (c) (Figure 7.6) arises from the Si-O-Si and Si-O-Al asymmetric stretching vibrations.[123, 184] The addition of Cu_2O/TiO_2 to the geopolymer produces a small shift in the position of the asymmetric Si–O–Si stretching vibration at 1000 cm^{-1} and a reduction in the intensity of this band. This fact is evidence of a small change in the geopolymer structure. As previously observed (chapter 6), the vibration corresponding to the CH$_2$ stretching mode of

the amine is located at 2918 and 2929 cm^{-1} in the reference CTAB and CTAB-modified geopolymer respectively. The presence of this band confirms the presence of CTAB at the surface or inside the geopolymer matrix.

At lower wave numbers, the Si-O-Si bands of the geopolymer matrix are observed at 437 cm^{-1} and 694 cm^{-1} (Si–O–Si symmetric stretching mode) with slight shift to the higher wave number, probably due to the superposition of Cu/Ti–O–Cu/Ti.

7.6 ^{29}Si and ^{27}Al solid state MAS NMR

The ^{29}Si MAS NMR spectra of the geopolymer and geopolymer composites are presented in Figure 7.7. The spectra of these samples are essentially identical to those shown in chapter 6, showing a principal resonance at about -87 ppm except the sample containing 50% Cu_2O/TiO_2 in which the peak is slightly shifted to a less-shielded position of -89 ppm. This peak remains essentially unchanged after the addition of different percentages of the Cu_2O/TiO_2 nano-heterostructure. As discussed in earlier chapters, the small broad peak at about -107 ppm corresponds to SiO_4 units, and the presence of CTAB in the geopolymer matrix results in a small peak at about -72 ppm corresponding to a range of monosilicates of the single tetrahedra type of silicon-oxygen (Q^0).[16] This peak is slightly shifted to -70 and -71 ppm by the shielding effect of additions of 10 and 15 wt% Cu_2O/TiO_2 nano-heterostructures. The positions of the ^{29}Si NMR resonances are shown in Table 7.3. With increasing content of Cu_2O/TiO_2, the ^{29}Si spectra become broader, reflecting an increased randomness of the matrix structure; this appears to result in a change in the relative intensities of the peaks at -89 and -107 ppm; this is however an artefact caused by the more poorly resolved spectra of the composites containing the higher Cu/Ti contents.
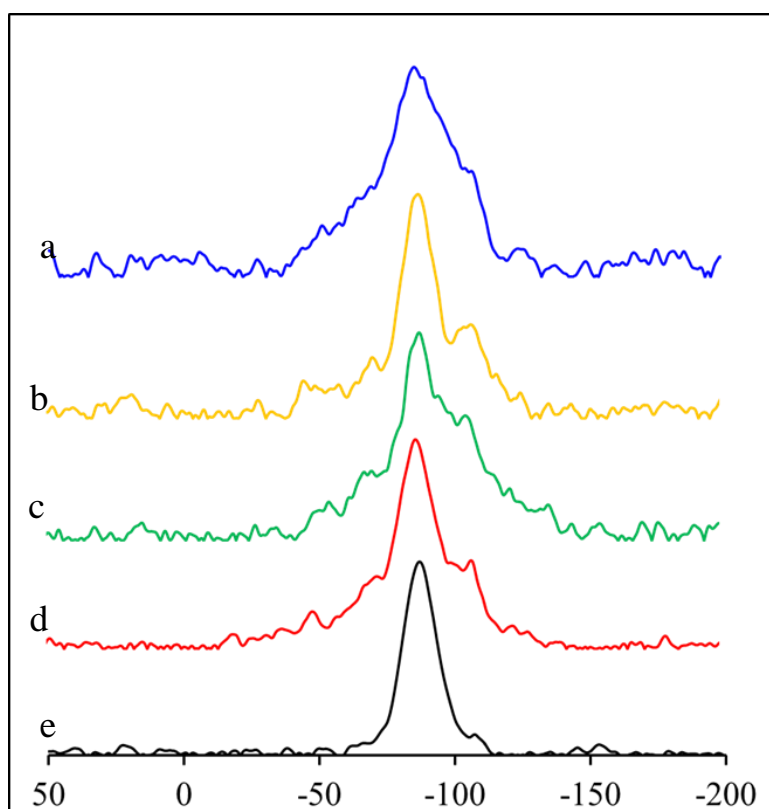
Figure 7.7. 11.7 T ^{29}Si MAS NMR spectra (a) M-GP 50 wt% Cu_2O/TiO_2 (b) M-GP 15 wt% Cu_2O/TiO_2, (c) M-GP 10 wt% Cu_2O/TiO_2, (d) M-GP, (e) GP.

Table 7.3. Peaks related to the 11.7 T 29Si MAS NMR spectra

GP	M-GP	M-GP 10 wt% Cu_2O/TiO_2	M-GP 15 wt% Cu_2O/TiO_2	M-GP 50 wt% Cu_2O/TiO_2
-87	-87.2	-87.4	-87.8	-85.9 -89.2
	-72.3	-70.4	-71.3	
-107.6	-107.6	-105.5	-107.9	-106.3

The corresponding ^{27}Al MAS NMR spectra (Figure 7.8) are identical to the spectra already discussed in previous chapters, the principal sharp resonance at about 59 ppm corresponding to tetrahedral AlO$_4$ units of a well-developed geopolymer structure[188, 194]. The positions of this resonance in the various samples are shown in Table 7.4. The small broad feature in some of the samples arises from Al-O in octahedral coordination,[120] from a trace of unreacted metakaolin.[141] These spectra confirm the successful formation of aluminosilicate

geopolymer composites in the presence of the CTAB surfactant and are unchanged by the presence of homogeneously distributed nanosized Cu_2O/TiO_2 particles.
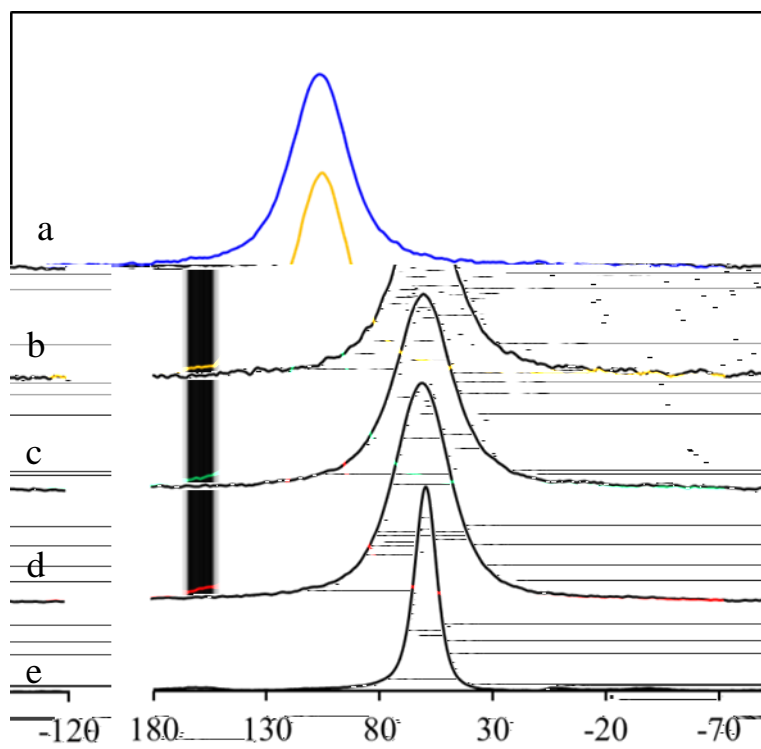
Figure 7.8. 11.7 T ^{27}Al MAS NMR spectra (a) M-GP 50 wt% Cu_2O/TiO_2 (b) M-GP 15 wt% Cu_2O/TiO_2, (c) M-GP 10 wt% Cu_2O/TiO_2, (d) M-GP, (e) GP.

Table 7.4. Peaks related to the 11.7 T ^{27}Al MAS NMR spectra

GP	59.6
M-GP	59.65
M-GP 10 wt% Cu₂O/TiO₂	59.18
M-GP 15wt% Cu₂O/TiO₂	58.65
M-GP 50 wt% Cu₂O/TiO₂	59.24

7.7 Nuclear quadrupole resonance (^{63}Cu NQR)

^{63}Cu NQR spectra of the Cu_2O and CTAB-modified geopolymer/Cu_2O and CTAB-modified geopolymer/Cu_2O/TiO_2 composites (Figure 7.9) show the expected single line for pure Cu_2O (Figure 7.9a) and the Cu_2O component of the composite containing Cu_2O before UV irradiation (Figure 7.9b). However, by contrast with the ^{63}Cu NQR spectra of the composites formed with the unmodified geopolymer matrix (chapter 4), UV irradiation of these samples

results in the loss of the NQR spectrum (Figure 7.9 c,e). There are three possible explanations for this behaviour: (i) it may be due to a change of the copper valence upon UV irradiation, thus transforming the original Cu_2O to an entity that is sufficiently structurally different to produce a different quadrupole frequency and be obscured by paramagnetic broadening (i.e. CuO), (ii) complete destruction of the Cu_2O due to the presence of an increased concentration of residual acid sites and/or OH concentration by virtue of the different synthesis route (i.e. the inclusion of TiO_2 resulting in a different OH/Al/Si ratio) or (iii) dilution of the Cu_2O content by its inclusion in the geopolymer/Cu_2O/TiO_2 composite is the reason why it is not detected in these samples. In view of the fact that the presence of Cu_2O is suggested by XRD in all the samples, both unirradiated and UV irradiated, explanation (iii) may be the most likely. It is worth noting however that these samples appear to be darker in colour, raising the possibility that the Ti^{4+} is being reduced to paramagnetic Ti^{3+}; since the Ti and Cu species are in reasonable proximity to each other in the pore spaces of the matrix, Ti^{4+}-Ti^{3+} reduction could be triggered by the more energetically favourable Cu^{+}-Cu^{2+} oxidation in these dark samples, producing paramagnetic species (both Ti^{3+} and Cu^{2+}) and removing the NQR signal.
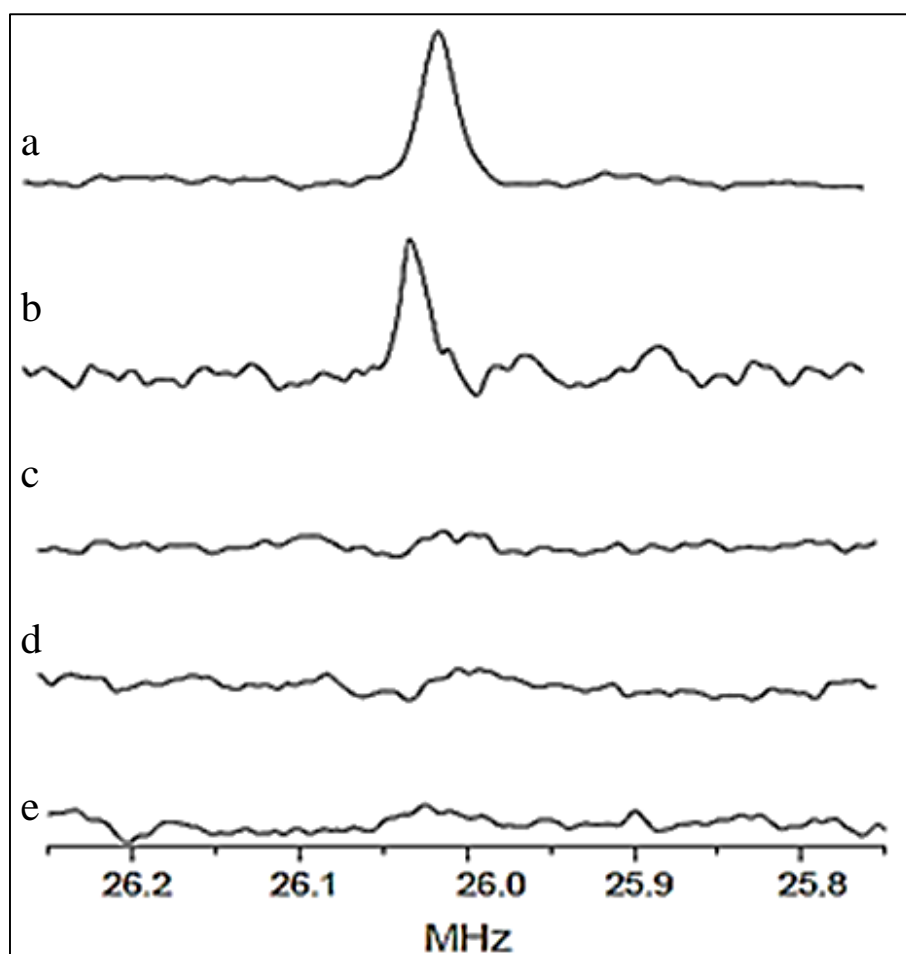
Figure 7.9. ^{63}Cu NQR spectra of nanoparticle Cu_2O and M-GP composites. (a) as-synthesized Cu_2O, (b) M-GP-Cu_2O before UV irradiation, (c) M-GP-Cu_2O after UV irradiation, (d) M-GP-Cu_2O/TiO_2 before UV irradiation, (e) M-GP-Cu_2O/TiO_2 after UV irradiation

7.8 Adsorption of MB

7.8.1 Reactions under dark conditions

As described in the previous chapter, composites based on geopolymer matrices modified with CTAB removed MB dye from solution by a combination of adsorption (in the dark) and photodegradation (under UV illumination), but unlike the composites based on the unmodified geopolymer matrix, these two processes could be distinguished in the same experiment in the CTAB-matrix composites. Therefore, a series of experiments similar to those outlined in Chapter 6 were carried out on the CTAB-modified Cu_2O/TiO_2 composites, in which the composite was initially exposed to MB dye in the dark, and the system was allowed to equilibrate. Measurements of MB dye removal made in this step correspond to adsorption but not photodecomposition.

As found in the previous chapter, the metal oxide particles alone cannot adsorb MB from solution in the dark, but when combined with the CTAB-modified geopolymer matrix, they show substantial dye adsorption abilities (Figure 7.10). The CTAB-modified geopolymers composite containing 5-15 wt% of the Cu_2O/TiO_2 heterostructure show the greatest degree of MB removal after 12 hour, but at higher heterostructure loadings, the adsorption process becomes more hindered (Figure 7.10).
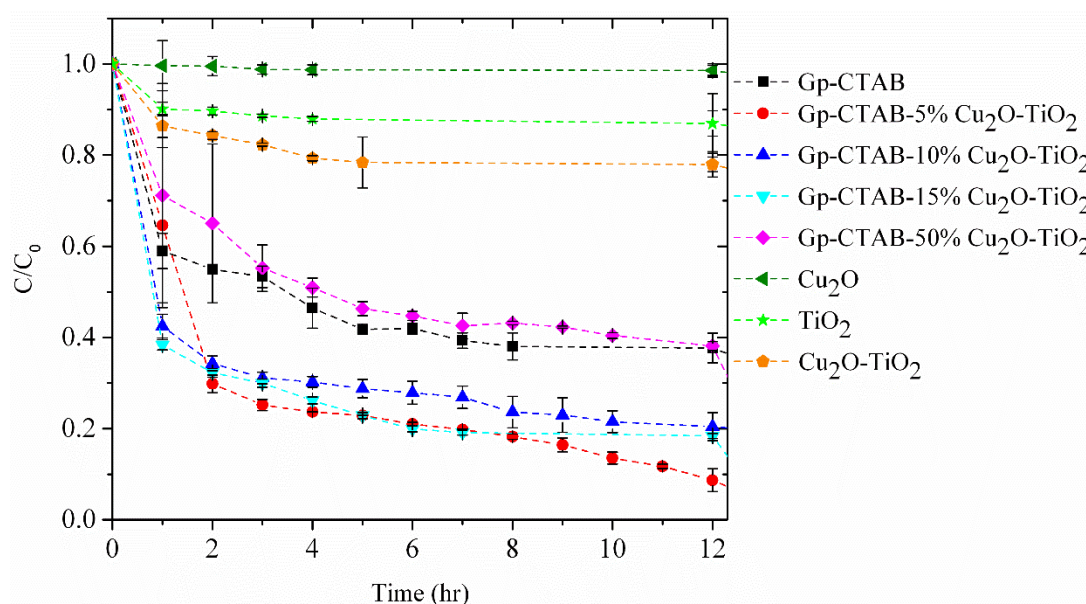
Figure 7.10. Plots of the residual concentration (C/C_0) *vs.* time (t) onto the M-GP matrix, M-GP 5,10, 15, and 50 wt% Cu_2O (monitored at 664 nm in dark)

Figure 7.11 shows the results of fitting the experimental data for MB adsorption on the CTAB-modified geopolymer matrix and geopolymer composites by pseudo-first-order and pseudo-second-order kinetic models (eqs. 27 and 28).[182, 196] The resulting plots of the data (Figure 7.11 a,b) are only poorly fitted by the pseudo-first-order model but very good fits are obtained to the pseudo-second-order model. The amount of MB adsorbed at equilibrium (q_e) obtained from the pseudo-first and second-order model and the correlation coefficients R^2 are presented in Table 7.5, showing that the R^2 values of the pseudo-second-order kinetic model are all >0.90 except for the composite containing 15% Cu_2O/TiO_2. Moreover, comparison of the experimental values q_{exp} with the q_e values calculated from equations (eq. 27-28) (Table 7.5) indicates that pseudo-second-order model delivers a better fit to the experimental data under dark conditions, as was found to be the case with CTAB-modified composites containing Cu_2O (Chapter 6).

Table 7.5. Parameters for kinetic models of MB adsorption on samples

Sample	Kinetic model	q_{exp} (mg/g)	q_e (mg/g)	k	R^2
M-GP	1st-order	14.40	12.86	240.78	0.97
"	2nd-order	"	14.91	0.52	0.97
M-GP-5 wt% Cu_2O/TiO_2	1st-order	19.70	18.54	87.30	0.79
" "	2nd-order	"	20.11	0.002	0.98
M-GP-10 wt% Cu_2O/TiO_2	1st-order	18.12	16.92	0.02	0.91
" "	2nd-order	"	18.38	0.002	0.96
M-GP-15 wt% Cu_2O/TiO_2	1st-order	8.66	3.53	120.94	0.96
" "	2nd-order	"	6.55	2.49^{e-07}	0.70
M-GP-50 wt% Cu_2O/TiO_2	1st-order	14.34	11.88	44.68	0.90
" "	2nd-order	"	16.70	5.96^{e-04}	0.92
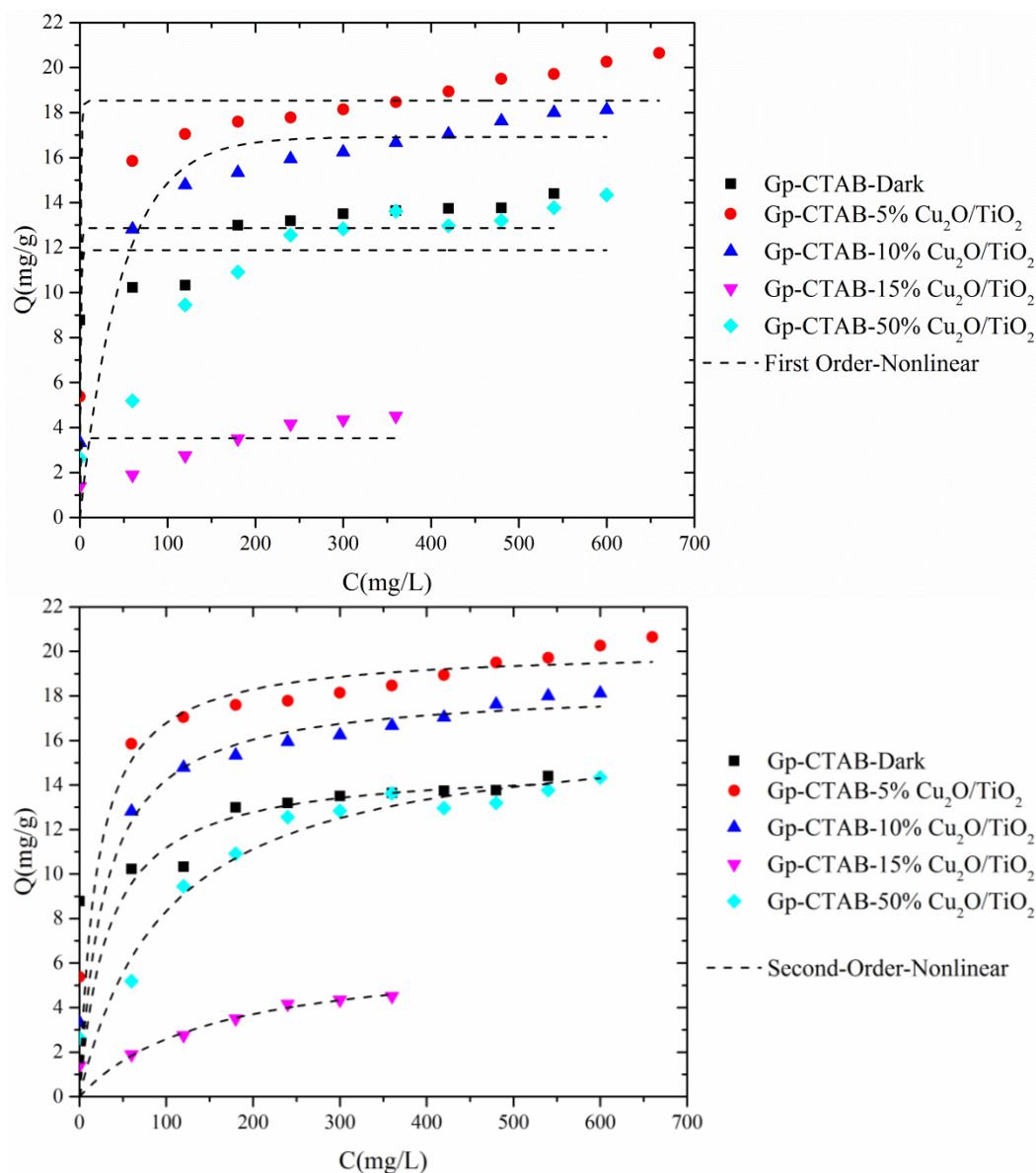
Figure 7.11. Experimental data for the adsorption of MB dye in the dark on to the M-GP matrix and the M-GP-Cu_2O/TiO_2 composites fitted to (a) pseudo first-order kinetic model, (b) pseudo second-order kinetic model.

7.8.2 MB dye adsorption isotherms under dark conditions

As outlined in previous chapters, the adsorption isotherms of the CTAB-modified geopolymer and geopolymer composites were determined using the Langmuir, Freundlich and Langmuir-Freundlich equations (eqs. 29-31)[17, 178] (Figure 7.12 (a-c)). The resulting adsorption parameters and correlation coefficients from these three equations are shown in Table 7.6.
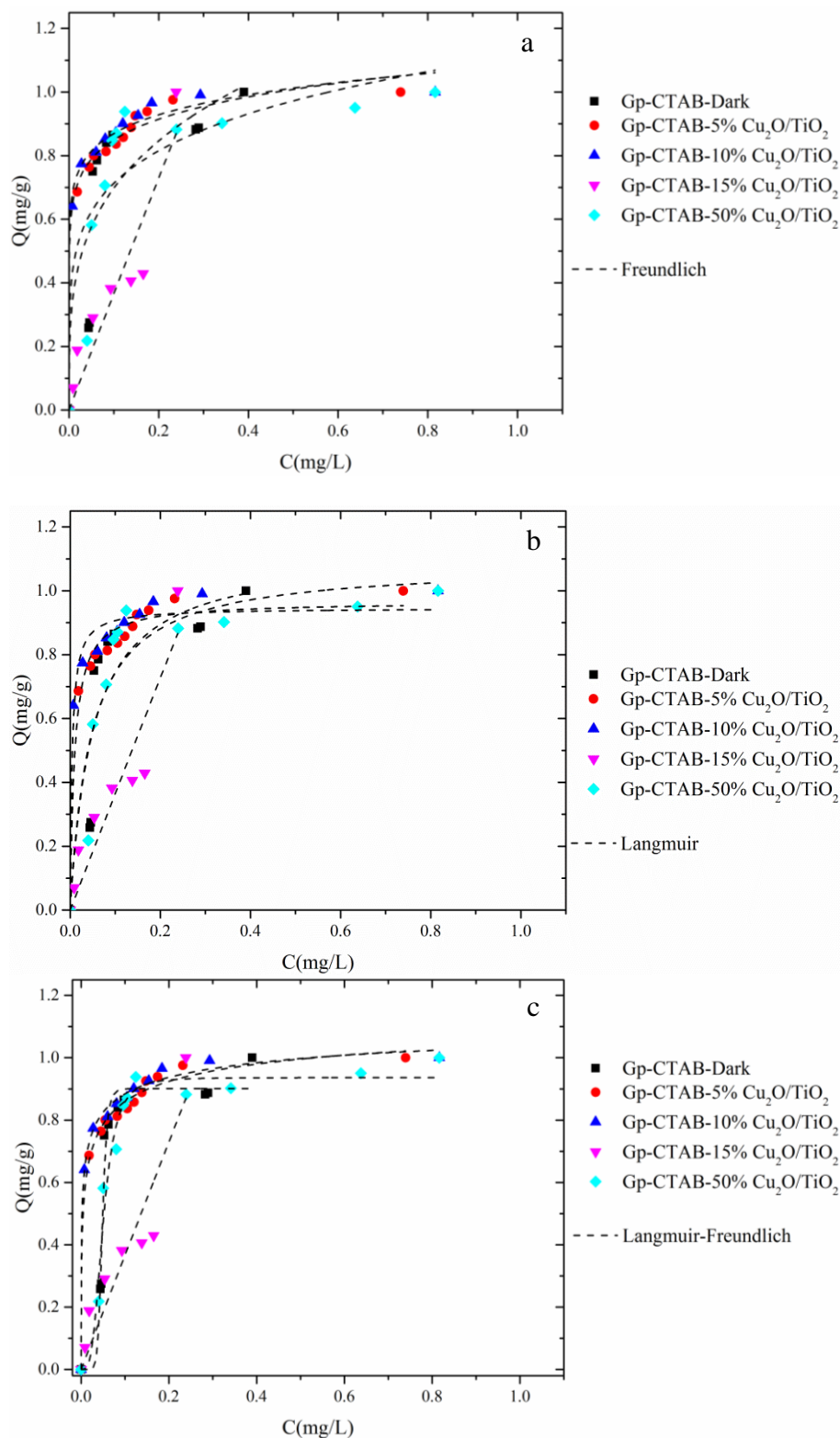
Figure 7.12. (a-c) Adsorption isotherms for MB adsorption fitted to Freundlich, Langmuir and Langmuir-Freundlich models (dashed lines).

Adsorption by the CTAB-modified geopolymer is fitted well by the Langmuir and Freundlich models which have R^2 values >0.99. The Cu_2O/TiO_2-geopolymer

composites (5, 10 and 50 wt%) are fitted best by the three-parameter Langmuir-Freundlich model, giving higher R^2 values (0.99, 0.99 and 0.96 respectively). The Langmuir and Langmuir-Freundlich constants provide an indication of the actual adsorption mechanisms and indicate the favourable adsorption of MB on the geopolymer composites.

7.8.3 Reactions under UV irradiation

As described in the previous chapter, the photodegradation of MB under UV irradiation by the CTAB-modified composites was determined at ambient temperature after allowing the system to equilibrate in the dark for 12 hour Figure 7.13 shows the MB degradation under both dark and UV conditions as a function of elapsed time. As previously found, under dark conditions neither of the metal oxides or their mixture is particularly effective in removing MB from solution but in combination with the geopolymer matrix, adsorption occurs on the geopolymer by a pseudo-second order kinetic model (see section 7.2.1 above). Under UV illumination, significant photodegradation occurs in all the samples (Figure 7.13), particularly at a concentration of 15 wt% Cu_2O/TiO_2, but this sample has already proved to be one of the most efficient composites in removing MB in the previous adsorption step. Considering the photodegradation step alone, the sample containing 50 wt% Cu_2O/TiO_2 is the most efficient, which is not unexpected in view of its highest content of photoactive components. These results show enhanced photocatalytic behaviour of the Cu_2O/TiO_2-CTAB-modified geopolymer composites compared with nanoparticle Cu_2O/TiO_2 heterostructures alone and also with Cu_2O/TiO_2 composites synthesised with an unmodified geopolymer matrix.
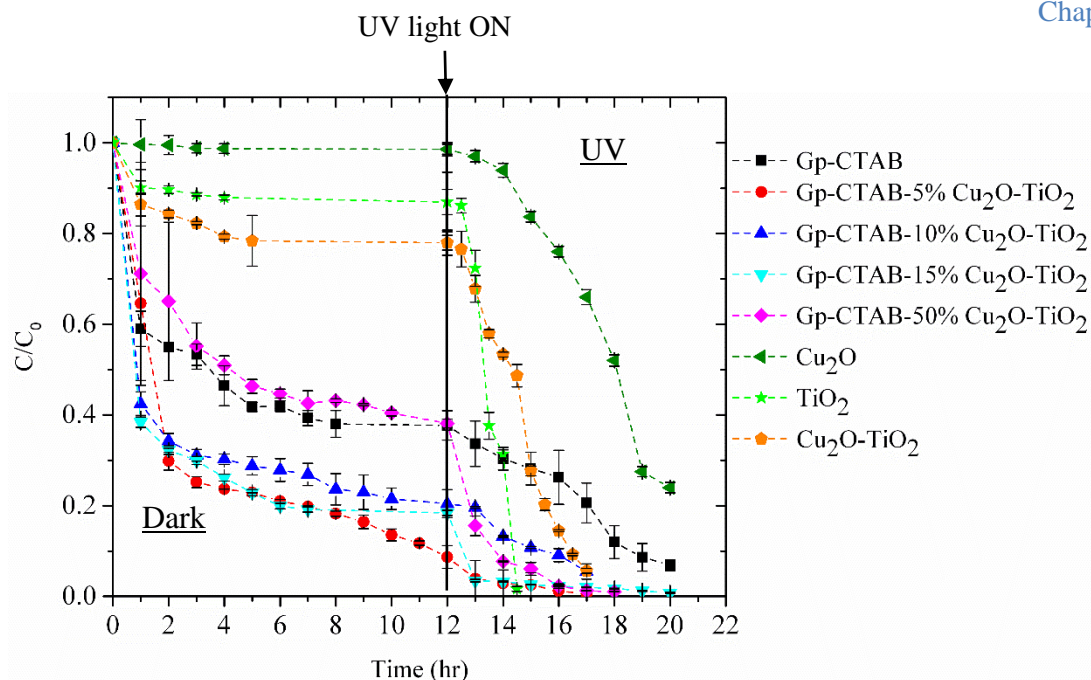
Figure 7.13. Plots of the residual concentration (C/C₀) *vs.* time (t) onto the M-GP, M-GP-5, 10, 15 and 50 wt% Cu₂O, Cu₂O, TiO₂, Cu₂O/TiO₂ (monitored at 664 nm).

These points are illustrated more clearly in Figure 7.14 which compares the removal of MB after 60 min. by the CTAB-modified geopolymer composites containing different percentages of Cu_2O/TiO_2 and the metal oxide components alone, in the dark and under UV irradiation. This figure confirms the result that after 60 min. the adsorption step of MB removal is most eficient in the composites containing 5-15 wt% Cu_2O/TiO_2, by comparison wih the CTAB-modified geopolymer matrix alone, and the Cu_2O, TiO_2 and Cu_2O/TiO_2 photoactive elements alone. The removal of MB dye by photodegradation is equally efficient in the geopolymers containing 5-15 wt% Cu_2O/TiO_2 (Figure 7.14), and all these composites are more efficient than TiO_2 alone. Thus, the performance of all these composites, in both the adsorption and photodegradation steps, is superior to that of the oxides when they are not combined with the geopolymer matrix.
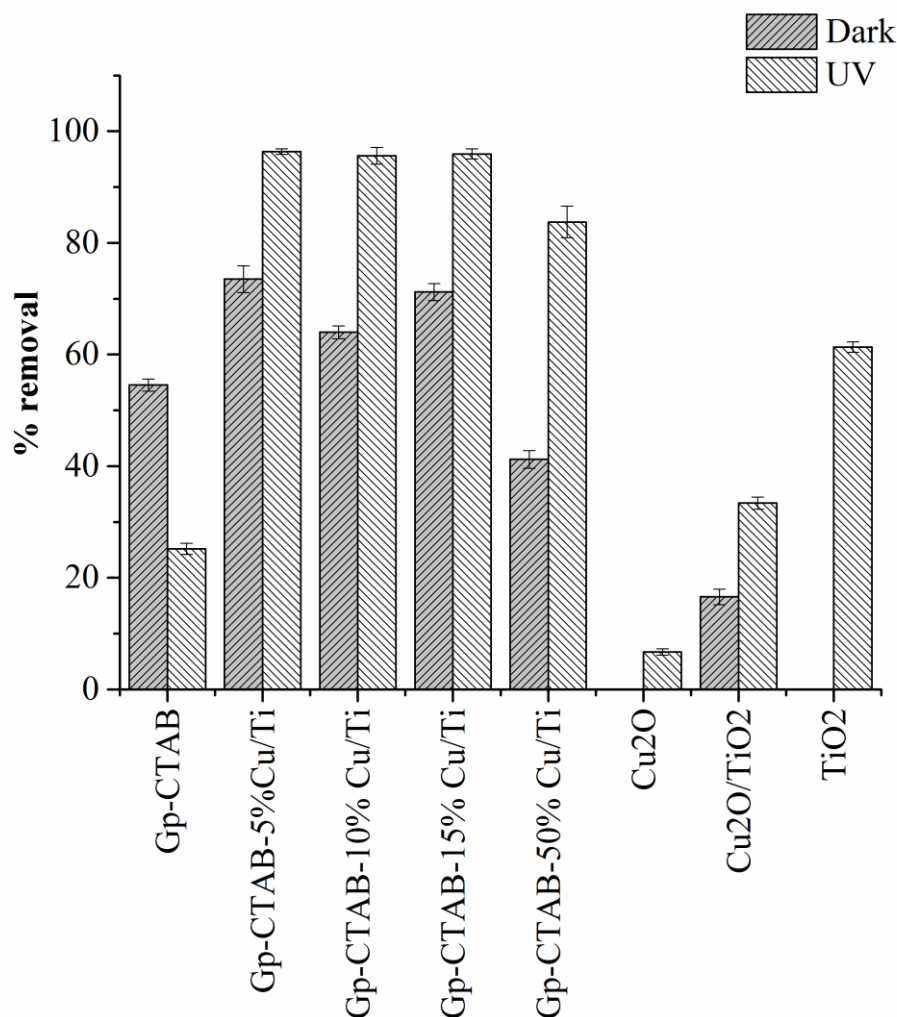
Figure 7.14. MB removal by the M-GP matrix, M-GP composites containing 5,10,15 and 50 wt% Cu_2O/TiO_2, Cu_2O, TiO_2, and Cu_2O/TiO_2 alone after 60 min.

7.8.4 Nitrogen Adsorption/Desorption Isotherms

N_2 adsorption-desorption isotherms of the composites formed using the CTAB-modified geopolymer matrix are presented in Figure 7.15. The specific surface areas resulting from the adsorption/desorption isotherms (Table 7.6) indicate an increase in the surface area from 17.0 m^2/g in the CTAB-modified geopolymer matrix to 34.8 m^2/g and 33.6 m^2/g in the composites containing 10 and 15 wt% Cu_2O/TiO_2 respectively. Similar trends are seen in the Langmuir surface areas and the cumulative surface areas of the pores calculated by the BJH method. Increasing specific surface areas confirm the dispersion of Cu_2O/TiO_2 inside the geopolymer matrix, but the average pore diameters, calculated by the BET method, decrease from 43.09

nm in the CTAB-modified geopolymer matrix to 29.7 nm in the composite containing 10 wt% Cu_2O, remaining approximately constant at 27.9 nm in the composite containing 15 wt% Cu_2O. Thus, the presence of the oxide nanoparticles in the pore structure of the geopolymer matrix increases the surface area of the pores available for adsorption and decreases the average pore size. Therefore, the greater photoactivity of the composite containing 10 wt% Cu_2O under both dark and UV conditions is related to the dispersion of the oxide in the geopolymer matrix, as confirmed by the decreased the pore diameter and increased surface area.
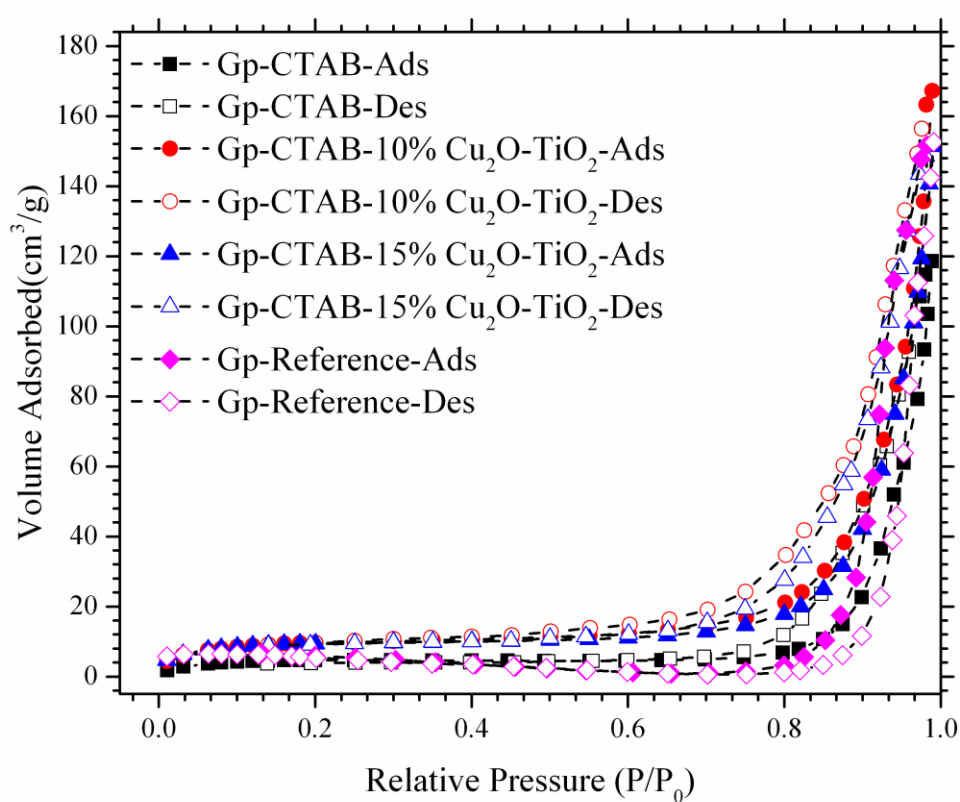
Figure 7.15. Nitrogen sorption isotherms of the M-GP (■, adsorption □, desorption), M-GP-10 wt% Cu_2O/TiO_2 (●, adsorption ○, desorption) and M-GP-15 wt% Cu_2O/TiO_2 (▲, adsorption △, desorption) GP (◊, adsorption ◊, desorption)

Table 7.6. Specific surface areas and pore parameters of CTAB-modified geopolymer matrix and geopolymer composites

	GP	M-GP	M-GP-10 wt% Cu_2O/TiO_2	M-GP-15 wt% Cu_2O/TiO_2
Single Point Surface Area	18.4 m²/g	16.1 m²/g	33.2m²/g	32.5 m²/g
S_{BET}	17.2 m²/g	17.0m²/g	34.8 m²/g	33.6 m²/g
$S_{Langmuir}$	21.9 m²/g	23.4 m²/g	48.1 m²/g	45.9 m²/g
$S_{BJH\ Adsorption\ Cumulative}$	23.1 m²/g	21.4 m²/g	35.3 m²/g	31.1 m²/g
$S_{BJH\ Desorption\ Cumulative}$	38.9 m²/g	33.6 m²/g	53.1 m²/g	47.8 m²/g
Volume				
Single Point Adsorption	0.24 cm³/g	0.18 cm³/g	0.26 cm³/g	0.23cm³/g
$V_{pore\ BJH\ Adsorption\ Cumulative}$	0.24 cm³/g	0.18 cm³/g	0.26 cm³/g	0.23 cm³/g
$V_{pore\ BJH\ Desorption\ Cumulative}$	0.24 cm³/g	0.18 cm³/g	0.26 cm³/g	0.23 cm³/g
Pore Size				
$D_{Adsorption}$	55 nm	43 nm	30 nm	28 nm
$D_{BJH\ Adsorption}$	41 nm	34 nm	29 nm	30 nm
$D_{BJH\ Desorption}$	24 nm	22 nm	20 nm	20 nm

7.9 CTAB-Modified-geopolymer composites of P25 titania alone

7.9.1 XRD Analysis

Figure 7.16 shows the XRD patterns of CTAB-modified composites containing different percentages of P25 TiO_2. The specific broad X-ray amorphous feature for geopolymer and the sharp reflections of rutile and anatase of titania are as expected.
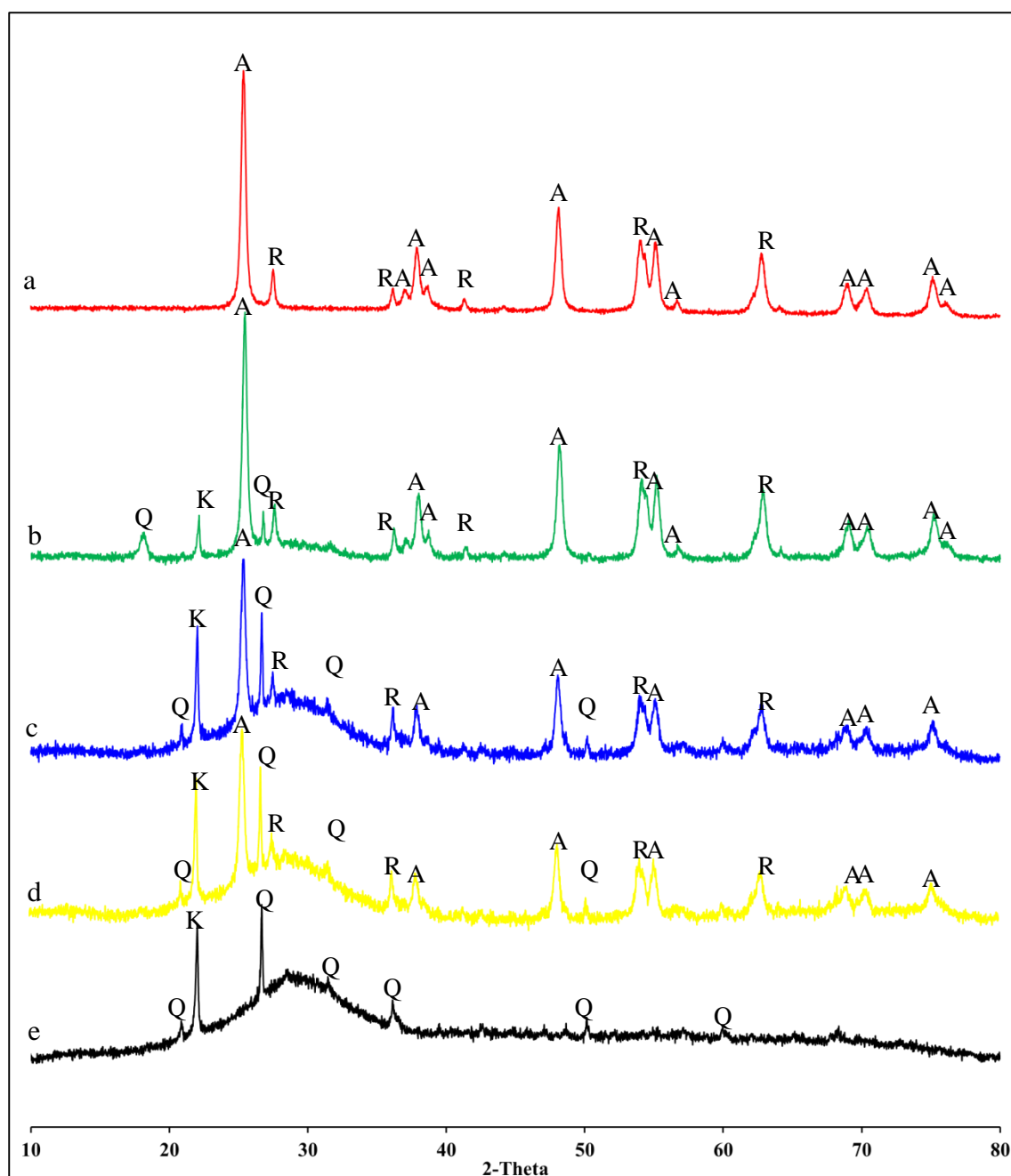
Figure 7.16. XRD patterns of TiO$_2$ and TiO$_2$ supported by M-GP with different loading contents; (a) TiO$_2$, (b-d) M-GP 50, 10 and 5 wt% TiO$_2$, (e) M- GP.

7.9.2 Scanning electron microscopy

The SEM micrographs of Figure 7.17 confirm the dispersion of the P25 TiO$_2$ particles over the surface of the CTAB-modified geopolymer composites with no sign of particle aggregation. The backscattered images (Figure7.17 b,d,f) show the increased presence of bright spots corresponding to the TiO$_2$ particles.
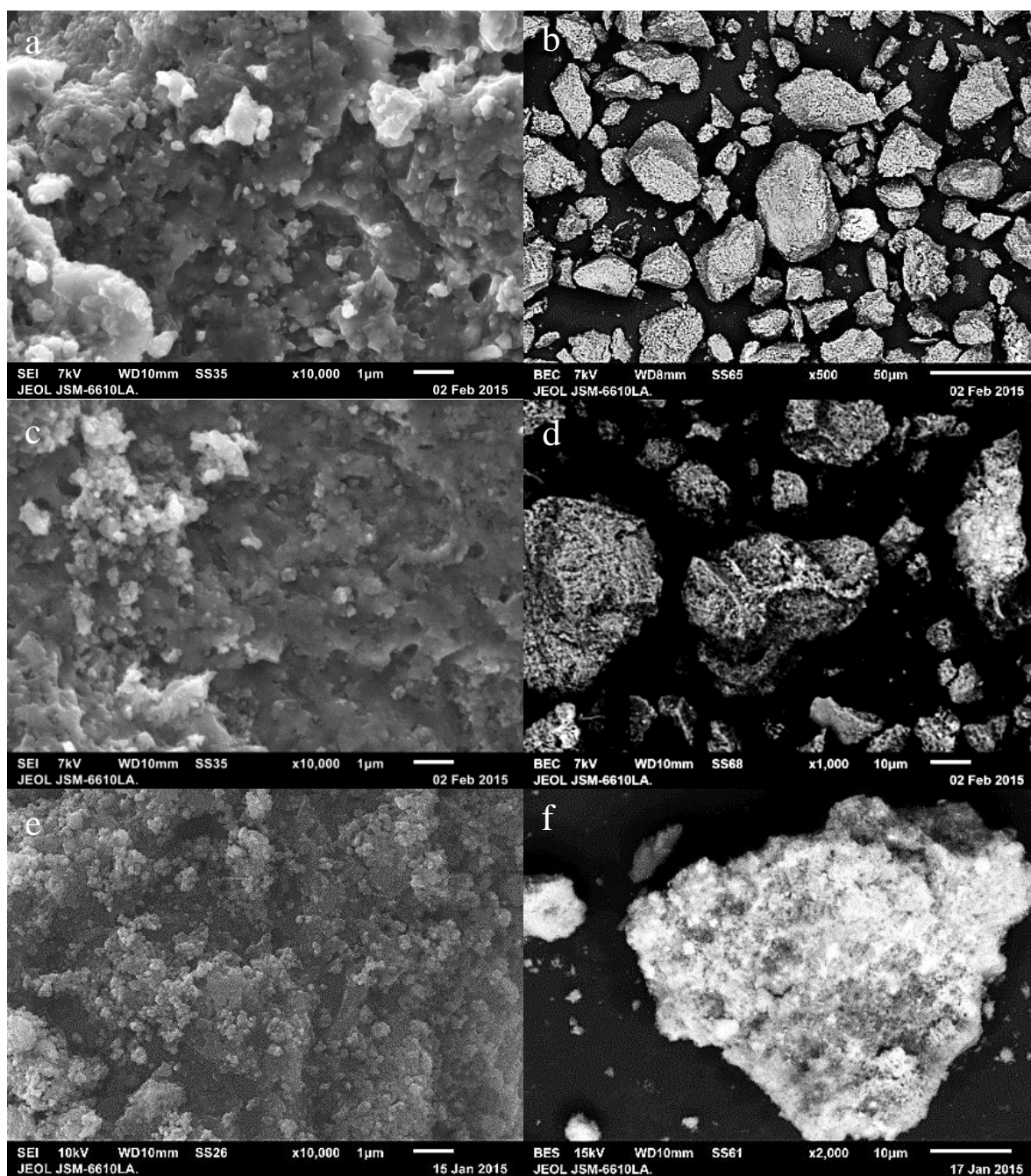
Figure 7.17. SEM micrographs of (a-f) M-GP composite containing 5, 10, 15 wt% TiO_2. Right hand micrographs are BSE, left hand are SE.

The EDS elemental analysis and the Figure 7.18 confirms the presence of all the expected elements (Si, Al, Na, and Ti) in the CTAB-modified geopolymer composite and the absence of any additional impurities.
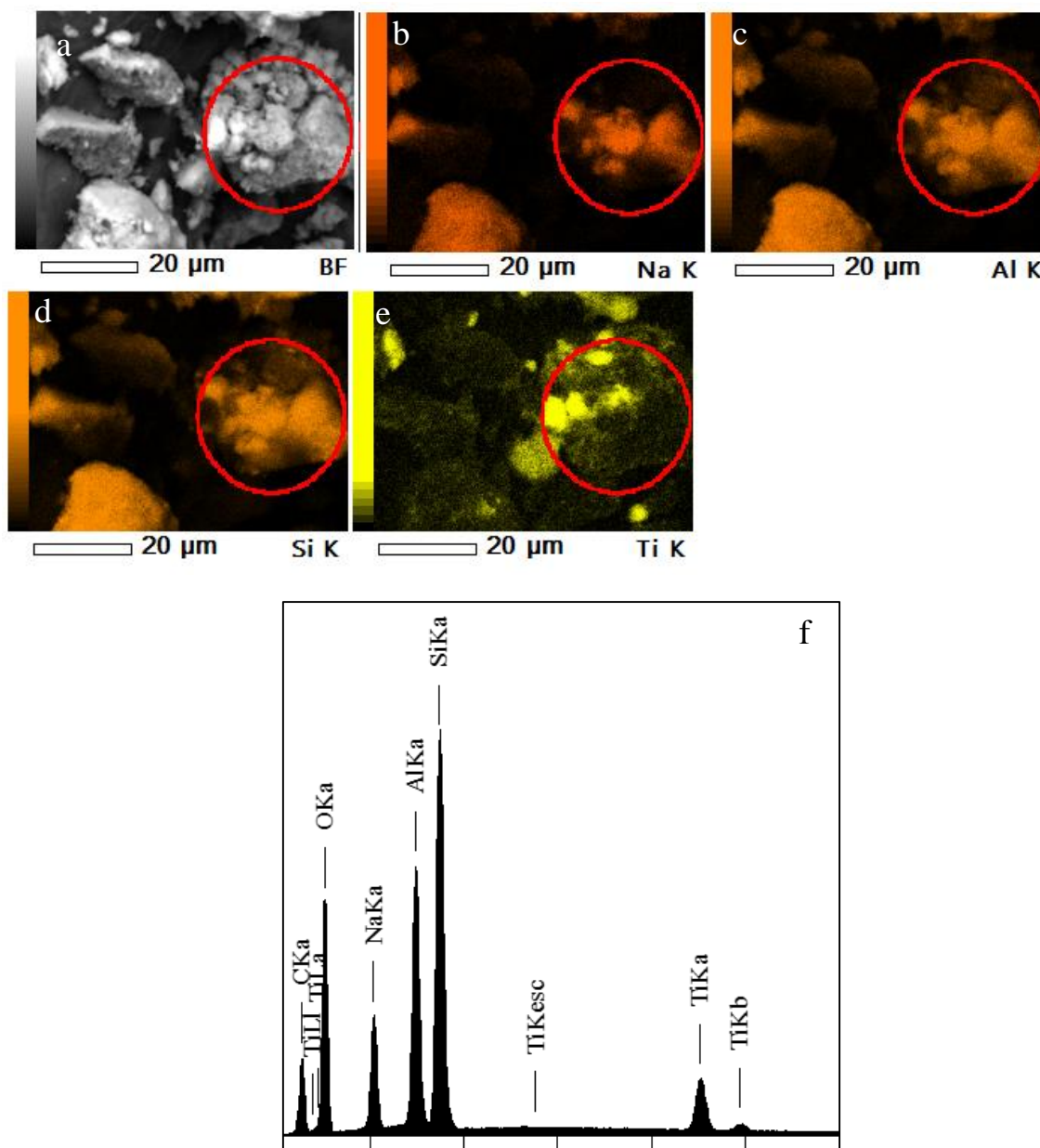
Figure 7.18 (a) Backscattered image, (b) Na, (c) Al, (d) Si, (e) Ti elemental map (f) EDS spectrum of the red-circled area of M-GP-15 wt% TiO_2.

7.9.3 High-Resolution Transmission Electron Microscopy

The HRTEM micrographs (Figure 7.19) confirm the entry of the TiO_2 particles into the pore structure of the geopolymer matrix. The average lattice fringe spacings measured for 10 lattice fringes show distance of 0.18, 0.38 and 0.37 nm between them arising from the (201) and (101) plane of the TiO_2, consistent with the result obtained for the unmodified geopolymer composite containing P25 TiO_2.
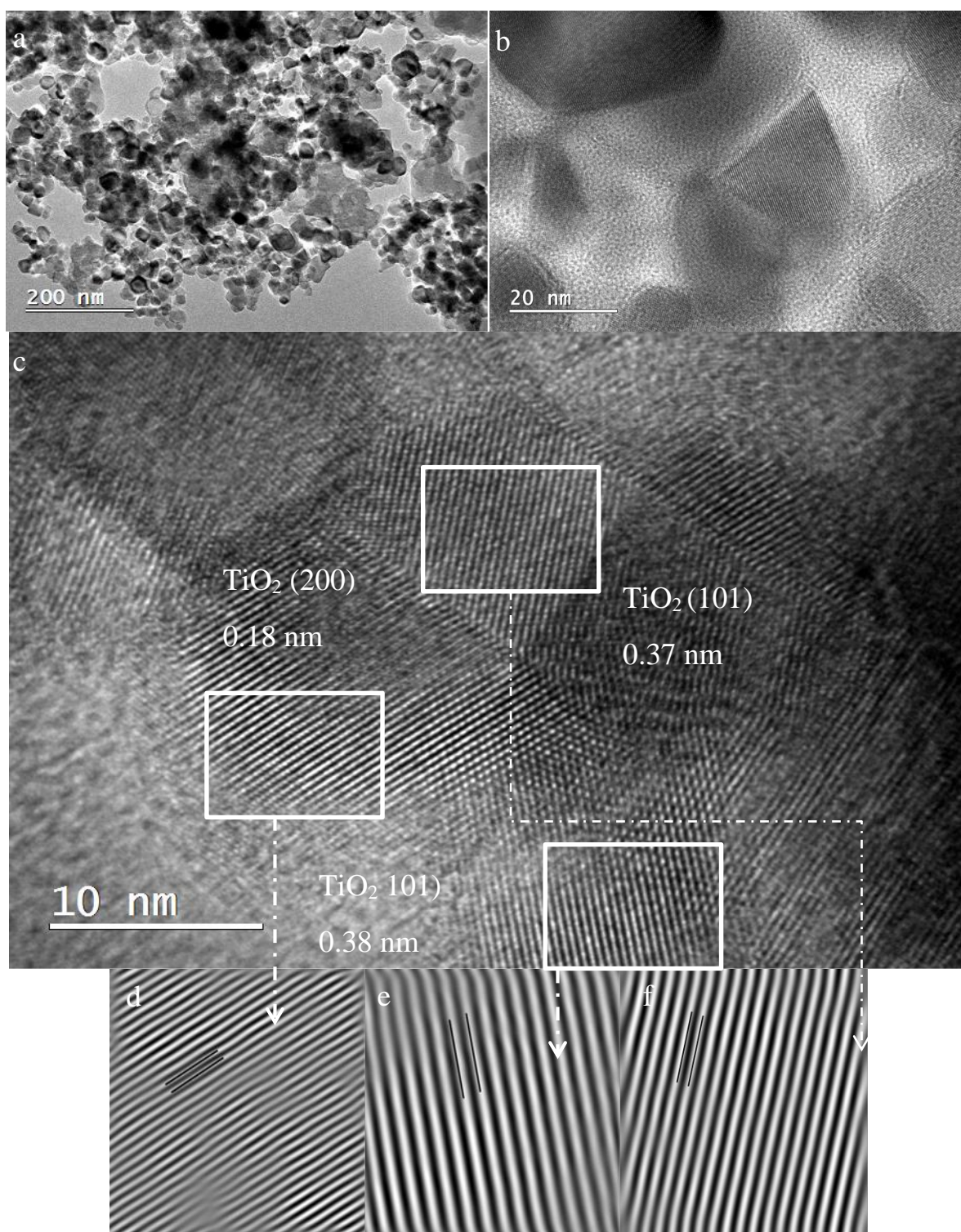
Figure 7.19. (a-c) TEM images of GP-10%-TiO$_2$ composite with, (d-f) HRTEM images of selected area in c.

7.9.4 Adsorption and degradation of MB dye by P25 titania, Cu$_2$O, Cu$_2$O/TiO$_2$ and their CTAB-modified geopolymer composites

The behaviour of P25 titania alone and incorporated in the CTAB-modified geopolymer matrix was measured in the both dark and UV condition and compared with the Cu$_2$O/TiO$_2$ and Cu$_2$O CTAB-modified geopolymer composites (Figure 7.20). The metal oxide nanoparticles themselves do not have the ability to remove MB from solution under dark conditions, but, in combination with the CTAB-modified geopolymer matrix, adsorption occurs by a process that can be described by the pseudo-second order kinetic equation. In addition, these data are well fitted to isotherms of the Langmuir-Freundlich type, as was found to be the case for composites of Cu$_2$O with CTAB-modified geopolymer matrices (chapter 6).
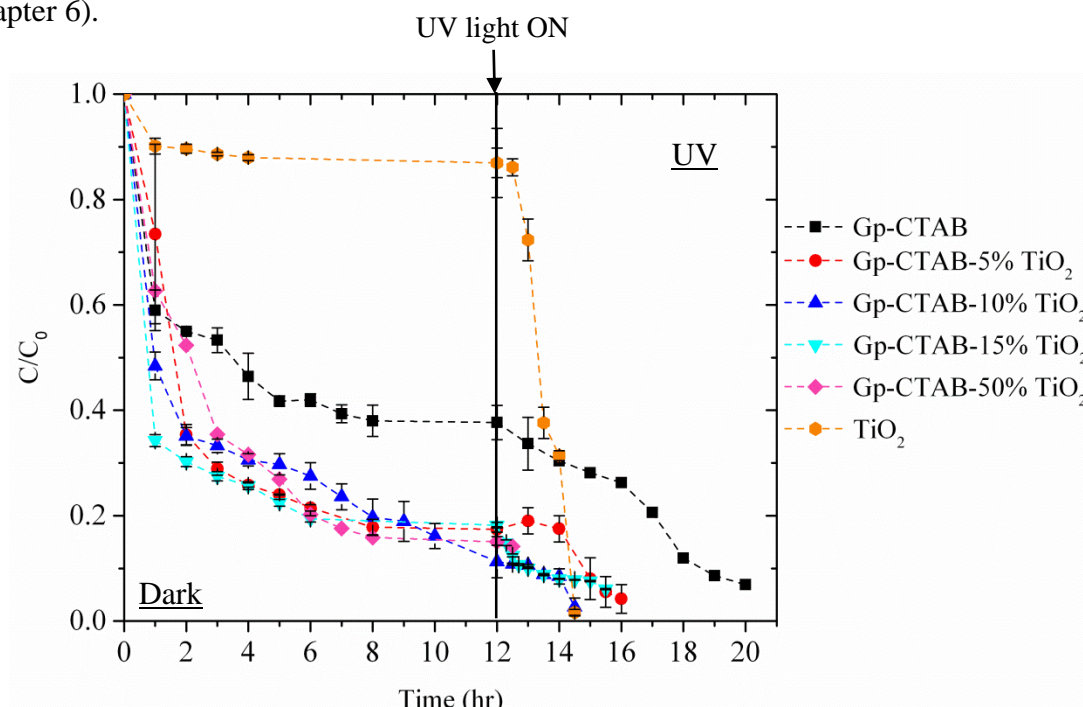
Figure 7.20. Plots of the residual concentration (C/C$_0$) *vs.* time (t) onto the M-GP, TiO$_2$ and M-GP 5, 10, 15 and 50 wt% TiO$_2$ (monitored at 664 nm).

Under the UV irradiation, the most rapid destruction of MB dye, starting from the equilibrium position, is by the composite containing 10 wt% P25 TiO$_2$ (Figure 7.21), but this composite has the advantage of starting from a vale in which a good deal of the MB has already been adsorbed under dark conditions. Figure 7.21 shows that all the photocatalysts prepared from CTAB-modified geopolymer have very rapid photodegradation properties.
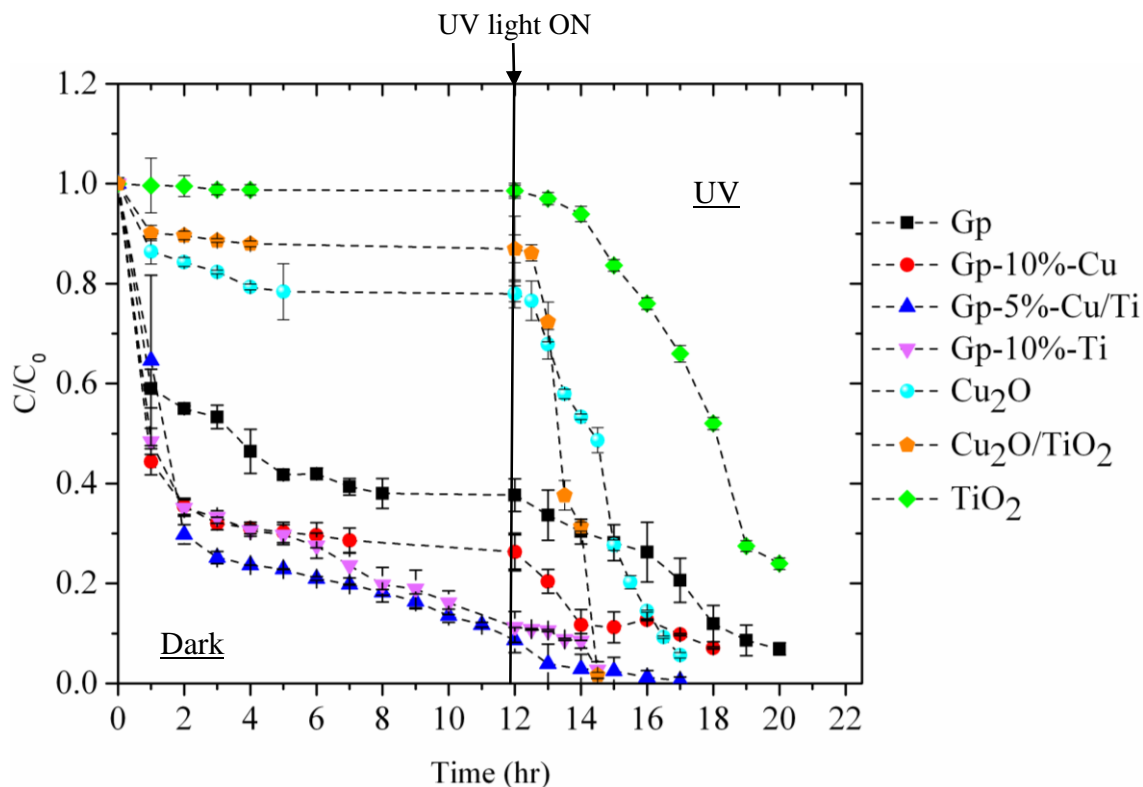
Figure 7.21. Plots of the residual concentration (C/C$_0$) vs. time (t) onto the M-GP, Cu$_2$O, TiO$_2$, Cu$_2$O/ iO$_2$, M-GP-10 wt% Cu$_2$O, M-GP-5 wt% Cu$_2$O/TiO$_2$, M-GP-10 wt% TiO$_2$ (monitored at 664 nm).

Figure 7.22 compares the removal of MB after 60 min. CTAB-modified geopolymer containing different percentages of TiO$_2$ and TiO$_2$ alone, in the dark and under UV irradiation. This figure confirms the removal of MB dye by photodegradation in the the CTAB-modified geopolymers containing 5-50 wt% is correspondingly effective and all these composites are more efficient than TiO$_2$ alone (Figure 7.22) The adsorption process is more efficient in the composites containing 15 wt% TiO$_2$ and the highest degree of MB removal by both the adsorption and photodegradation processes occurs in the CTAB-modified geopolymer containing 10 wt% TiO$_2$ contents.
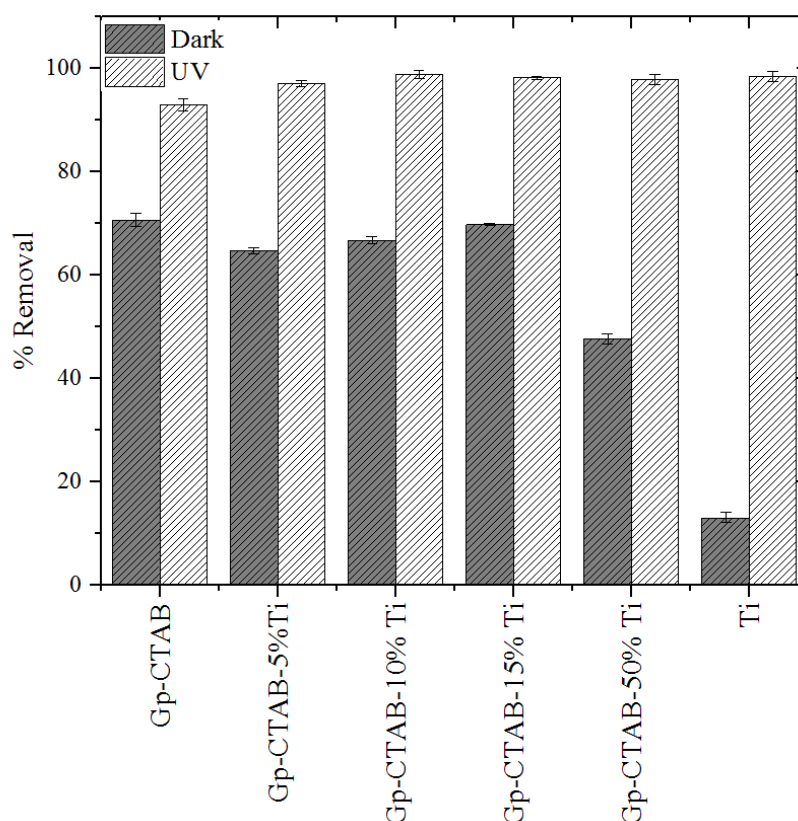
Figure 7.22. MB removal by the M-GP, M-GP-5,10,15 and 50 wt% TiO_2, TiO_2 alone after 60 min.

7.9.5 Nitrogen Adsorption/Desorption Isotherms

The nitrogen adsorption/desorption isotherms of these composites are shown in Figure 7.21. The specific surface areas derived from these isotherms (Table 7.8) show a major decrease from 16.14 m^2/g in the CTAB-modified geopolymer composite to 0.46 m^2/g in the composite containing 15 wt% TiO_2. This is possibly due to blocking of the pores by the TiO_2 particles, and is in marked contrast to the *increase* in surface area produced by the inclusion of 15 wt% Cu_2O (Table 7.6). The composites containing TiO_2 also show anomalous behaviour in their pore size and volume, the former being much larger than in the CTAB-modified matrix and the latter being much smaller than the matrix (Table 7.6). Both these effects may be understood in terms of the ready entry of the titania particles into the matrix, causing the pores to expand but blocking the access of the nitrogen gas to the pore surfaces, as reflected in the decreased BET surface area.
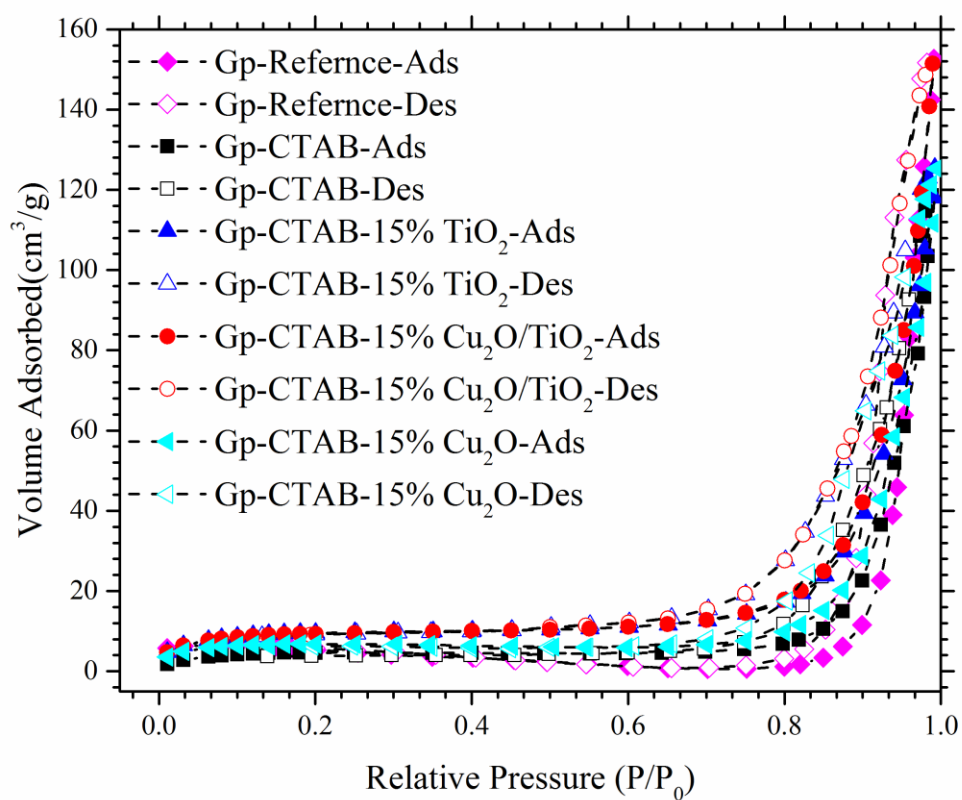
Figure 7.23. Nitrogen sorption isotherms of the GP (◆, adsorption◇, desorption), M-GP (■, adsorption□, desorption), M-GP-15 wt% TiO_2 (▲, adsorption△, desorption) M-GP-15 wt% Cu_2O(◀, adsorption◁, desorption)

Table 7.7. Specific surface areas and pore parameters of GP, M-GP and their composites containing TiO_2, Cu_2O and Cu_2O/TiO_2

	GP	M-GP	M-GP-15 wt% Cu_2O	M-GP-15 wt% Cu_2O/TiO_2	M-GP-15 wt% TiO_2
Single Point Surface Area	18.44 m²/g	16.14 m²/g	23.52 m²/g	32.54 m²/g	0.46 m²/g
S $_{BET}$	17.23 m²/g	17.02 m²/g	23.73 m²/g	33.57 m²/g	0.30 m²/g
S $_{Langmuir}$	21.92 m²/g	23.44 m²/g	31.95 m²/g	45.89 m²/g	0.32 m²/g
S $_{BJH\ Adsorption\ Cumulative}$	23.06 m²/g	21.41 m²/g	23.96 m²/g	31.09 m²/g	0.40 m²/g
S $_{BJH\ Desorption\ Cumulative}$	38.94 m²/g	33.63 m²/g	39.70 m²/g	47.77 m²/g	1.01m²/g
Volume					
Single Point Adsorption	0.24 cm³/g	0.18 cm³/g	0.19 cm³/g	0.23cm³/g	0.019 cm³/g
V $_{pore\ BJH\ Adsorption\ Cumulative}$	0.24 cm³/g	0.18 cm³/g	0.19 cm³/g	0.23 cm³/g	0.016 cm³/g
V $_{pore\ BJH\ Desorption\ Cumulative}$	0.24 cm³/g	0.18 cm³/g	0.19 cm³/g	0.23 cm³/g	0.018 cm³/g
Pore Size					
D $_{Adsorption}$	55 nm	43 nm	33 nm	28 nm	27 nm
D $_{BJH\ Adsorption}$	41 nm	34 nm	32 nm	30 nm	165 nm
D $_{BJH\ Desorption}$	24 nm	22 nm	20 nm	20 nm	71 nm

Conclusions

This chapter establishes the effective synthesis and structure of composites based on a combination of the most promising materials identified in the previous chapters, namely, a matrix of CTAB-modified geopolymer with a photoactive component of a spherical Cu_2O/TiO_2 nano-heterostructure. As in the previous chapters, SEM/EDS and TEM was used to confirm the homogenous distribution of the nano oxide particles within the geopolymer matrix and on the surface of the composite. The entry of the Cu_2O/TiO_2 nanoparticles into the

internal pores of the geopolymer matrix was evidenced by an increase of the composite surface area and a decrease of the pore size upon the addition of the oxide nanoparticles. As in the previous chapter, the use of CTAB to modify the pore structure and facilitate the ingress of the nano oxides also has the effect of maintaining a stable pH during MB dye removal from solution, and also permits the adsorption and desorption processes to be separately observed. The adsorption of MB by these CTAB-modified composites follows pseudo second-order kinetics and Freundlich-Langmuir type isotherms. The most effective composite in removing MB dye from solution under UV irradiation contains 5 wt% Cu_2O/TiO_2, representing the most efficient combination of the adsorption and photodegradation steps.

Chapter 8

Overall Conclusions from This Research and Possible Directions for Further Work

8.1 Conclusions from This Research

The initial aim of this research was to develop metakaolin-based geopolymer composites containing Cu_2O nanoparticles as the photoactive element able to remove organic pollutants from water or the atmosphere. The first part of the project was therefore to determine a suitable synthesis protocol for the Cu_2O oxide nanoparticles and to characterize their size and shape using electron microscopy. The synthesis method producing nanoparticles of the most suitable size ($\sim$ 100 nm) was found to be one that produced cubic morphologies. Composites of these cubic nanocrystals were prepared with a geoplymer matrix of standard composition ("unmodified geopolymer") by pre-synthesising the nanoparticles and mechanically mixing them with the geopolymer matrix prior to curing. The homogeneity of the oxide nanoparticle distribution within the geopolymer matrix was confirmed by SEM/EDS and TEM, while XRD, FTIR, ^{27}Al and ^{29}Si MAS NMR and ^{63}Cu NQR spectroscopy showed that the geopolymer matrix was well-reacted geopolymer matrix and was unaffected by the insertion of the Cu_2O nanoparticles. These composites proved to be very successful in removing from solution a model organic pollutant (MB dye, chosen for its colour stability at the high pH of the geopolymer matrix). The removal of the dye followed a two-step process, namely, adsorption by the geopolymer matrix (under dark conditions) and photodegradation by the Cu_2O (under UV illumination) but since these two processes occurred simultaneously, they could not be studied separately. The adsorption process carried out in the dark was shown to follow a pseudo-first order kinetic model and be described by an empirical Langmuir-type isotherm.

As an approach to improving the photocatalytic performance of these composites, a combination of Cu_2O with P25 TiO_2 in a 50% weight ratio as produced in the form of a nano-heterostructure, following a procedure documented in the literature. This Cu_2O/TiO_2 photoactive component was incorporated in varying amounts in the unmodified geopolymer matrix, and the resulting composites proved to have improved photoactivity over composites

containing either Cu_2O or TiO_2 alone, although the dual processes of dye adsorption and photodegradation were still indistinguishable, being a property of the matrix rather than the photoactive element. As with the composites containing Cu_2O alone, the pseudo-first-order kinetic model was more appropriate for describing the adsorption data, and they were also best described by a Langmuir-type isotherm.

Attention was then turned to the effect of the geopolymer matrix on the performance of these composites, and a novel approach was adopted to modify the geopolymer structure by the use of the large quaternary ammonium cation CTAB. This had not previously been used with geopolymers, but proved to be successful in acting as a pH buffer, enabling the two processes of dye adsorption and photodegradation to be distinguished by allowing the adsorption step to reach equilibrium under dark conditions before phototodegradation under UV illumination. By contrast with the composites of unmodified geopolymer matrices, the dye adsorption kinetics on composites with CTAB-modified geopolymer matrices followed a pseudo-second order kinetic model and could be described by Freundlich-Langmuir type isotherms.

N_2 adsorption-desorption isotherms of the composites formed using the CTAB-modified geopolymer matrix showed thir specific surface areas to increase significantly with the insertion of the photoactive Cu_2O/TiO_2 nano-heterostructures, suggesting that the modified matrix structure facilitates the entry of the nano oxides into the matrix. On the other hand, the average pore diameters decrease significantly with the entry of the nano oxides, possibly due to blocking of the pores by the oxide nanoparticles.

The photoactive efficiency of these composites was found to depend on a number of factors, including the content of the photactive component, in addition to the nature of the photocatalyst and the matrix, which was capable of removing >99% of MB dye under UV irradiation.

Overall, the most effective composite in removing MB dye from solution under UV irradiation contained 5 wt% Cu_2O/TiO_2, supported on a CTAB-modified geopolymer matrix, which was capable of removing >98% of the dye under UV irradiation after 4 hour.

These results demonstrate that composites of nanosized Cu_2O particles combined with photoreactive TiO_2 supported by an aluminosilicate geopolymer matrix modified with CTAB constitute new and novel materials with potential environmental protection applications to efficiently remove organic pollutants from water or the atmosphere.

To summarise,

Composites of nanoparticle sized Cu_2O in a geopolymer matrix have successfully been synthesised and their structures characterized before and after their use as photocatalysts, using XRD, SEM, TEM, FTIR, MAS NMR and ^{63}Cu NQR

These composites act to photodegrade a model organic chemical (MB dye) by a dual mechanism of adsorption and photodegradation which cannot be distinguished but the kinetics of dye adsorption on the matrix could be measured under dark conditions.

More efficient removal of MB dye was achieved using a photoactive nano-heterostructure of Cu_2O and TiO_2 in the geopolymer matrix

Modification of the geopolymer matrix with CTAB enables the two processes of adsorption and photodegradation to be distinguished and produces even more efficient removal of MB from solution.

8.2 Recommendations for Future Work

Based on the results and conclusions of this present study, it is recommended that the following possibilities be further investigated in future studies:

Other combinations of small band gap semiconducting oxides could be tried with the CTAB-modified geopolymer matrix to improve the photoactivity of the composite.

Experiments could be carried out under solar radiation wavelengths to develop photoactive devices of greater efficiency under real conditions.

Additional modification studies could be carried out to explore other means of modifying the geopolymer matrix to improve its acceptance of oxide nanoparticles and improve the photocatalytic properties of the resulting composites.

The use of CTAB could be investigated to modify the structure of other geopolymer matrices derived from even cheaper materials, e.g. fly ash.

The next major challenge in the development of "green" geopolymer concrete is to incorporate the metal oxides into coatings for building materials and apply the principles developed here to practical situations.

Bibliography

1.   N. P. Rajamane, N. L., Nataraja M C Geopolymer Concrete - A New Eco-friendly Material of Construction. http://www.nbmcw.com/articles/concrete/10827-geopolymer-concrete-a-new-eco-friendly-material-of-construction.html

2.   Smog, S., Concrete that Cleans itself and the Air. *Concrete international* **2009**, 31.

3.   Biello, D., Cement from CO_2: a concrete cure for global warming. *Scientific American* **2008**.

4.   Hardjito, D.; Pui, N. T., The Use of Fly Ash to Reduce the Environmental Impact of Concrete.

5.   Giussani, B. A Concrete Step Toward Cleaner Air. http://www.businessweek.com/stories/**2006**-11-08/a-concrete-step-toward-cleaner-airbusinessweek-business-news-stock-market-and-financial-advice

6.   Cassar, L., Pepe, C., Tognon, G., Guerrini, G.L. and Amadelli, R., White cement for architectural concrete, possessing photocatalytic properties. In *Chemistry of Cement*, Durban/South Africa, **2012**; Vol. 4.

7.   Italcementi The Photocatalytic Active Principle. http://www.italcementigroup.com/NR/rdonlyres/96036B14-4C6D-4E07-9854-1B1CE1AD6593/0/TXactivetechnicalreport **2009**.pdf

8.   Elvin, G. *Nanotechnology for Green Building* Green Technology Forum: Wiley and Princeton Architectural Press, **2007**.

9.   Chen, D.; Zhu, Q.; Zhou, F.; Deng, X.; Li, F., Synthesis and photocatalytic performances of the TiO 2 pillared montmorillonite. *Journal of hazardous materials* **2012,** *235*, 186-193.

10.   Kuo, C.-H.; Huang, M. H., Morphologically controlled synthesis of Cu_2O nanocrystals and their properties. *Nano Today* **2010,** *5*, 106-116.

11.   Pollack, G.; Trivich, D., Photoelectric properties of cuprous oxide. *Journal of Applied Physics* **1975,** *46*, 163-172.

12.   Yang, H.; Ouyang, J.; Tang, A.; Xiao, Y.; Li, X.; Dong, X.; Yu, Y., Electrochemical synthesis and photocatalytic property of cuprous oxide nanoparticles. *Materials Research Bulletin* **2006,** *41*, 1310-1318.

13.   Huang, L.; Peng, F.; Yu, H.; Wang, H., Preparation of cuprous oxides with different sizes and their behaviors of adsorption, visible-light driven photocatalysis and photocorrosion. *Solid State Sciences* **2009,** *11*, 129-138.

14.   Chang, Y.; Teo, J. J.; Zeng, H. C., Formation of Colloidal CuO Nanocrystallites and Their Spherical Aggregation and Reductive Transformation to Hollow Cu_2O Nanospheres. *Langmuir* **2004,** *21*, 1074-1079.

15.   Legrini, O.; Oliveros, E.; Braun, A. M., Photochemical processes for water treatment. *Chemical Reviews* **1993,** *93*, 671-698.

16. Mills, A.; Davies, R. H.; Worsley, D., Water purification by semiconductor photocatalysis. *Chemical Society Reviews* **1993,** *22*, 417-425.

17. Robert, D.; Malato, S., Solar photocatalysis: a clean process for water detoxification. *Science of the total environment* **2002,** *291*, 85-97.

18. Nick Serpone, E. P., *Photocatalysis: Fundamentals and Applications*. New York [u.a.]: 1989.

19. Beeldens, A., An environmental friendly solution for air purification and self-cleaning effect: the application of TiO_2 as photocatalyst in concrete. In *International Conference on Concrete Block Paving*, San Francisco, California USA, **2006**.

20. S.E Braslavsky, K. N. H., Glossary of Terms used in Photochemstry. *Pure Appl. Chem.* **1988,** *60*, 1055-1106.

21. Fujishima, A., Electrochemical photolysis of water at a semiconductor electrode. *Nature* **1972,** *238*, 37-38.

22. Zhao, J.; Yang, X., Photocatalytic oxidation for indoor air purification: a literature review. *Building and Environment* **2003,** *38*, 645-654.

23. Linsebigler, A. L.; Lu, G. Q.; Yates, J. T., Photocatalysis on TiO_2 Surfaces - Principles, Mechanisms, and Selected Results. *Chemical Reviews* **1995,** *95*, 735-758.

24. Herrmann, J.-M., Heterogeneous photocatalysis: fundamentals and applications to the removal of various types of aqueous pollutants. *Catalysis Today* **1999,** *53*, 115-129.

25. Dr. N . K. Verma, P. S. K. K. D. B. K., *Comprehensive Chemistry XII*. Laxmi Publications.

26. Farnetti, E.; Di Monte, R.; Kašpar, J., Homogeneous and Heterogeneous Catalysis.

27. S. L. Kakani, K. C. B., *Electronics Theory And Applications*. New Age International Ltd. Pub: New Delhi, **2005**.

28. Kittel, C., *Introduction to solid state physics,*. 8de ed.; Wiley: Hoboken, NJ 2005.

29. Emeline, A. V.; Ryabchuk, V.; Serpone, N., Factors affecting the efficiency of a photocatalyzed process in aqueous metal-oxide dispersions: Prospect of distinguishing between two kinetic models. *Journal of Photochemistry and Photobiology A: Chemistry* **2000,** *133*, 89-97.

30. Yoder, M. N., Wide bandgap semiconductor materials and devices. *Ieee Transactions on Electron Devices* **1996,** *43*, 1633-1636.

31. Alfano, O. M.; Bahnemann, D.; Cassano, A. E.; Dillert, R.; Goslich, R., Photocatalysis in water environments using artificial and solar light. *Catalysis Today* **2000,** *58*, 199-230.

32. Xu, H.; Van Deventer, J. S. J., The geopolymerisation of alumino-silicate minerals. *International Journal of Mineral Processing* **2000,** *59*, 247-266.

33. Litter, M. I.; Navío, J. A., Photocatalytic properties of iron-doped titania semiconductors. *Journal of Photochemistry and Photobiology A: Chemistry* **1996,** *98*, 171-181.

34. Hoffmann, M. R.; Martin, S. T.; Choi, W.; Bahnemann, D. W., Environmental Applications of Semiconductor Photocatalysis. *Chemical Reviews* **1995,** *95*, 69-96.

35.   Peral, J.; Domènech, X.; Ollis, D. F., Heterogeneous Photocatalysis for Purification, Decontamination and Deodorization of Air. *Journal of Chemical Technology & Biotechnology* **1997,** *70*, 117-140.

36.   Litter, M. I., Heterogeneous photocatalysis: Transition metal ions in photocatalytic systems. *Applied Catalysis B: Environmental* **1999,** *23*, 89-114.

37.   Saien, J.; Soleymani, A. R., Feasibility of using a slurry falling film photo-reactor for individual and hybridized AOPs. *Journal of Industrial and Engineering Chemistry* **2012,** *18*, 1683-1688.

38.   Chen, F.; Xie, Y.; Zhao, J.; Lu, G., Photocatalytic degradation of dyes on a magnetically separated photocatalyst under visible and UV irradiation. *Chemosphere* **2001,** *44*, 1159-1168.

39.   Galindo, C.; Jacques, P.; Kalt, A., Photodegradation of the aminoazobenzene acid orange 52 by three advanced oxidation processes: UV/H_2O_2, UV/TiO_2 and VIS/TiO_2: Comparative mechanistic and kinetic investigations. *Journal of Photochemistry and Photobiology A: Chemistry* **2000,** *130*, 35-47.

40.   Peill, N. J.; Hoffmann, M. R., Mathematical Model of a Photocatalytic Fiber-Optic Cable Reactor for Heterogeneous Photocatalysis. *Environmental Science & Technology* **1998,** *32*, 398-404.

41.   Zaleska, A., Doped-TiO_2: a review. *Recent Patents on Engineering* **2008,** *2*, 157-164.

42.   Konstantinou, I. K.; Albanis, T. A., TiO_2 assisted photocatalytic degradation of azo dyes in aqueous solution: kinetic and mechanistic investigations: A review. *Applied Catalysis B: Environmental* **2004,** *49*, 1-14.

43.   Houas, A.; Lachheb, H.; Ksibi, M.; Elaloui, E.; Guillard, C.; Herrmann, J.-M., Photocatalytic degradation pathway of methylene blue in water. *Applied Catalysis B: Environmental* **2001,** *31*, 145-157.

44.   Rauf, M.; Ashraf, S. S., Fundamental principles and application of heterogeneous photocatalytic degradation of dyes in solution. *Chemical Engineering Journal* **2009,** *151*, 10-18.

45.   Zhang, J.; Liu, J.; Peng, Q.; Wang, X.; Li, Y., Nearly Monodisperse Cu_2O and CuO Nanospheres: Preparation and Applications for Sensitive Gas Sensors. *Chemistry of Materials* **2006,** *18*, 867-871.

46.   Zhao, Z. Y.; He, X. J.; Yi, J.; Ma, C. S.; Cao, Y. C.; Qiu, J. B., First-principles study on the doping effects of nitrogen on the electronic structure and optical properties of Cu_2O. *RSC Advances* **2013,** *3*, 84-90.

47.   Poizot, P.; Laruelle, S.; Grugeon, S.; Dupont, L.; Tarascon, J., Nano-sized transition-metal oxides as negative-electrode materials for lithium-ion batteries. *Nature* **2000,** *407*, 496-499.

48.   Hara, M.; Kondo, T.; Komoda, M.; Ikeda, S.; Shinohara, K.; Tanaka, A.; Kondo, J. N.; Domen, K., Cu_2O as a photocatalyst for overall water splitting under visible light irradiation. *Chemical Communications* **1998**, 357-358.

49.   Briskman, R. N., A study of electrodeposited cuprous oxide photovoltaic cells. *Solar Energy Materials and Solar Cells* **1992,** *27*, 361-368.

50.   Martínez-Ruiz, A.; Moreno, M. G.; Takeuchi, N., First principles calculations of the electronic properties of bulk Cu_2O, clean and doped with Ag, Ni, and Zn. *Solid State Sciences* **2003,** *5*, 291-295.

51.   Yao, X.; Zhang, Z.; Zhu, H.; Chen, Y., Geopolymerization process of alkali–metakaolinite characterized by isothermal calorimetry. *Thermochimica Acta* **2009,** *493*, 49-54.

52.   Kiaune, L.; Singhasemanon, N., Pesticidal copper (I) oxide: environmental fate and aquatic toxicity. *Rev Environ Contam Toxicol* **2011,** *213*, 1-26.

53.   Zhang, D. F.; Zhang, H.; Guo, L.; Zheng, K.; Han, X. D.; Zhang, Z., Delicate control of crystallographic facet-oriented Cu_2O nanocrystals and the correlated adsorption ability. *Journal of Materials Chemistry* **2009,** *19*, 5220-5225.

54.   Xiong, Y.; Wiley, B. J.; Xia, Y., Nanocrystals with unconventional shapes--a class of promising catalysts. *Angew Chem Int Ed Engl* **2007,** *46*, 7157-9.

55.   Zhang, Y.; Deng, B.; Zhang, T. R.; Gao, D. M.; Xu, A. W., Shape Effects of Cu_2O Polyhedral Microcrystals on Photocatalytic Activity. *Journal of Physical Chemistry C* **2010,** *114*, 5073-5079.

56.   Ho, J. Y.; Huang, M. H., Synthesis of Submicrometer-Sized Cu_2O Crystals with Morphological Evolution from Cubic to Hexapod Structures and Their Comparative Photocatalytic Activity. *Journal of Physical Chemistry C* **2009,** *113*, 14159-14164.

57.   Takata, T.; Furumi, Y.; Shinohara, K.; Tanaka, A.; Hara, M.; Kondo, J. N.; Domen, K., Photocatalytic Decomposition of Water on Spontaneously Hydrated Layered Perovskites. *Chemistry of Materials* **1997,** *9*, 1063-1064.

58.   Domen, K.; Kondo, J. N.; Hara, M.; Takata, T., Photo-and Mechano-Catalytic Overall Water Splitting Reactions to Form Hydrogen and Oxygen on Heterogeneous Catalysts. *Bulletin of the Chemical Society of Japan* **2000,** *73*, 1307-1331.

59.   Fernando, C. A. N.; Bandara, T. M. W. J.; Wethasingha, S. K., H2 evolution from a photoelectrochemical cell with n-Cu_2O photoelectrode under visible light irradiation. *Solar Energy Materials and Solar Cells* **2001,** *70*, 121-129.

60.   Senevirathna, M.; Pitigala, P.; Tennakone, K., Water photoreduction with Cu_2O quantum dots on TiO_2 nano-particles. *Journal of Photochemistry and Photobiology A: Chemistry* **2005,** *171*, 257-259.

61.   Siripala, W.; Ivanovskaya, A.; Jaramillo, T. F.; Baeck, S. H.; McFarland, E. W., A Cu_2O/TiO_2 heterojunction thin film cathode for photoelectrocatalysis. *Solar Energy Materials and Solar Cells* **2003,** *77*, 229-237.

62.   Duxson, P.; Provis, J. L.; Lukey, G. C.; Mallicoat, S. W.; Kriven, W. M.; van Deventer, J. S. J., Understanding the relationship between geopolymer composition, microstructure and mechanical properties. *Colloids and Surfaces A: Physicochemical and Engineering Aspects* **2005,** *269*, 47-58.

63.   Lu, C. H.; Qi, L. M.; Yang, J. H.; Wang, X. Y.; Zhang, D. Y.; Xie, J. L.; Ma, J. M., One-pot synthesis of octahedral Cu_2O nanocages via a catalytic solution route. *Advanced Materials* **2005,** *17*, 2562-+.

64.   Luo, F.; Wu, D.; Gao, L.; Lian, S.; Wang, E.; Kang, Z.; Lan, Y.; Xu, L., Shape-controlled synthesis of Cu_2O nanocrystals assisted by Triton X-100. *Journal of Crystal Growth* **2005,** *285*, 534-540.

65.   Luo, F.; Wu, D.; Gao, L.; Lian, S.; Wang, E.; Kang, Z.; Lan, Y.; Xu, L., Shape-controlled synthesis of Cu_2O nanocrystals assisted by Triton X-100. *Journal of Crystal Growth* **2005,** *285*, 534-540.

66.   Li, J.; Liu, L.; Yu, Y.; Tang, Y.; Li, H.; Du, F., Preparation of highly photocatalytic active nano-size TiO_2–Cu_2O particle composites with a novel electrochemical method. *Electrochemistry Communications* **2004,** *6*, 940-943.

67.   Shi, H.; Yu, K.; Sun, F.; Zhu, Z. Q., Controllable synthesis of novel Cu_2O micro/nano-crystals and their photoluminescence, photocatalytic and field emission properties. *CrystEngComm* **2012,** *14*, 278-285.

68.   Gratzel, M., Photoelectrochemical cells. *Nature* **2001,** *414*, 338-44.

69.   Lu, X.; Xie, S.; Yang, H.; Tong, Y.; Ji, H., Photoelectrochemical hydrogen production from biomass derivatives and water. *Chemical Society Reviews* **2014,** *43*, 7581-7593.

70.   Xie, S.; Zhai, T.; Li, W.; Yu, M.; Liang, C.; Gan, J.; Lu, X.; Tong, Y., Hydrogen production from solar driven glucose oxidation over Ni(OH)2 functionalized electroreduced-TiO_2 nanowire arrays. *Green Chemistry* **2013,** *15*, 2434-2440.

71.   Esposito, D. V.; Forest, R. V.; Chang, Y.; Gaillard, N.; McCandless, B. E.; Hou, S.; Lee, K. H.; Birkmire, R. W.; Chen, J. G., Photoelectrochemical reforming of glucose for hydrogen production using a WO3-based tandem cell device. *Energy & Environmental Science* **2012,** *5*, 9091-9099.

72.   Wang, G.; Ling, Y.; Lu, X.; Zhai, T.; Qian, F.; Tong, Y.; Li, Y., A mechanistic study into the catalytic effect of $Ni(OH)_2$ on hematite for photoelectrochemical water oxidation. *Nanoscale* **2013,** *5*, 4129-4133.

73.   Hoang, S.; Guo, S.; Hahn, N. T.; Bard, A. J.; Mullins, C. B., Visible Light Driven Photoelectrochemical Water Oxidation on Nitrogen-Modified TiO_2 Nanowires. *Nano Letters* **2012,** *12*, 26-32.

74.   Zheng, Z. K.; Huang, B. B.; Wang, Z. Y.; Guo, M.; Qin, X. Y.; Zhang, X. Y.; Wang, P.; Dai, Y., Crystal Faces of Cu_2O and Their Stabilities in Photocatalytic Reactions. *Journal of Physical Chemistry C* **2009,** *113*, 14448-14453.

75.   de Jongh, P. E.; Vanmaekelbergh, D.; Kelly, J. J., Cu_2O: Electrodeposition and Characterization. *Chemistry of Materials* **1999,** *11*, 3512-3517.

76.   Dong, J.; Xu, H.; Zhang, F.; Chen, C.; Liu, L.; Wu, G., Synergistic effect over photocatalytic active Cu_2O thin films and their morphological and orientational transformation under visible light irradiation. *Applied Catalysis A: General* **2014,** *470*, 294-302.

77.   Aazam, E. S.; Mohamed, R. M., Environmental remediation of Direct Blue dye solutions by photocatalytic oxidation with cuprous oxide. *Journal of Alloys and Compounds* **2013,** *577*, 550-555.

78.   Fujishima, A.; Rao, T. N.; Tryk, D. A., Titanium dioxide photocatalysis. *Journal of Photochemistry and Photobiology C: Photochemistry Reviews* **2000,** *1*, 1-21.

79.   Domen, K.; Kondo, J. N.; Hara, M.; Takata, T., Photo- and Mechano-Catalytic Overall Water Splitting Reactions to Form Hydrogen and Oxygen on Heterogeneous Catalysts. *Bulletin of the Chemical Society of Japan* **2000,** *73*, 1307-1331.

80.   Senevirathna, M. K. I.; Pitigala, P. K. D. D. P.; Tennakone, K., Water photoreduction with Cu 2O quantum dots on TiO_2 nano-particles. *Journal of Photochemistry and Photobiology A-chemistry* **2005,** *171*, 257-259.

81.   Liu, L.; Yang, W.; Li, Q.; Gao, S.; Shang, J. K., Synthesis of Cu_2O Nanospheres Decorated with TiO_2 Nanoislands, Their Enhanced Photoactivity and Stability under Visible Light Illumination, and Their Post-illumination Catalytic Memory. *ACS Appl Mater Interfaces* **2014,** *6*, 5629-5639.

82.   Helaïli, N.; Bessekhouad, Y.; Bouguelia, A.; Trari, M., Visible light degradation of Orange II using xCuyOz/TiO_2 heterojunctions. *Journal of hazardous materials* **2009,** *168*, 484-492.

83.   Han, C.; Li, Z.; Shen, J., Photocatalytic degradation of dodecyl-benzenesulfonate over TiO_2–Cu_2O under visible irradiation. *Journal of hazardous materials* **2009,** *168*, 215-219.

84.   Bessekhouad, Y.; Robert, D.; Weber, J. V., Photocatalytic activity of Cu_2O/TiO_2, Bi_2O_3/TiO_2 and $ZnMn_2O_4/TiO_2$ heterojunctions. *Catalysis Today* **2005,** *101*, 315-321.

85.   Huang, L.; Peng, F.; Wang, H.; Yu, H.; Li, Z., Preparation and characterization of Cu_2O/TiO_2 nano–nano heterostructure photocatalysts. *Catalysis Communications* **2009,** *10*, 1839-1843.

86.   Xue, J.; Shen, Q.; Liang, W.; Liu, X.; Xu, B., Controlled synthesis of coaxial core–shell TiO_2/Cu_2O heterostructures by electrochemical method and their photoelectrochemical properties. *Materials Letters* **2013,** *92*, 239-242.

87.   Du, Y.; Rabani, J., The Measure of TiO_2 Photocatalytic Efficiency and the Comparison of Different Photocatalytic Titania. *The Journal of Physical Chemistry B* **2003,** *107*, 11970-11978.

88.   Mitchell, J. K.; Soga, K., Fundamentals of soil behavior. *Wiley, New York* **2005**.

89.   Salvador, S., Pozzolanic Properties of Flash-Calcined Kaolinite - a Comparative-Study with Soak-Calcined Products. *Cement and Concrete Research* **1995,** *25*, 102-112.

90.   Grim, R. E., *Applied clay mineralogy*. **1962**.

91.   Zhang, G.; He, J.; Gambrell, R. P., Synthesis, characterization, and mechanical properties of red mud-based geopolymers. *Transportation Research Record: Journal of the Transportation Research Board* **2010,** *2167*, 1-9.

92. Y. Zhang, W. S., Z. Li, Hydrogen process of potassium polysialate (K-PSDS) geopolymer cement. **2004,** *15*.

93. Kriven, W. M., Inorganic polysialates or 'geopolymers'. *American Ceramic Society Bulletin* **2010,** *89*, 31-34.

94. Barbosa, V. F. F.; MacKenzie, K. J. D., Synthesis and thermal behaviour of potassium sialate geopolymers. *Materials Letters* **2003,** *57*, 1477-1482.

95. Malone, P. G., Kirkpatrick, T., and Randall, C. A., *Potential Applications of Alkali-Activated alumino-silicate binders in military applications*. US Army Corps of Engineers, **1986**.

96. Lyon, R. E., Balaguru, P. N., Foden, A., Sorathia, U., Davidovits, J. and Davidovics, M., Fire-resistant Aluminosilicate Composites. *Fire and materials* **1997,** *21*, 67-73.

97. Giancaspro, J., Balaguru, P., and Lyon, R., Use of Inorganic Polymer to Improve the Fire Response of Balsa Sandwich Structures. *Journal of Materials in Civil Engineering* **2006,** *18*, 390-397.

98. Balaguru, P. *Geopolymer for protective coating of transportation infrastructures*; **1998**.

99. Buchwald, A.; Hohmann, M.; Kaps, C.; Bettzieche, H.; Kuhnert, J. T. In *Stabilised Foam Clay Material with High Performance Thermal Insulation Properties*, Ceramic Forum International, **2004**.

100. Bell, J.; Gordon, M.; Kriven, W., Use of Geopolymeric Cements as a Refractory Adhesive for Metal and Ceramic Joins. In *Advances in Ceramic Coatings and Ceramic-Metal Systems: Ceramic Engineering and Science Proceedings*, John Wiley & Sons, Inc.: **2008**; pp 407-413.

101. Zhang, S.; Gong, K.; Lu, J., Novel modification method for inorganic geopolymer by using water soluble organic polymers. *Materials Letters* **2004,** *58*, 1292-1296.

102. Li, Z.; Zhang, Y.; Zhou, X., Short fiber reinforced geopolymer composites manufactured by extrusion. *Journal of Materials in Civil Engineering* **2005,** *17*, 624-631.

103. Allahverdi, A.; Mehrpour, K.; Kani, E. N., Investigating the possibility of utilizing pumice-type natural pozzonal in production of geopolymer cement. *Ceramics-Silikaty* **2008,** *52*, 16.

104. Verdolotti, L.; Iannace, S.; Lavorgna, M.; Lamanna, R., Geopolymerization reaction to consolidate incoherent pozzolanic soil. *Journal of Materials Science* **2008,** *43*, 865-873.

105. Davidovits, J., Geopolymers - Inorganic polymeric new materials. *Journal of Thermal Analysis* **1991,** *37*, 1633-1656.

106. Duxson, P.; Fernández-Jiménez, A.; Provis, J.; Lukey, G.; Palomo, A.; van Deventer, J. S. J., Geopolymer technology: the current state of the art. *Journal of Materials Science* **2007,** *42*, 2917-2933.

107. Van Jaarsveld, J.; Van Deventer, J.; Lukey, G., The effect of composition and temperature on the properties of fly ash-and kaolinite-based geopolymers. *Chemical Engineering Journal* **2002,** *89*, 63-73.

108.   Swanepoel, J.; Strydom, C., Utilisation of fly ash in a geopolymeric material. *Applied Geochemistry* **2002,** *17*, 1143-1148.

109.   Khale, D.; Chaudhary, R., Mechanism of geopolymerization and factors influencing its development: a review. *Journal of Materials Science* **2007,** *42*, 729-746.

110.   Ramón Gasca-Tirado, J.; Manzano-Ramírez, A.; Villaseñor-Mora, C.; Muñiz-Villarreal, M.; Sampieri-Bulbarela, S.; Rubio-Ávalos, J.; Amigó Borrás, V.; Mendoza, R. N., Incorporation of photoactive TiO_2 in an aluminosilicate inorganic polymer by Ion exchange. *Microporous and Mesoporous Materials* **2011**.

111.   Lange, J. P.; Klier, K., Uv-Vis-Nir Studies of Fe(Ii)-a-Zeolite. *Zeolites* **1994,** *14*, 462-468.

112.   Palomo, A.; Grutzeck, M.; Blanco, M., Alkali-activated fly ashes: A cement for the future. *Cement and Concrete Research* **1999,** *29*, 1323-1329.

113.   Davidovits, J., Geopolymers: Man-Made Rock Geosynthesis and the Resulting Development of Very Early High Strength Cement. *Journal of Material Education* **1994,** *16*, 91-137.

114.   MacKenzie, K. J. D.; Brew, D.; Fletcher, R.; Nicholson, C.; Vagana, R.; Schmücker, M., Advances in Understanding the Synthesis Mechanisms of New Geopolymeric Materials. *In Novel Processing of Ceramics and Composites*, John Wiley & Sons, Inc.: **2006**; pp 185-199.

115.   Olivia, M.; Nikraz, H. R., Strength and Water Penetrability of Fly Ash Geopolymer Concrete. *Parameters* **2006,** *1*, 3.

116.   Davidovits, J., Geopolymer Chemistry and Properties. In *First European Conference on Soft Mineralurgy*, Orlinski, J. D. a. J., Ed. Geopolymer Institute and Technical University, Compiègne, France, **1988**; pp 25-48.

117.   Davidovits, J., Geopolymers. *Journal of Thermal Analysis and Calorimetry* **1991,** *37*, 1633-1656.

118.   Xu, H. Geopolymerization of Aluminosilicate Minerals. University of Melbourne, **2002**.

119.   Xu, H.; Van Deventer, J., The geopolymerisation of alumino-silicate minerals. *International Journal of Mineral Processing* **2000,** *59*, 247-266.

120.   Rowles, M. R.; Hanna, J. V.; Pike, K. J.; Smith, M. E.; O'Connor, B. H., Si-29, Al-27, H-1 and Na-23 MAS NMR study of the bonding character in aluminosilicate inorganic polymers. *Applied Magnetic Resonance* **2007,** *32*, 663-689.

121.   Barbosa, V. F.; MacKenzie, K. J.; Thaumaturgo, C., Synthesis and characterisation of materials based on inorganic polymers of alumina and silica: sodium polysialate polymers. *International Journal of Inorganic Materials* **2000,** *2*, 309-317.

122.   Barbosa, V. F.; MacKenzie, K. J., Thermal behaviour of inorganic geopolymers and composites derived from sodium polysialate. *Materials Research Bulletin* **2003,** *38*, 319-331.

123.   Barbosa, V. F. F.; MacKenzie, K. J. D.; Thaumaturgo, C., Synthesis and characterisation of materials based on inorganic polymers of alumina and silica: sodium polysialate polymers. *International Journal of Inorganic Materials* **2000,** *2*, 309-317.

124. MacKenzie, K., Applications of solid state NMR spectroscopy to ceramic research. *British ceramic transactions* **2000,** *99*, 231-240.

125. Miao, S.; Liu, Z.; Han, B.; Zhang, J.; Yu, X.; Du, J.; Sun, Z., Synthesis and characterization of TiO$_2$-montmorillonite nanocomposites and their application for removal of methylene blue. *Journal of Materials Chemistry* **2006,** *16*, 579-584.

126. Gasca-Tirado, J. R.; Manzano-Ramírez, A.; Villaseñor-Mora, C.; Muñiz-Villarreal, M. S.; Zaldivar-Cadena, A. A.; Rubio-Ávalos, J. C.; Borrás, V. A.; Mendoza, R. N., Incorporation of photoactive TiO$_2$ in an aluminosilicate inorganic polymer by ion exchange. *Microporous and Mesoporous Materials* **2012,** *153*, 282-287.

127. Gasca-Tirado, J.; Manzano-Ramírez, A.; Vazquez-Landaverde, P.; Herrera-Díaz, E.; Rodríguez-Ugarte, M.; Rubio-Ávalos, J.; Amigó-Borrás, V.; Chávez-Páez, M., Ion-exchanged geopolymer for photocatalytic degradation of a volatile organic compound. *Materials Letters* **2014,** *134*, 222-224.

128. Černý, Z.; Jakubec, I.; Bezdička, P.; Štengl, V., Preparation of Photocatalytic Layers Based on Geopolymer. In *Developments in Strategic Materials: Ceramic Engineering and Science Proceedings, Volume 29, Issue 10*, John Wiley & Sons, Inc.: 2009; pp 113-121.

129. Anderson, C.; Bard, A. J., An Improved Photocatalyst of TiO$_2$/SiO$_2$ Prepared by a Sol-Gel Synthesis. *The Journal of Physical Chemistry* **1995,** *99*, 9882-9885.

130. Anpo, M.; Nakaya, H.; Kodama, S.; Kubokawa, Y.; Domen, K.; Onishi, T., Photocatalysis over binary metal oxides. Enhancement of the photocatalytic activity of titanium dioxide in titanium-silicon oxides. *The Journal of Physical Chemistry* **1986,** *90*, 1633-1636.

131. Anderson, C.; Bard, A. J., Improved Photocatalytic Activity and Characterization of Mixed TiO$_2$/SiO$_2$ and TiO$_2$/Al$_2$O$_3$ Materials. *The Journal of Physical Chemistry B* **1997,** *101*, 2611-2616.

132. Minero, C.; Catozzo, F.; Pelizzetti, E., Role of adsorption in photocatalyzed reactions of organic molecules in aqueous titania suspensions. *Langmuir* **1992,** *8*, 481-486.

133. Yoneyama, H.; Torimoto, T., Titanium dioxide/adsorbent hybrid photocatalysts for photodestruction of organic substances of dilute concentrations. *Catalysis Today* **2000,** *58*, 133-140.

134. Yuan, R.; Guan, R.; Shen, W.; Zheng, J., Photocatalytic degradation of methylene blue by a combination of TiO$_2$ and activated carbon fibers. *Journal of Colloid and Interface Science* **2005,** *282*, 87-91.

135. Mogyorósi, K.; Farkas, A.; Dékány, I.; Ilisz, I.; Dombi, A., TiO$_2$-Based Photocatalytic Degradation of 2-Chlorophenol Adsorbed on Hydrophobic Clay. *Environmental Science & Technology* **2002,** *36*, 3618-3624.

136. Shimizu, K.-I.; Kaneko, T.; Fujishima, T.; Kodama, T.; Yoshida, H.; Kitayama, Y., Selective oxidation of liquid hydrocarbons over photoirradiated TiO$_2$ pillared clays. *Applied Catalysis A: General* **2002,** *225*, 185-191.

137.   Yamashita, H.; Ichihashi, Y.; Anpo, M.; Hashimoto, M.; Louis, C.; Che, M., Photocatalytic Decomposition of NO at 275 K on Titanium Oxides Included within Y-Zeolite Cavities: The Structure and Role of the Active Sites. *The Journal of Physical Chemistry* **1996,** *100*, 16041-16044.

138.   Bhattacharyya, A.; Kawi, S.; Ray, M. B., Photocatalytic degradation of orange II by TiO_2 catalysts supported on adsorbents. *Catalysis Today* **2004,** *98*, 431-439.

139.   Miao, S.; Liu, Z.; Han, B.; Zhang, J.; Yu, X.; Du, J.; Sun, Z., Synthesis and characterization of TiO 2–montmorillonite nanocomposites and their application for removal of methylene blue. *Journal of Materials Chemistry* **2006,** *16*, 579-584.

140.   Shichi, T.; Takagi, K., Clay minerals as photochemical reaction fields. *Journal of Photochemistry and Photobiology C: Photochemistry Reviews* **2000,** *1*, 113-130.

141.   MacKenzie, K. J.; Bradley, S.; Hanna, J. V.; Smith, M. E., Magnesium analogues of aluminosilicate inorganic polymers (geopolymers) from magnesium minerals. *Journal of Materials Science* **2013,** *48*, 1787-1793.

142.   Aranda, P.; Kun, R.; Martín-Luengo, M. A.; Letaïef, S.; Dékány, I.; Ruiz-Hitzky, E., Titania−sepiolite nanocomposites prepared by a surfactant templating colloidal route. *Chemistry of Materials* **2007,** *20*, 84-91.

143.   de Paiva, L. B.; Morales, A. R.; Valenzuela Díaz, F. R., Organoclays: Properties, preparation and applications. *Applied Clay Science* **2008,** *42*, 8-24.

144.   Jordan, J. W.; Hook, B. J.; Finlayson, C. M., The Organophilic Bentonites. II. Organic Liquid Gels. *The Journal of Physical and Colloid Chemistry* **1950,** *54*, 1196-1208.

145.   Wang, L.; Wang, A., Adsorption properties of Congo Red from aqueous solution onto surfactant-modified montmorillonite. *Journal of hazardous materials* **2008,** *160*, 173-180.

146.   Chen, D.; Du, G.; Zhu, Q.; Zhou, F., Synthesis and characterization of TiO_2 pillared montmorillonites: Application for methylene blue degradation. *Journal of Colloid and Interface Science* **2013,** *409*, 151-157.

147.   Li, Y.; Liu, J. R.; Jia, S. Y.; Guo, J. W.; Zhuo, J.; Na, P., TiO_2 pillared montmorillonite as a photoactive adsorbent of arsenic under UV irradiation. *Chemical Engineering Journal* **2012,** *191*, 66-74.

148.   Manova, E.; Aranda, P.; Martín-Luengo, M. A.; Letaïef, S.; Ruiz-Hitzky, E., New titania-clay nanostructured porous materials. *Microporous and Mesoporous Materials* **2010,** *131*, 252-260.

149.   Dvininov, E.; Popovici, E.; Pode, R.; Cocheci, L.; Barvinschi, P.; Nica, V., Synthesis and characterization of TiO_2-pillared Romanian clay and their application for azoic dyes photodegradation. *Journal of hazardous materials* **2009,** *167*, 1050-1056.

150.   Okada, K.; Yoshizawa, A.; Kameshima, Y.; Isobe, T.; Nakajima, A.; Mackenzie, K. J. D., Adsorption and photocatalytic properties of TiO_2/mesoporous silica composites from two silica sources (acid-leached kaolinite and Si-alkoxide). *Journal of Porous Materials* **2011,** *18*, 345-354.

151.   Sterte, J., Synthesis and properties of titanium oxide cross-linked montmorillonite. *Clays and Clay Minerals* **1986,** *34*, 658-664.

152.   Ooka, C.; Akita, S.; Ohashi, Y.; Horiuchi, T.; Suzuki, K.; Komai, S.-i.; Yoshida, H.; Hattori, T., Crystallization of hydrothermally treated TiO_2 pillars in pillared montmorillonite for improvement of the photocatalytic activity. *Journal of Materials Chemistry* **1999,** *9*, 2943-2952.

153.   Zhu, H. Y.; Ding, Z.; Barry, J. C., Porous Solids from Layered Clays by Combined Pillaring and Templating Approaches. *The Journal of Physical Chemistry B* **2002,** *106*, 11420-11429.

154.   Yan, L.-G.; Wang, J.; Yu, H.-Q.; Wei, Q.; Du, B.; Shan, X.-Q., Adsorption of benzoic acid by CTAB exchanged montmorillonite. *Applied Clay Science* **2007,** *37*, 226-230.

155.   Kibanova, D.; Trejo, M.; Destaillats, H.; Cervini-Silva, J., Synthesis of hectorite–TiO_2 and kaolinite–TiO_2 nanocomposites with photocatalytic activity for the degradation of model air pollutants. *Applied Clay Science* **2009,** *42*, 563-568.

156.   He, H.; Ding, Z.; Zhu, J.; Yuan, P.; Xi, Y.; Yang, D.; Frost, R. L., Thermal characterization of surfactant-modified montmorillonites. *Clays and Clay Minerals* **2005,** *53*, 287-293.

157.   Bai, Y.; Yang, T.; Gu, Q.; Cheng, G.; Zheng, R., Shape control mechanism of cuprous oxide nanoparticles in aqueous colloidal solutions. *Powder Technology* **2012,** *227*, 35-42.

158.   Shah, M. A., Preparation of Copper (Cu) and Copper Oxide (Cu_2O) Nanoparticles under Supercritical Conditions. *Materials Sciences and Applications* **2011,** *02*, 977-980.

159.   Darezereshki, E.; Bakhtiari, F., A novel technique to synthesis of tenorite (CuO) nanoparticles from low concentration $CuSO_4$ solution. *Journal of Mining and Metallurgy Section B-Metallurgy* **2011,** *47*, 73-78.

160.   Zohra, B.; Aicha, K.; Fatima, S.; Nourredine, B.; Zoubir, D., Adsorption of Direct Red 2 on bentonite modified by cetyltrimethylammonium bromide. *Chemical Engineering Journal* **2008,** *136*, 295-305.

161.   Stanjek, H.; Häusler, W., Basics of X-ray Diffraction. *Hyperfine Interactions* **2004,** *154*, 107-119.

162.   Atkins, P.; Jones, L., *Chemical principles*. WH Freeman: **2006**.

163.   MooreD. M. and Reynolds, R. C., *X-Ray Diffraction and the Identification and Analysis of Clay Minerals*. Oxford University Press, New York, **1997**.

164.   Dunlap, M., Introduction to the Scanning Electron Microscope.

165.   Petherbridge, J. R. Diagnostics of microwave activated novel gas mixtures for diamond chemical vapour deposition. University of Bristol, **2002**.

166.   Smith, B. C., *Fundamentals of FourierTransform Infrared Spectroscopy*. CRC: **2009**.

167.   Sathyanarayana, D. N., *Vibrational spectroscopy: Theory and applications*. New Age International: **2007**.

168.   Sattler, K. D., *Handbook of Nanophysics: Functional Nanomaterials*. 1 ed.; CRC Press: **2010**.

169.   Steehler, J. K., Ewing's Analytical Instrumentation Handbook, 3rd Edition (Cazes, Jack). *Journal of Chemical Education* **2005,** *82*, 1315.

170.   Akolekar, D.; Chaffee, A.; Howe, R. F., The transformation of kaolin to low-silica X zeolite. *Zeolites* **1997,** *19*, 359-365.

171.   Panias, D.; Giannopoulou, I. P.; Perraki, T., Effect of synthesis parameters on the mechanical properties of fly ash-based geopolymers. *Colloids and Surfaces A: Physicochemical and Engineering Aspects* **2007,** *301*, 246-254.

172.   Mackenzie, K.; Smith, M., Chapter 6 17O NMR. In *Pergamon Materials Series*, Kenneth, J. D. M.; Mark, E. S., Eds. Pergamon: **2002**; Vol. Volume 6, pp 333-395.

173.   Mackenzie, K.; Smith, M., Chapter 1 Introduction. In *Pergamon Materials Series*, Kenneth, J. D. M.; Mark, E. S., Eds. Pergamon: **2002**; Vol. Volume 6, pp 3-19.

174.   Kroeker, S.; Wasylishen, R. E.; Hanna, J. V., The structure of solid copper (I) cyanide: A multinuclear magnetic and quadrupole resonance study. *Journal of the American Chemical Society* **1999,** *121*, 1582-1590.

175.   Vega, A. J., 63Cu NQR Nutation Spectroscopy and Spin Counting in Copper Oxides. *Israel journal of chemistry* **1992,** *32*, 195-204.

176.   Kroeker, S.; Hanna, J. V.; Wasylishen, R. E.; Ainscough, E. W.; Brodie, A. M., Anisotropy in the 31 P, 63/65 Cu Indirect Spin–Spin Coupling and 31 P Nuclear Shielding Tensors of Linear Copper (I) Phosphines. *Journal of Magnetic Resonance* **1998,** *135*, 208-215.

177.   Kroeker, S.; Wasylishen, R. E.; Hanna, J. V., The Structure of Solid Copper(I) Cyanide: A Multinuclear Magnetic and Quadrupole Resonance Study. *Journal of the American Chemical Society* **1999,** *121*, 1582-1590.

178.   Li, L.; Wang, S.; Zhu, Z., Geopolymeric adsorbents from fly ash for dye removal from aqueous solution. *Journal of Colloid and Interface Science* **2006,** *300*, 52-59.

179.   Skoog, D. A.; Holler, F. J.; Crouch, S. R., *Principles of Instrumental Analysis*. Brooks/Cole: 2007.

180.   John Crocker, D. B., *The Science of Laboratory Diagnosis*. 2 ed.; Wiley: **2005**.

181.   Cardoso, N. F.; Lima, E. C.; Pinto, I. S.; Amavisca, C. V.; Royer, B.; Pinto, R. B.; Alencar, W. S.; Pereira, S. F., Application of cupuassu shell as biosorbent for the removal of textile dyes from aqueous solution. *Journal of Environmental Management* **2011,** *92*, 1237-1247.

182.   Pujol, J., The solution of nonlinear inverse problems and the Levenberg-Marquardt method. *GEOPHYSICS* **2007,** *72*, W1-W16.

183.   Zhang, X.; Song, J.; Jiao, J.; Mei, X., Preparation and photocatalytic activity of cuprous oxides. *Solid State Sciences* **2010,** *12*, 1215-1219.

184.   Phair, J. W.; Van Deventer, J. S. J.; Smith, J. D., Mechanism of Polysialation in the Incorporation of Zirconia into Fly Ash-Based Geopolymers. *Industrial & Engineering Chemistry Research* **2000,** *39*, 2925-2934.

185.   Xue, W.; He, H.; Zhu, J.; Yuan, P., FTIR investigation of CTAB–Al–montmorillonite complexes. *Spectrochimica Acta Part A: Molecular and Biomolecular Spectroscopy* **2007,** *67*, 1030-1036.

186.   Madejová, J.; Janek, M.; Komadel, P.; Herbert, H. J.; Moog, H. C., FTIR analyses of water in MX-80 bentonite compacted from high salinary salt solution systems. *Applied Clay Science* **2002,** *20*, 255-271.

187.   Vega, A. J., 63Cu NQR Nutation Spectroscopy and Spin Counting in Copper Oxides. *Israel journal of chemistry* **1992,** *32*, 195-204.

188.   MacKenzie, K. J.; Smith, M. E., *Multinuclear solid-state nuclear magnetic resonance of inorganic materials*. Elsevier: **2002**; Vol. 6.

189.   Atun, G.; Hisarli, G.; Sheldrick, W. S.; Muhler, M., Adsorptive removal of methylene blue from colored effluents on fuller's earth. *Journal of Colloid and Interface Science* **2003,** *261*, 32-39.

190.   Bickley, R. I.; Gonzalez-Carreno, T.; Lees, J. S.; Palmisano, L.; Tilley, R. J., A structural investigation of titanium dioxide photocatalysts. *Journal of Solid State Chemistry* **1991,** *92*, 178-190.

191.   Hurum, D. C.; Agrios, A. G.; Gray, K. A.; Rajh, T.; Thurnauer, M. C., Explaining the enhanced photocatalytic activity of Degussa P25 mixed-phase TiO_2 using EPR. *The Journal of Physical Chemistry B* **2003,** *107*, 4545-4549.

192.   Ohtani, B.; Prieto-Mahaney, O. O.; Li, D.; Abe, R., What is Degussa (Evonik) P25 Crystalline composition analysis, reconstruction from isolated pure particles and photocatalytic activity test. *Journal of Photochemistry and Photobiology A: Chemistry* **2010,** *216*, 179-182.

193.   Zhou, Q.; He, H. P.; Zhu, J. X.; Shen, W.; Frost, R. L.; Yuan, P., Mechanism of p-nitrophenol adsorption from aqueous solution by HDTMA+-pillared montmorillonite—implications for water purification. *Journal of hazardous materials* **2008,** *154*, 1025-1032.

194.   Johnston, C.; Sposito, G.; Erickson, C., Vibrational probe studies of water interactions with montmorillonite. *Clays and Clay Minerals* **1992,** *40*, 722-730.

195.   Mall, I. D.; Srivastava, V. C.; Agarwal, N. K.; Mishra, I. M., Removal of congo red from aqueous solution by bagasse fly ash and activated carbon: Kinetic study and equilibrium isotherm analyses. *Chemosphere* **2005,** *61*, 492-501.

196.   Cardoso, N. F.; Lima, E. C.; Pinto, I. S.; Amavisca, C. V.; Royer, B.; Pinto, R. B.; Alencar, W. S.; Pereira, S. F., Application of cupuassu shell as biosorbent for the removal of textile dyes from aqueous solution. *J Environ Manage* **2011,** *92*, 1237-47.